AN ABSTRACT OF A THESIS

MODELING, CONTROL AND ANALYSIS OF A DOUBLY FED INDUCTION GENERATOR BASED WIND TURBINE SYSTEM WITH VOLTAGE REGULATION

Bijaya Pokharel

Master of Science in Electrical Engineering

Wind power is the most reliable and developed renewable energy source. The share of wind power with respect to total installed power capacity is increasing worldwide. The Doubly Fed Induction Generator (DFIG) based wind turbine with variable-speed variable-pitch control scheme is the most popular wind power generator in the wind power industry. This machine can be operated either in grid connected or standalone mode. A thorough understanding of the modeling, control, and dynamic as well as the steady state analysis of this machine in both operation modes is necessary to optimally extract the power from the wind and accurately predict its performance.

In this thesis, a detailed electromechanical model of a DFIG-based wind turbine connected to power grid as well as autonomously operated wind turbine system with integrated battery energy storage is developed in the Matlab/Simulink environment and its corresponding generator and turbine control structure is implemented. A thorough explanation of this control structure as well as the steady state behaviour of the overall wind turbine system is presented. The steady state reactive power capability of the DFIG is studied.

Typically, most of the wind turbines are located at remote places or offshore where the power grid is usually long and weak characterized by under voltage condition. Because of the limited reactive power capability, DFIG cannot always supply required reactive power; as a result, its terminal voltage fluctuates. Hence, a voltage regulation device is required for the secure operation of the overall wind turbine together with power grid during normal operation as well as disturbances in the grid. Flexible ac transmission system (FACTS) devices, through their fast, flexible, and effective control capability, provide solution to this challenge. Therefore, this thesis examines the use of Static Synchronous Compensator (STATCOM) at the Point of Common Coupling (PCC) to regulate terminal voltage of the DFIG wind turbine system. The series compensation in the transmission line to improve steady state voltage and enhance power carrying capability of the line is also examined. Simulation results verify the effectiveness of the proposed system for steady state as well as dynamic voltage regulation.

MODELING, CONTROL AND ANALYSIS OF A DOUBLY FED INDUCTION GENERATOR BASED WIND TURBINE SYSTEM WITH VOLTAGE REGULATION

A Thesis

Presented to

The Faculty of the Graduate School

Tennessee Technological University

By

Bijaya Pokharel

In Partial Fulfillment

Of the Requirements of the Degree

MASTER OF SCIENCE

Electrical Engineering

December 2011

CERTIFICATE OF APPROVAL OF THESIS

MODELING, CONTROL AND ANALYSIS OF A DOUBLY FED INDUCTION GENERATOR BASED WIND TURBINE SYSTEM WITH VOLTAGE REGULATION

By

Bijaya Pokharel

Graduate Advisory Committee:

Joseph O. Ojo, Chairperson	Date
Ghadir Radman	Date
Periasamy K. Rajan	Date

Approved for the Faculty:

Francis Otuonye
Associate Vice President
for Research and Graduate Studies

Date

DEDICATION

This work is dedicated to my parents who have supported me throughout my education.

ACKNOWLEDGEMENTS

I would like to express my sincere thanks to Dr. Joseph O. Ojo, my advisor and the chairperson of the advisory committee, for his continuous guidance and encouragement throughout this research work. I would like to take this opportunity to thank Dr. Ghadir Radman and Dr. Periasamy K. Rajan for their support as members of my advisory committee. I would also like to thank all the lab members of Power Electronics and Drives Lab; especially to Hossein, Meharegzi, Melaku, Kennedy and Amrit for their valuable advice and continuous support during the completion of this work.

I am thankful to the Center for Energy Systems Research (CESR), and Department of Electrical and Computer Engineering for the financial support during my study. I would like to thank Mr. Tony Greenway and Mr. Robert Craven for their help with computer and software.

I would like to thank my parents for their lifetime support, generous love, never-ending patience, and inspiration. Finally, I am thankful to my friends for their valueable time and support.

TABLE OF CONTENTS

LIST OF FIGURES

Page

LIST OF TABLES

Page

LIST OF ABBREVIATIONS AND ACRONYMS

AC - Alternating Current

DC - Direct Current

DFIG - Doubly Fed Induction Generator

FACTS - Flexible Alternating Current Transmission Systems

GSC - Grid Side Converter

HVRT - High Voltage Ride Through

IGBT - Insulated Gate Bipolar Transistor

LPF – Low Pass Filter

LSC - Load Side Converter

LVRT - Low Voltage Ride Through

MPPT - Maximum Power Point Tracking

PCC - Point of Common Coupling

PLL - Phase Locked Loop

PWM - Pulse Width Modulation

RSC - Rotor Side Converter

SC - Series Compensation

STATCOM - Static Synchronous Compensator

VFC - Voltage to Frequency Converter

VSC - Voltage Source Converter

WECS - Wind Energy Conversion System

CHAPTER 1

INTRODUCTION

1.1 Introduction to Wind Energy Conversion System

Wind Energy Conversion System (WECS) is the overall system for converting wind energy into useful mechanical energy that can be used to power an electrical generator for generating electricity. The WECS basically consists of three types of components: aerodynamics, mechanical, and electrical as shown in Figure 1.1 [1].

1.1.1 Wind Turbines

I. VAWT/HAWT

From the physical setup viewpoint, there are horizontal axis wind turbines (HAWT) and vertical axis wind turbines (VAWT) [2]. Initially, vertical axis designs were considered due to their expected advantages of omni-directionality (hence do not need

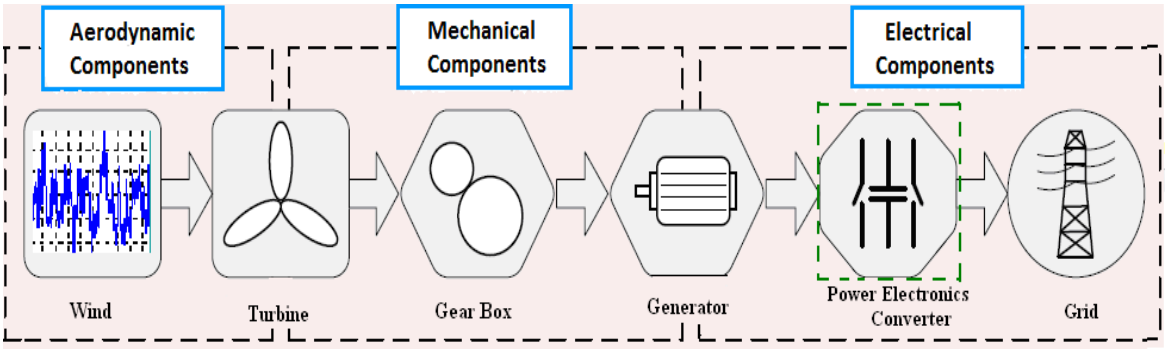

Figure 1.1 Block Diagram showing the components of WECS connected to grid [1] (dashed item is architecture dependent)

Figure 1.2 Examples of HAWT (a) and VAWT (b, c and d) [2]

yaw-system) and having gears and generating equipments at the tower base. However, the following disadvantages caused the VAWT to have a diminished presence in the commercial market:

- Reduced aerodynamic efficiency: much of the blade surface is close to the axis.
- Housing usually at ground level so it is not feasible to have the gearbox of large VAWT at ground level because of the weight and cost of the transmission shaft.

In HAWT, the wind turbine blades rotate about an axis parallel to the ground and wind flow. Almost all the larger turbines employed in modern wind farms are HAWT because they are more suitable for harnessing more wind energy. However, HAWT are subjected to reversing gravitational loads (structural load is reversed when the blade goes from upwards to downwards position) which impose a limit on the size of such turbines

[2]. The rotation of both HAWT and VAWT can be powered primarily by lift or drag force depending on the design of the blade as shown in Figure 1.2.

II. Variable-speed, Pitch-regulated Wind Turbine

A variable speed wind turbine can incorporate a pitch regulation feature that involves turning the blades about their lengthwise axes (pitching the blades) to regulate the power extracted by the rotor.

Advantages:

- Turbine can operate at ideal tip-speed ratios over a larger range of wind speeds so as to capture maximum energy from wind.
- Ability to supply power at a constant voltage and frequency while the rotor speed varies.
- Control of the active and reactive power.

Disadvantages:

- Generates variable frequency current/voltage so needs power electronic converter.

III. Fixed-speed, Stall-regulated Wind Turbine

When the wind speed increases, the blades become increasingly stalled to limit power to acceptable levels without any additional active control hence the rotor speed is held essentially constant.

Advantage:

- Simple and robust construction, hence lower capital cost.

Disadvantages:

- Cannot extract optimum energy from wind.

- Do not have the capability of independent control of active and reactive power.
- Generates more mechanical stress on gearbox during variable wind speed.

The modern wind turbine industry is shifting towards variable speed because of their better overall performance. They take full advantage of variations in the wind speed; encounter lower mechanical stress and less power fluctuations and provide 10 - 15% higher energy output compared with constant speed operation [3].

Number of Blades:

To extract maximum possible amount of wind energy from wind, the blades should interact as much as possible with the wind blowing within swept area. Theoritically, more the number of blades a wind turbine has, the more efficient it should be. But in reality, when the number of blades increases; there will be more interference within blades. As a result, it is more likely that blade will pass through the disturbed weaker windflow region. From a structural stability viewpoint, the number of blades of HAWT should be odd and greater or equal to 3, in which case the dynamic properties of the turbine rotor are similar to those of a disc [4]. Hence most of the commercially available modern wind turbines are three-bladed.

Betz Limit:

Betz law says that we can only convert less than 16/27 (or 59.3%) of the kinetic energy in the wind to mechanical energy using a wind turbine [4]. It is because the wind after passing through wind turbine still has some velocity. Within the turbine, most of the energy is converted into useful electrical energy, while some of it is lost in gearbox, bearings, generator, power converter, transmission and others [4]. Most practical rotors with three blades can reach an overall efficiency of about 50%.

1.1.2 Components of Wind Turbines

The major components of a wind turbine system are shown in Figure 1.3 (drawing not to scale). The turbine is formed by the blades, the rotor hub and the connecting components. The drive train is formed by the turbine rotating mass, low-speed shaft, gearbox, high-speed shaft, and generator rotating mass. It transfers turbine mechanical output power up to the generator rotor where it is converted to electrical power. The wind strikes the rotor on the horizontal-axis turbine, causing it to spin. The low-speed shaft transfers energy to the gear box, which steps up in speed and rotates the high speed shaft. The high speed shaft causes the generator to spin, hence generating electricity. The yaw system is used to turn the nacelle so that the rotor faces into the wind. The low speed

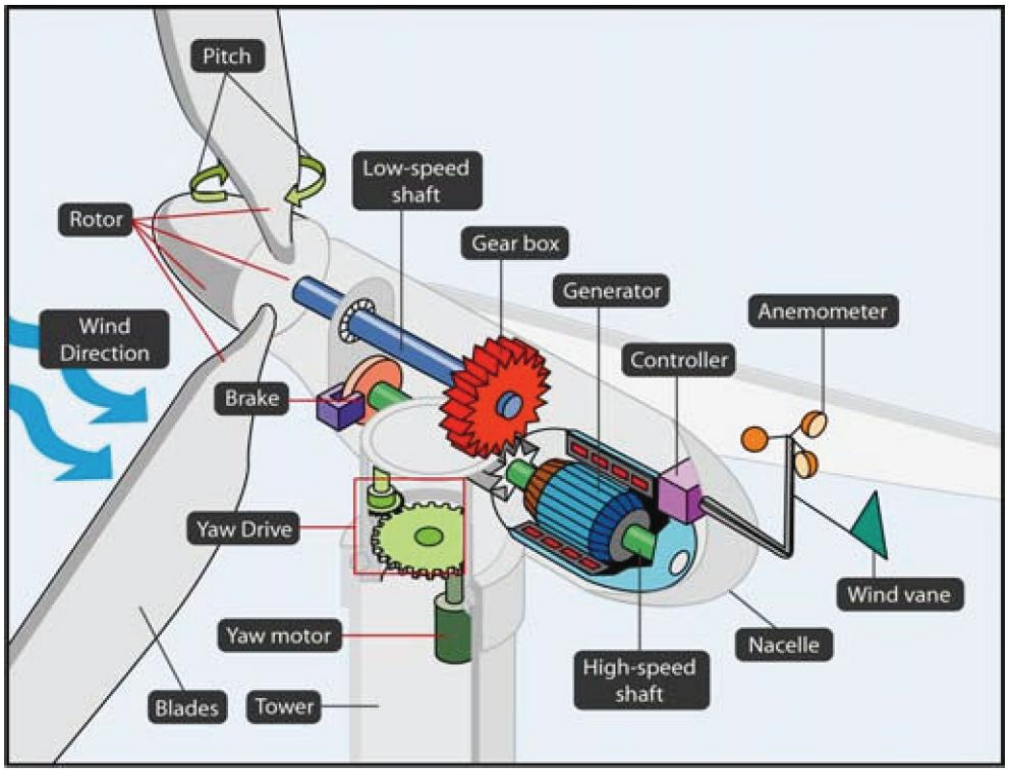

Figure 1.3 HAWT showing mechanical, electrical, and control components [5]

Shaft contains pipes for the hydraulics system that operates the aerodynamic brake [4]. The high speed shaft is equipped with an emergency mechanical brake which is used in case of failure of the aerodynamic brake [4].

The generator converts mechanical power of wind into electrical power. Usually the generator produces power at low voltage and the transformer steps up the generator output voltage to connected grid voltage. The transformer may be placed at the bottom of the tower [4] or in the nacelle for losses minimization [2].

Other components of wind turbine system are the anemometer to measure wind speed and a wind vane which measure the wind direction. Wind speed information is used to determine when the wind speed is sufficient to start up the turbine and when, due to high winds, the turbine must be shut down for safety whereas wind direction measurement is used by the yaw-control mechanism which helps in orienting the rotor to the wind direction [5]. Electric fans and oil coolers are used to cool the gearbox and generator.

1.1.3 Operating Region of the Wind Turbine

The operating region of a variable-speed variable-pitch wind turbine can be illustrated by their power curve, which gives the estimated power output as function of wind speed as shown in Figure 1.4. Three distinct wind speed points can be noticed in this power curve:

- Cut-in wind speed: The lowest wind speed at which wind turbine starts to generate power.

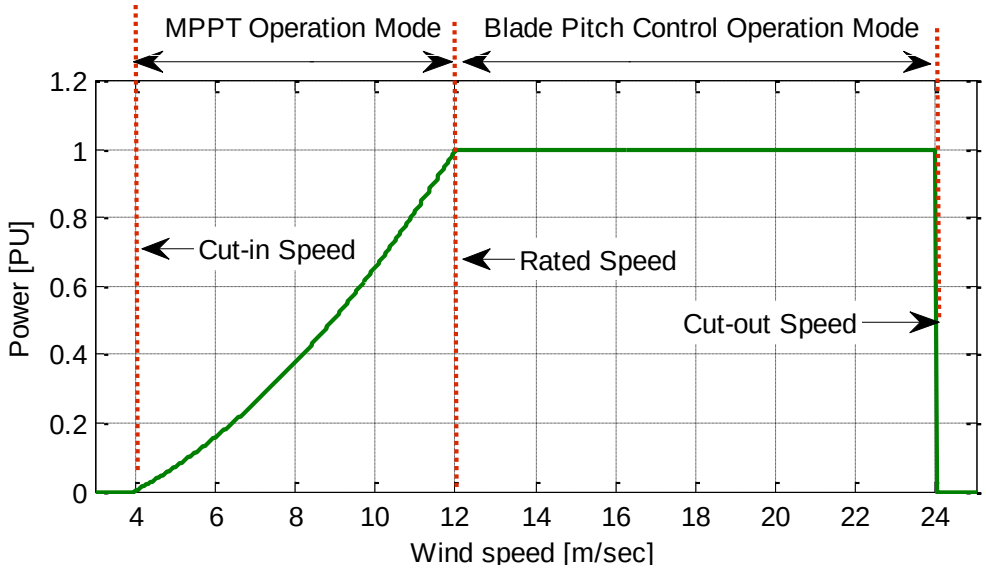

Figure 1.4 Power curve of a variable speed wind turbine

- Rated wind speed: Wind speed at which the wind turbine generates the rated power, which is usually the maximum power wind turbine can produce.
- Cut-out wind speed: Wind speed at which the turbine ceases power generation and is shut down (with automatic brakes and/or blade pitching) to protect the turbine from mechanical damage [2].

1.1.4 Control of Wind Turbine System

With the increase in wind turbine size and power, its control system plays a major role to operate it in safe region and also to improve energy conversion efficiency and output power quality. The main objectives of a wind turbine control system are [6]:

- Energy capture: The wind turbine is operated to extract the maximum amount of wind energy considering the safety limits like rated power, rated speed.

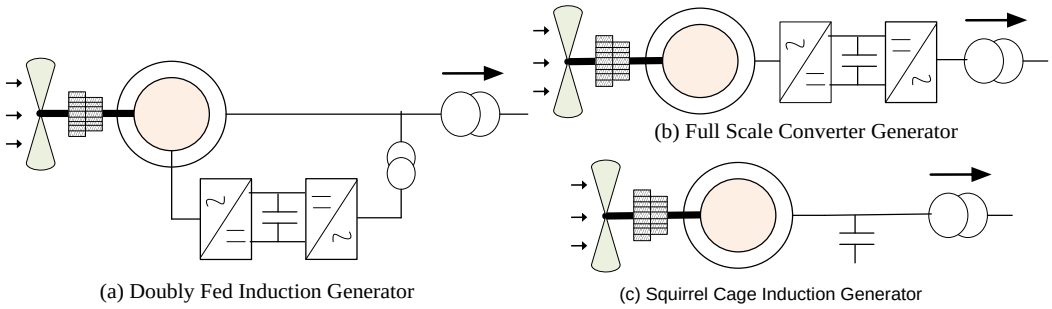

Figure 1.5 Electrical generators used in commercial wind turbines

- Power quality: Conditioning the generated power with grid interconnection standards.

The various control techniques used in wind turbines are pitch control, yaw control and stall control. But in the modern variable speed-variable pitch wind turbines, pitch control is the most popular control scheme [7]. In this control scheme, the horizontal axis wind turbine blades are rotated around its tower to orient the turbine blades in upwind or down wind direction.

1.1.5 Wind Turbine Generators

Wind Turbine Generators in the current market can be classified into three types according to their operation speed and the size of the associated converters as below:

- Fixed Speed Wind Turbine (FSWT)
- Variable Speed Wind Turbine (VSWT) with:
  - Partial Scale Frequency Converter Wind Turbine (PSFCWT)
  - Full Scale Frequency Converter Wind Turbine (FSFCWT)

Variable-speed variable-pitch wind turbines utilizing DFIG, also called PSFCWT, are the most popular in the wind power industry especially for multi-megawatt wind turbine generators [8]. The DFIG consists of a wound rotor induction generator with the stator side connected directly to the constant frequency three-phase grid and the rotor windings connected to grid through a bidirectional back-to-back ac/dc/ac IGBT voltage source converter as shown in Figure 1.5 (a). Its output power can be controlled via pitch control as well as back to back converter control.

The term 'Doubly Fed' refers to the fact that the voltage on the stator is applied from the grid and the voltage on the rotor is induced by the power converter. This system allows a variable-speed operation over a large, but restricted, range [9]. The converter compensates the difference between the mechanical and electrical frequencies by injecting a rotor current with a variable frequency [9]. Hence, the operation and behavior of the DFIG is governed by the power converter and its controllers.

Table 1.1 Summary of features of FSWT and FSFCWT generators [6]:

	FSWT	**FSFCWT**
Structure	Figure 1.5(c)	Figure 1.5(b)
Machines	Squirrel Cage Induction Generator	Permanent Magnet Synchronous Generator
Merits	• Simple construction • Low cost • Low maintenance	• Complete control of active and reactive powers • High efficiency
Demerits	• No control on real/reactive power • Less efficiency • Poor power factor • High mechanical stress on turbine	• Additional cost of power electronics • Limited fault ride through capability

The power converter consists of two converters, the Rotor Side Converter (RSC) and the Grid Side Converter (GSC), which are controlled independently of each other. The RSC controls the active and reactive power by controlling the rotor current components, while the GSC controls the DC link voltage and DFIG terminal voltage or power factor of the overall DFIG system by controlling amount of reactive power exchanged with the power grid.

Stator side always feeds active power to the grid whereas active power is fed into or out of the rotor depending on the operating condition of the drive. In super-synchronous speed, power flows from the rotor via the converter to the grid, whereas it flows in the opposite direction in sub-synchronous speed of the drive.

Advantages of DFIG wind turbine system:

- It has ability to control reactive power and decouple control of active and reactive power by independently controlling the rotor excitation current. So power factor control can be implemented in this system [10].
- DFIG is wound rotor induction machine which is simple in construction and cheaper than the synchronous machine. In DFIG, converter rating is typically 25-30 % of total system power which results: reduced converter cost, less harmonics injection to the connected grid and improved overall efficiency (approx. 2-3% more than full scale frequency converter) of the wind turbine system [10].
- In the case of a weak grid, where the voltage may fluctuate, the DFIG can produce or absorb an amount of reactive power to or from the grid within its capacity, to regulate the terminal voltage.
- High energy conversion efficiency.

- Smaller power rated DFIG can be used with higher power rated wind turbine.

Disadvantages of DFIG wind turbine system:

- Inevitable need of slip rings and gear box which requires frequent maintenance [9].
- Limited reactive power capability [8] and fault ride through capability [6].

1.2 Motivation of the Research

Wind power is the most reliable and developed renewable energy source over past decades. The increased awareness of people towards renewable energy, support from governmental institution, and rapid advancement in the power electronics industry, which is the core of wind power systems, are the most contributing factors for the development of wind power systems. As a result, the share of wind power with respect to total installed power capacity is increasing worldwide. The WECS utilizing variable-speed variable-pitch wind turbine with DFIG is the most popular in the wind power industry especially for multi-megawatt size. The beauty of the DFIG-based WECS is its efficient power conversion capability at variable wind speed with reduced mechanical stress and low price because of partial size rated power converters needed to achieve the full control of the machine. These favorable technical and economical characteristics have encouraged the commercialization of this wind turbine in the modern wind power industry quickly. Unfortunately, these kinds of wind turbines have limited reactive power capability and are typically connected at remote areas and offshore mainly because of favourable wind condition, noise pollution, physical dimension and impact on the scenery. These areas usually have electrically weak power grids characterized by low short circuit ratios and under-voltage conditions.

Hence, to assist its further integration into the modern power system, it is therefore important to assess its dynamical behavior, steady state performance, and impacts on the interconnected power network with regard to its reactive power capability and voltage control. The voltage at the particular bus in the power system is a local quantity. It is very difficult or even impossible to regulate the node voltage at the remote location using conventional power stations located elsewhere in the grid. So, a local reactive power source is needed. With the fast advancement in power electronics technology, FACTS devices having excellent dynamic response are technically and economically feasible in power system application. Therefore, in this study, reactive power compensation using the STATCOM at the PCC is studied to enhance the reactive power capability and voltage controllability of the DFIG wind turbine system for improving dynamic and steady state stability of the wind turbine system as well as the interconnected weak power system.

Additionally, series compensation of transmission line helps in steady state voltage regulation and enhances the transmission line power carrying capability. Moreover, off grid applications of the DFIG-based WECS is very important to supply power to the remote places where there is no grid supply. This operation mode involves standalone operation of DFIG-based WECS. Standalone operation of grid connected DFIG system is also needed in case of failure of the main supply due to breaking of the transmission line or permanent short circuit in the grid to supply part of an isolated load. This increases the reliability of the power supply system. Hence, this thesis is motivated at contributing to the better understanding of the DFIG-based WECS and its interaction with the STATCOM as well as series compensated line in regard to those aspects.

1.3 Objectives of the Thesis

The main objective of this thesis is to develop a dynamic model and analyze the steady state performance of the grid connected DFIG-based WECS. Moreover, to assess the integration of this kind of wind turbine into a particularly weak power system, it is important to study its steady state reactive power capability and voltage controllability. The DFIG wind turbine system has limited reactive power capability so an additional reactive power source is needed to meet the power factor requirement and to secure the voltage regulation in the system during all the operation time including periods with transient disturbances in the connected grid. STATCOM has better dynamic reactive power capabilities than other FACTS devices so it is used as an additional dynamic reactive power source in this study. Hence, modeling and control of STATCOM is the another objective of this thesis. Series compensated line provides steady state voltage regulation and enhances the power transferring capability of the line. Modelling and analysis of the DFIG wind turbine interfaced with series compensated line is another objective of this thesis. Standalone operation of the DFIG system is required: 1) to supply off grid loads in remote area and 2) to supply local loads connected to grid in case of failure of the main supply. Standalone operation of the DFIG system needs more complex control system development. Modeling and control of the autonomous operation of the DFIG system with integrated battery energy storage system is also an objective of this thesis.

1.4 Methodology

The following methodology has been adopted in order to carry out the research work:

- The complete modeling and control of DFIG-based WECS connected to power grid is done so that its behavior and interaction with the power grid during transient and steady state conditions can be determined.
- The steady state reactive power capability of the DFIG wind turbine system is derived to understand when the DFIG needs additional reactive power in the steady state to maintain the desired power factor.
- The complete modeling and control of STATCOM connected to power grid is developed to know its interaction with the DFIG wind turbine system during transient and steady state conditions. Based on the necessary reactive power to meet the power factor requirement, the maximum MVA rating of STATCOM is calculated.
- Complete model of the DFIG-based wind turbine interfaced with series compensated line is built to study the effect of series compensation on voltage regulation of this wind turbine and power transferring capability of the line.
- The model of the autonomously operated DFIG-based WECS connected with a integrated battery energy storage system is developed and its control is implemented in Matlab/Simulink to study its transient and steady state characteristics.

1.5 Organization of the Thesis

This thesis is organized into eight chapters. Chapter 1 gives the introduction of the DFIG-based WECS and the motivation and objectives of the thesis. Chapter 2 provides a literature review for modeling and control of the DFIG-based WECS connected to power grid, steady state reactive power capability of the DFIG, and grid code requirements for connecting wind turbines to power grid. Moreover, Chapter 2 also presents the literature review for necessity of additional reactive power source in the DFIG-based wind turbine system, modeling and control of the STATCOM, and control and operation of autonomously operated DFIG-based wind turbine system. Chapter 3 describes the modeling and control of the grid connected DFIG system, different operation modes of variable-speed variable-pitch wind turbine system and controllers design for the DFIG-based WECS. In Chapter 4, steady state characteristics of the DFIG-based WECS and its steady state control settings are discussed. The steady state reactive power capability of the DFIG is derived and steps of drawing PQ diagram of overall DFIG and STATCOM to meet the power factor requirement is presented through the flowchart. In Chapter 5, modeling and controller design of STATCOM is discussed along with dynamic and steady state voltage regulation in the DFIG wind turbine system using STATCOM. Chapter 6 presents the modeling and analysis of a DFIG wind turbine connected to power grid through series compensated line. Chapter 7 illustrates the modeling, controller design, operation, and analysis of the autonomously operated DFIG-based WECS with integrated battery energy storage. Finally, in Chapter 8, a summary of research 99contributions and extensions for future work are presented.

CHAPTER 2

LITERATURE REVIEW

2.1 Introduction

This chapter presents the relevant literature review done to carry out this research work. Section 2.2 gives a survey and comparison of various approaches for the DFIG wind turbine system dynamic modeling. In Section 2.3, a literature survey related to steady state analysis and reactive power capability of the DFIG system are presented. Section 2.4 describes the work done on the voltage regulation in the DFIG wind turbine system using STATCOM. The interaction of the DFIG wind turbine system with the series compensated line is discussed in Section 2.5. Finally, in Section 2.6, existing methods of control for the autonomous operation of the DFIG wind turbine system with integrated energy storage is discussed.

2.2 Dynamic Modeling and Control of the DFIG System

Global concern about the environmental pollution and continuously increasing energy demand has led to the growing interest in innovative technologies for generation of clean and renewable electrical energy. Among a variety of renewable energy sources, wind power is the most rapidly growing one in the power industry.

The traditional wind turbine generator (WTG) systems employ squirrel-cage induction generators (SCIGs) to generate wind power. These WTGs have no speed control capability and cannot provide voltage or frequency support when connected to the power grid [11]. During the past decade, the concept of a variable-speed wind turbine driving a doubly fed induction generator (DFIG) has received increasing attention because of its noticeable advantages over other WTG systems [12]-[15]. Most existing wind farms and those in planning employ this type of WTGs. Compared to the fixed-speed SCIG wind turbines, the DFIG wind turbines can provide decoupled active and reactive power control of the generator, more efficient energy production, improved power quality and improved dynamic performance [8-10]. All of those above mentioned advantages of the DFIG are possible because of the control scheme that can be implemented in the back-to-back converters of the DFIG. Hence, the method of controlling this back-to-back converter plays a significant role in achieving better performance of the DFIG system. Different types of the modeling and control schemes for the DFIG system can be found in the literatures which are discussed here.

The Doubly Fed Induction Machine using an ac/dc/ac converter in the rotor circuit (Schrebius drive) has long been a standard drive option for high power applications involving a limited speed range. The power converters only need to handle the rotor side power. In 1980, Leonhard explains the vector control technique used for the independent control of torque and excitation current [16]. The converter design and control technique are well explained in [17]. Pena, Clare and Asher [18] gave a detailed design of the DFIG using back-to-back PWM voltage source converters in the rotor circuit and they also validated the system experimentally considering a grid connected system.

Energy extraction from a DFIG wind turbine depends not only on the induction generator but also on the control strategies developed using different orientation frames. The DFIG usually operates in vector control mode based on the PI controllers in a synchronous reference frame either to the stator-flux-oriented (SFO) or stator-voltage-oriented (SVO) frames. The DFIG with PI controllers and its performance under normal operation conditions has been discussed in a number of publications [19-23]. It is well known that the DFIG performance with PI controllers is excellent in normal grid conditions, allowing independent control of the grid active and reactive power [24, 25]. In [26, 27], the SFO frame is used to develop the DFIG wind power extraction mechanisms. Another approach, for example, direct-power-control strategies for DFIG wind turbines using the SFO frame [28], has also been proposed recently. Although, the SVO frame is normally not used in a DFIG design, [29] and [30] report special approaches to improve DFIG stability under unbalanced conditions using the SVO frame. In [29], a DFIG system model in the positive and negative synchronous reference frames is presented to enhance the stability of the DFIG under unbalanced voltage supply. In [30], it is shown that a DFIG control strategy can enhance the standard speed and reactive power control with controllers that can compensate for the problems caused by an unbalanced grid by balancing the stator currents and eliminating torque and reactive power pulsations. In [31], a rotor position Phase-Locked Loop (PLL) is used which acquires the rotor position and rotor speed simultaneously for the implementation of the decoupled P-Q control in the DFIG. The rotor position PLL is designed to operate without the knowledge of any parameter of the DFIG except the magnetization reactance. In [32], comparison between SFO and SVO reference frames is done and it is shown that

the performance of DFIG wind power extraction is similar to using both SVO and SFO frames. But, it is found that a conventional wind power extraction approach using the SFO frame could deteriorate the power quality of the DFIG system while it is more stable to estimate the position of the stator-flux space vector by simply adding -90 degree to the stator-voltage space vector [32].

Hence, in this thesis, the variable-speed, variable-pitch wind turbine is designed to operate in maximum power point operation mode at low and medium wind speeds and in pitch control mode at higher wind speed. The vector control technique using SVO reference frame is used to get de-coupled control of active and reactive power from the DFIG based wind turbine. The PI controller design for Rotor Side Converter and Grid Side Converter is presented clearly.

2.3 Real and Reactive Power Capability of the DFIG

With the increased penetration level of wind power in the power system, grid utilities want wind turbine generator system to behave like a conventional synchronous generator in terms of real and reactive power settings [33]. In other words, wind turbines have to contribute not only to active power generation but also to the reactive power. Hence, wind turbines should have extended reactive power capability not only during voltage dips but also in steady state operation [8]. Although, the DFIG wind turbines are able to control active and reactive power independently of one another by virtue of ac/dc/ac power electronic converter present on it, the reactive power capability of those generators depend on the active power generated, the slip and the limitation due to

following design parameters: 1) rotor voltage, 2) stator current and 3) rotor current [34, 35]. The grid side inverter reactive power capability can be taken into consideration, but in commercial system, this converter usually works with unity power factor, i.e. zero reactive power, so the total reactive power capability of the generator is equal to the stator reactive power capability [34, 35].

Therefore, in this thesis, the steady state operation of the DFIG wind turbine system is described clearly through the characteristic curves. The steady state active power flow in the stator and rotor side is presented for sub-synchronous and super-synchronous operation modes of the DFIG. The reactive power capability of the DFIG is studied through the P-Q diagram. The reactive power capability is obtained for maximum power point operation mode and is extended to the pitch control operation mode of the DFIG as well which is not found in the literature. The reactive power capability curve of the overall DFIG with the STATCOM connected at the PCC is derived to meet the steady state power factor requirement.

2.4 Voltage Regulation in the DFIG Wind Turbine System Using STATCOM at PCC

The reactive power capability of the DFIG system is limited [8, 34 and 35]. Typically most large size wind turbines are usually installed at remote places or offshore because of their dimension and impact on the scenery [36]. Those areas usually have electrically weak power grids characterized by low short circuit ratios and under-voltage conditions [37], which means, they require special consideration in connecting those wind turbines to the grid [38]. In such grid conditions and during a grid side disturbance,

the DFIGs may not be able to provide sufficient reactive power support. Without any external dynamic reactive compensation, there can be a risk of voltage instability in the power grid [12]. The aerodynamic behaviour of wind turbine causes its output voltage fluctuation [39]. Voltage instability problems occur in a power system that cannot supply the reactive power demand during disturbances like faults, heavy loading, voltage swelling and voltage sagging [40]. This problem is more severe in case of the weak power grids having under-voltage. During the grid side disturbances, the power electronic converters in the DFIG may be damaged because of the high voltage induced in it [40]. To prevent such contingencies, utilities typically immediately disconnect the WTGs from the grid, and reconnect them when normal operation has been restored. This is possible, as long as wind power penetration remains low. However, with the rapid increase in penetration of wind power in power systems, tripping of many WTGs in a large wind farm during grid faults may begin to influence the overall power system stability. Therefore, it will become necessary to require WTGs to support the network voltage and frequency not only during steady-state conditions but also during grid side disturbances. Moreover, the particular bus voltage is local quantity and hence it is very difficult and costly to control the bus voltage at the remote node by the use of conventional power stations consisting of synchronous generators and synchronous condensers located elsewhere in the grid [36]. It is because the reactive power flow in the power system is associated with changes in voltage which in turn increases the power losses (mainly I^2R loss) in the system. Hence it is necessary to install local voltage control devices in the transmission/distribution network even if the wind turbine itself has voltage controlling capability [36].

At the same time, the decentralization concept of power generation is becoming popular [36]. As a result, the contribution of conventional power plants to the voltage control in transmission network is diminishing. It is becoming more difficult to control the voltage in the entire transmission network from conventional power stations only [36]. Hence grid companies are installing dedicated local voltage control equipments and demanding distributed generation equipments to have reactive power capability irrespective of applied technology [36]. So there will not be any exception for wind power plants.

Recently, the utility companies are asking to fulfill certain criteria (grid codes) for the interconnection of wind turbines to the power grid. The grid codes mainly demand wind turbines to have low voltage ride-through capability and reactive power capability [35]. The first specification seeks to improve transient stability in a power system with a high penetration of wind energy, while the second specification targets to support steady state voltage regulation in such power system [35]. Another key requirement for wind power interconnection is that the power factor at the PCC must remain between 0.95 leading and 0.9 lagging [41]. The reason for this ruling is that reactive power capability for a wind plant is a significant additional cost compared to conventional units which possess inherent reactive power capability [41].

The problem of voltage fluctuation can be solved by using dynamic reactive power compensation technique installing the Flexible Alternating Current Transmission Systems (FACTS) devices [42]. FACTS devices are becoming more and more popular in power system these days because of rapid advancement in power electronics technology [40]. Among various FACTS devices, those based on the VSC concept have some

attractive features [43], such as rapid and continuous response characteristics for smooth dynamic control, allowing advanced control methodologies for the high-performance operation, elimination or reduced requirements for harmonic filtering, ability to add energy storage devices, allowing simultaneous active and reactive power exchange with the ac system. The VSC based FACTS devices include the static synchronous compensator (STATCOM), the static synchronous series compensator (SSSC), and the unified power flow controller (UPFC). In [39] and [44], STATCOM is proposed to minimize DFIG-based wind turbine terminal voltage fluctuation. In [40, 45], reactive power compensation using the STATCOM is proposed for improving the fault ride-through capability and transient voltage stability in the DFIG wind turbine system.

In this thesis, a STATCOM connected at the PCC to regulate voltage fluctuation during grid side disturbances like voltage swelling and voltage sagging is presented. The use of STATCOM to provide steady state voltage regulation of the DFIG wind turbine terminal is described. It is also shown that the MVA rating of the Grid Side Converter (GSC) has to be increased more than three times compared to unity power factor operation of the GSC if it has to supply the reactive power to meet the power factor demanded by the grid code.

2.5 Interaction of a DFIG Wind Turbine System with the Series Compensated Line

Traditionally, series compensation is used in long transmission line to increase the power transfer capability of the line [46]. Series compensation also helps in the steady state voltage regulation [46]. Series compensation is also used to enable power to be

transmitted stably over a greater distance than is possible without compensation [46]. The DFIG wind turbines are installed in remote areas and offshore due to favorable wind conditions and are therefore connected to the power system via weak and long transmission lines. Hence, to evacuate large amounts of electrical power from the wind farms, it is quite likely that the transmission lines will be series compensated [47].

In this thesis, the grid side converter (GSC) is designed to regulate the DFIG terminal voltage of the series compensated line. The steady state analysis of the overall system is done to evaluate the effect of different compensation levels. It is shown through the dynamic simulation and steady state analysis that the series compensation helps in improving the steady state voltage regulation and enhances the power carrying capability of the transmission line. It is clearly shown that the reactive power that GSC has to supply to regulate the terminal voltage keeps on decreasing when the compensation level increases.

2.6 Autonomous Operation of DFIG Wind Energy Conversion System with Integrated Energy Storage

The majority of research interests related to DFIG systems in the literature have concentrated on the grid connected wind power applications. However, in order to assess the full potential of the DFIG, control strategies of the standalone operation mode should be also examined. For the autonomous operation of the wind turbine, two issues need to be addressed [48]: 1) integration of properly sized energy storage system into the WECS to mitigate the power fluctuations and consequent power quality problems, and 2) development of effective control strategies. To control the voltage and frequency of the

standalone operated system, traditional reactive power versus voltage (Q-V) and real power versus frequency (P-ω) droop techniques have been adopted and successfully implemented [49]. Moreover, the variability of wind speed causes fluctuation in the power output of wind generator as a result the voltage and frequency of the isolated power system gets affected. To increase the reliability and performance of the system, energy storage is required [48]. Many investigations have been done for technical and/or economical advantages of augmenting a wind power unit with energy storage for instance fuel cell [50], batteries [48, 51], flywheel [51], compressed air [51] and super-capacitor [51, 52]. In the case of small-scale wind power system with energy storage system peak power less than 1 MW, lead-acid battery energy storage systems constitute a technically mature solution with considerable application potential [53].

In this thesis, the standalone operation of the DFIG system with integrated battery energy storage connected across the DC-link of ac/dc/ac converter is modeled. The connected load consisting of RL load, linear load and non-linear load is modeled. The Grid Side Converter is designed to control frequency and load bus voltage magnitude using droop control technique.

CHAPTER 3

DOUBLY FED INDUCTION GENERATOR BASED WIND ENERGY CONVERSION SYSTEM

3.1 Introduction

This chapter presents a detailed explanation about DFIG-based WECS. The overall components of DFIG-based WECS are discussed first. Its operation modes, modeling, control system design, and the detail explanations about each significant component are presented later.

Among different wind generation technologies available, variable-speed variable-pitch wind turbines utilizing DFIGs are the most popular in the wind power industry especially for multimegawatt wind turbine generators [8].

3.2 Components of DFIG-based WECS

The DFIG-based WECS basically consists of generator, wind turbine with drive train system, RSC, GSC, DC-link capacitor, pitch controller, coupling transformer, and protection system as shown in Figure 3.1. The DFIG is a wound-rotor induction generator with the stator terminals connected directly to the grid and the rotor terminals to the mains via a partially rated variable frequency ac/dc/ac converter, which only needs to handle a fraction (25-30 %) of the total power to accomplish full control of the generator. The functional principle of this variable speed generator is the combination of DFIG and four-quadrant ac/dc/ac VFC equipped with IGBTs. The ac/dc/ac converter system

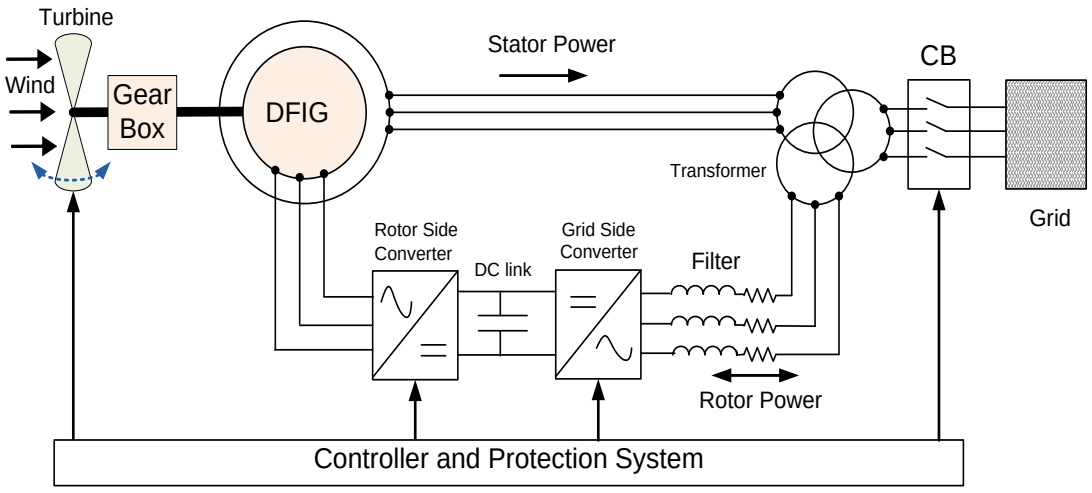

Figure 3.1 Components of DFIG-based WECS

consists of a RSC and a GSC connected back-to-back by a DC-link capacitor. The rotor current is controlled by RSC to vary the electro-magnetic torque and machine excitation. Since the power converter operates in bi-directional power mode, the DFIG can be operated either in sub-synchronous or in super-synchronous operational modes.

The general structure of control block diagram in the DFIG-based WECS having two levels of control is shown in Figure 3.2. The highest level is the WECS optimization; wherein the speed of the wind turbine is set in such a way that optimum wind power can be captured. This control level is mechanical system control. The lower level control being the electrical system control, i.e. torque and reactive power control. The mechanical control system acts slower compared to the electrical control system.

The DFIG-based WECS block diagram model built in MATLAB/Simulink is shown in Figure 3.3 where the actual flow of different signals among various components of the overall system is shown clearly.

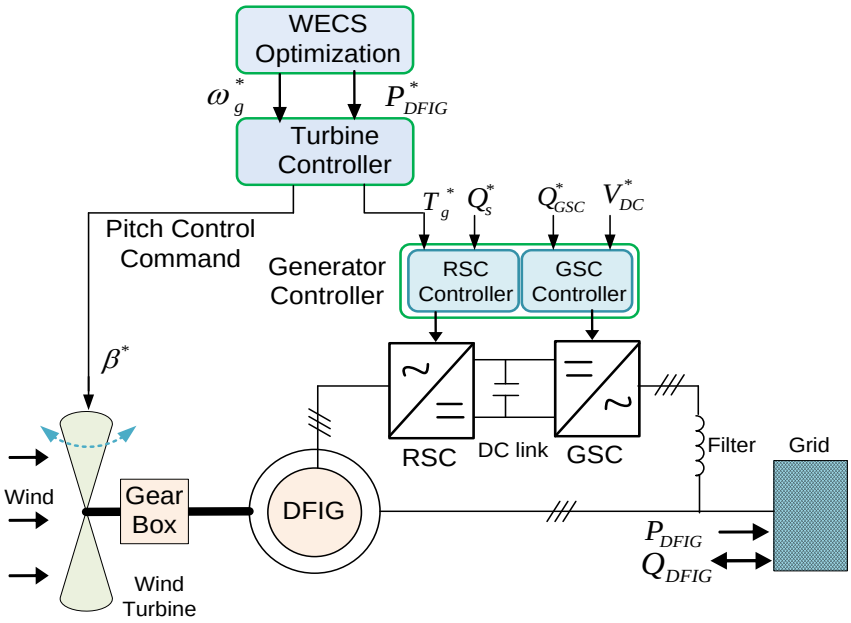

Figure 3.2 Control block diagram of DFIG-based WECS

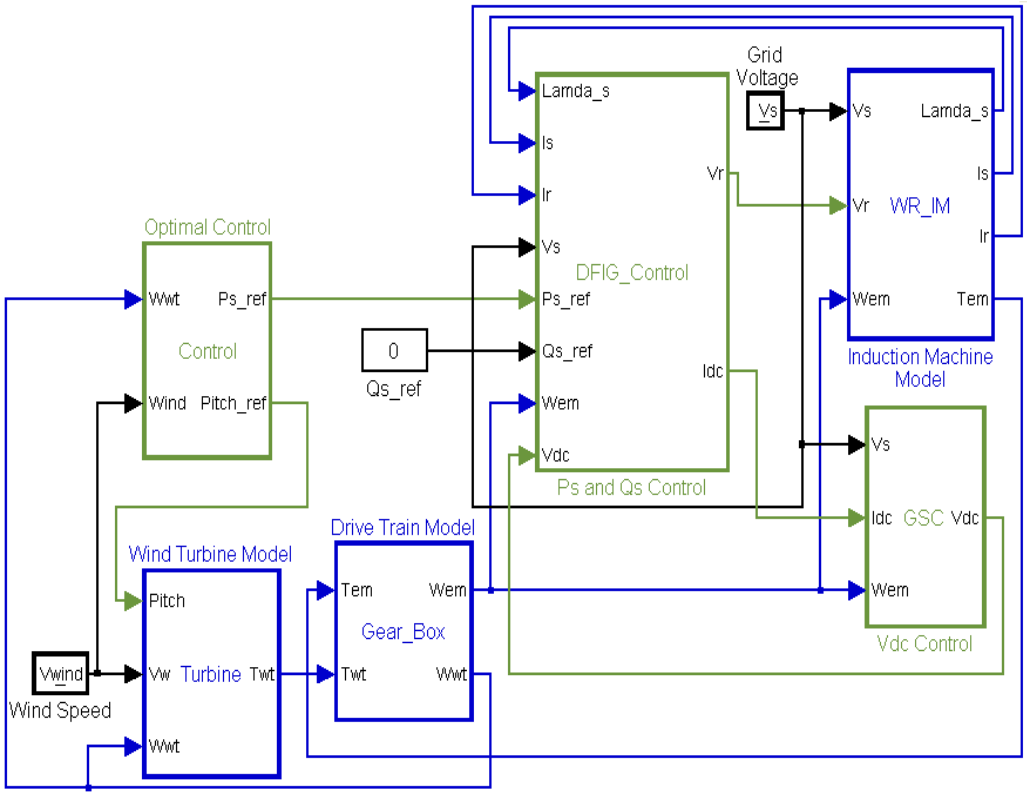

Figure 3.3 Matlab/Simulink block diagram of DFIG-based WECS model

3.3 DFIG Model

The DFIG consists of stator winding and the rotor winding equipped with slip rings. The stator is provided with three-phase insulated windings making up a desired pole design and is connected to the grid through a three-phase transformer. Similar to the stator, the rotor is also constructed of three-phase insulated windings. The rotor windings are connected to an external stationary circuit via a set of slip rings and brushes. By means of these components, the controlled rotor current can be either injected to or absorbed from the rotor windings.

The stator and rotor windings are usually coated with insulation and are mechanically assembled to form a closed structure to protect the machine from dust, damp, and other unwanted intrusions ensuring proper magnetic coupling between rotor and stator windings. In wind energy conversion system, this generator is mounted in the nacelle of the wind turbine system as shown in Figure 1.3.

The dynamics of the DFIG is represented by a fourth-order state space model using the synchronously rotating reference frame (qd-frame) as given in (3.1)-(3.4) [54]:

$$V_{qs} = r_s I_{qs} + \omega_e \lambda_{ds} + \frac{d}{dt}\lambda_{qs} \tag{3.1}$$

$$V_{ds} = r_s I_{ds} - \omega_e \lambda_{qs} + \frac{d}{dt}\lambda_{ds} \tag{3.2}$$

$$V_{qr} = r_r I_{qr} + (\omega_e - \omega_r)\lambda_{dr} + \frac{d}{dt}\lambda_{qr} \tag{3.3}$$

$$V_{dr} = r_r I_{dr} + (\omega_e - \omega_r)\lambda_{qr} + \frac{d}{dt}\lambda_{dr} \tag{3.4}$$

where V_{qs}, V_{ds}, V_{qr}, V_{dr} are the q and d-axis stator and rotor voltages, respectively. I_{qs}, I_{ds}, I_{qr}, I_{dr} are the q and d-axis stator and rotor currents, respectively. λ_{qs}, λ_{ds}, λ_{qr}, λ_{dr} are the q and d-axis stator and rotor fluxes, respectively. ω_e is the angular velocity of the synchronously rotating reference frame. ω_r is rotor angular velocity, r_s and r_r are the stator and rotor resistances, respectively. The flux linkage equations are given as:

$$\lambda_{qs} = L_s I_{qs} + L_m I_{qr} \tag{3.5}$$

$$\lambda_{ds} = L_s I_{ds} + L_m I_{dr} \tag{3.6}$$

$$\lambda_{qr} = L_m I_{qs} + L_r I_{qr} \tag{3.7}$$

$$\lambda_{dr} = L_m I_{ds} + L_r I_{dr} \tag{3.8}$$

where L_s, L_r and L_m are the stator, rotor, and mutual inductances, respectively, with $L_s = L_{ls} + L_m$ and $L_r = L_{lr} + L_m : L_{ls}$ being the self inductance of stator and L_{lr} being the self inductance of rotor.

Solving (3.5) - (3.8) in terms of current equations:

$$I_{qs} = \frac{1}{\sigma L_s}\lambda_{qs} - \frac{L_m}{\sigma L_s L_r}\lambda_{qr} \tag{3.9}$$

$$I_{ds} = \frac{1}{\sigma L_s}\lambda_{ds} - \frac{L_m}{\sigma L_s L_r}\lambda_{dr} \tag{3.10}$$

$$I_{qr} = -\frac{L_m}{\sigma L_s L_r}\lambda_{qs} + \frac{1}{\sigma L_r}\lambda_{qr} \tag{3.11}$$

$$I_{dr} = -\frac{L_m}{\sigma L_s L_r}\lambda_{ds} + \frac{1}{\sigma L_r}\lambda_{dr} \tag{3.12}$$

where leakage coefficient $\sigma = \frac{L_s L_r - L_m^2}{L_s L_r}$

3.3.1 Dynamic Modeling of DFIG in State Space Equations

The dynamic modeling in state space form is necessary to carry out simulation using different simulation tools such as MATLAB. The basic state space form helps to analyze the system in the transient condition.

According to the basic definition, the space whose co-ordinate axes are the 'n' state variables with time as the implicit variable is called the state space. The variables of the state space (state variables) are involved to determine the state of the dynamic system. Basically these are the energy storing elements contained in the system like inductor and capacitor. The fundamental equation of the state space is as follows:

$$\begin{cases} \dot{X}(t) = AX(t) + BU(t) \\ Y(t) = CX(t) + DU(t) \end{cases} \tag{3.13}$$

Equation (3.13) is for linear time invariant system, where A, B, C, and D are state, input, output and feed forward matrices, respectively, X is the state vector and Y is the output vector. Equation (3.14) is for linear time variant system, where A, B, C, and D are time dependent matrices.

$$\begin{cases} \dot{X}(t) = A(t)X(t) + B(t)U(t) \\ Y(t) = C(t)X(t) + D(t)U(t) \end{cases} \tag{3.14}$$

In the DFIG system, the state variables are normally currents or fluxes. In the following section, the state space equations for the DFIG in synchronously rotating frame has been derived with flux linkages as the state variables. Substituting (3.9) - (3.12) into (3.1) - (3.4) gives the DFIG dynamics in the state space form as:

$$\frac{d}{dt}\lambda_{qs} = -\frac{r_s}{\sigma L_s}\lambda_{qs} - \omega_e\lambda_{ds} + \frac{r_s L_m}{\sigma L_s L_r}\lambda_{qr} + V_{qs} \tag{3.15}$$

$$\frac{d}{dt}\lambda_{ds} = \omega_e \lambda_{qs} - \frac{r_s}{\sigma L_s}\lambda_{ds} + \frac{r_s L_m}{\sigma L_s L_r}\lambda_{dr} + V_{ds} \tag{3.16}$$

$$\frac{d}{dt}\lambda_{qr} = \frac{r_r L_m}{\sigma L_s L_r}\lambda_{qs} - (\omega_e - \omega_r)\lambda_{dr} - \frac{r_r}{\sigma L_r}\lambda_{qr} + V_{qr} \tag{3.17}$$

$$\frac{d}{dt}\lambda_{dr} = \frac{r_r L_m}{\sigma L_s L_r}\lambda_{ds} - \frac{r_r}{\sigma L_r}\lambda_{dr} + (\omega_e - \omega_r)\lambda_{qr} + V_{dr} \tag{3.18}$$

Equations (3.15) - (3.18) are written in state space matrix form as:

$$\begin{bmatrix} \dot{\lambda}_{qs} \\ \dot{\lambda}_{ds} \\ \dot{\lambda}_{qr} \\ \dot{\lambda}_{dr} \end{bmatrix} = \begin{bmatrix} -\frac{r_s}{\sigma L_s} & -\omega_e & \frac{r_s L_m}{\sigma L_s L_r} & 0 \\ \omega_e & -\frac{r_s}{\sigma L_s} & 0 & \frac{r_s L_m}{\sigma L_s L_r} \\ \frac{r_r L_m}{\sigma L_s L_r} & 0 & \frac{r_r}{\sigma L_r} & (\omega_e - \omega_r) \\ 0 & \frac{r_r L_m}{\sigma L_s L_r} & (\omega_e - \omega_r) & -\frac{r_r}{\sigma L_r} \end{bmatrix} \begin{bmatrix} \lambda_{qs} \\ \lambda_{ds} \\ \lambda_{qr} \\ \lambda_{dr} \end{bmatrix} + \begin{bmatrix} 1 & 0 & 0 & 0 \\ 0 & 1 & 0 & 0 \\ 0 & 0 & 1 & 0 \\ 0 & 0 & 0 & 1 \end{bmatrix} \begin{bmatrix} V_{qs} \\ V_{ds} \\ V_{qr} \\ V_{dr} \end{bmatrix} \tag{3.19}$$

3.3.2 Active Power, Reactive Power and Torque Calculation

All the equations above are induction motor equations. When the induction motor operates as a generator, current direction will be opposite. Assuming negligible power losses in stator and rotor resistances, the active and reactive power outputs from stator and rotor side are given as:

$$P_s = -\frac{3}{2}\left[V_{qs} I_{qs} + V_{ds} I_{ds}\right] \tag{3.20}$$

$$Q_s = -\frac{3}{2}\left[V_{qs} I_{ds} - V_{ds} I_{qs}\right] \tag{3.21}$$

$$P_r = -\frac{3}{2}\left[V_{qr} I_{qr} + V_{dr} I_{dr}\right] \tag{3.22}$$

$$Q_r = -\frac{3}{2}\left[V_{qr} I_{dr} - V_{dr} I_{qr}\right] \tag{3.23}$$

The total active and reactive power generated by DFIG is:

$$P_{Total} = P_s + P_r \tag{3.24}$$

$$Q_{Total} = Q_s + Q_r \tag{3.25}$$

If P_{Total} and/or Q_{Total} is positive, DFIG is supplying power to the power grid, else it is drawing power from the grid.

In the induction machine, the electromagnetic torque is developed by the interaction of air-gap flux and the rotor magneto-motive force (mmf). At synchronous speed, the rotor cannot see the moving magnetic field; as a result, there is no question of induced emf as well as the rotor current, so the torque becomes zero. But at any speed other than synchronous speed, the machine will experience torque. That is true in case of motor, where as in case of wind turbine generator; electromechanical torque is provided by means of prime mover which is wind turbine in DFIG-based WECS.

The rotor speed dynamics of the DFIG is given as:

$$\frac{d}{dt}\omega_r = \frac{P}{2J}(T_m - T_e - C_f \omega_r) \tag{3.26}$$

where P is the number of poles of the machine, C_f is friction coefficient, J is inertia of the rotor, T_m is the mechanical torque generated by wind turbine, and T_e is the electromagnetic torque generated by the machine which can be written in terms of flux linkages and currents as follows:

$$T_e = \frac{3}{2}\left[\lambda_{qs} I_{ds} - \lambda_{ds} I_{qs}\right] \tag{3.27}$$

where positive (negative) values of T_e means DFIG works as a generator (motor) [55].

3.4 Drive Train Model

The generator in a DFIG-based WECS is driven by the wind turbine through a gearbox system to attain a suitable speed range for the rotor. By means of the gearbox, the low rotational speed of the wind turbine is transformed into high rotational speed on the generator side. For 2-3 MW wind turbines, a gearbox ratio of around 70-100 is common [56].

The actual gearbox ratio is chosen considering the optimum operation speed of the generator. The optimum speed of the generator is selected based on annual wind speed distribution and the size of the power converter. The annual efficiency of the generator is somehow influenced by the operating speed of the generator, whether it operates at sub-synchronous or super-synchronous speed. Another aspect to be considered when selecting a gearbox ratio is the weight of the gearbox, which increases along with gearbox ratio [56].

It is important to analyze the transient stability of power system including wind generators. Since, in general, the turbine shaft of wind generator is not as stiff as that of usual synchronous generator; analysis based on a single-mass shaft model system may give significant error in the transient stability analysis. It is because the low-speed shaft encounters a torque N_g (Gear Ratio) times greater than the high-speed shaft torque that turns N_g times more quickly than the low-speed shaft. As the low-speed shaft encounters a higher torque, it is subject to more deviation and it is more convenient to take it into consideration.

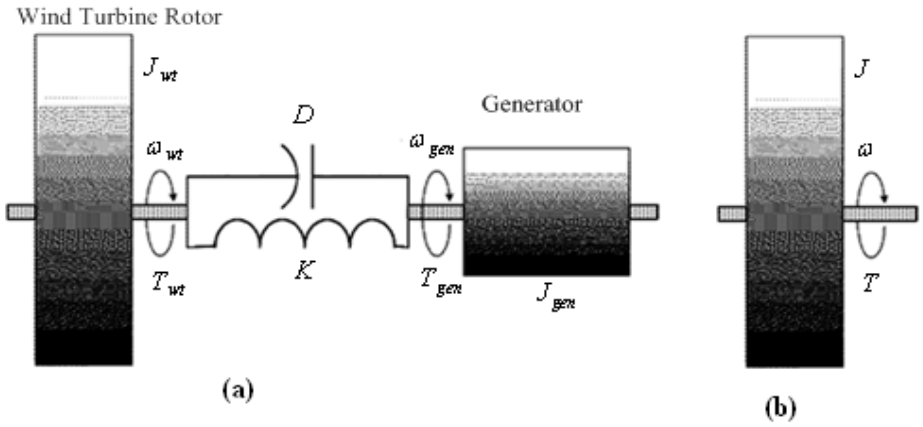

Figure 3.4 (a) Two-mass drive-train [57] and (b) One-mass drive-train model

Although, more complex models of wind turbine drive train system using a six-mass and three-mass [57] are studied; two-mass shaft model is simplest one and sufficient, with reasonable accuracy, for the transient stability analysis of wind turbine generation systems [58]. The equivalent two-mass model of a wind turbine drive train is presented in Figure 3.4(a). The masses correspond to a large mass of the wind turbine rotor and a mass for generator. The mass and moment of inertia for the shafts and the gearbox wheels can be neglected (which is considered in three-mass model) because they are small compared with the moment of inertia of the wind turbine or generator. The dynamic equations of the two-mass drive-train written on the generator side are [57]:

$$T'_{wt} = J'_{wt}\frac{d\omega'_{wt}}{dt} + D(\omega'_{wt} - \omega_{gen}) + K(\theta'_{wt} - \theta_{gen}) \tag{3.28}$$

$$-T_{gen} = J_{gen}\frac{d\omega_{gen}}{dt} + D(\omega_{gen} - \omega'_{wt}) + K(\theta_{gen} - \theta'_{wt}) \tag{3.29}$$

where T_{wt} – wind turbine torque, J_{wtr} – wind turbine moment of inertia, ω_{wt} – wind turbine mechanical speed, K_{wtr} – spring constant indicating the torsional stiffness of the

shaft on wind turbine part, T_{gen} – generator torque, J_{gen} – generator moment of inertia, ω_{gen} - generator mechanical speed, and K_{gen} – spring constant indicating the torsional stiffness of the shaft on generator part. The torque and the speed of the shaft are transmitted via the gearbox with a gear ratio N_g. Also the angular speeds are given as:

Rotor speed, $\omega'_{wt} = \frac{d\theta'_{wt}}{dt}$ and

Generator speed, $\omega_{gen} = \frac{d\theta_{gen}}{dt}$

The equivalent stiffness and moment of inertia for the rotor is given by [57]:

$$\begin{cases} \frac{1}{K} = \frac{1}{\frac{K_{wtr}}{N_g^2}} + \frac{1}{K_{gen}} \\ J_{wt} = \frac{1}{N_g^2} J_{wtr} \end{cases} \tag{3.30}$$

If a perfectly rigid low speed shaft is assumed, then the two-mass drive-train model reduces to a one-mass drive-train model as shown in Figure 3.4(b). The governing dynamic equation is given as:

$$\frac{d}{dt}\omega = \frac{P}{2J}(T_m - T - C_f\omega) \tag{3.31}$$

where ω is the mechanical speed of the shaft, P is the number of poles of the machine, C_f is the friction coefficient, J is the inertia of the rotor, T_m is the mechanical torque generated by wind turbine, and T is the electromagnetic torque generated by the machine. One-mass drive-train model is used for the simulation study in this thesis.

3.5 Power Converters

The power converter is made up of a back-to-back converter connecting the rotor circuit and the grid as shown in Figure 3.5. The converters are typically made up of voltage source inverters equipped with IGBTs provided with freewheeling diodes (see Figure 3.5), which enable a bi-directional power flow. A RL-filter is provided on the GSC output to minimize switching harmonics supplied to the grid.

3.5.1 Rotor Side Converter

The power rating of the RSC is determined by two factors, namely maximum slip power and reactive power control capability. The rotor-side converter can be seen as a current controlled voltage source converter. The control objective of RSC is to regulate

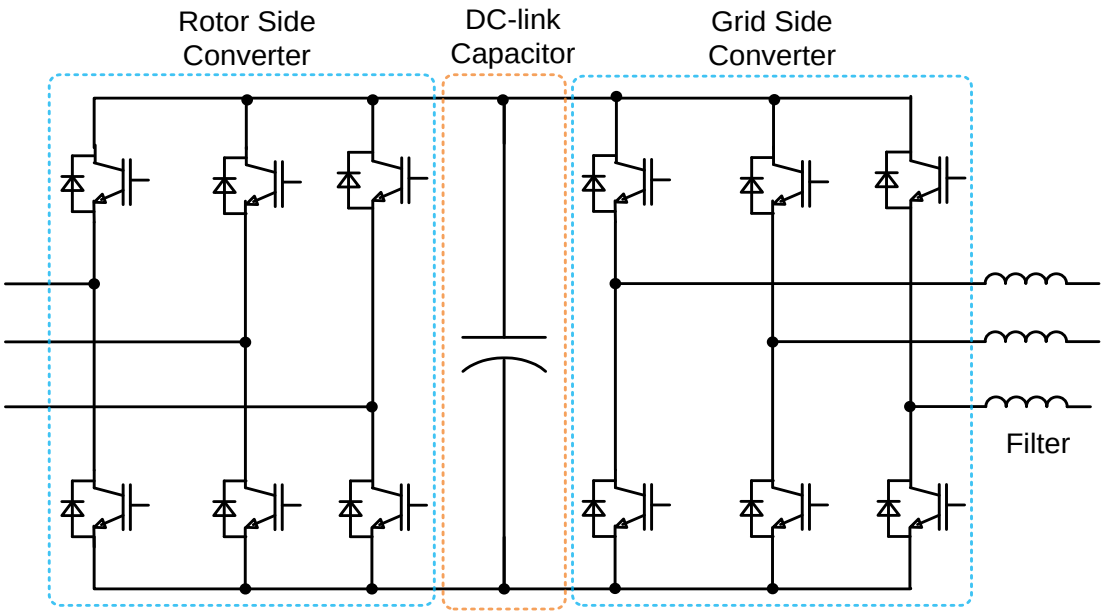

Figure 3.5 The ac/dc/ac bidirectional power converter in DFIG

the stator side active power (or rotor speed) and the stator side reactive power independently.

3.5.2 Grid Side Converter

The power rating of the GSC is mainly determined by maximum slip power since it usually operates at a unity power factor to minimize the losses in the converter [59]. The GSC is normally dedicated to controlling the DC-link voltage only. The converter can also be utilized to support grid reactive power during a fault [60]. The grid-side converter can also be used to enhance grid power quality [61]. However, these abilities are rarely utilized since they require a larger converter rating which is discussed more in Chapter 5.

The amount of energy stored in the dc-link capacitor can be written as:

$$E_C = \int P\,dt = \frac{1}{2} C V_{DC}^2 \tag{3.32}$$

where P is the net power flow into the capacitor, C is the DC-link capacitor value and V_{DC} is the capacitor voltage. P is equal to P_r - P_g, where P_r is the rotor power inflow and P_g is the grid power outflow.

3.6 Wind Speed Model

A wind speed signal generated by an autoregressive moving average (ARMA) model described in [62] is utilized in this simulation study, and its development is described here. The wind speed V_{wind} (t) has two constituent parts expressed as [62]:

$$V_{wind}(t) = V_{w\_mean} + V_t(t) \tag{3.33}$$

where V_{w_mean} is the mean wind speed at hub height and $V_t(t)$ is the instantaneous turbulent part, whose linear model is composed by a first-order filter exciteded by Gaussian noise [62]:

$$\dot{V}_t(t) = -\frac{1}{T_w} V_t(t) + \alpha_t \tag{3.34}$$

where T_w is the time constant and α_t is the white noise process with zero mean. The white noise is smoothed by a signal shaping filter, thereby transforming it to colored noise V_t, as shown in Figure 3.6. The instantaneous turbulence component of wind speed is obtained as [62]:

$$V_t(t) = \sigma_t V_t \tag{3.35}$$

where σ_t is the standard deviation and V_t is the ARMA time series model, which is expressed as [62]:

$$V_t = aV_{t-1} - bV_{t-2} + cV_{t-3} + \alpha_t - d\alpha_{t-1} + e\alpha_{t-2} \tag{3.36}$$

where a, b, and c are the autoregressive parameters and d and e are moving average parameters whose values being: a =1.7901, b=0.9087, c=0.0948, d=1.0929 and e = 0.2892.

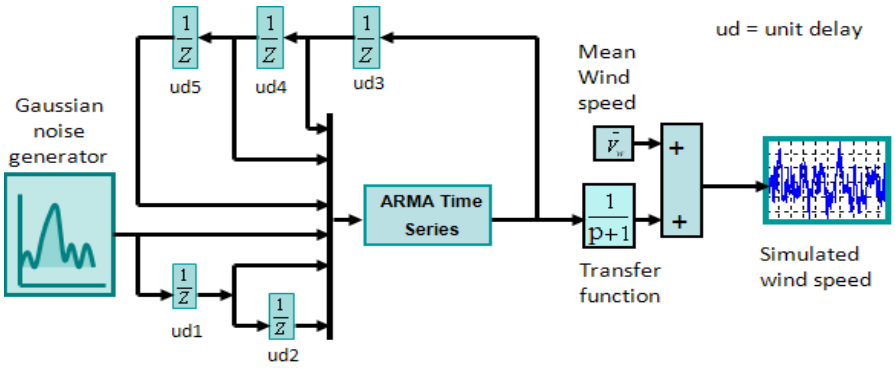

Figure 3.6 Generation of wind speed by ARMA model in MATLAB/Simulink [62]

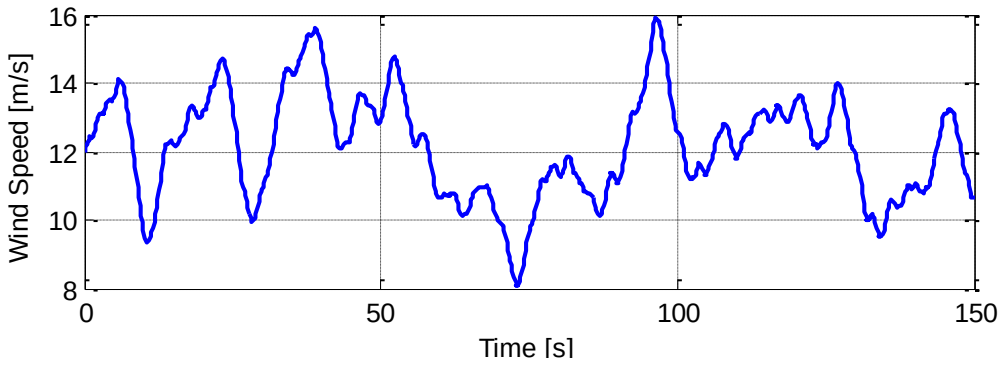

Figure 3.7 Sample wind speed (mean speed being 12 m/s) obtained using ARMA model

3.7 Wind Turbine and Pitch Controller

The turbine is the prime mover of WECS that enables the conversion of kinetic energy of wind E_w into mechanical power P_m and eventually into electricity [62].

$$\begin{cases} P_m = \dfrac{\partial E_w}{\partial t} \quad C_p = \dfrac{1}{2}\rho\, A V_w^{\,3}\, C_p \\ C_p(\lambda,\beta) = 0.5176\left(\dfrac{116}{\lambda_i} - 0.4\beta - 5\right)e^{-21/\lambda_i} + 0.0068\lambda \end{cases} \tag{3.37}$$

where V_w is the wind speed at the center of the rotor (m/sec), ρ is the air density (Kg/m^3), $A = \Pi R^2$ is the frontal area of the wind turbine (m^2) and R is the rotor radius. C_p is the performance coefficient which in turn depends upon the turbine characteristics (β - blade pitch angle and λ - tip speed ratio) that is responsible for the losses in the energy conversion process. The numerical approximation of C_p used in this study is taken from [62] and $\lambda_i = f(\lambda,\beta)$ is given by [62]:

$$\begin{cases} \lambda = \dfrac{\omega_t R}{V_w} \\ \dfrac{1}{\lambda_i} = \dfrac{1}{\lambda + 0.08\beta} - \dfrac{0.035}{\beta^3 + 1} \end{cases} \tag{3.38}$$

where ω_t is the turbine speed and R is the blade radius of the wind turbine. Since $C_p = f(\lambda, \beta)$, the plot of C_p vs λ at various values of β is shown in Figure 3.8. When the wind speed increases beyond the rated value, the electromagnetic torque is not sufficient to control rotor speed since this leads to an overload on the generator and the converter. To prevent rotor speed from becoming too high, the extracted power from incoming wind must be limited. This can be done by reducing the coefficient of performance of the turbine (the C_p value). As explained earlier, the C_p value can be manipulated by changing the pitch angle (see Figure 3.8). Altering the pitch angle β means slightly rotating the turbine blades along the axis. The blades are considerably heavy in a large turbine. Therefore, the rotation must be facilitated by either hydraulic or electric drives. The pitch controller model is given in Figure 3.9. The lower part of the pitch controller shown in the Figure 3.9 is the turbine speed regulator, while the upper part is an aerodynamic power limiter. The entire control can be realized by means of PI controllers.

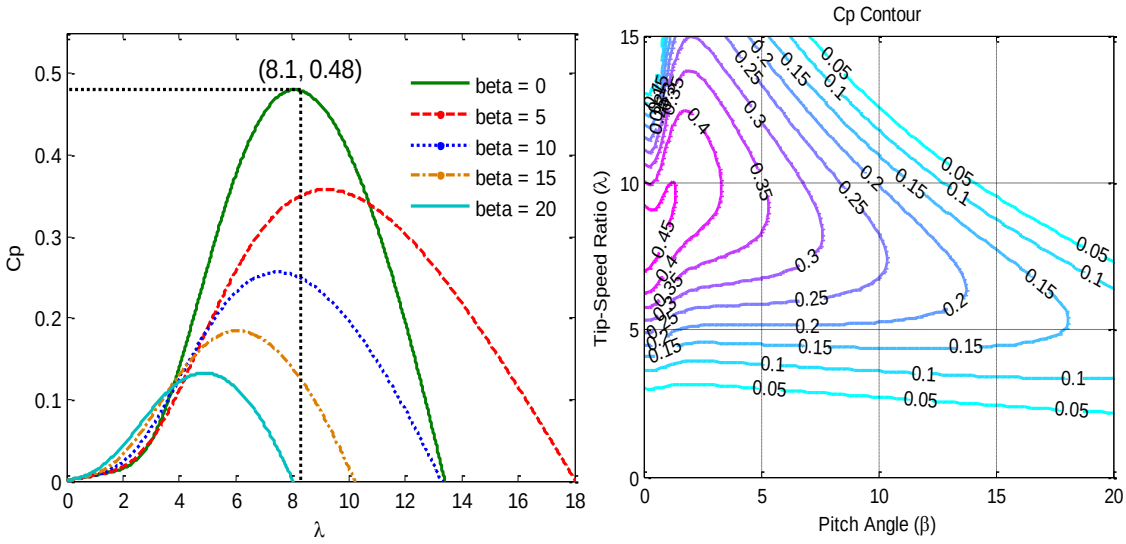

Figure 3.8 Wind turbine characteristic curves

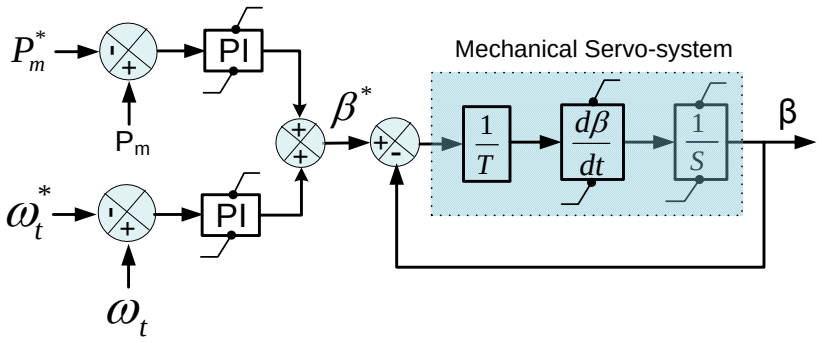

Figure 3.9 Pitch angle control scheme using PI controllers

3.8 Protection System

The main task of a protection system is to protect the wind turbine system from damage caused by the high currents that can happen when the DFIG terminal voltage drops as a result of short circuit (fault) in the grid. It also prevents DFIG from islanding. Islanding is the situation in power system in which part of the system continues to be energized by distributed generation after the system is isolated from main power grid. If those two cases happen in the DFIG system, the protection system operates the Circuit Breaker (CB) to isolate it from the power grid. Similarly, CB can be operated to isolate DFIG from power grid during its repair and maintenance operation.

3.9 Operating Regions

Two distinct operating regions of a variable-speed variable-pitch DFIG-based wind turbine system can be defined based on incoming wind speed and the generator power output required. The output power from wind turbine (P_e) can be defined as shown

below. Assuming P_e varies when wind speed V_w varies between cut-in (V_c) and rated (V_r) wind speeds, the closed form expression for energy production is [62]:

$$\begin{cases} P_e = 0, \quad for \ (V_w \le V_c) \\ P_e = a + bV_w{}^k, \quad for \ (V_c \le V_w \le V_r) \\ P_e = P_r, \quad for \ (V_w \ge V_r) \end{cases} \tag{3.39}$$

where P_r = rated electrical power, k is Weibull shape parameter = 2 for the studied system and the coefficients a and b are given as: $a = \frac{P_r V_c{}^k}{V_c{}^k - V_r{}^k}$ and $b = \frac{P_r}{V_r{}^k - V_c{}^k}$

As shown in Figure 1.4, the variable speed WECS can be operated in MPPT mode and blade pitch control mode (constant power mode) depending upon the velocity of wind to extract maximum power from the wind as well as regulate the power output from the wind turbine.

3.10 Operating Modes

Variable-speed variable-pitch wind turbine can be operated in three distinct operating modes depending upon the wind speed available and amount of power output needed from the wind turbine system.

3.10.1 Mode I: Maximum Power Point Tracking

From the plot shown in Figure 3.8, it can be stated that, for β= 0^o, $\lambda_{opt} = 8.1$ and $C_{p\_\max} = 0.48$. Now the rotor mechanical torque extracted from the wind that in turn drives wind generator is:

$$T_t = \frac{P_m}{\omega_t} \tag{3.40}$$

Now from Equations (3.37) and (3.40):

$$T_t = \frac{1}{2\omega_t}\rho A V_w{}^3 C_p = \frac{R}{2\lambda}\rho A V_w{}^2 C_p \tag{3.41}$$

Since $C_p = C_{p\_\max}$ = constant, in this mode, from (3.37):

$$P_m = K V_w^3 \tag{3.42}$$

where $K = \frac{1}{2}\rho\ A\ C_{p\_\max}$ = constant

From Equation (3.42), if the wind generator is run at a particular speed that corresponds to wind speed V_w in such a way that wind turbine will be operating at maximum power point (as shown in Figure 3.10) then we can extract maximum available power from the available wind speed via wind turbine.

The objective of the MPPT operation mode is to maximize power extraction at low to medium wind speeds by following the maximum value of the wind power coefficient (C_{p_max}) as depicted in Figure 3.10.

3.10.2 Mode II: Pitch Control (Rated Power Operation)

When the wind speed increases beyond the rated value, the electromagnetic torque is not sufficient to control rotor speed because this leads to an overload on the generator and the converter. To prevent rotor speed from becoming too high, the extracted power from incoming wind must be limited. This can be done by reducing the coefficient of performance of the turbine (the C_p value). As explained earlier, the C_p

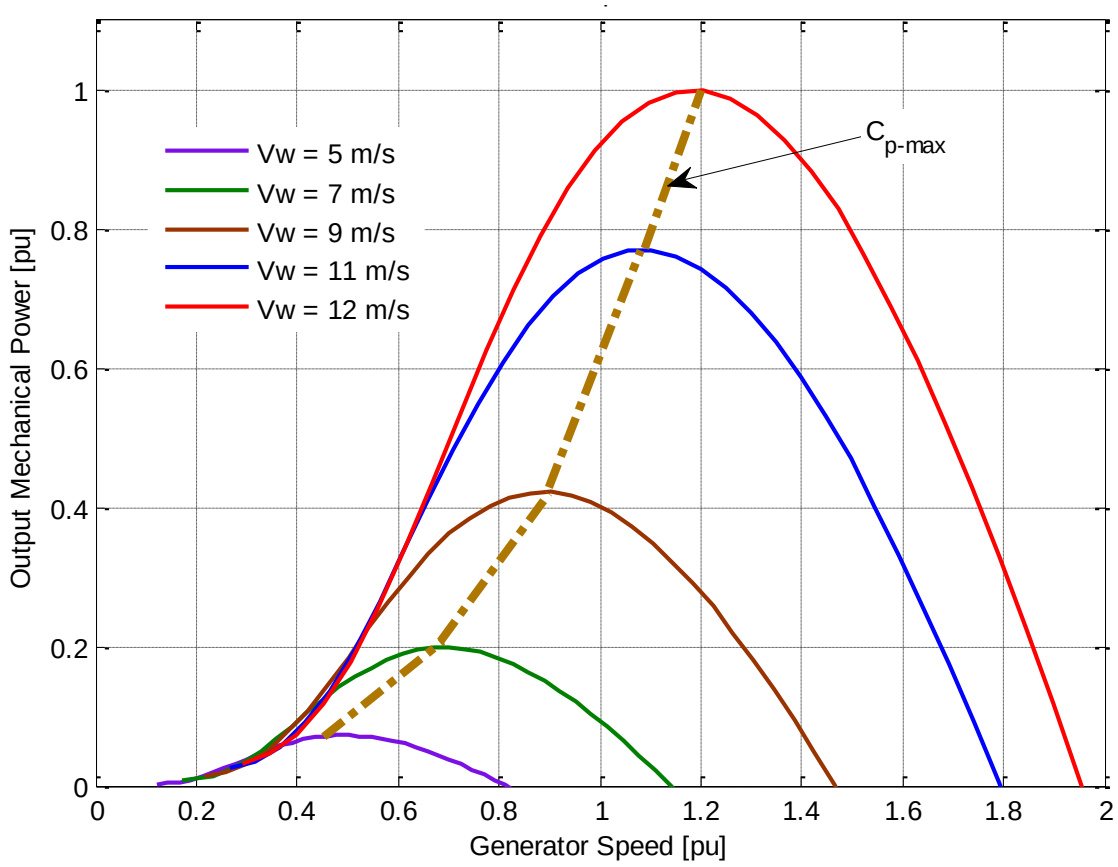

Figure 3.10 Wind Turbine mechanical power output vs rotor speed (dotted line shows the MPPT operation points)

value can be manipulated by changing the pitch angle (see Figure 3.8). Altering the pitch angle β means slightly rotating the turbine blades along the axis.

The wind speed is varied, turbine speed is maintained at rated speed ($\omega_t = \omega_{t\_rated}$) and corresponding λ is calculated using (3.43). The power output is maintained at rated power ($P = P_{rated}$). The C_p corresponding to rated power is calculated using (3.43). The

$$\begin{cases} \lambda = \dfrac{\omega_{t\_rated} R}{V_w} \\ C_p = \left(\dfrac{P_{rated}}{0.5 A \rho V_w} \right) \end{cases} \tag{3.43}$$

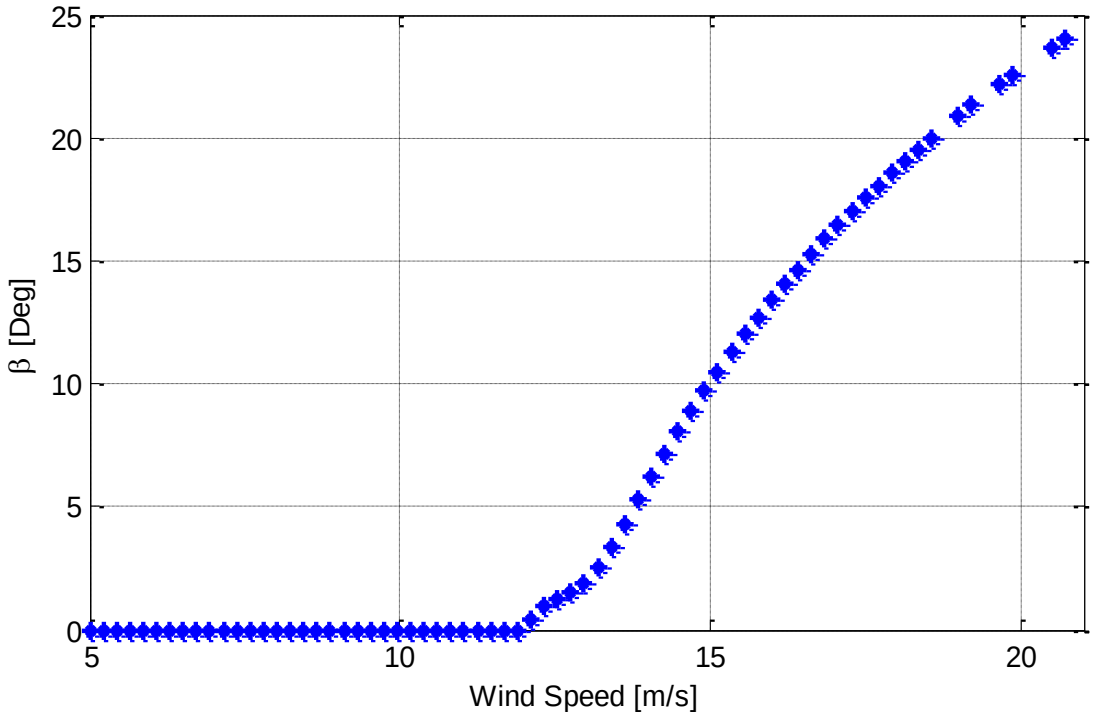

Figure 3.11 Pitch angle for various wind speeds in a variable-speed variable-pitch wind turbine system

value of pitch angle is obtained solving (3.37). The pitch angle for various wind speeds is shown in Figure 3.11.

3.10.3 Mode III: Power Regulation

With the increased penetration level of wind power in a power system, it is not always possible to operate wind turbine in MPPT mode and constant power mode only. For maintaining regulated frequency and voltage in the power system, the generated power should be equal to the demanded power. Hence in that condition, the variable-speed variable-pitch wind turbine should be operated in power regulation mode. When the load decreases, the power output from the turbine should be reduced to match the

load. When the wind speed is less than the rated speed, the pitch angle is always kept at zero ($\beta = 0$) and the λ is varied and corresponding C_p is calculated to obtain demanded power output from the wind turbine. Then, the wind speed is calculated based upon the demanded power output (P) given by (3.44).

$$\begin{cases} V_w = \left(\dfrac{P}{0.5 A \rho C_p} \right)^{1/3} \\ \omega_r = \dfrac{\lambda V_w}{R} * Gear\ Ratio \end{cases} \tag{3.44}$$

Figure 3.12 shows the rotor speed vs. wind speed operating points for various demanded power outputs (P). As shown in Fig. 3.12, DFIG wind turbine system can be operated at more than one speed to generate particular power output (P) from wind turbine. In that case, wind turbine should be operated in the closest possible speed from the previous speed to minimize the transient operation period. In that way disturbance to the pitch controller is also reduced significantly.

If the wind speed is more than the rated speed, then the turbine speed is maintained at rated turbine speed ($\omega_t = \omega_{t\_rated}$) and wind speed is varied. The corresponding λ is calculated and pitch angle is obtained for various values of demanded power (P), which gives corresponding C_p using (3.45); by solving (3.38).

$$\begin{cases} \lambda = \dfrac{\omega_{t\_rated} R}{V_w} \\ C_p = \left(\dfrac{P}{0.5 A \rho V_w} \right) \end{cases} \tag{3.45}$$

Figure 3.13 shows the pitch angle vs. wind speed operating points for various demanded power outputs.

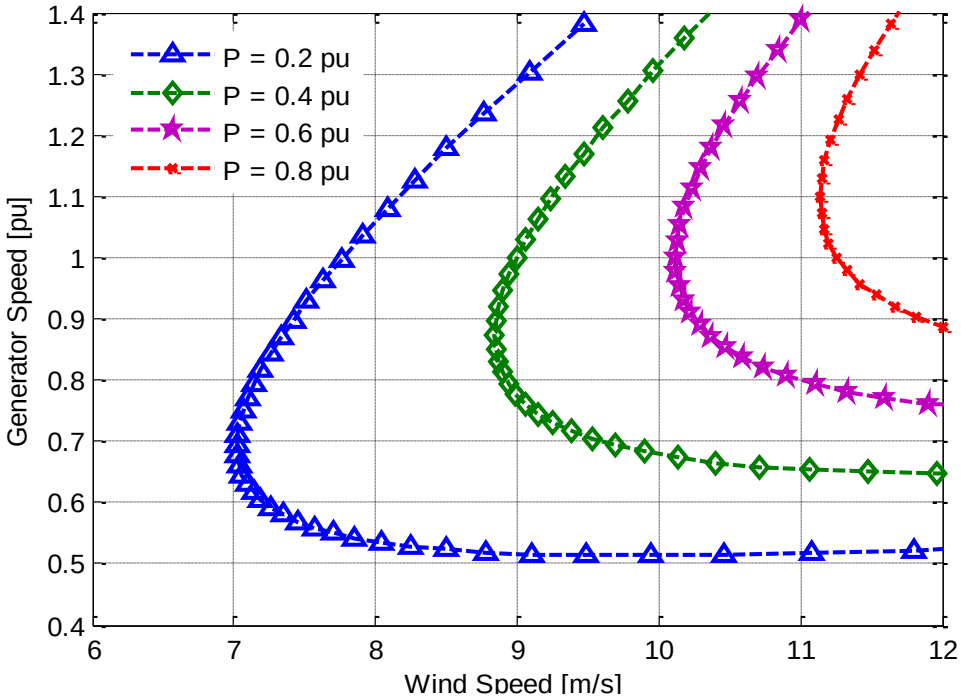

Figure 3.12 Power Regulation Operation with wind speed less than rated wind speed

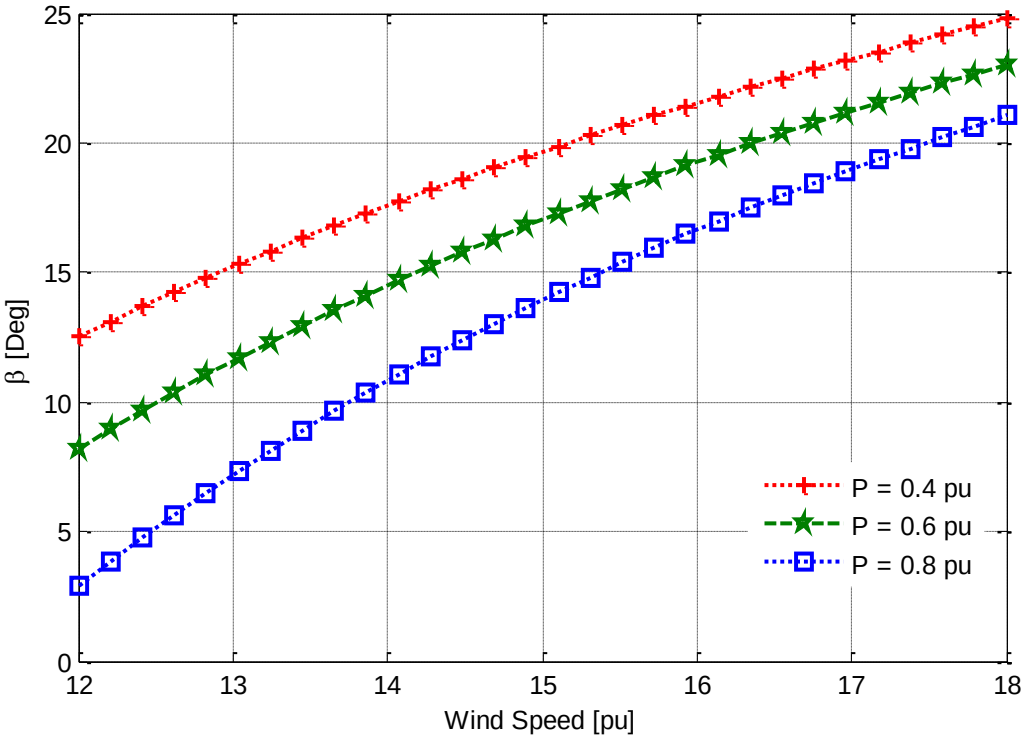

Figure 3.13 Power Regulation Operation with wind speed more than rated wind speed

3.11 Control of DFIG-based WECS

The DFIG-based WECS control system consists of two parts: the electrical control of the DFIG and the mechanical control of the wind turbine speed and blade pitch angle as shown in Figure 3.2. Control of the DFIG is achieved by control of the variable frequency converter, which includes control of the RSC and control of the GSC. The objective of the RSC is to allow the DFIG wind turbine for decoupled control of active and reactive power. This facilitates high flexibility which enables the turbine to capture maximum energy from wind and at the same time to provide reactive power support to the grid. The objective of the GSC is to keep the DC-link voltage constant regardless of the magnitude and direction of the rotor power.

3.11.1 Design of the RSC Controller

The RSC control scheme consists of two cascaded vector control structure with inner current control loops which regulates independently the d-axis and q-axis rotor currents, i.e. I_{dr} and I_{qr}, according to some synchronously rotating reference frame. The outer control loop regulates the stator active power (or DFIG rotor speed) and reactive power (or DFIG terminal voltage) independently. The stator voltage orientation (SVO) control principle for a DFIG is described in [31], where the q-axis of the rotating reference frame is aligned to the stator voltage i.e V_{ds} = 0 and V_{qs} = V_s. From (3.15) and (3.16), the stator side flux can be controlled using PI controller. In this study, the q-axis

flux is regulated to zero ($\lambda_{qs} = 0$) and ($\lambda_{ds} = \lambda_s$) for the de-coupled control of active and reactive power as described below (where $p = \frac{d}{dt}$ throughout the thesis):

$$\begin{cases} p\lambda_{qs} + \dfrac{r_s}{\sigma L_s}\lambda_{qs} = -\omega_e \lambda_{ds} + \dfrac{r_s L_m}{\sigma L_s L_r}\lambda_{qr} + V_{qs} \\ \sigma_{\lambda qs} = -\omega_e \lambda_{ds} + \dfrac{r_s L_m}{\sigma L_s L_r}\lambda_{qr} + V_{qs} \\ \lambda_{ds}^{*} = \dfrac{1}{\omega_e}\left(\dfrac{r_s L_m}{\sigma L_s L_r}\lambda_{qr} + V_{qs} - \sigma_{\lambda qs} \right) \end{cases} \tag{3.46}$$

$$\begin{cases} p\lambda_{ds} + \dfrac{r_s}{\sigma L_s}\lambda_{ds} = \omega_e \lambda_{qs} + \dfrac{r_s L_m}{\sigma L_s L_r}\lambda_{dr} + V_{ds} \\ \sigma_{\lambda ds} = \omega_e \lambda_{qs} + \dfrac{r_s L_m}{\sigma L_s L_r}\lambda_{dr} + V_{ds} \\ \lambda_{qs}^{*} = \dfrac{1}{\omega_e}\left(\sigma_{\lambda ds} - \dfrac{r_s L_m}{\sigma L_s L_r}\lambda_{qr} - V_{qs} \right) \end{cases} \tag{3.47}$$

where $\sigma_{\lambda qs} = p\lambda_{qs} + \dfrac{r_s}{\sigma L_s}\lambda_{qs} = \left(k_{P\lambda s} + \dfrac{k_{I\lambda s}}{p} \right)(\lambda_{qs}^{*} - \lambda_{qs})$ and

$\sigma_{\lambda ds} = p\lambda_{ds} + \dfrac{r_s}{\sigma L_s}\lambda_{ds} = \left(k_{P\lambda s} + \dfrac{k_{I\lambda s}}{p} \right)(\lambda_{ds}^{*} - \lambda_{ds})$ are the outputs from the PI controllers as shown in Figure 3.14.

The PI parameters are determined by comparing with the Butterworth polynomial which is described in the below section, are given as:

$$k_{P\lambda s} = \sqrt{2}\omega_0 - \frac{r_s}{\sigma L_s} \tag{3.48}$$

$$k_{I\lambda s} = \omega_0^{\,2} \tag{3.49}$$

Now, neglecting frictional losses in (3.26) gives:

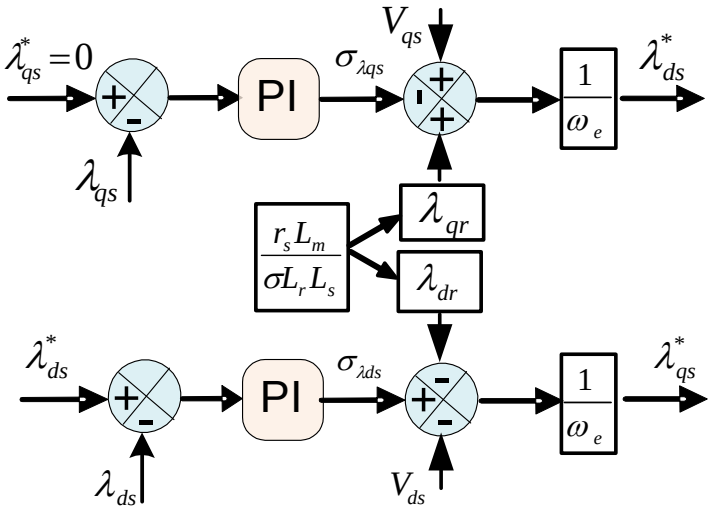

33

Figure 3.14 Stator fluxes control using PI controllers

$$p\omega_r = \frac{P}{2J}(T_m - T_e) \tag{3.50}$$

where T_m is the mechanical torque from the wind turbine. When the wind speed (V_w) is less than the rated speed, the T_m is given as:

$$T_m = k_{opt} V_w^{\,2} \tag{3.51}$$

where $k_{opt} = \frac{R}{2\lambda_{opt}} \rho\, A\, C_{p\_opt}$ = constant and if the wind speed (V_w) is more than the rated speed, the T_m is given as:

$$T_m = \frac{P_{rated}}{\omega_{rated}} \tag{3.52}$$

where P_{rated} is rated power of the wind turbine and ω_{rated} is the rated speed of the wind turbine.

Equation (3.46) can be re-written as:

$$\frac{2J}{P} p\omega_r = (T_m - T_e) = \sigma_{wr} = k_{wr}(\omega_r^* - \omega_r) \tag{3.53}$$

where k_{wr} is the PI controller for rotor speed controller, given as: $k_{wr} = \left(k_{Pwr} + \frac{k_{Iwr}}{p} \right)$

Then (3.53) will be:

$$\begin{cases} \frac{2J}{P} p\omega_r = \left(k_{Pwr} + \frac{k_{Iwr}}{p} \right)\omega_r^* - \left(k_{Pwr} + \frac{k_{Iwr}}{p} \right)\omega_r \\ \frac{\omega_r}{\omega_r^*} = \frac{\frac{P}{2J}\left(pk_{Pwr} + k_{Iwr} \right)}{p^2 + p\frac{Pk_{Pwr}}{2J} + \frac{Pk_{Iwr}}{2J}} \end{cases} \tag{3.54}$$

Substituting λ_{qs} = 0 in (3.27) and (3.5) results in (3.55).

$$\begin{cases} T_e = \frac{3}{2}\lambda_{ds} I_{qs} \\ I_{qs} = -\frac{L_m}{L_s} I_{qr} \end{cases} \tag{3.55}$$

A further substitution of (3.54) into (3.53) and in combination with (3.49) results in:

$$T_e = \frac{3}{2}\lambda_{ds}(-\frac{L_m}{L_s})I_{qr} \tag{3.56}$$

$$I_{qr} = \left(\sigma_{wr} - T_m\right)\frac{2}{3}\frac{L_s}{L_m \lambda_{ds}} \tag{3.57}$$

Now, the stator active power can be written as:

$$P_s = \frac{3}{2}\left(V_{qs} I_{qs} + V_{ds} I_{ds}\right) = -\frac{3}{2}\frac{L_m}{L_s} V_{qs} I_{qr} \tag{3.58}$$

Now, the stator supplied reactive power is given as:

$$Q_s = \frac{3}{2}(V_{qs} I_{ds} - V_{ds} I_{qs}) = \frac{3}{2} V_{qs} I_{ds} \tag{3.59}$$

Substituting V_{qs} in (3.57) gives:

$$Q_s = \frac{3}{2}(r_s I_{qs} + \omega_e \lambda_{ds} + p\lambda_{qs}) I_{ds} \tag{3.60}$$

Assuming constant stator flux, neglecting the stator resistance and substituting I_{ds} from (3.10) gives:

$$Q_s = \frac{3}{2}\frac{\omega_e}{\sigma L_s}\left(\lambda_{ds}^2 - \frac{L_m}{L_r}\lambda_{ds}\lambda_{dr}\right) \tag{3.61}$$

Differentiating (3.59) w.r.t. time gives:

$$pQ_s = -\frac{3}{2}\frac{\omega_e}{\sigma L_s}\frac{L_m}{L_r}\lambda_{ds} p\lambda_{dr} \tag{3.62}$$

From (3.60) and (3.4) and solving λ_{qr} in terms of I_{qr} gives (3.63)

$$\begin{cases} pQ_s = -\frac{3}{2}\frac{\omega_e}{\sigma L_s}\frac{L_m}{L_r}\lambda_{ds}\left(V_{dr} - r_r I_{dr} + (\omega_e - \omega_r)\lambda_{qr}\right) \\ pQ_s = -\frac{3}{2}\frac{\omega_e}{\sigma L_s}\frac{L_m}{L_r}\lambda_{ds}\left(V_{dr} - r_r I_{dr} + (\omega_e - \omega_r)\sigma L_r I_{qr}\right) \\ \nabla pQ_s = \sigma_{Qs} = k_{Qs}(Q_s^* - Q_s) \end{cases} \tag{3.63}$$

where $\nabla = \frac{2\sigma L_s L_r}{3\omega_e L_m}$ and k_{Qs} is the PI controller for stator side reactive power controller, given as: $k_{Qs} = \left(k_{PQs} + \frac{k_{IQs}}{p}\right)$. So, (3.63) can be re-written as:

$$\nabla pQ_s = \left(k_{PQs} + \frac{k_{IQs}}{p}\right)Q_s^* - \left(k_{PQs} + \frac{k_{IQs}}{p}\right)Q_s \tag{3.64}$$

$$\frac{Q_s}{Q_s^*} = \frac{\frac{1}{\nabla}\left(pk_{PQs} + k_{IQs}\right)}{p^2 + p\frac{k_{PQs}}{\nabla} + \frac{k_{IQs}}{\nabla}} \tag{3.65}$$

From (3.62) and (3.63) gives:

$$I_{dr}^{*} = \frac{1}{r_r}\left(V_{dr} + (\omega_e - \omega_r)\sigma L_r I_{qr} + \frac{\sigma_{Q_s}}{\lambda_{ds}} \right) \tag{3.66}$$

It can be seen from Equations (3.56) and (3.66) that, P_s and Q_s are proportional to I_{qr} and I_{dr}, respectively. The mutual coupling term $(\omega_e - \omega_r)\sigma L_r I_{qr}$ in (3.66) is very small so its effect is negligible. The rotor current can be regulated by means of rotor voltages.

The relation between rotor current and rotor voltage is obtained by substituting values of λ_{dr} and λ_{qr} from (3.7) and (3.8) in Equations (3.3) and (3.4), respectively, and further simplification yields:

$$V_{qr} = r_r I_{qr} + \sigma L_r p I_{qr} + \omega_{so}\left(\frac{L_m}{L_s}\lambda_{ds} + \sigma L_r I_{dr} \right) \tag{3.67}$$

$$V_{dr} = r_r I_{dr} + \sigma L_r p I_{dr} - \omega_{so}\sigma L_r I_{qr} \tag{3.68}$$

where $\omega_{so} = (\omega_e - \omega_r)$ and $\sigma = 1 - \frac{L_m^{\,2}}{L_s L_r}$

In the Equations (3.67) and (3.68), there is the term including I_{dr} in the q-axis equation and there is the term including I_{qr} in the d-axis equation. So these two equations are coupled and the traditional linear controllers cannot be used. However, through the exact linearization method, these equations can be linearized by putting the terms other than the currents control to one side.

$$r_r I_{qr} + \sigma L_r p I_{qr} = V_{qr} - \omega_{so}\left(\frac{L_m}{L_s}\lambda_{ds} + \sigma L_r I_{dr} \right) \tag{3.69}$$

$$r_r I_{dr} + \sigma L_r p I_{dr} = V_{dr} + \omega_{so}\sigma L_r I_{qr} \tag{3.70}$$

Then linear controllers are used to regulate the currents as shown in Figure 3.15, where:

$$\sigma_{qr} = r_r I_{qr} + \sigma L_r p I_{qr} \tag{3.71}$$

$$\sigma_{dr} = r_r I_{dr} + \sigma L_r p I_{dr} \tag{3.72}$$

The idea behind this is to use the linear controllers that include integrations to calculate the derivative terms. And the nonlinear equations become linear when all the nonlinear terms are moved to the other side of the equations. Then the q and d-axis voltages are calculated as shown in Figure 3.15.

$$V_{qr}^{*} = \sigma_{qr} + \omega_{so}\left(\frac{L_m}{L_s}\lambda_{ds} + \sigma L_r I_{dr}\right) \tag{3.73}$$

$$V_{dr}^{*} = \sigma_{dr} - \omega_{so}\sigma L_r I_{qr} \tag{3.74}$$

Using the inner current control loop has a significant advantage for the protection of the DFIG. It can naturally protect the system from over-current since current limiters can be easily inserted in the control system shown in Figure 3.15.

Since the general PI controllers are widely used and proved to be effective, they are also applied in the following analysis [63]. For I_{qr} current control loop from (3.69):

$$V_{qr}^{'} = r_r I_{qr} + \sigma L_r p I_{qr} = (r_r + p\sigma L_r) I_{qr} \tag{3.75}$$

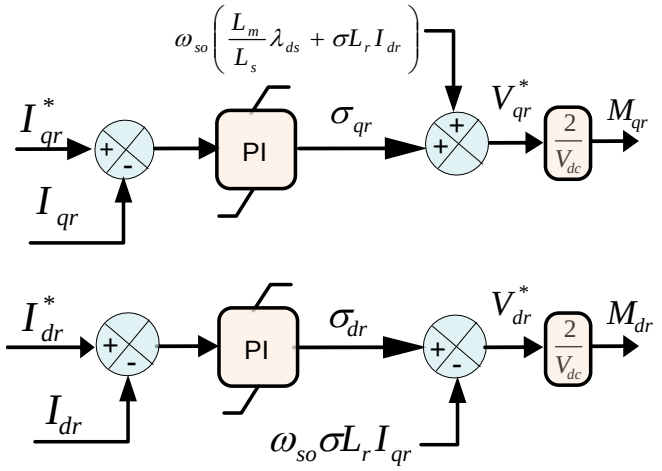

Figure 3.15 Inner current controller

$$V_{qr}^{'} = \left(k_{qp} + \frac{k_{qi}}{p}\right)\left(I_{qr}^{*} - I_{qr}\right) \tag{3.76}$$

$$\left(r_r + p\sigma L_r\right)I_{qr} = \left(k_{qp} + \frac{k_{qi}}{p}\right)I_{qr}^{*} - \left(k_{qp} + \frac{k_{qi}}{p}\right)I_{qr} \tag{3.77}$$

Similarly, for I_{dr} current control loop from (3.70):

$$V_{dr}^{'} = r_r I_{dr} + \sigma L_r p I_{dr} = \left(r_r + p\sigma L_r\right)I_{dr} \tag{3.78}$$

$$V_{dr}^{'} = \left(k_{dp} + \frac{k_{di}}{p}\right)\left(I_{dr}^{*} - I_{dr}\right) \tag{3.79}$$

$$\left(r_r + p\sigma L_r\right)I_{dr} = \left(k_{dp} + \frac{k_{di}}{p}\right)I_{dr}^{*} - \left(k_{dp} + \frac{k_{di}}{p}\right)I_{dr} \tag{3.80}$$

Then the transfer functions between the reference and actual currents are changed to the following:

$$\frac{I_{qr}}{I_{qr}^{*}} = \frac{pk_{qp} + k_{qi}}{p^2\sigma L_r + p(r_r + k_{qp}) + k_i} = \frac{\frac{1}{\sigma L_r}\left(pk_{qp} + k_{qi}\right)}{p^2 + p\frac{1}{\sigma L_r}(r_r + k_{qp}) + \frac{1}{\sigma L_r}k_{qi}} \tag{3.81}$$

$$\frac{I_{dr}}{I_{dr}^{*}} = \frac{pk_{dp} + k_{di}}{p^2\sigma L_r + p(r_r + k_{dp}) + k_{di}} = \frac{\frac{1}{\sigma L_r}\left(pk_{dp} + k_{di}\right)}{p^2 + p\frac{1}{\sigma L_r}(r_r + k_{dp}) + \frac{1}{\sigma L_r}k_{di}} \tag{3.82}$$

Choosing the appropriate control parameters is very important to gain good performance although the whole system might be able to work for a wide range of parameters. Many researchers select the gains based on the experience or just by trial and error. This is not good especially when the control system is designed for a new system. The most important objective is to maintain the system stability by selecting appropriate control parameters. And then those parameters can be tuned up corresponding to the

specified performance requirement. There are some methods that can be used to determine the system parameters that can keep the whole system in the stable region.

One of the methods is by using Butterworth polynomial to optimize the closed-loop eigen value locations [63]. The Butterworth method locates the eigen values uniformly in the left-half s-plane on a circle with radius ω_o, with its center at the origin as shown in Figure 3.16.

The Butterworth polynomial for a transfer function with a second order denominator is given as:

$$p^2 + \sqrt{2}\omega_0 p + \omega_0^{\ 2} = 0 \tag{3.83}$$

The PI parameters are determined by comparing the coefficients in (3.79) with the denominators of the corresponding transfer functions and then choosing appropriate ω_0.

$$k_{qp} = k_{dp} = \sqrt{2}\omega_0 \sigma L_r - r_r \tag{3.84}$$

$$k_{qi} = k_{di} = \sigma L_r \omega_0^{\ 2} \tag{3.85}$$

Here ω_0 is the bandwidth of the current controller, which depends upon the design value. The overall vector control scheme of the RSC is shown in Figure 3.17.

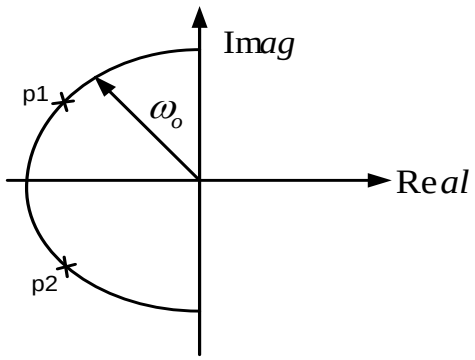

Figure 3.16 Location of poles for second order Butterworth polynomial

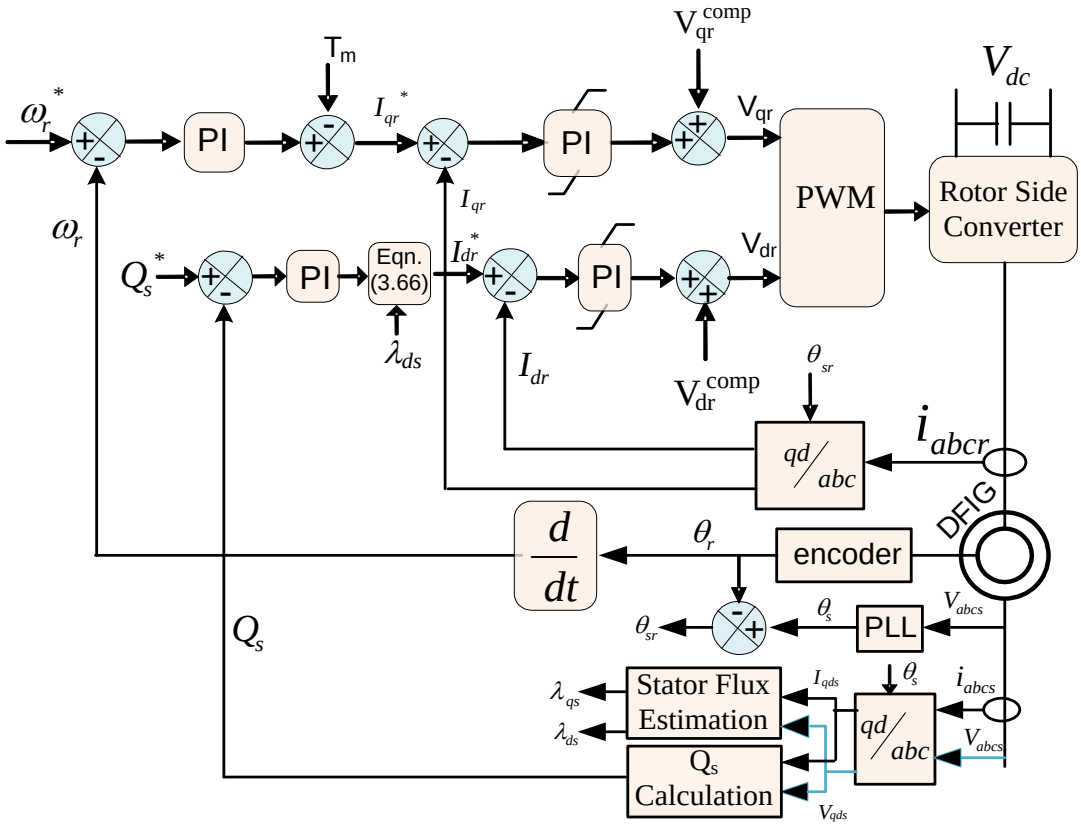

Figure 3.17 Block diagram of RSC control system: $V_{dr}^{\ comp} = -\omega_{so}\sigma L_r I_{qr}$ and $V_{qr}^{\ comp} = \omega_{so}\left(\frac{L_m}{L_s}\lambda_{ds} + \sigma L_r I_{dr}\right)$

Similarly, comparing denominator of (3.51) with Butterworth second order polynomial, i.e. $p^2 + \sqrt{2}\omega_{0wr}p + \omega_{0wr}^2$, PI controller gains are obtained as:

$$k_{Pwr} = \sqrt{2}\omega_{0wr}\frac{2J}{P} \tag{3.86}$$

$$k_{Iwr} = \frac{2J}{P}\omega_{0wr}^{\ 2} \tag{3.87}$$

where ω_{0wr} is the bandwidth frequency of the speed controller.

Similarly, comparing denominator of (3.65) with Butterworth second order polynomial, i.e. $p^2 + \sqrt{2}\omega_{Qs} p + \omega_{Qs}^2$, PI controller gains are obtained as:

$$k_{PQs} = \sqrt{2}\omega_{0Qs}\Delta \tag{3.88}$$

$$k_{IQs} = \Delta\omega_{Qs}{}^2 \tag{3.89}$$

3.11.2 Design of the GSC Controller

Figure 3.18 shows the general vector control scheme of the GSC where control of DC-link voltage V_{dc} and reactive power exchange between GSC and power grid is achieved by controlling current in synchronous reference frame [54].

Now, DC voltage dynamics in DC-link is given by:

$$C\ pV_{dc} = \frac{3}{4}(M_{qr}I_{qr} + M_{dr}I_{dr}) + \frac{3}{4}\left(M_{df}I_{df} + M_{qf}I_{qf}\right) \tag{3.90}$$

where C is the DC-link capacitance, M_{dr} and M_{qr} are q and d-axis modulation indexes of RSC and M_{df} and M_{qf} are q and d-axis modulation indexes of GSC, respectively. Hence, (3.90) can be re-written as (3.91) which can be solved to get I_{qf}.

$$C\ pV_{dc} = \frac{3}{4}(M_{qr}I_{qr} + M_{dr}I_{dr}) + \frac{3}{4}\left(M_{df}I_{df} + M_{qf}I_{qf}\right) = \sigma_{dc} \tag{3.91}$$

Equation (3.91) can be re-written as:

$$C\ pV_{dc} = \sigma_{dc} = k_{dc}(V_{dc}^{*} - V_{dc}) \tag{3.92}$$

where k_{dc} is the PI controller for DC-voltage control given as: $k_{dc} = \left(k_{Pdc} + \frac{k_{Idc}}{p}\right)$. Then (3.92) will be:

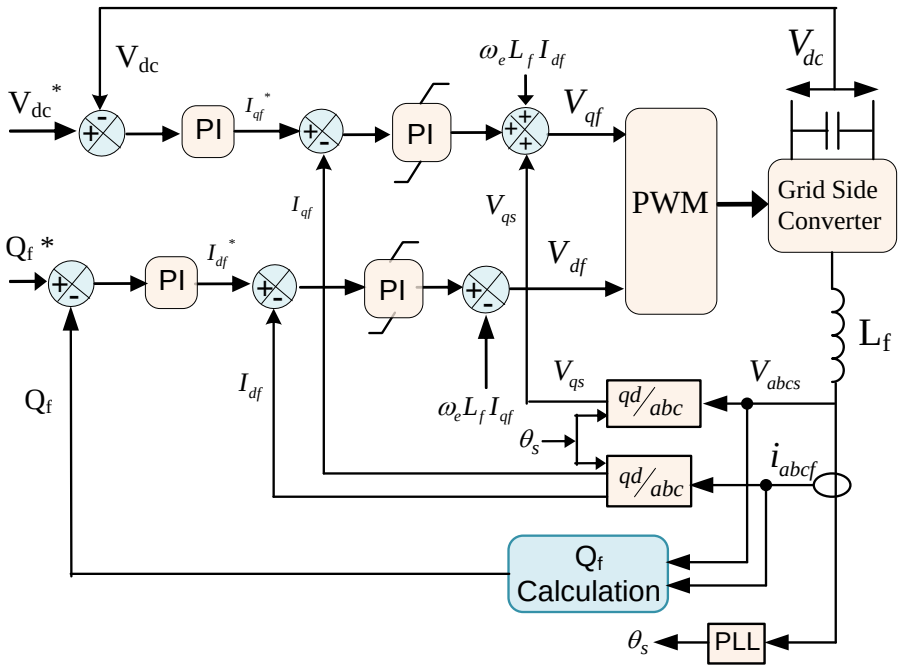

Figure 3.18 Block diagram of GSC control system

$$C\ pV_{dc} = \left(k_{Pdc} + \frac{k_{Idc}}{p}\right)V_{dc}^{\ *} - \left(k_{Pdc} + \frac{k_{Idc}}{p}\right)V_{dc} \tag{3.93}$$

$$\frac{V_{dc}}{V_{dc}^{\ *}} = \frac{\frac{1}{C_{dc}}\left(pk_{Pdc} + k_{Idc}\right)}{p^2 + p\frac{k_{Pdc}}{C_{dc}} + \frac{k_{Idc}}{C_{dc}}} \tag{3.94}$$

Comparing denominator of (3.94) with Butterworth second order polynomial, i.e. $p^2 + \sqrt{2}\omega_{0dc}p + \omega_{0dc}^2$, PI controller gains are obtained as:

$$k_{Pdc} = \sqrt{2}\omega_{0dc}C_{dc} \tag{3.95}$$

$$k_{Idc} = C_{dc}\omega_{0dc}^{\ 2} \tag{3.96}$$

where ω_{0dc} is the bandwidth frequency of the DC-voltage controller. From (3.91):

$$I_{qf}^{*} = \frac{4}{3}\frac{1}{M_{qf}}\left(\sigma_{dc} - \frac{3}{4}(M_{qr}I_{qr} + M_{dr}I_{dr})\right) - \frac{M_{df}}{M_{qf}}I_{df} \tag{3.97}$$

Using KVL across the RL filter gives:

$$V_{qf} = r_f I_{qf} + L_f pI_{qf} + \omega_e L_f I_{df} + \frac{V_{qs}}{N} = M_{qf} \frac{V_{dc}}{2} \tag{3.98}$$

$$V_{df} = r_f I_{df} + L_f pI_{df} - \omega_e L_f I_{qf} = M_{df} \frac{V_{dc}}{2} \tag{3.99}$$

Since the q-axis of the rotating reference frame is aligned to the stator voltage i.e V_{ds} = 0 and V_{qs} = V_s. So, the GSC supplied reactive power to the grid is controlled using d-axis current.

$$Q_f = \frac{3}{2N} V_s I_{df} \tag{3.100}$$

where N is the transformer turns ratio connected between GSC and stator.

$$pQ_f = \frac{3V_s}{2N} pI_{df} \tag{3.101}$$

Substituting (3.99) in (3.101) gives:

$$pQ_f = \frac{3V_s}{2N} \frac{1}{L_f} (V_{df} - r_f I_{df} + \omega_e L_f I_{qf}) \tag{3.102}$$

$$\Gamma pQ_f = (V_{df} - r_f I_{df} + \omega_e L_f I_{qf}) = \sigma_{Qf} \tag{3.103}$$

where $\Gamma = \frac{2NL_f}{3V_s}$.

$$\Gamma pQ_f = \sigma_{Qf} = k_{Qf} (Q_f^* - Q_f) \tag{3.104}$$

where k_{Qf} is the PI controller for reactive power supplied by GSC given as:

$k_{Qf} = \left(k_{PQf} + \frac{k_{IQf}}{p} \right)$. Then (3.104) will be:

$$\Gamma p Q_f = \left(k_{PQf} + \frac{k_{IQf}}{p} \right) Q_f^{\,*} - \left(k_{PQf} + \frac{k_{IQf}}{p} \right) Q_f \tag{3.105}$$

$$\frac{Q_f}{Q_f^{\,*}} = \frac{\frac{1}{\Gamma}\left(p k_{PQf} + k_{IQf} \right)}{p^2 + p\frac{k_{PQf}}{\Gamma} + \frac{k_{IQf}}{\Gamma}} \tag{3.106}$$

Comparing denominator of (3.106) with Butterworth second order polynomial, i.e.

$p^2 + \sqrt{2}\omega_{0Qf} p + \omega_{0Qf}^2$, PI controller gains are obtained as:

$$k_{PQf} = \sqrt{2}\omega_{0Qf}\Gamma \tag{3.107}$$

$$k_{IQf} = \Gamma \omega_{0Qf}^{\,2} \tag{3.108}$$

where ω_{0Qf} is the bandwidth frequency of the reactive power controller. From (3.103):

$$I_{df}^{*} = \frac{1}{r_f}\left(V_{df} + \omega_e L_f I_{qf} - \sigma_{Qf} \right) \tag{3.109}$$

Equations (3.98) and (3.99) give the inner current control loop for the GSC control.

Inner current control:

If we assume:

$$r_f I_{qf} + L_f p I_{qf} = k_{qf}(I^{*}_{qf} - I_{qf}) = \sigma_{qf} \tag{3.110}$$

$$r_f I_{df} + L_f p I_{df} = k_{df}(I^{*}_{df} - I_{df}) = \sigma_{df} \tag{3.111}$$

Then, (3.98) and (3.99) can be written as:

$$M_{qf} = (\sigma_{qf} + \omega_e L_f I_{df} + \frac{V_{qs}}{N})\frac{2}{V_{dc}} \tag{3.112}$$

$$M_{df} = (\sigma_{df} - \omega_e L_f I_{qf})\frac{2}{V_{dc}} \tag{3.113}$$

Equations (3.112) and (3.113) give modulation indexes which are the output of the converter. And k_{qf} and k_{df} are PI current controllers for q and d-axis currents, respectively and $k_{qf} = k_{df} = \left(k_{P1} + \frac{k_{I1}}{p} \right)$. Then, (3.110) can be re-written as:

$$\frac{I_{qf}}{I_{qf}^{*}} = \frac{\frac{1}{L_f}\left(pk_{P1} + k_{I1}\right)}{p^2 + p\frac{1}{L_f}(r_f + k_{P1}) + \frac{1}{L_f}k_{I1}} \tag{3.114}$$

Comparing denominator of (3.114) with the Butterworth second order polynomial gives:

$$k_{P1} = \sqrt{2}\omega_{0c}L_f - r_f \tag{3.115}$$

$$k_{I1} = L_f \omega_{0c}^{\ 2} \tag{3.116}$$

where ω_{0c} is the bandwidth frequency of the current controller.

3.11.3 Transfer Function of RSC and GSC Controllers

In the above mentioned controller design for RSC and GSC, each controllers are designed separately and finally combined together. This procedure is only valid when the controlled variables are independent of each other, i.e. they should be mutually decoupled. To check whether they are independent of each other or not, or if there should be any conditions to be fulfilled for the decoupled control of those two controllers, the transfer functions of the RSC and GSC are derived in this section. The conclusion is made at the end of this section.

From the flux control:

$$\begin{cases} \sigma_{\lambda qs} = -\omega_e \lambda_{ds} + \dfrac{r_s L_m}{\sigma L_s L_r} \lambda_{qr} + V_{qs} \\ \sigma_{\lambda qs} = -\omega_e \lambda_{ds} + \dfrac{r_s L_m}{\sigma L_s L_r} (\sigma L_r I_{qr} + \dfrac{L_m}{L_s} \lambda_{qs}) + V_{qs} \\ \sigma_{\lambda qs} = -\omega_e \lambda_{ds} + \dfrac{r_s L_m}{L_s} I_{qr} + \dfrac{r_s L_m^2}{\sigma L_s^2 L_r} \lambda_{qs} + V_{qs} \\ K_{\lambda s}(\lambda_{qs}^* - \lambda_{qs}) = -\omega_e \lambda_{ds} + r_s \left(\dfrac{p8J\omega_r - 4PT_m}{3P^2 \lambda_{ds}} \right) + \dfrac{r_s L_m^2}{\sigma L_s^2 L_r} \lambda_{qs} + V_{qs} \end{cases} \tag{3.117}$$

$$\lambda_{qs} = \frac{\sigma L_s^2 L_r (3P^2 K_{\lambda s} \lambda_{qs}^* + 3P^2 \lambda_{ds} - 3P^2 V_{qs})}{3 r_s L_m^2 P^2 + 3P^2 \sigma L_s^2 L_r K_{\lambda s}} - \frac{\sigma L_s^2 L_r r_s (p8J\omega_r - 4PT_m)}{\lambda_{ds}(3 r_s L_m^2 P^2 + 3P^2 \sigma L_s^2 L_r K_{\lambda s})} \tag{3.118}$$

Similarly,

$$\begin{cases} \sigma_{\lambda ds} = \omega_e \lambda_{qs} + \dfrac{r_s L_m}{\sigma L_s L_r} \lambda_{dr} + V_{ds} \\ \sigma_{\lambda ds} = \omega_e \lambda_{qs} + \dfrac{r_s L_m}{\sigma L_s L_r} (\dfrac{L_m}{L_s} \lambda_{ds} + L_r \sigma I_{dr}) + V_{ds} \\ \sigma_{\lambda ds} = \omega_e \lambda_{qs} + \dfrac{r_s L_m^2}{\sigma L_s^2} \lambda_{ds} + \dfrac{r_s L_m}{L_s} I_{dr} + V_{ds} \\ K_{\lambda s}(\lambda_{ds}^* - \lambda_{ds}) = \omega_e \lambda_{qs} + \dfrac{r_s L_m^2}{\sigma L_s^2} \lambda_{ds} - \dfrac{2r_s}{3} \dfrac{Q_s}{\omega_e \lambda_{ds}} + V_{ds} \end{cases} \tag{3.119}$$

$$\lambda_{ds} = \frac{K_{\lambda s} \lambda_{ds}^* - \omega_e \lambda_{qs} + \dfrac{2r_s}{3} \dfrac{Q_s}{\omega_e \lambda_{ds}} - V_{ds}}{\left(K_{\lambda s} + \dfrac{r_s L_m^2}{\sigma L_s^2} \right)} \tag{3.120}$$

From (3.118) and (3.120), it is clear that the relations between control variable ($\lambda_{ds}, \lambda_{qs}$) and reference variable ($\lambda_{ds}^*, \lambda_{qs}^*$) are non-linear. Hence, transfer function cannot be obtained. Therefore, in the later part of the transfer function derivation, the stator fluxes are assumed constant as a result the relationship between control variables and reference variable is linear.

In the RSC, from (3.49):

$$\sigma_{wr} = k_{wr}(\omega_r^* - \omega_r) = (T_m - T_e) \tag{3.121}$$

$$\sigma_{wr} = T_m + \frac{3P}{4}\frac{\hat{L}_m}{\hat{L}_s}\lambda_{ds} I^*_{qr} \tag{3.122}$$

$$I^*_{qr} = (\sigma_{wr} - T_m)\frac{4\hat{L}_s}{3P\hat{L}_m\lambda_{ds}} \tag{3.123}$$

where ($\hat{}$) shows the measured value. Similarly, from (3.63):

$$\sigma_{Qs} = k_{Qs}(Q_s^* - Q_s)_s = \lambda_{ds}\left(V_{dr} - \hat{r}_r I_{dr} + \hat{\omega}_{so}\hat{\sigma}\hat{L}_r I_{qr}\right) \tag{3.124}$$

$$\sigma_{Qs} = \lambda_{ds}\left(\hat{r}_r I_{dr} + p\hat{\sigma}\hat{L}_r I_{dr} - \hat{\omega}_{so}\hat{\sigma}\hat{L}_r I_{qr} - \hat{r}_r I_{dr} + \hat{\omega}_{so}\hat{\sigma}\hat{L}_r I_{qr}\right) \tag{3.125}$$

$$I_{dr}^* = \frac{\sigma_{Qs}}{p\hat{\sigma}\hat{L}_r\lambda_{ds}} \tag{3.126}$$

From (3.123) and (3.126):

$$\begin{bmatrix} I_{qr}^* \\ I_{dr}^* \end{bmatrix} = \underbrace{\begin{bmatrix} \frac{4\hat{L}_s}{3P\hat{L}_m\lambda_{ds}} & 0 \\ 0 & \frac{1}{p\hat{\lambda}_{ds}\hat{\sigma}\hat{L}_r} \end{bmatrix}}_{C}\begin{bmatrix} \sigma_{wr} \\ \sigma_{Qs} \end{bmatrix} + \underbrace{\begin{bmatrix} -\frac{4\hat{L}_s T_m}{3P\hat{L}_m\lambda_{ds}} \\ 0 \end{bmatrix}}_{D} \tag{3.127}$$

Here, the mechanical torque from the wind turbine is considered as a disturbance to the RSC controller.

From (3.46):

$$p\omega_r = \frac{P}{2J}(T_m - T_e) \tag{3.128}$$

$$p\omega_r = \frac{P}{2J}(T_m + \frac{3P}{4}\frac{L_m}{L_s}\lambda_{ds} I_{qr}) \tag{3.129}$$

$$I_{qr} = \frac{p8J}{3P^2}\frac{L_s\omega_r}{L_m\lambda_{ds}} - \frac{4T_mL_s}{3PL_m\lambda_{ds}} \tag{3.130}$$

From (3.62):

$$pQ_s = -\frac{3}{2}\frac{\omega_e}{\sigma L_s}\frac{L_m}{L_r}\lambda_{ds}\left(V_{dr} - r_rI_{dr} + \omega_{so}\sigma L_rI_{qr}\right) \tag{3.131}$$

$$pQ_s = -\frac{3}{2}\frac{\omega_e}{\sigma L_s}\frac{L_m}{L_r}\lambda_{ds}\left(r_rI_{dr} + p\sigma L_rI_{dr} - \omega_{so}\sigma L_rI_{qr} - r_rI_{dr} + \omega_{so}\sigma L_rI_{qr}\right) \tag{3.132}$$

$$I_{dr} = -\frac{2Q_sL_s}{3\omega_eL_m\lambda_{ds}} \tag{3.133}$$

$$\begin{bmatrix} I_{qr} \\ I_{dr} \end{bmatrix} = \underbrace{\begin{bmatrix} \frac{p8JL_s}{3PL_m\lambda_{ds}} & 0 \\ 0 & -\frac{2L_s}{3\omega_eL_m\lambda_{ds}} \end{bmatrix}}_{E}\begin{bmatrix} \omega_r \\ Q_s \end{bmatrix} + \underbrace{\begin{bmatrix} -\frac{4L_sT_m}{3PL_m\lambda_{ds}} \\ 0 \end{bmatrix}}_{D} \tag{3.134}$$

From (3.77):

$$\left(\hat{r}_r + p\hat{\sigma}\hat{L}_r\right)I_{qr} = k_{iqr}I_{qr}^{\ *} - k_{iqr}I_{qr} \tag{3.135}$$

From (3.80):

$$\left(\hat{r}_r + p\hat{\sigma}\hat{L}_r\right)I_{dr} = k_{idr}I_{dr}^{\ *} - k_{idr}I_{dr} \tag{3.136}$$

Combining (3.135) and (3.136):

$$\begin{bmatrix} I_{qr}^{\ *} \\ I_{dr}^{\ *} \end{bmatrix} = \underbrace{\begin{bmatrix} \frac{\hat{r}_r + p\hat{\sigma}\hat{L}_r + k_{iqr}}{k_{iqr}} & 0 \\ 0 & \frac{\hat{r}_r + p\hat{\sigma}\hat{L}_r + k_{idr}}{k_{idr}} \end{bmatrix}}_{K}\begin{bmatrix} I_{qr} \\ I_{dr} \end{bmatrix} \tag{3.137}$$

Substituting (3.127) and (3.134) in (3.137) gives:

$$C\begin{bmatrix}\sigma_{wr}\\ \sigma_{Qs}\end{bmatrix}+D=KE\begin{bmatrix}\omega_r\\ Q_s\end{bmatrix}+KD \tag{3.138}$$

$$\begin{bmatrix}\dfrac{4\hat{L}_s}{3P\hat{L}_m\lambda_{ds}} & 0\\ 0 & \dfrac{1}{p\lambda_{ds}\hat{\sigma}\hat{L}_r}\end{bmatrix}\begin{bmatrix}k_{wr}(\omega_r^*-\omega_r)\\ k_{Qs}(Q_s^*-Q_s)\end{bmatrix}+\begin{bmatrix}-\dfrac{4\hat{L}_s T_m}{3P\hat{L}_m\lambda_{ds}}\\ 0\end{bmatrix} \tag{3.139}$$

$$=\begin{bmatrix}\dfrac{\hat{r}_r+p\hat{\sigma}\hat{L}_r+k_{iqr}}{k_{iqr}}\dfrac{p8JL_s}{3PL_m\lambda_{ds}} & 0\\ 0 & -\dfrac{\hat{r}_r+p\hat{\sigma}\hat{L}_r+k_{idr}}{k_{idr}}\dfrac{2L_s}{3\omega_e L_m\lambda_{ds}}\end{bmatrix}\begin{bmatrix}\omega_r\\ Q_s\end{bmatrix}+\begin{bmatrix}-\dfrac{\hat{r}_r+p\hat{\sigma}\hat{L}_r+k_{iqr}}{k_{iqr}}\dfrac{4L_s T_m}{3PL_m\lambda_{ds}}\\ 0\end{bmatrix}$$

Solving (3.139) gives:

$$\omega_r=\frac{\hat{k}_2}{\hat{k}_1}\omega_r^*+\frac{\hat{k}_3}{\hat{k}_1}T_m \tag{3.140}$$

where $\hat{k}_1=\dfrac{2pJL_s}{L_m\lambda_{ds}}\dfrac{\hat{r}_r+p\hat{\sigma}\hat{L}_r+k_{iqr}}{k_{iqr}}+\dfrac{\hat{L}_s k_{wr}}{\hat{L}_m\lambda_{ds}}$

$$\hat{k}_2=\frac{k_{wr}\hat{L}_s}{\hat{L}_m\lambda_{ds}} \text{ and } \hat{k}_3=\frac{\hat{r}_r+p\hat{\sigma}\hat{L}_r+k_{iqr}}{k_{iqr}}\frac{L_s}{L_m\lambda_{ds}}-\frac{\hat{L}_s}{\hat{L}_m\lambda_{ds}}$$

Similarly,

$$Q_s=\frac{\hat{k}_4}{\hat{k}_5}Q_s^* \tag{3.141}$$

where $\hat{k}_4=\dfrac{k_{Qs}}{p\lambda_{ds}\hat{\sigma}\hat{L}_r}$ and $\hat{k}_5=\dfrac{k_{Qs}}{p\lambda_{ds}\hat{\sigma}\hat{L}_r}-\dfrac{\hat{r}_r+p\hat{\sigma}\hat{L}_r+k_{idr}}{k_{idr}}\dfrac{2L_s}{3\omega_e L_m\lambda_{ds}}$

If the measured parameters are assumed to be equal to the actual quantities, solving (3.139) gives:

$$\omega_r = \frac{k_2}{k_1}\omega_r^* + \frac{k_3}{k_1}T_m \tag{3.142}$$

where $k_1 = \frac{2pJL_s}{L_m\lambda_{ds}}\frac{r_r + p\sigma L_r + k_{iqr}}{k_{iqr}} + \frac{L_s k_{wr}}{L_m\lambda_{ds}}$, $k_2 = \frac{k_{wr}L_s}{L_m\lambda_{ds}}$ and

$k_3 = \frac{r_r + p\sigma L_r + k_{iqr}}{k_{iqr}}\frac{L_s}{L_m\lambda_{ds}} - \frac{L_s}{L_m\lambda_{ds}}$

Similarly,

$$Q_s = \frac{k_4}{k_5}Q_s^* \tag{3.143}$$

where $k_4 = \frac{k_{Qs}}{p\lambda_{ds}\sigma L_r}$ and $k_5 = \frac{k_{Qs}}{p\lambda_{ds}\sigma L_r} - \frac{r_r + p\sigma L_r + k_{idr}}{k_{idr}}\frac{2L_s}{3\omega_e L_m\lambda_{ds}}$

Here it should be noted that the inner current controller parameters are same for q and d-axis currents, i.e. $k_{iqr} = k_{idr}$.

Similarly, in the GSC, from (3.91):

$$\sigma_{dc} = k_{dc}(V_{dc}^* - V_{dc}) = \frac{3}{4}(M_{qr}I_{qr} + M_{dr}I_{dr}) + \frac{3}{4}\left(M_{df}I_{df} + M_{qf}I_{qf}\right) \tag{3.144}$$

$$I_{qf}^* = \frac{1}{M_{qf}}\left(\frac{4}{3}(\sigma_{dc} - \frac{3}{4}(M_{qr}I_{qr} + M_{dr}I_{dr})) - M_{df}I_{df}\right) \tag{3.145}$$

where $M_{qr} = \frac{2V_{qr}^*}{V_{dc}}$ and $M_{dr} = \frac{2V_{dr}^*}{V_{dc}}$. Here, $\frac{3}{4}(M_{qr}I_{qr} + M_{dr}I_{dr})$ is the DC-link current coming out from RSC.

And we also know from (3.73) and (3.74) that-

$$V_{qr}^* = k_{Iqr}(I_{qr}^* - I_{qr}) + \omega_{so}\left(\frac{L_m}{L_s}\lambda_{ds} + \sigma L_r I_{dr}\right) \tag{3.146}$$

$$V_{dr}^* = k_{Idr}(I_{dr}^* - I_{dr}) - \omega_{so}\sigma L_r I_{qr} \tag{3.147}$$

Using (1.146), (3.147), (3.127) and (3.134), DC-link current is expressed as:

$$\frac{3}{4}(M_{qr}I_{qr}+M_{dr}I_{dr})=$$
$$\frac{3}{2V_{dc}}\left[\begin{array}{l} k_{Iqr}k_{wr}\dfrac{p8JL_s}{3P^2L_m\lambda_{ds}}(\omega_r^*\omega_r-\omega_r^2)-\dfrac{4T_mL_s}{3PL_m\lambda_{ds}}k_{Iqr}k_{wr}(\omega_r^*-\omega_r)+\dfrac{\omega_{so}p8J\omega_r}{3P^2} \\ -\dfrac{\omega_{so}4T_m}{3P}+\dfrac{2L_sk_{Idr}k_{Qs}}{3p\sigma L_r\omega_eL_m\lambda_{ds}^2}(Q_sQ_s^*-Q_s^2)-\dfrac{4L_s^2k_{Idr}}{9\omega_e{}^2L_m^2\lambda_{ds}^2} \end{array}\right] \tag{3.148}$$

Here, λ_{ds} is regulated to constant value using flux control. Hence, it is clear from (3.148) that the DC-current flowing in ac/dc/ac converter has a non-linear relationship between control variables like ω_r, Q_s and V_{dc}. So it can be concluded that decoupled control of Q_f, Q_s, ω_r and V_{dc} can be done if the DC-link current coming out from RSC is taken as a disturbance for the GSC control.

Now, from (3.104):

$$\begin{cases} \sigma_{Qf}=(V_{df}-\hat{r}_f\,I_{df}+\hat{\omega}_e\hat{L}_f\,I_{qf}) \\ \sigma_{Qf}=(\hat{r}_f\,I_{df}+p\hat{L}_f\,I_{df}-\hat{\omega}_e\hat{L}_f\,I_{qf}-\hat{r}_f\,I_{df}+\hat{\omega}_e\hat{L}_f\,I_{qf}) \\ I_{df}^*=\dfrac{\sigma_{Qf}}{p\hat{L}_f} \end{cases} \tag{3.149}$$

From (3.149) and (3.145):

$$I_{qf}^*=\frac{1}{M_{qf}}\left(\frac{4}{3}(\sigma_{dc}-\frac{3}{4}(M_{qr}I_{qr}+M_{dr}I_{dr}))-M_{df}\frac{\sigma_{Qf}}{p\hat{L}_f}\right) \tag{3.150}$$

Combining (3.150) and (3.145) gives:

$$\begin{bmatrix} I_{qf}^{\ *} \\ I_{df}^{\ *} \end{bmatrix} = \underbrace{\begin{bmatrix} \dfrac{4}{3M_{qf}} & -\dfrac{M_{df}}{p\hat{L}_f M_{qf}} \\ 0 & \dfrac{1}{p\hat{L}_f} \end{bmatrix}}_{O} \begin{bmatrix} \sigma_{dc} \\ \sigma_{Qf} \end{bmatrix} + \underbrace{\begin{bmatrix} -\dfrac{1}{M_{qf}}(M_{qr}I_{qr} + M_{dr}I_{dr}) \\ 0 \end{bmatrix}}_{P} \tag{3.151}$$

From (3.90):

$$pC\,V_{dc} = \frac{3}{4}(M_{qr}I_{qr} + M_{dr}I_{dr}) + \frac{3}{4}\left(M_{df}I_{df} + M_{qf}I_{qf}\right) \tag{3.152}$$

$$I_{qf} = \frac{4}{3M_{qf}}(pC\,V_{dc} - \frac{3}{4}(M_{qr}I_{qr} + M_{dr}I_{dr})) - \left(\frac{M_{df}}{M_{qf}}I_{df}\right) \tag{3.153}$$

From (3.102):

$$pQ_f = \frac{3V_{qs}}{2L_f}(V_{df} - r_f I_{df} + \omega_e L_f I_{qf}) \tag{3.154}$$

$$\begin{cases} pQ_f = \dfrac{3V_{qs}}{2L_f}(r_f I_{df} + pL_f I_{df} - \omega_e L_f I_{qf} - r_f I_{df} + \omega_e L_f I_{qf}) \\ I_{df} = \dfrac{2Q_f}{3V_{qs}} \end{cases} \tag{3.155}$$

Substituting (3.155) into (3.153):

$$I_{qf} = \frac{4}{3M_{qf}}(pC\,V_{dc} - \frac{3}{4}(M_{qr}I_{qr} + M_{dr}I_{dr})) - \left(\frac{2M_{df}}{3M_{qf}}\frac{Q_f}{V_{qs}}\right) \tag{3.156}$$

Combining (3.156) and (3.155)

$$\begin{bmatrix} I_{qf} \\ I_{df} \end{bmatrix} = \underbrace{\begin{bmatrix} \dfrac{4}{3M_{qf}}pC & -\dfrac{2M_{df}}{3V_{qs}M_{qf}} \\ 0 & \dfrac{2}{3V_{qs}} \end{bmatrix}}_{Q} \begin{bmatrix} V_{dc} \\ Q_f \end{bmatrix} + \underbrace{\begin{bmatrix} -\dfrac{1}{M_{qf}}(M_{qr}I_{qr} + M_{dr}I_{dr}) \\ 0 \end{bmatrix}}_{R} \tag{3.157}$$

From (3.110):

$$\left(\hat{r}_f + p\hat{L}_f\right) I_{qf} = k_{iqf} I_{qf}^{*} - k_{iqf} I_{qf} \tag{3.158}$$

From (3.111):

$$\left(\hat{r}_f + p\hat{L}_f\right) I_{df} = k_{idf} I_{df}^{*} - k_{idf} I_{df} \tag{3.159}$$

Combining (3.158) and (3.159) gives:

$$\begin{bmatrix} I_{qf}^{*} \\ I_{df}^{*} \end{bmatrix} = \underbrace{\begin{bmatrix} \dfrac{\hat{r}_f + p\hat{L}_f + k_{iqf}}{k_{iqf}} & 0 \\ 0 & \dfrac{\hat{r}_f + p\hat{L}_f + k_{idf}}{k_{idf}} \end{bmatrix}}_{F} \begin{bmatrix} I_{qf} \\ I_{df} \end{bmatrix} \tag{3.160}$$

Substituting (3.150) and (3.157) in (3.160):

$$O\begin{bmatrix} \sigma_{dc} \\ \sigma_{Qf} \end{bmatrix} + P = FQ\begin{bmatrix} V_{dc} \\ Q_f \end{bmatrix} + FR \tag{3.161}$$

$$\begin{bmatrix} \dfrac{4}{3M_{qf}} & -\dfrac{M_{df}}{p\hat{L}_f M_{qf}} \\ 0 & \dfrac{1}{p\hat{L}_f} \end{bmatrix} \begin{bmatrix} k_{dc}(V_{dc}^{*} - V_{dc}) \\ k_{Qf}(Q_f^{*} - Q_f) \end{bmatrix} + \begin{bmatrix} -\dfrac{1}{M_{qf}}(M_{qr} I_{qr} + M_{dr} I_{dr}) \\ 0 \end{bmatrix}$$

$$= \begin{bmatrix} \dfrac{4pC}{3M_{qf}} \dfrac{\hat{r}_f + p\hat{L}_f + k_{iqf}}{k_{iqf}} & -\dfrac{2M_{df}}{3V_{qs}M_{qf}} \dfrac{\hat{r}_f + p\hat{L}_f + k_{iqf}}{k_{iqf}} \\ 0 & \dfrac{\hat{r}_f + p\hat{L}_f + k_{idf}}{k_{idf}} \dfrac{2}{3V_{qs}} \end{bmatrix} \begin{bmatrix} V_{dc} \\ Q_f \end{bmatrix} + \begin{bmatrix} -\dfrac{(M_{qr} I_{qr} + M_{dr} I_{dr})}{M_{qf}} \dfrac{\hat{r}_f + p\hat{L}_f + k_{iqf}}{k_{iqf}} \\ 0 \end{bmatrix} \tag{3.162}$$

Solving (3.162) gives:

$$V_{dc} = \frac{k_{dc}}{\hat{\tau}_1} V_{dc}^{*} - \frac{3}{4} \frac{\hat{\gamma}_f - 1}{\hat{\tau}_1} (M_{qr} I_{qr} + M_{dr} I_{dr}) \tag{3.163}$$

where $\hat{\gamma}_f = \dfrac{\hat{r}_f + p\hat{L}_f + k_{idf}}{k_{idf}}$ and $\hat{\tau}_1 = pC\hat{\gamma}_f + k_{dc}$. Similarly,

$$Q_f = \frac{\hat{\eta}_1}{\hat{\eta}_2} Q_f^* \tag{3.164}$$

where $\hat{\eta}_1 = \dfrac{k_{Qf}}{p\hat{L}_f}$ and $\hat{\eta}_2 = \hat{\gamma}_f \dfrac{2}{3V_{qs}} + \dfrac{k_{Qf}}{p\hat{L}_f}$

If the measured quantities are assumed to be equal to the actual quantities, solving (3.162) gives:

$$V_{dc} = \frac{k_{dc}}{\tau_1} V_{dc}^* - \frac{3}{4}\frac{\gamma_f - 1}{\tau_1}(M_{qr} I_{qr} + M_{dr} I_{dr}) \tag{3.165}$$

where $\gamma_f = \dfrac{r_f + pL_f + k_{idf}}{k_{idf}}$ and $\tau_1 = pC\gamma_f + k_{dc}$

Similarly,

$$Q_f = \frac{\eta_1}{\eta_2} Q_f^* \tag{3.166}$$

where $\eta_1 = \dfrac{k_{Qf}}{sL_f}$ and $\eta_2 = \gamma_f \dfrac{2}{3V_{qs}} + \dfrac{k_{Qf}}{pL_f}$

Here it should be noted that the inner current controller parameters are same for q and d-axis currents, i.e. $k_{iqf} = k_{idf}$.

Combining (3.140), (3.141), (3.163) and (3.166) gives:

$$\begin{bmatrix} \omega_r \\ Q_s \\ V_{dc} \\ Q_f \end{bmatrix} = \underbrace{\begin{bmatrix} \hat{k}_{11} & 0 & 0 & 0 \\ 0 & \hat{k}_{22} & 0 & 0 \\ 0 & 0 & \hat{k}_{33} & 0 \\ 0 & 0 & 0 & \hat{k}_{44} \end{bmatrix}}_{A} \begin{bmatrix} \omega_r^* \\ Q_s^* \\ V_{dc}^* \\ Q_f^* \end{bmatrix} + \begin{bmatrix} \hat{\sigma}_{11} T_m \\ 0 \\ 0 \\ 0 \end{bmatrix} + \begin{bmatrix} 0 \\ 0 \\ \hat{\mu}_{33} \\ 0 \end{bmatrix} \tag{3.167}$$

where $\hat{k}_{11}=\frac{\hat{k}_2}{\hat{k}_1}$, $\hat{k}_{22}=\frac{\hat{k}_4}{\hat{k}_5}$, $\hat{k}_{33}=\frac{\hat{k}_{dc}}{\hat{\tau}_1}$, $\hat{k}_{44}=\frac{\hat{\eta}_1}{\hat{\eta}_2}$, $\hat{\sigma}_{11}=\frac{\hat{k}_3}{\hat{k}_1}$ and

$$\hat{\mu}_{33}=\frac{3}{2V_{dc}}\frac{\hat{\gamma}_f-1}{\hat{\tau}_1}\begin{bmatrix} k_{Iqr}k_{wr}\frac{p8JL_s}{3P^2L_m\lambda_{ds}}(\omega_r^*\omega_r-\omega_r^2)-\frac{4T_mL_s}{3PL_m\lambda_{ds}}k_{Iqr}k_{wr}(\omega_r^*-\omega_r)+\frac{\omega_{so}p8J\omega_r}{3P^2} \\ -\frac{\omega_{so}4T_m}{3P}+\frac{2L_sk_{Idr}k_{Qs}}{3p\sigma L_r\omega_eL_m\lambda_{ds}^2}(Q_sQ_s^*-Q_s^2)-\frac{4L_s^2k_{Idr}}{9\omega_e{}^2L_m^2\lambda_{ds}^2} \end{bmatrix}$$

Combining (3.142), (3.143), (3.165) and (3.166) gives:

$$\begin{bmatrix}\omega_r\\ Q_s\\ V_{dc}\\ Q_f\end{bmatrix}=\underbrace{\begin{bmatrix}k_{11}&0&0&0\\0&k_{22}&0&0\\0&0&k_{33}&0\\0&0&0&k_{44}\end{bmatrix}}_{\theta}\begin{bmatrix}\omega_r^*\\ Q_s^*\\ V_{dc}^*\\ Q_f^*\end{bmatrix}+\begin{bmatrix}\sigma_{11}T_m\\0\\0\\0\end{bmatrix}+\begin{bmatrix}0\\0\\ \mu_{33}\\0\end{bmatrix} \quad (3.168)$$

where $k_{11}=\frac{k_2}{k_1}$, $k_{22}=\frac{k_4}{k_5}$, $k_{33}=\frac{k_{dc}}{\tau_1}$, $k_{44}=\frac{\eta_1}{\eta_2}$, $\sigma_{11}=\frac{k_3}{k_1}$ and

$$\mu_{33}=\frac{3}{2V_{dc}}\frac{\gamma_f-1}{\tau_1}\begin{bmatrix} k_{Iqr}k_{wr}\frac{p8JL_s}{3P^2L_m\lambda_{ds}}(\omega_r^*\omega_r-\omega_r^2)-\frac{4T_mL_s}{3PL_m\lambda_{ds}}k_{Iqr}k_{wr}(\omega_r^*-\omega_r)+\frac{\omega_{so}p8J\omega_r}{3P^2} \\ -\frac{\omega_{so}4T_m}{3P}+\frac{2L_sk_{Idr}k_{Qs}}{3p\sigma L_r\omega_eL_m\lambda_{ds}^2}(Q_sQ_s^*-Q_s^2)-\frac{4L_s^2k_{Idr}}{9\omega_e{}^2L_m^2\lambda_{ds}^2} \end{bmatrix}$$

As shown in (3.167) and (3.168), the transfer function matrices A and θ are both diagonal which verifies that all the four controlled quantities are independent of each other regardless of error in parameter estimation. That means, the controller design can be done independent of each other and combined them together for the overall control. According to (3.167) and (3.168), there exists a non-linear relation through the DC-link voltage controller which can be considered as a disturbance for the GSC control.

3.11.4 Phase Locked Loop (PLL)

A PLL is designed to define the reference angle for qd transformation so that the stator voltage can be aligned along the q-axis and is included in the overall model of the system to make the designed system more realistic. Figure 3.19 shows the 3-phase PLL which takes the input as the measured DFIG terminal voltage V_s and transforms it to qd-reference frame. PLL aligns the stator side voltage to q-axis by comparing d-axis load voltage with zero reference voltage. The voltage error signal is passed through the PI controller to obtain the angular frequency of the terminal bus voltage. Hence in the PLL system:

$$V_{ds} = -V_s \sin(\theta_i - \theta_s) \Rightarrow 0 = -V_s \sin(\theta_i - \theta_s) \Rightarrow \theta_i = \theta_s \tag{3.169}$$

Now the error signal is given as: $e = 0 - V_{ds} = V_s \sin(\theta_i - \theta_s)$

If $(\theta_i - \theta_s)$ is very small, then we can write: $\sin(\theta_i - \theta_s) \approx (\theta_i - \theta_s)$

From the block diagram shown in Figure 3.19, $V_s(\theta_i - \theta_s)$ is the input to the controller and ω_e is the output from the controller. Hence,

$$\begin{cases} V_s(\theta_i - \theta_s)K_{pll} = \omega_e \\ \dfrac{1}{V_s} p\theta_s = (\theta_i - \theta_s)K_{pll} = \sigma_\theta \end{cases} \tag{3.170}$$

where, $K_{pll} = k_{P\_pll} + \dfrac{k_{I\_pll}}{p}$

$$\frac{1}{V_s} p\theta_s = \left(k_{P\_pll} + \frac{k_{I\_pll}}{p}\right)\theta_i - \left(k_{P\_pll} + \frac{k_{I\_pll}}{p}\right)\theta_s \tag{3.171}$$

$$\frac{\theta_s}{\theta_i} = \frac{pV_s k_{P\_pll} + V_s k_{I\_pll}}{p^2 + pV_s k_{P\_pll} + V_s k_{I\_pll}} \tag{3.172}$$

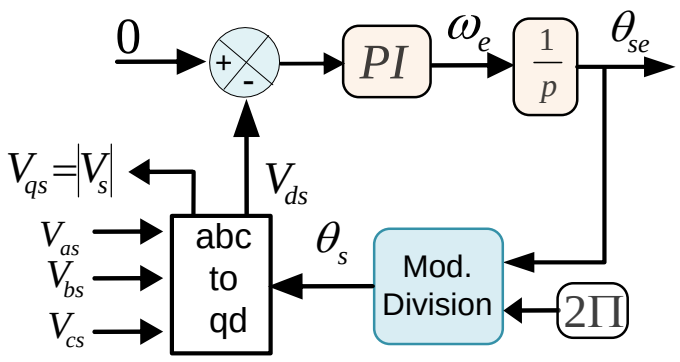

Figure 3.19 Block diagram of PLL control

Now comparing the denominator of (3.172) with the Butterworth second order polynomial $p^2+\sqrt{2}\omega_{0\_pll}p+\omega_{0\_pll}^2$, the parameters of the controller are:

$$k_{I\_pll}=\frac{\omega_{0\_pll}^2}{V_s} \tag{3.174}$$

where ω_{0_pll} is the bandwidth frequency of the PLL controller.

Table 3.1 gives the PI controllers values used for the simulation study following above procedure. The switching frequency is taken as 1 kHz and the bandwidth of inner current controller is taken ten times that of outer loop controller, i.e.

$\omega_{sw}=2*\pi*f_{sw}=6280\ rad/\sec$ and $\omega_{inner}=\frac{\omega_{sw}}{10}$; $\omega_{outer}=\frac{\omega_{inner}}{10}$

$\omega_{inner}=\omega_0=\omega_{oc}=628\ rad/s$, $\omega_{outer}=\omega_{odc}=\omega_{oQs}=\omega_{oQf}=62.8\ rad/s$ and $\omega_{owr}=0.628\ rad/s$

From (3.84): $k_{qp}=k_{dp}=\sqrt{2}\omega_0\sigma L_r-r_r=1.76$ and from (3.85): $k_{qi}=k_{di}=\sigma L_r\omega_0^2=783.6$

From (3.86): $k_{Pwr}=\sqrt{2}\omega_{owr}\frac{2J}{P}=8.26$ and from (3.87): $k_{Iwr}=\frac{2J}{P}\omega_{owr}^2=3.65$

From (3.95): $k_{Pdc}=\sqrt{2}\omega_{odc}C_{dc}=5.32$ and from (3.96): $k_{Idc}=\omega_{odc}^2C_{dc}=236.63$

Table 3.1 Parameters of the machine and PI controller coefficients

r_s	2.3 mΩ	C_{dc}	60 mF	k_{qp} / k_{dp}	1.76	k_{qi} / k_{di}	783.6
r_r	2 mΩ	L_f	2 mH	k_{Pwr}	8.26	k_{Iwr}	3.65
L_s	2.93 mH	r_f	2 mΩ	k_{Pdc}	5.32	k_{Idc}	236.63
L_r	2.97 mH	J	18.7	k_{P1}	1.77	k_{I1}	788.76
L_m	2.88 mH	P	4	k_{PQs}	0.00022	k_{IQs}	0.001
σ	0.046			k_{PQf}	0.00022	k_{IQf}	0.00093
				$k_{P\lambda s}$	72.06	$k_{I\lambda s}$	3943.8
V_s	563.38 V	N	1	k_{P_pll}	2.10	k_{I_pll}	1244.4

From (3.115): $k_{P1} = \sqrt{2}\omega_{oc} L_f - r_f = 1.77$ and from (3.116): $k_{I1} = \omega_{oc}^2 L_f = 788.76$

From (3.88): $k_{PQs} = \sqrt{2}\omega_{0Qs}\Delta = 0.00022$ and from (3.89): $= k_{IQs} = \Delta\omega_{Qs}^{\ 2} = 0.001$

From (3.107): $k_{PQf} = \sqrt{2}\omega_{0Qf}\Gamma = 0.0002$ and from (3.108): $k_{IQf} = \Gamma\omega_{0Qf}^{\ 2} = 0.0093$

In PLL controller design, the switching frequency is taken as 2 kHz and the bandwidth of the PLL controller is taken as: $\omega_{sw} = 2 * \pi * f_{sw} = 12560\ rad/s$ and

$\omega_0 = \frac{\omega_{sw}}{15} = 837.3\ rad/s$

From (3.173): $k_{P\_pll} = \frac{\sqrt{2}\omega_0}{V_s} = 2.10$ and from (3.174): $k_{I\_pll} = \frac{\omega_0^2}{V_s} = 1244.4$

3.11.5 Stator Flux Estimation

As shown in Figure 3.17, the stator side flux should be estimated as accurately as possible for the RSC control implementation. Therefore this section explains the stator flux estimation using Low Pass Filter (LPF).

The stator flux in stationary reference frame is given as:

$$V_{qds}^{s} = r_s I_{qds}^{s} + p\lambda_{qds}^{s} \tag{3.175}$$

$$\lambda_{qds}^{s} = \int \left(V_{qds}^{s} - r_s I_{qds}^{s} \right) dt \tag{3.176}$$

Flux can be estimated using (3.176) but the pure integration ($1/p$) involves the DC offsets and drifts [64]. To solve these problems, the pure integrator is replaced by a LPF. The estimated stator flux by the LPF can be given as:

$$\frac{\hat{\lambda}_{sl}}{V_e} = \frac{1}{p + a} \tag{3.177}$$

where $\hat{\lambda}_{sl}$ is the estimated stator flux by LPF, a = pole and $V_e = V_{qds} - r_s I_{qds}$ the phase lag and the gain of (3.177) can be given as:

$$\phi = -\tan^{-1} \frac{\hat{\omega}_e}{a} \tag{3.178}$$

$$M = \left| \frac{\hat{\lambda}_{sl}}{V_e} \right| = \frac{1}{\sqrt{a^2 + \hat{\omega}_e^2}} \tag{3.179}$$

where $\hat{\omega}_e$ is the estimated synchronous angular frequency given as [64]:

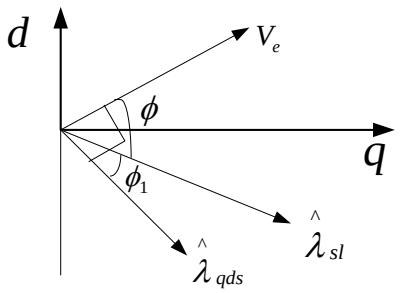

Figure 3.20 Vector diagram of the LPF and the pure integrator [64]

$$\hat{\omega}_e = \frac{(V_{qs} - r_s I_{qs})\lambda_{ds} - (V_{ds} - r_s I_{ds})\lambda_{qs}}{|\lambda_s|^2} \tag{3.180}$$

The LPF eliminates the saturation and reduces the effect of DC offsets but at the same time it brings the magnitude and phase angle error due to the cut off frequency of the LPF. Figure 3.20 shows the phase lag of $\hat{\lambda}_{sl}$ estimated by the LPF and the phase lag of $\hat{\lambda}_{qds}$ estimated by the pure integrator. The phase lag of $\hat{\lambda}_{qds}$ is 90° and the gain is $1/\left|\hat{\omega}_e\right|$. However, the phase lag of the LPF is not 90° and the gain is not $1/\left|\hat{\omega}_e\right|$. Hence, an error will be produced by this effect of the LPF. When the machine frequency is lower than the cutoff frequency of the LPF, the error is more severe. In order to remove this error, the LPF in (3.177) should have a very low cutting frequency. However, there still remains the drift problem due to the very large time constant of the LPF. For the exact estimation of the stator flux, the phase lag and the gain of $\hat{\lambda}_{sl}$ in (3.177) have to be 90° and $1/\left|\hat{\omega}_e\right|$, respectively. Furthurmore, to solve the drift problem, the pole should be located far from the origin.

Hence, the decrement in the gain of the LPF is compensated by multiplying a gain compensator, G in (3.181) and the phase lag is compensated by multiplying a phase compensator, P in (3.182) given as:

$$G = \frac{\sqrt{a^2 + \hat{\omega}_e^2}}{\left|\hat{\omega}_e\right|} \tag{3.181}$$

$$P = \exp(-j\phi_1) \tag{3.182}$$

$$\phi_1 = \tan^{-1}\frac{\hat{\omega}_e}{a} - \frac{\pi}{2} \tag{3.183}$$

$$\frac{\hat{\lambda}_{qds}}{V_e} = \frac{1}{p+a}\frac{\sqrt{a^2+\hat{\omega}_e^2}}{\left|\hat{\omega}_e\right|}\exp(-j\phi_1) \tag{3.184}$$

The cutoff frequency in LPF cannot be located at fixed point far from the origin. If the pole is varied proportionally to the machine speed, the proportion of the machine frequency to the cutoff frequency of the LPF is constant. If the proportion is large, the estimation error will be very small. Consequently, the pole is determined to be varied proportionally to the motor speed as (3.185). Therefore, the pole is located close to the origin in very low speed range and far from the origin in high speed range.

$$a = \frac{\left|\hat{\omega}_e\right|}{K} \tag{3.185}$$

where K = constant. Finally, the complete equation for stator flux estimator can be derived as:

$$\frac{\hat{\lambda}_{qds}}{V_e} = \frac{1}{p+(\hat{\omega}_e/K)}\frac{\sqrt{(\hat{\omega}_e/K)^2+\hat{\omega}_e^2}}{\left|\hat{\omega}_e\right|}\exp(-j\phi_1) \tag{3.186}$$

where $\exp(-j\phi_1) = \cos(\phi_1) - j\sin(\phi_1)$, $\cos(\phi_1) = \dfrac{\left|\hat{\omega}_e\right|}{\sqrt{(\hat{\omega}_e/K)^2+\hat{\omega}_e^2}}$ and $\sin(\phi_1) = \dfrac{\hat{\omega}_e/K}{\sqrt{(\hat{\omega}_e/K)^2+\hat{\omega}_e^2}}$

Simplifying (3.181) and separating into real and imaginary parts gives:

$$\hat{\lambda}_{qs} = \frac{1}{p+(\hat{\omega}_e/K)}\frac{\sqrt{(\hat{\omega}_e/K)^2+\hat{\omega}_e^2}}{\left|\hat{\omega}_e\right|}\left\{\cos\phi_1(V_{qs}-r_sI_{qs}) + \sin\phi_1(V_{ds}-r_sI_{ds})\right\} \tag{3.187}$$

$$\hat{\lambda}_{ds} = \frac{1}{p + (\hat{\omega}_e / K)} \frac{\sqrt{(\hat{\omega}_e / K)^2 + \hat{\omega}_e^2}}{\left|\hat{\omega}_e\right|} \left\{\cos\phi_1 (V_{ds} - r_s I_{ds}) - \sin\phi_1 (V_{qs} - r_s I_{qs})\right\} \tag{3.188}$$

Figure 3.21 shows the overall block diagram of the system to estimate stator side flux using LPF and estimated synchronous speed of the machine. Similarly, Figure 3.22 shows the schematic diagram of the overall DFIG wind turbine control structure.

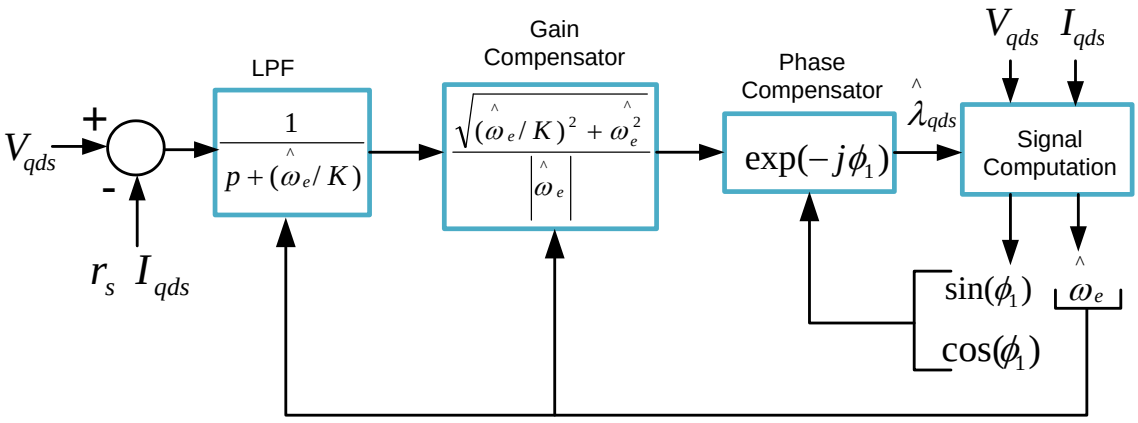

Figure 3.21 Overall block diagram of the stator flux estimation using LPF [64]

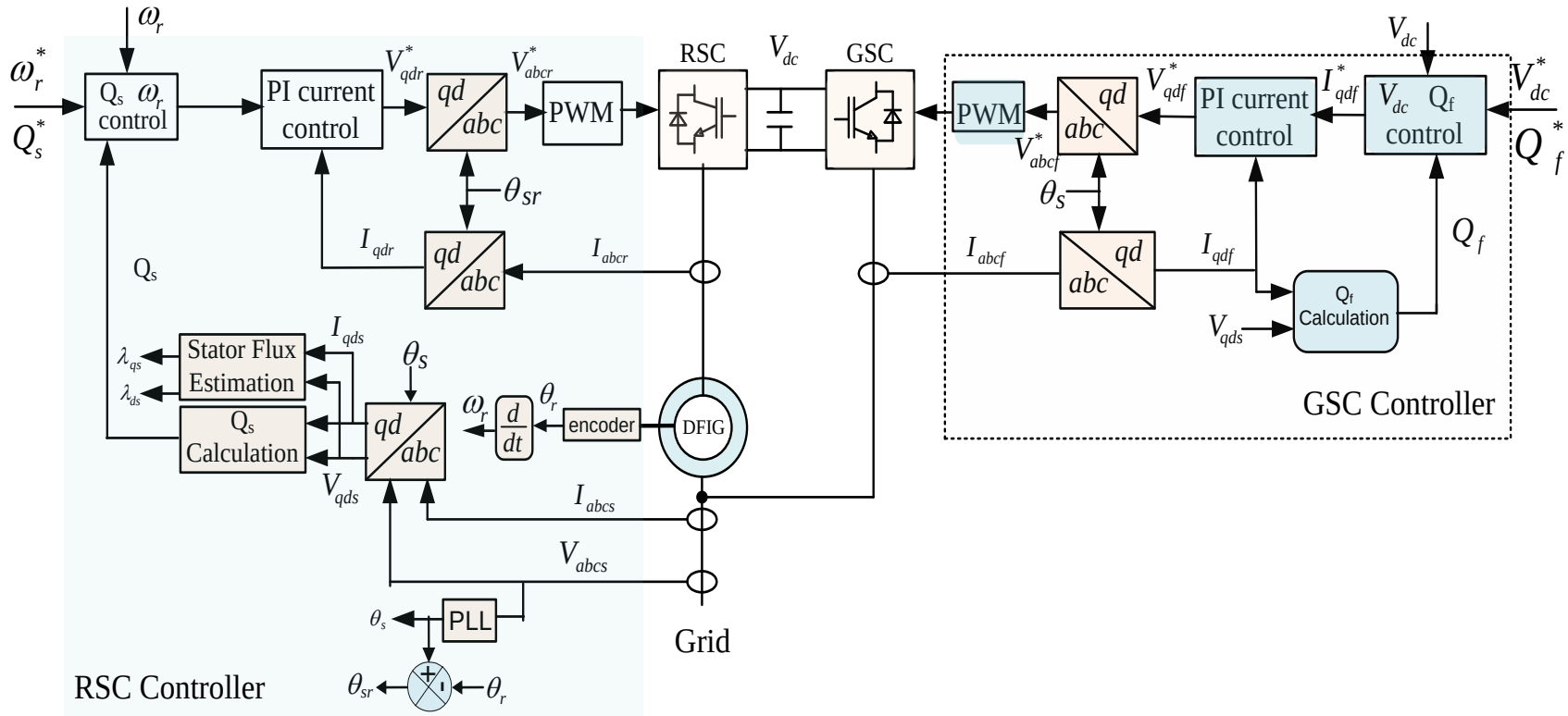

Figure 3.22 Schematic diagram of the DFIG wind turbine control structure

3.12 Simulation Results

Figure 3.23 shows the plot of stator voltage and fluxes in q and d axis. The stator voltage is aligned along q-axis using the reference angle given by PLL and the q-axis stator flux is regulated to be zero and d-axis flux gives the total stator flux.

Figure 3.24 shows the plot of reference angle given by PLL to align the stator voltage along the q-axis. Figure 3.25 depicts the angular synchronous frequency of the system measured by the PLL and estimated by the stator flux estimator.

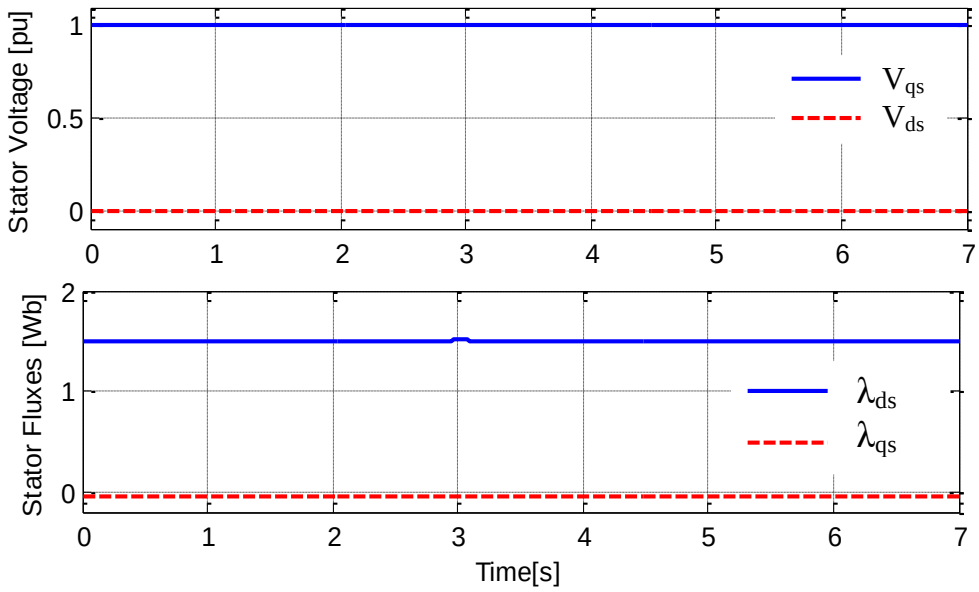

Figure 3.23 Stator voltage alignment and flux control for the decoupled control of active and reactive power

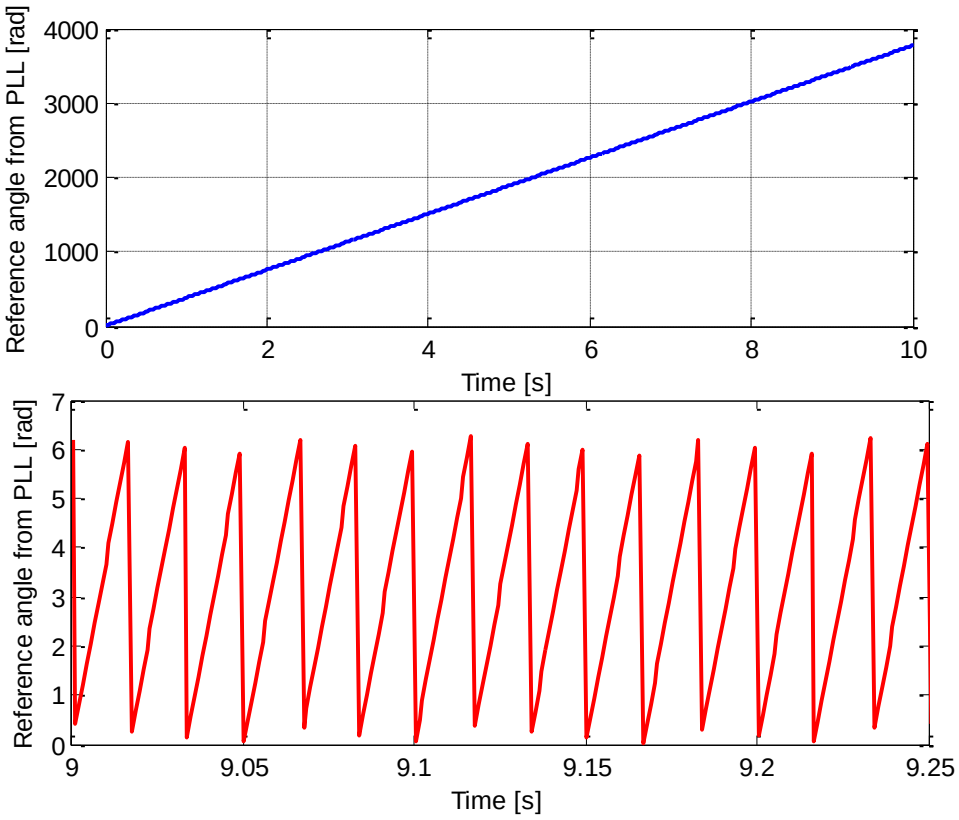

Figure 3.24 Reference angle output from PLL, θ_{se} (top) and reference angle after modular division by 2π, θ_s (bottom)

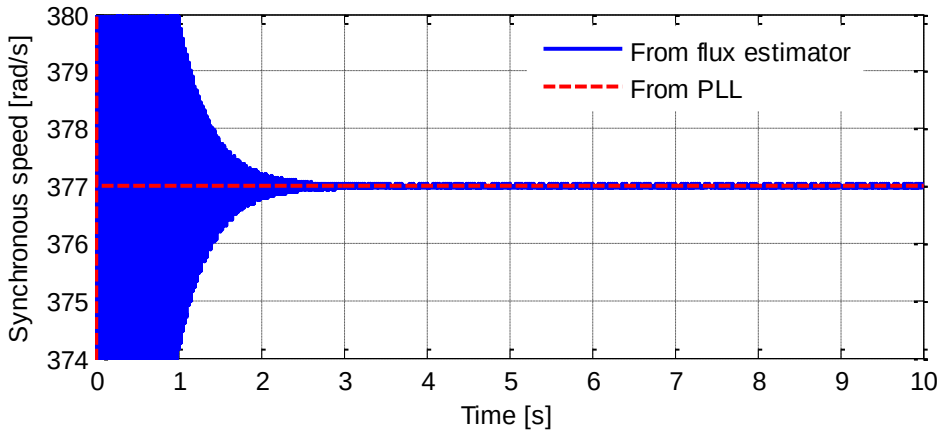

Figure 3.25 The angular synchronous frequency of the DFIG system measured by PLL and the stator flux estimator

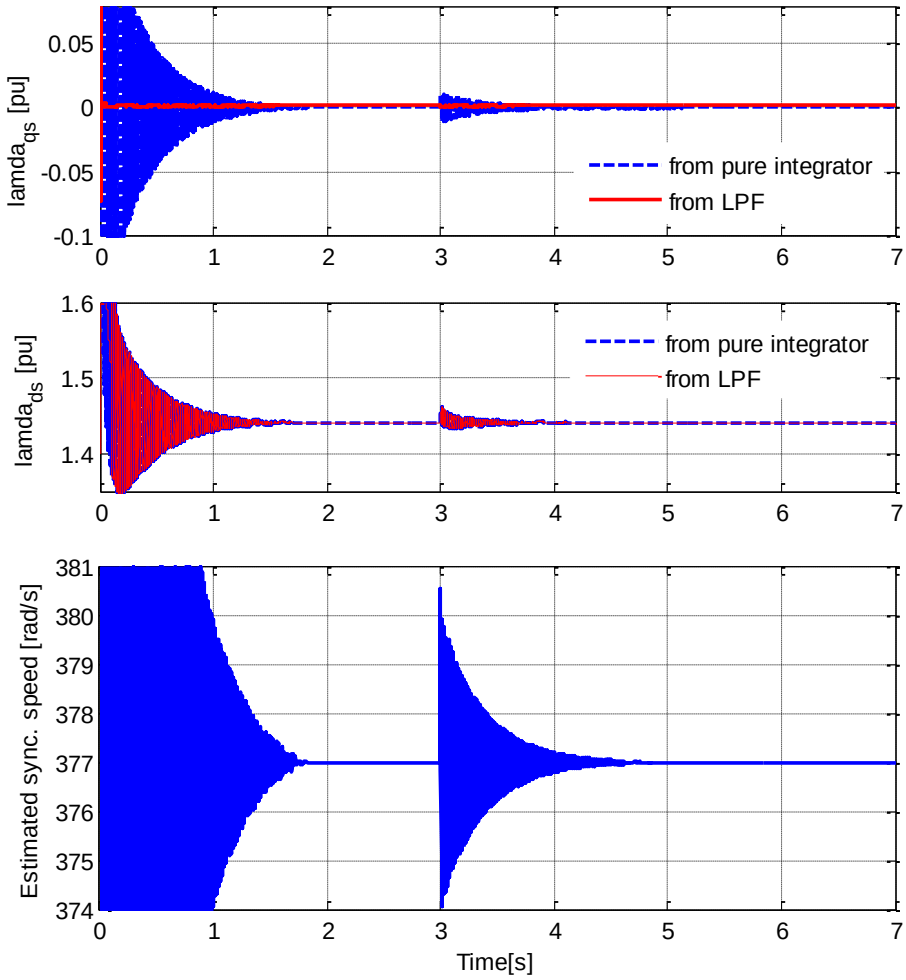

Figure 3.26 Estimated stator fluxes and synchronous speed of the machine

The estimated stator fluxes using pure integrater as well as LPF and estimated synchronous angular speed of the machine are presented in Figure 3.26. At t=3 sec., the step increase in rotor speed is applied from 391 rad/s to 400 rad/s as a result there is small oscillation in flux and speed estimated values which settles down quickly as shown in Figure 3.26.

Furthurmore, simulation studies are carried out for a 1.5 MW DFIG-based WECS to verify the effectiveness of above described control system under varying wind speed. Two different simulation studies are done for assessing the performance of the control

system discussed above. In the first case shown in Figures 3.27 and 3.28, the step decrease in wind speed from 12 m/s to 8 m/s is created at t = 8 s, the rotor speed and active power output varies according to wind speed where as reactive power is regulated to a constant value. Again at t = 5 s, step increase in reactive power supplied by stator side is applied and at t = 10 s, step increase in reactive power supplied by GSC is applied. Both cases do not affect the active power output of the DFIG which proves the decouple control of active and reactive power.

Figure 3.29 (a) shows the wind speed profile of DFIG-based WECS. The wind speed varies in a range of ± 4 m/s around its mean value of 12 m/s which is the rated wind speed of the turbine. The variation of wind speed causes change of operation mode in the wind turbine system. When the wind speed is less than rated speed, wind turbine is operating in MPPT mode so C_P = 0.48 and tip speed ratio = 8.1 with pitch angle = 0. When the wind speed is more than rated speed, pitching control starts operating as a result, $C_P < 0.48$, tip speed ratio < 8.1 and pitch angle > 0 as shown in Figure 3.29 (b), Figure 3.29 (c), and Figure 3.29 (d), respectively. Figure 3.29 (e) shows the independent control of active and reactive power in DFIG as explained above. When the wind speed varies, the active power output varies accordingly but the reactive power is always regulated to zero, i.e. unity power factor operation of both RSC and GSC. By doing so, the power factor of the overall DFIG wind turbine system can be regulated according to the requirement. During the entire operation period of the wind turbine, GSC maintains the DC-link voltage in back to back converter of the DFIG to a constant value.

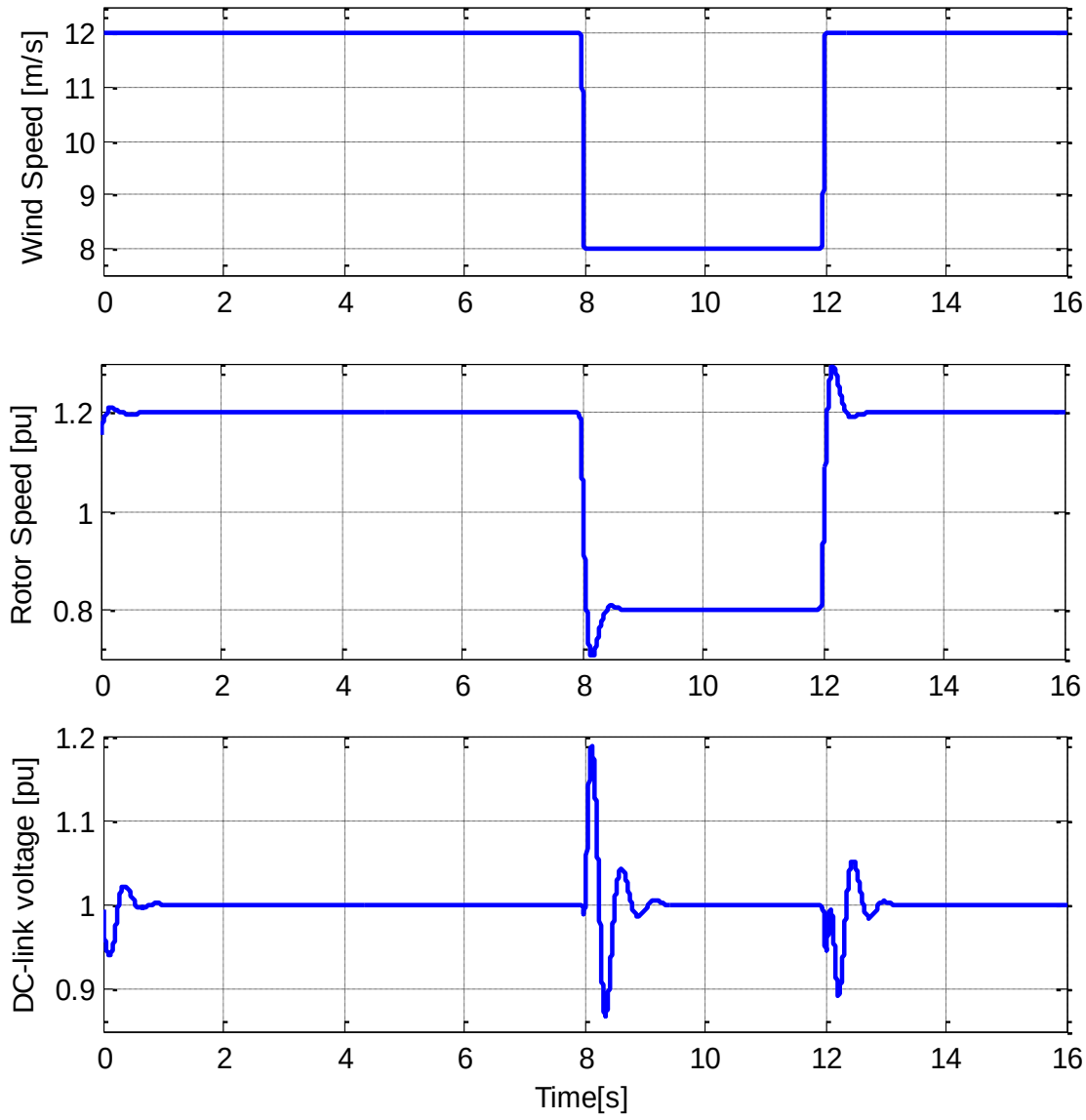

Figure 3.27 Simulation results of 1.5 MW DFIG-based WECS for step change in wind speed and corresponding rotor speed as well as DC-link voltage

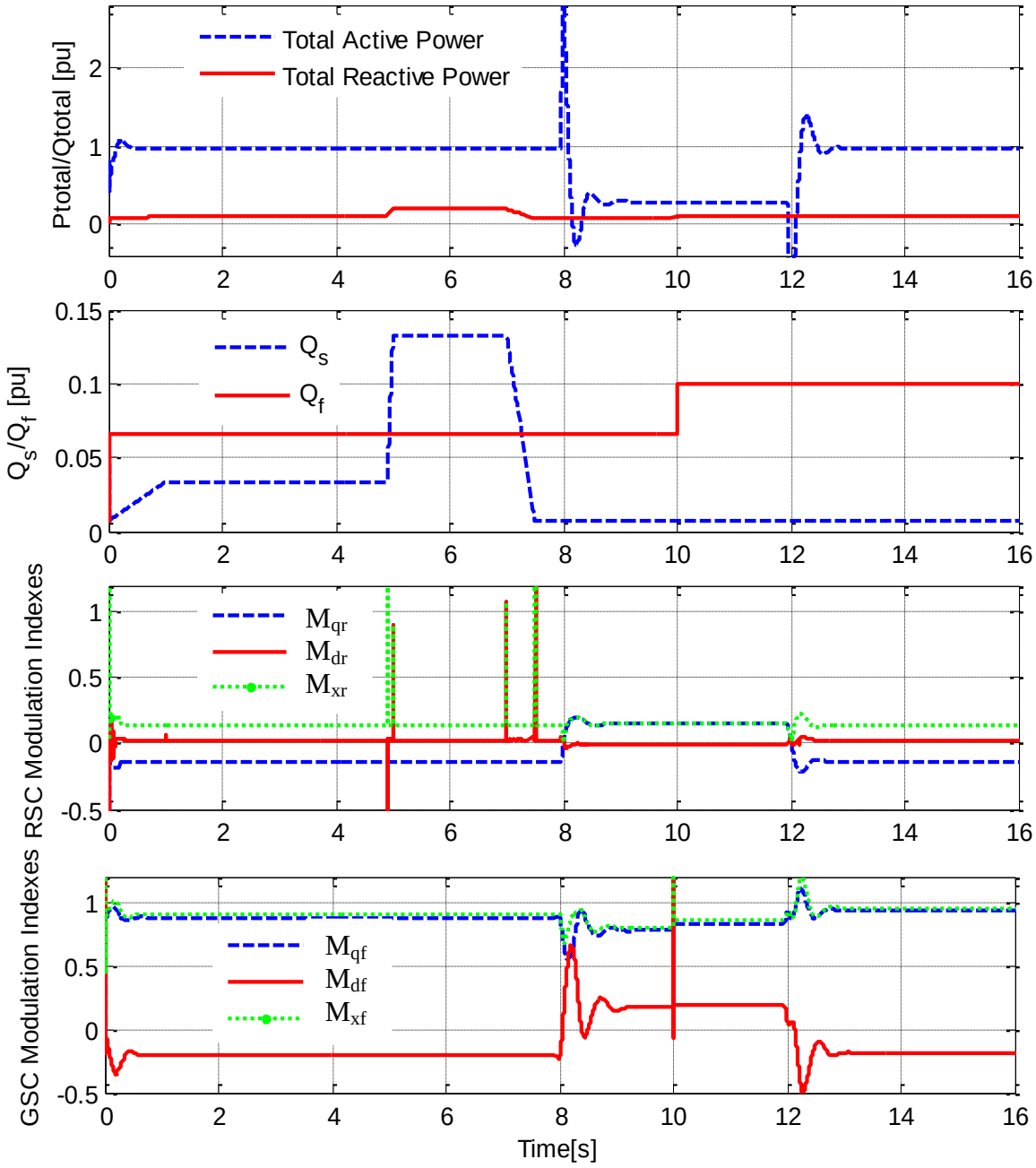

Figure 3.28 Simulation results of 1.5 MW DFIG-based WECS for step change in wind speed showing decoupled control of active and reactive power with corresponding modulation indexes in RSC and GSC

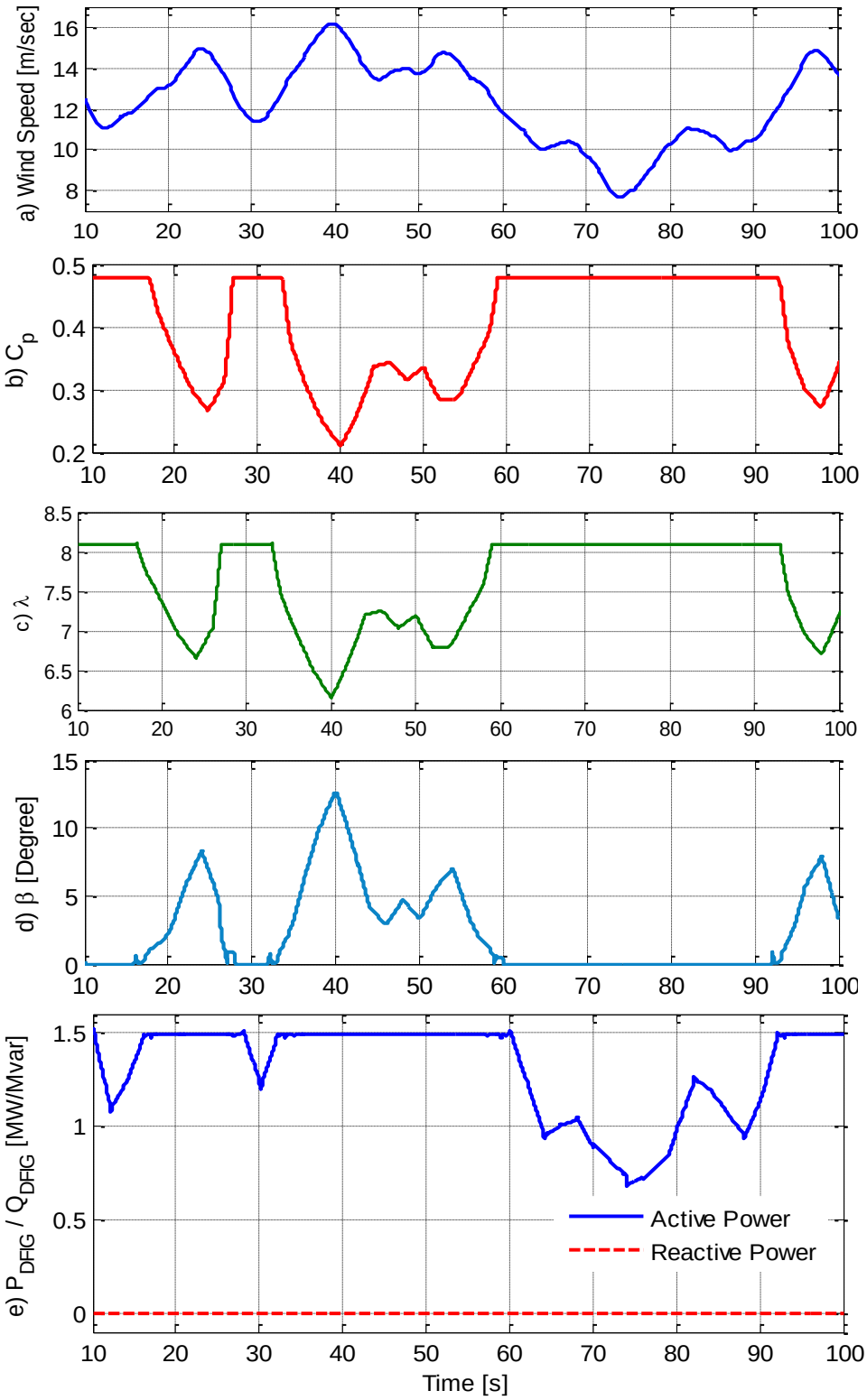

Figure 3.29 Simulation results of 1.5 MW DFIG-based WECS: (a) wind speed, (b) Coefficient of performance, (c) tip speed ratio (d) pitch angle and (e) Total active and reactive power output.

Hence, in this chapter, modeling and controller development for variable-speed variable-pitch wind turbine is presented. Vector control technique is implemented for decoupled control of active and reactive power in DFIG connected to power grid. The decoupled control of the rotor speed, stator side supplied reactive power, DC-link voltage and GSC supplied reactive power is verified by calculating the overall transfer function of the system. The dynamic characteristics of the DFIG-based WECS are studied during varying wind speed inputted to the wind turbine. In Chapter 4, the steady state characteristics of DFIG wind turbine system and its reactive power capability are presented.

CHAPTER 4

REAL AND REACTIVE POWER CAPABILITY OF DFIG WIND TURBINE SYSTEMS

In this chapter, the DFIG steady state behavior is investigated by analyzing its steady state operating characteristics. The aerodynamic, mechanical, and electrical steady state characteristics of the DFIG-based WECS are analyzed. The steady state reactive power capability study of the DFIG is done in the last section of this chapter.

4.1 Real Power Flow Analysis

In this section, set of steady state equations of the DFIG system are gathered. Those equations are solved simultaneously to obtain the steady state real power flow curves in the sator and rotor side of the DFIG by varying the rotor speed from sub-synchronous speed to super synchronous speed. The machine is assumed to be operating in unity power factor mode, i.e. reactive power output from the machine is zero.

4.1.1 Steady State Equations

The steady state equations of the DFIG are obtained from the machine voltage Equations (3.1) to (3.8) with all the time derivatives equal to zero as:

$$V_{qs} = r_s I_{qs} + \omega_e L_s I_{ds} + \omega_e L_m I_{dr} \tag{4.1}$$

$$V_{ds} = r_s I_{ds} - \omega_e L_s I_{qs} - \omega_e L_m I_{qr} \tag{4.2}$$

$$V_{qr} = r_r I_{qr} + (\omega_e - \omega_r) L_m I_{ds} + (\omega_e - \omega_r) L_r I_{dr} \tag{4.3}$$

$$V_{dr} = r_r I_{dr} - (\omega_e - \omega_r) L_m I_{qs} - (\omega_e - \omega_r) L_r I_{qr} \tag{4.4}$$

As shown in above four equations, for given stator voltage which is directly connected to grid (V_{qs}, V_{ds}), synchronous speed (ω_e) and rotor speed (ω_r) or wind speed (V_w), (4.1) - (4.4) is a system of four equations and six unknowns (V_{qr}, V_{dr}, I_{qs}, I_{ds}, I_{qr}, and I_{dr}). Hence, two more equations have to be specified so that an operating point can be determined. In the wind energy conversion applications, it is sensible to impose a constraint on the electrical torque (or rotor speed) for maximum power captured, and the other constraint on the reactive power (or power factor) for terminal voltage control. The two constraints can be written as: Mechanical Torque = Electro-magnetic Torque, i.e.:

$$T_m = \frac{3P}{4} L_m \left[I_{qr} I_{ds} - I_{dr} I_{qs} \right] \tag{4.5}$$

In wind turbine system, if wind speed is less than rated speed, from Equation (3.39):

$$\begin{cases} T_m = \dfrac{R}{\lambda * Gear\ Ratio} \rho A V_w{}^2 C_p \\ w_r = \dfrac{\lambda V_w}{R} Gear\ Ratio \end{cases} \tag{4.6}$$

If the wind speed is more than rated speed, the mechanical torque from the wind turbine is given as:

$$T_m = \frac{P_{m\_rated}}{\omega_{r\_rated}} \tag{4.7}$$

where P_{m_rated} is the rated power and ω_{r_rated} is the rated rotor speed of the DFIG wind turbine system.

If DFIG is operating in unity power factor operation mode:

$$Q_s = \frac{3}{2}(V_{qs}I_{ds} - V_{ds}I_{qs}) = 0 \tag{4.8}$$

If DFIG is operating in constant terminal voltage operation mode:

$$V_{qs}^2 + V_{ds}^2 = |V_t|^2 \tag{4.9}$$

where V_t is the desired DFIG terminal voltage magnitude.

As explained in Chapter 3, the constraints (4.5) and (4.8) or (4.9) are the control objectives of the RSC. The torque reference T_{ref} is such that maximum power tracking is achieved in MPPT operation mode and rated torque tracking is achieved in pitch control (constant power) operation mode. The reactive power Q_{s_ref} is determined by the desired power factor or terminal voltage and by the reactive power sharing policy with the GSC.

In the DFIG, rotor side is connected to the grid through back-to-back power converters whose steady state equations are discussed below. Since, DC-link capacitor does not exchange any DC current during steady state, i.e.:

$$\frac{3}{4}\left(M_{qr}I_{qr} + M_{dr}I_{dr}\right) + \frac{3}{4}\left(M_{qf}I_{qf} + M_{df}I_{df}\right) = 0 \tag{4.10}$$

where M_{qr} and M_{dr} are RSC modulation indexes, I_{qr} and I_{dr} are current flowing into RSC, M_{qf} and M_{df} are GSC modulation indexes, and I_{qf} and I_{df} are currents flowing out from GSC to grid. Here, it should be noted that during steady state, DC-link voltage V_{dc} is constant so $M_{qr} = \frac{2V_{qr}}{V_{dc}}$ and $M_{dr} = \frac{2V_{dr}}{V_{dc}}$.

Using Kirchhoff's voltage law (KVL) during steady state across RL filter given by (3.98) and (3.99) as:

$$\begin{cases} M_{qf}\dfrac{V_{dc}}{2} = r_f I_{qf} + \omega_e L_f I_{df} + V_{qs} \\ M_{df}\dfrac{V_{dc}}{2} = r_f I_{df} - \omega_e L_f I_{qf} + V_{ds} \end{cases} \tag{4.11}$$

If the GSC is operating in unity power factor mode, then:

$$Q_{GSC} = \frac{3}{2}(V_{qs} I_{df} - V_{ds} I_{qf}) = 0 \tag{4.12}$$

In overall DFIG system, we have ten steady state Equations (4.1)-(4.5), (4.8) or (4.9) and (4.10)-(4.12) and ten unknowns which are: I_{qs}, I_{ds}, I_{qr}, I_{dr}, I_{qf}, I_{df}, M_{qf}, M_{df}, M_{qr} and M_{dr}. Hence we can get a unique solution of the system, i.e. particular operating point.

4.1.2 Steady State Characteristics

The steady state aerodynamic characteristics of variable-speed variable-pitch wind turbine system are discussed based on the aerodynamic equations of the wind turbines system given by (3.37) and (3.38) is shown in (4.13). Variable speed-variable pitch wind turbine basically operates in two modes, MPPT mode in low wind speed and pitch control mode in higher wind speed more than rated speed (12 m/s in this study).

$$\begin{cases} P_m = \dfrac{1}{2}\rho\, A V_w{}^3\, C_p \\ C_p(\lambda,\beta) = 0.5176\left(\dfrac{116}{\lambda_i} - 0.4\beta - 5\right)e^{-21/\lambda_i} + 0.0068\lambda \end{cases} \tag{4.13}$$

As given by (4.13), mechanical power from wind is function of C_p which in turn is function of pitch angle and tip speed ratio (see Figure 3.8). So if wind turbine is operating in MPPT mode, C_p should be maximum (= 0.48 as shown in Figure 4.1) in which case,

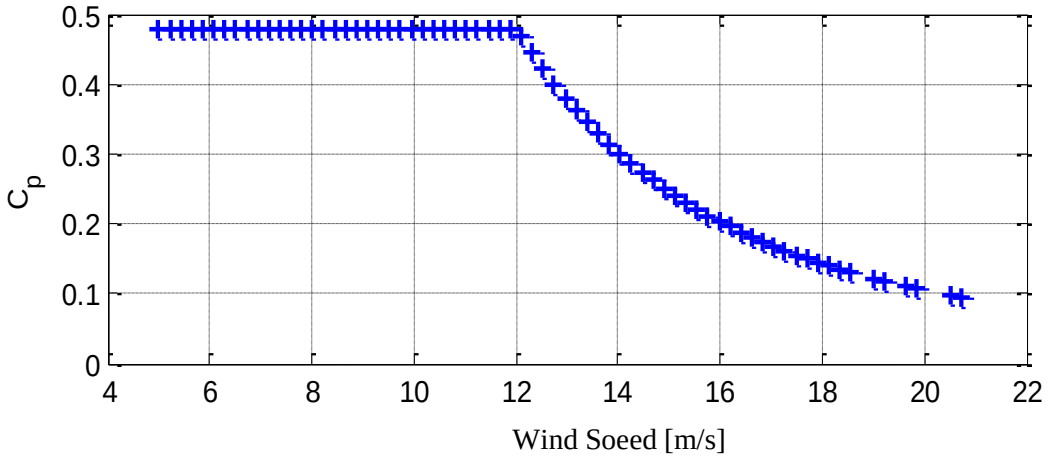

Figure 4.1 Steady state coefficient of performance in variable speed wind turbine

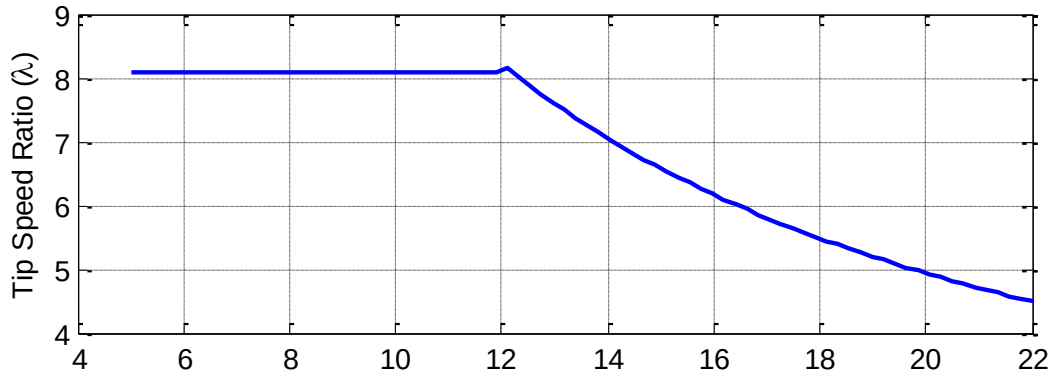

(a)

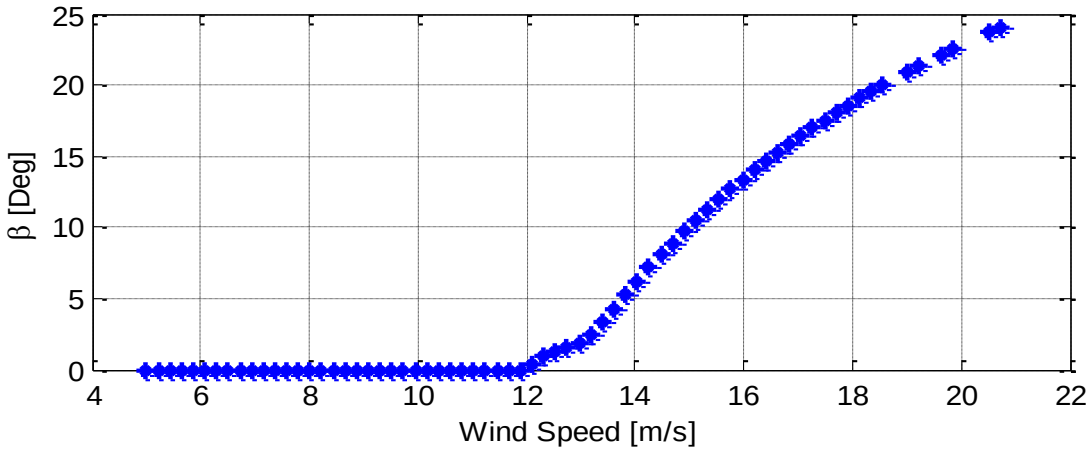

(b)

Figure 4.2 Steady state aerodynamic characteristics of wind turbine system, (a) tip speed ratio and (b) pitch angle

pitch angle will be zero and tip speed ratio will be maximum (see Figures 3.8, 4.2(a) and 4.2(b)). As the wind speed increases more than rated wind speed, pitch control should be activated so as to limit the wind turbine from getting overload. When the pitch angle increases, C_p decrease (so does the tip speed ratio) and less mechanical power from wind is extracted as shown in Figures 4.1 and 4.2. Figure 4.3 shows the various steady state control settings proposed in the DFIG-based WECS for MPPT mode and pitch regulation modes. In the low wind speed (MPPT mode), power output is proportional to the wind speed and rotor speed is also proportional to wind speed. At higher wind speed, control setting should be set in such a way that the wind turbine operates at rated power and rated rotor speed as depicted in Figure 4.3.

Figures 4.4 - 4.11 show the steady-state characteristics obtained by solving Equations (4.1)-(4.5), (4.8) or (4.9) and (4.10)-(4.13), under the assumptions that the terminal voltage is at nominal level ($V_{qs} = 1$ and $V_{ds} = 0$) and the DFIG is operating at unity power factor ($Q_s = Q_{GSC} = 0$). Figure 4.3 shows that DFIG is able to produce active power ($P_{DFIG} > 0$) at unity power factor regardless of the wind speed variation. In addition, the DFIG is able to operate optimally in low wind speed regime by capturing maximum input power over a wide range of wind speed and rotor speed. It is seen that choosing a higher rated rotor speed gives lower electrical torque in rated regime since the rated torque is defined as the rated air gap power (rated output power plus losses) divided by the rated rotor speed, i.e. $T_{e\_rated} = \dfrac{P_{output} + P_{losses}}{\omega_{rated}}$.

The control of the wind turbine shown in Figure 4.3 is targeted to maintain both the mechanical speed of the turbine shaft and the generator power output to be within rated

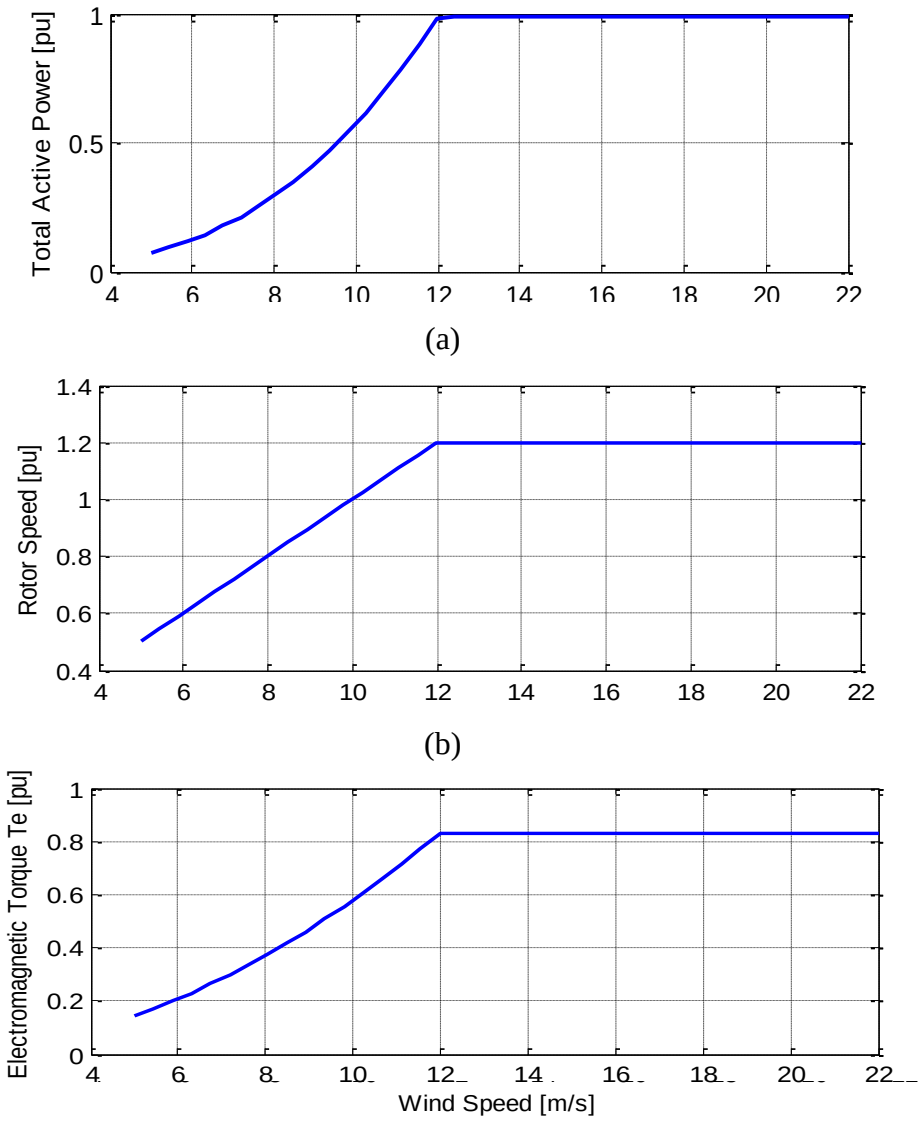

Figure 4.3 Steady state control settings of DFIG-based wind turbine system for various wind speeds, from top to bottom: (a) total active power, (b) rotor speed, and (c) T_e

limits, while at the same time extracting as much power from the wind as possible and converting it into electrical power.

Figure 4.4 and Figure 4.5 show the steady state power flow in stator side and rotor side and the total power flow in DFIG for different rotor speeds (W_r). As shown in Figure 4.4, the stator side is underutilized when the rotor speed exceeds rated speed, i.e. stator

supplied power decreases to maintain total output power within the turbine power rating. So if the turbine power rating is more than the DFIG, then the DFIG wind turbine system can be operated as shown in Figure 4.5 to extract more power from the wind utilizing the same DFIG at super-synchronous speed operation mode, i.e. generator can generate more

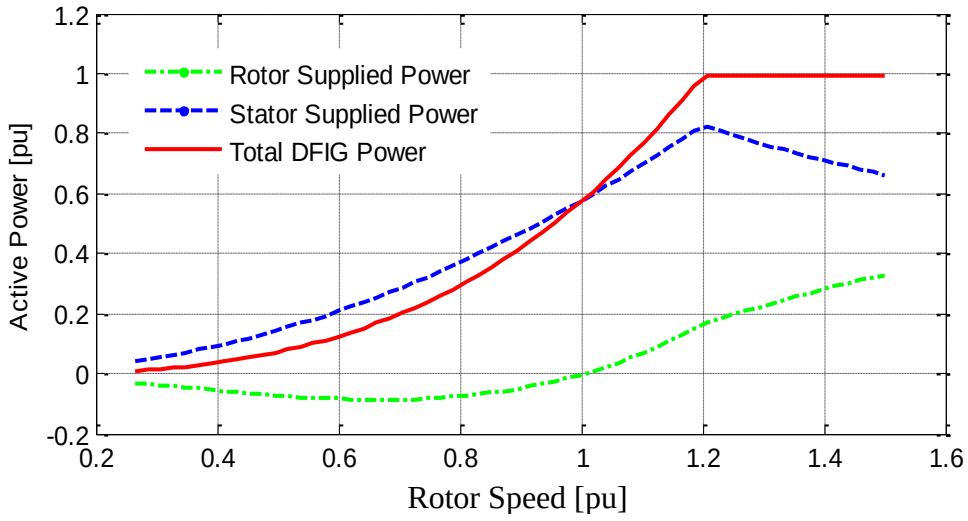

Figure 4.4 DFIG steady state power flows in the stator and rotor and the total power flow with the assumption that power ratings of DFIG and wind turbine are equal

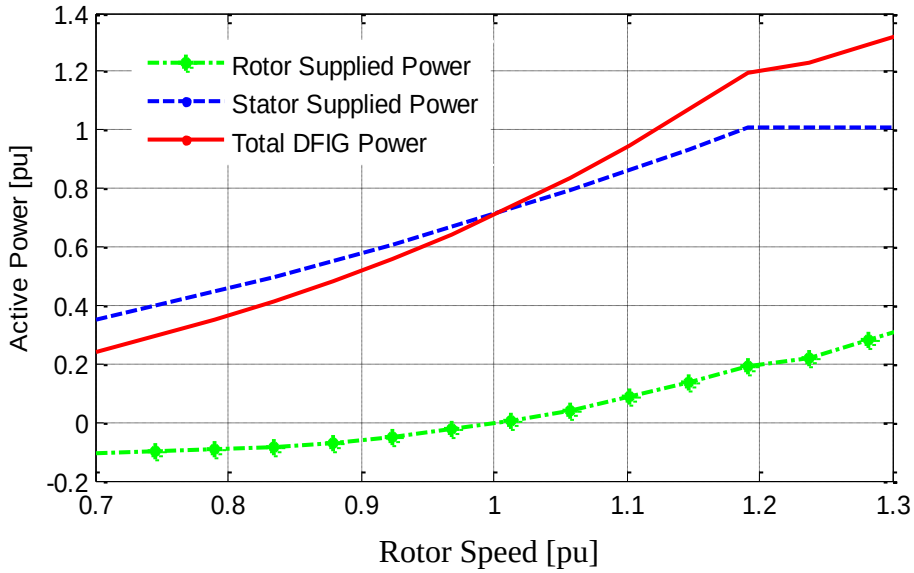

Figure 4.5 DFIG steady state power flows in the stator and rotor and the total power flow with assumption that power rating of wind turbine > power rating of DFIG

than 100% output power. In other words, smaller power rated DFIG can be coupled with bigger power rated wind turbine to generate the electrical power without overloading DFIG.

The DFIG consists of a three phase induction generator with three phase windings on the rotor. The rotor is connected to a converter which supplies power to the rotor via the slip rings. The power electronic converter is capable of handling power flow in both directions which permits the DFIG to operate at both sub-synchronous and super-synchronous speeds. The DFIG produces controlled voltage V_s at grid frequency f_s at the stator and variable voltage V_r is provided at the rotor at variable frequency f_r. The frequency of the rotor depends on the angular velocity of the rotor which in turn depends on the wind speed. Let f_w be the electrical frequency of revolution of the rotor. The following relation always holds true between these various frequencies:

$$f_w = f_s \pm f_r$$

The positive sign above is for the super-synchronous operation where rotor speed exceeds rated speed, $f_r = 0$ for synchronous speed and negative sign is for sub-synchronous operation when rotor speed is less than rated speed.

According to the steady state power flow curves shown in Figures 4.4 and 4.5, a DFIG has three distinct operation modes based on the direction of active power flow in the stator and rotor sides of the DFIG as represented clearly with equivalent block diagram in Figure 4.6. It can be observed from Figure 4.6 that, at sub-synchronous speed operation, the rotor speed is slower than the synchronous speed, i.e. the slip is positive. In order to generate power in this mode of operation, positive slip power must be obtained by injecting power from the grid into the rotor by means of a power converter, i.e. rotor

side absorbs power from grid to provide excitation to the DFIG. Therefore, closed loop power flow occurs through the rotor and the stator but still the net power output will be positive, i.e. DFIG generates power in the sub-synchronous operation speed range as well.

During the synchronous speed operation point, the rotor side is not involved in the power generation process, i.e. active power exchange via rotor side is zero and only the stator side will supply generated power to the grid.

In super-synchronous operation speed range, mechanical power from the shaft splits into two parts; the largest part of the power goes to the grid through the stator and a fraction of the power goes through the converter to the grid, i.e. both stator and rotor generate power and supply it to grid as a result the total power output will be high.

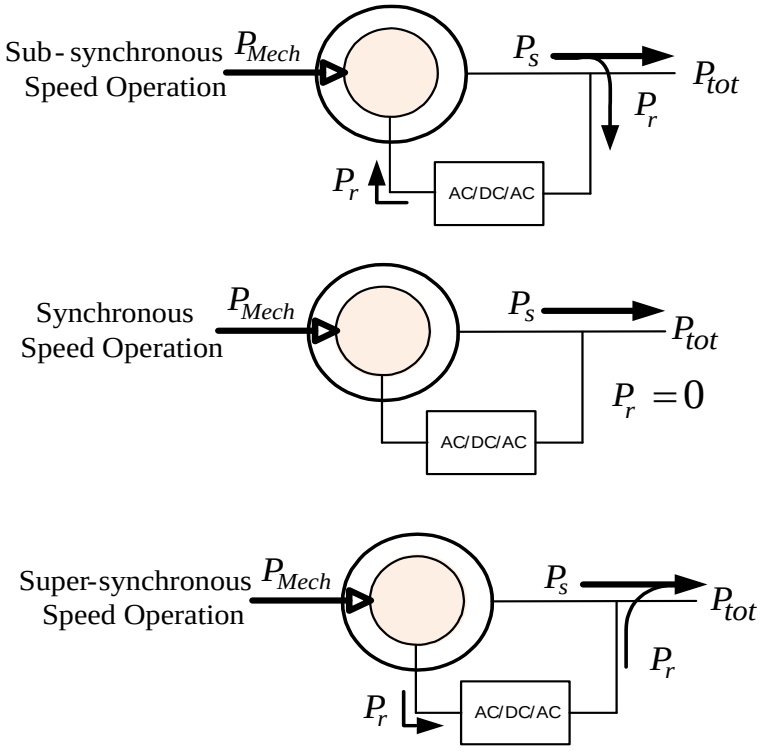

Figure 4.6 DFIG stator and rotor active power flow direction during different rotor speed

From Figure 4.7, it can be interpreted that at synchronous speed, the rotor voltage magnitude will be minimum, i.e. very close to zero but at both super-synchronous as well as sub-synchronous speed, (i.e. slip not equal to zero), the rotor voltage magnitude increases as the slip (both +ve and -ve) increases. It is well known fact that every electrical induction machine has a rated rotor side voltage so the rotor voltage magnitude is one of the constraints for limited speed range operation of DFIG. The rotor side draws the reactive power from RSC at sub-synchronous speed as a result the power factor of the machine is very poor (low) at sub-synchronous speed. But when the machine operates in super-synchronous speed, rotor side also supplies reactive power to the machine for its excitation as a result the rotor side power factor also improves.

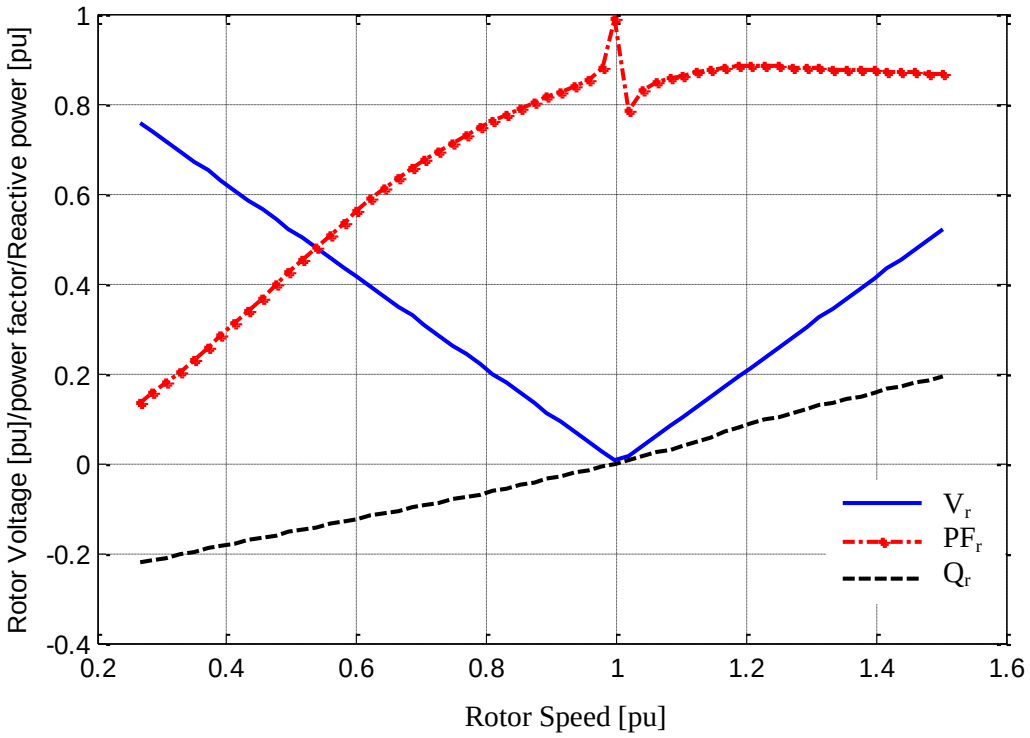

Figure 4.7 Rotor voltage magnitude, rotor side power factor and rotor supplied reactive power in DFIG

Figure 4.8 shows the modulation indexes of the RSC and the GSC when the rotor speed varies from 0.3 pu to 1.5 pu. The modulation indexes magnitude (shown by the red solid line) are less than 1 in both converters for the entire range of rotor speed.

From Figure 4.9, it is clear that to generate the same amount of total active power and reactive power from the same DFIG with two different rated rotor speeds, at higher

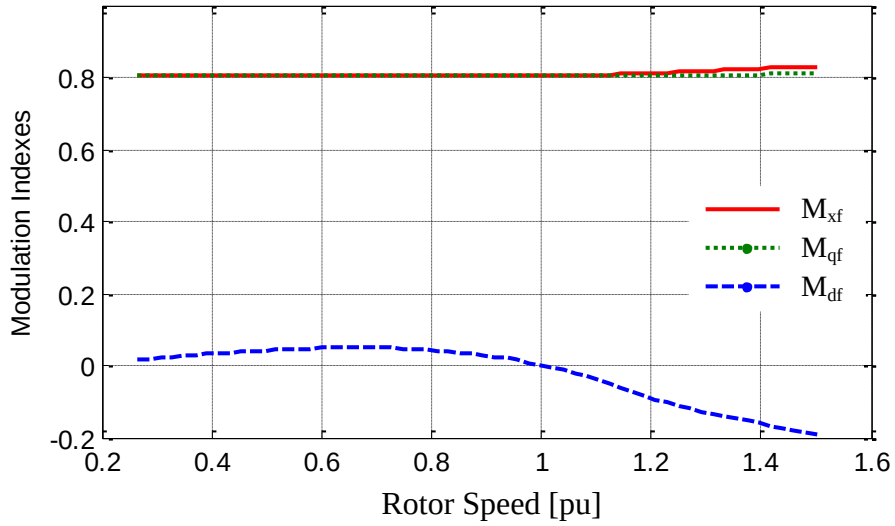

(a)

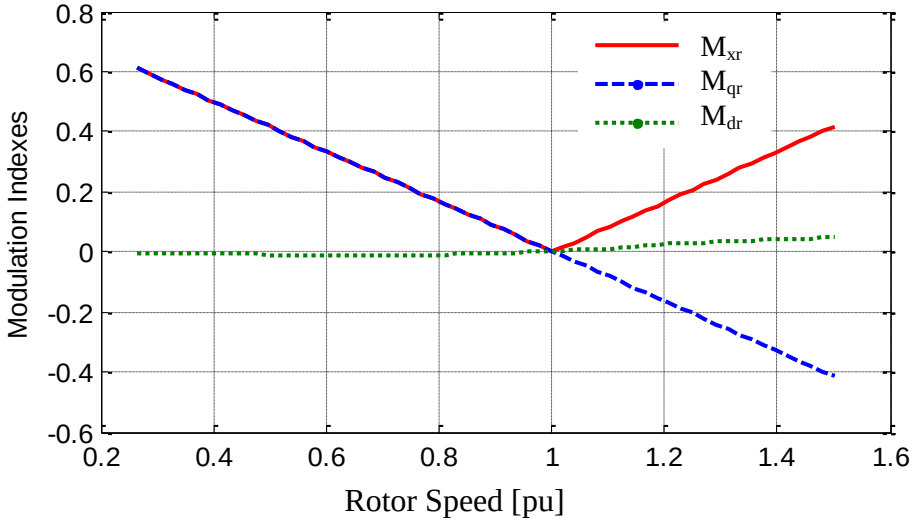

(b)

Figure 4.8 Modulation indexes of (a) Grid Side Converter (b) Rotor Side Converter

rated rotor speed, the electromagnetic torque that DFIG has to develop is lower. As a result, the stator side current magnitude as well as rotor side current magnitude is lower at higher rated rotor speeds which is depicted in Figures 4.10 and 4.11, respectively.

Hence, higher value of rated rotor speed is better from the converter rating viewpoint, as the current magnitudes in rated regime are lower. The rated rotor speed is usually chosen in the super-synchronous region at a value less than the maximum rated

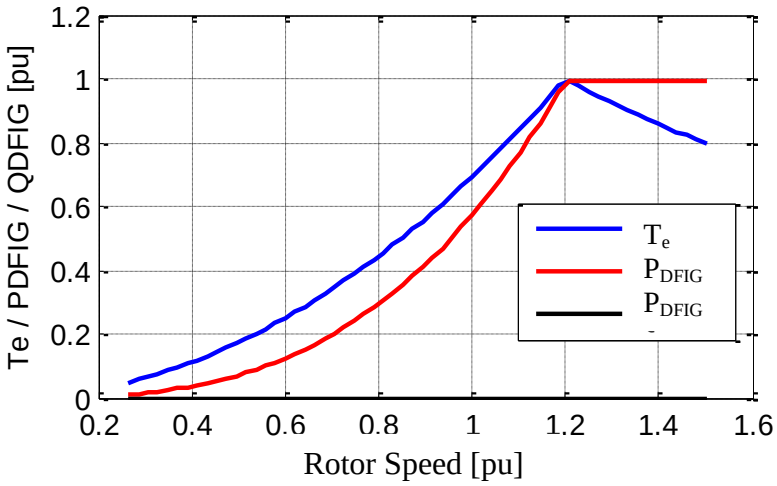

(a)

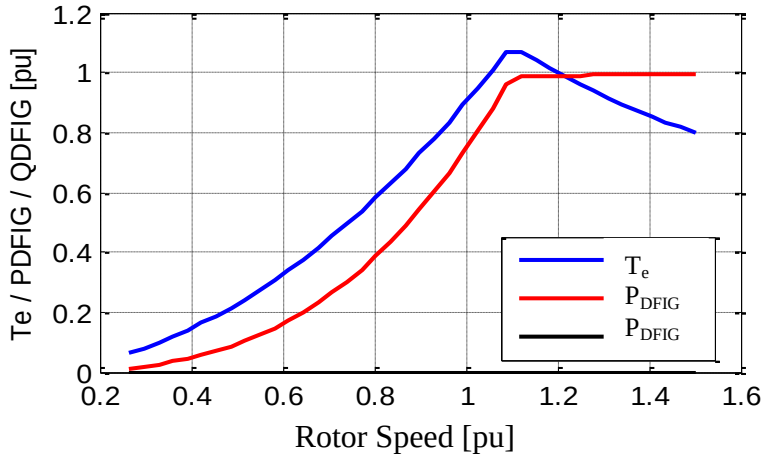

(b)

Figure 4.9 Electromagnetic torque, total active power and total reactive power developed by DFIG at two different rated rotor speeds (a) $\omega_{rated} = 1.2\omega_e$ and (b) $\omega_{rated} = 1.1\omega_e$

speed. The margin required between ω_{rated} and $\omega_{r\_\max}$ depends on the speed of the pitching mechanism and generator inertia. Lighter generators with slower pitching require a larger margin since they accelerate more quickly and the pitch control takes

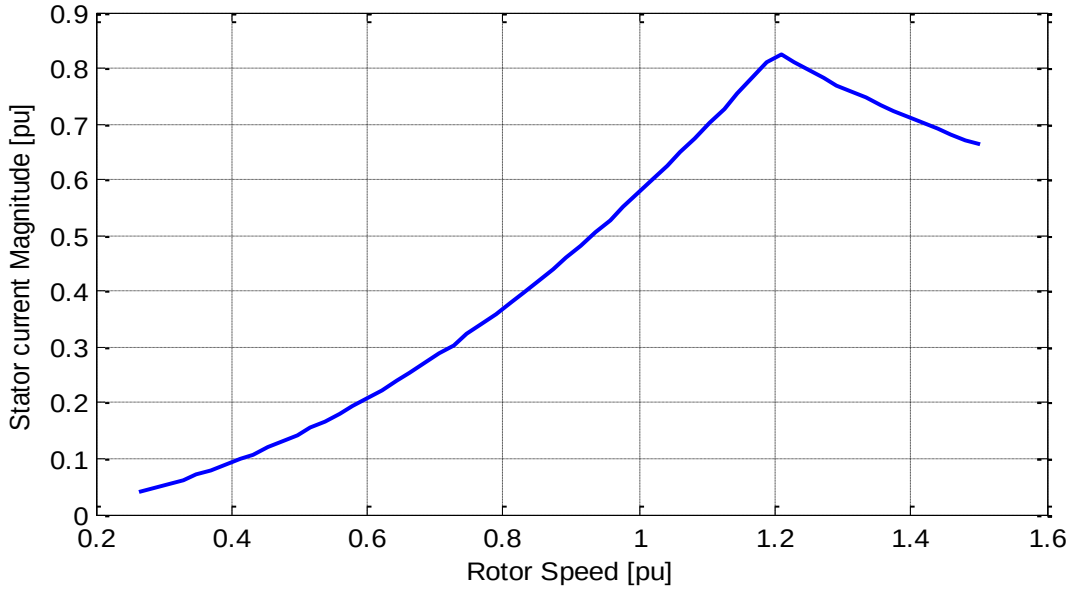

(a)

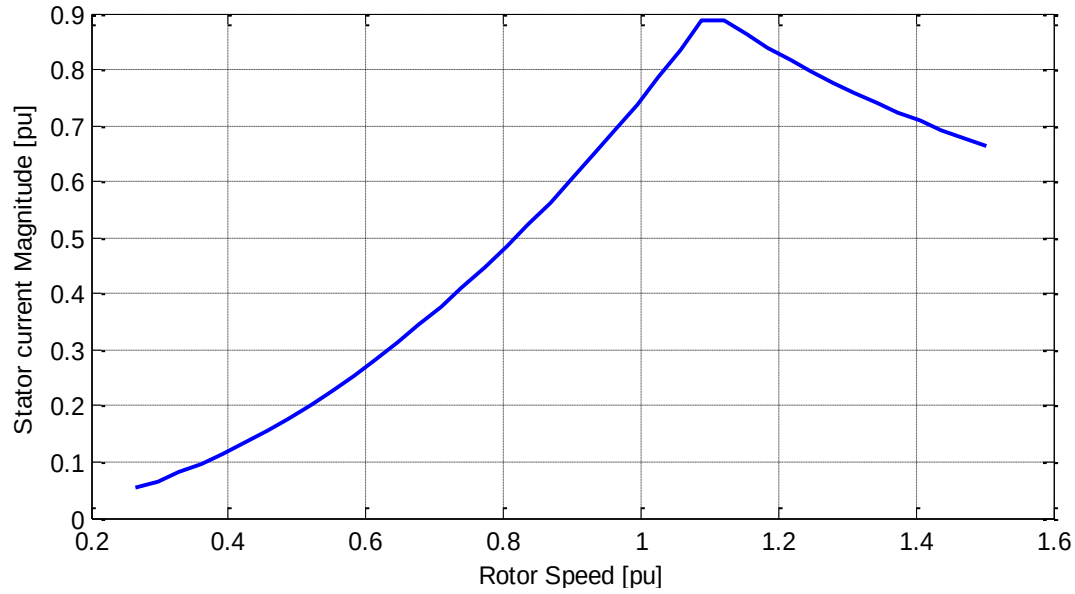

(b)

Figure 4.10 Stator Current Magnitude in DFIG at two different rated rotor speeds (a) $\omega_{rated} = 1.2\omega_e$ and (b) $\omega_{rated} = 1.1\omega_e$

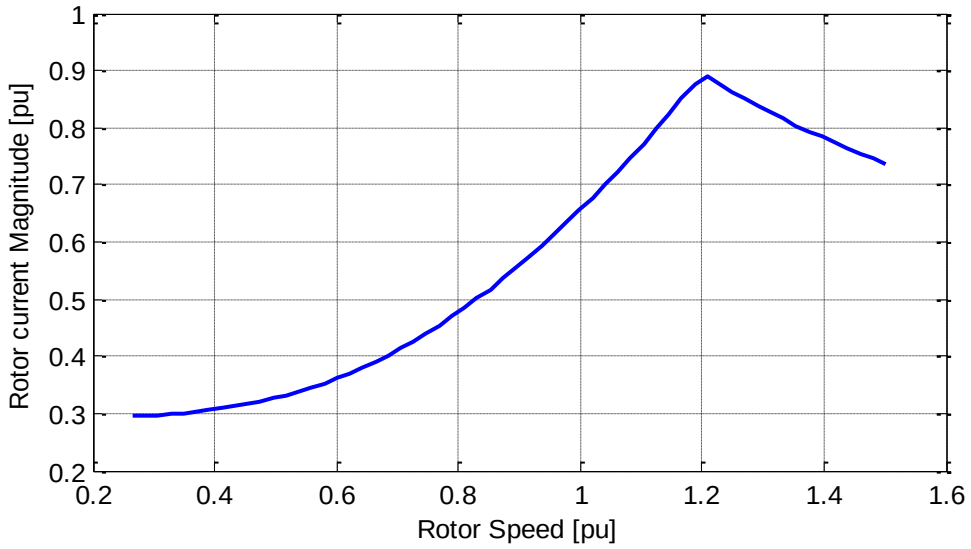

(a)

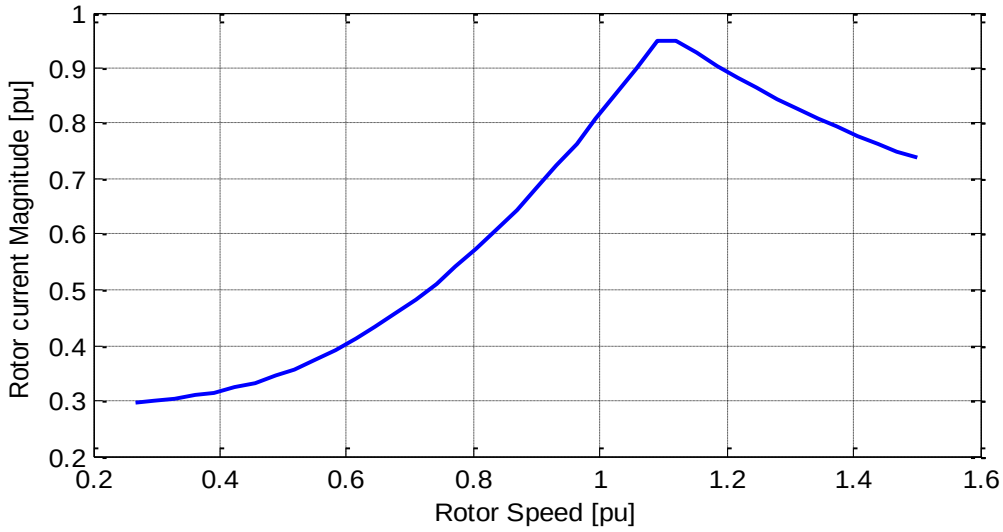

(b)

Figure 4.11 Rotor Current Magnitude in DFIG at two different rated rotor speeds (a) $\omega_{rated} = 1.2\omega_e$ and (b) $\omega_{rated} = 1.1\omega_e$

longer to limit the input torque. Usually the DFIG has $\omega_{r\_\max} = 1.3$ p.u. because of various constraints like rotor voltage magnitude, rotor current magnitude, and stator current magnitude ratings.

4.2 Reactive Power Capability

4.2.1 Introduction

Most of the newly installed megawatt size WECS are DFIGs. The increasing level of wind power penetration into the power grid has generated a widespread concern over its impact on power system performance. As a result, utility companies have set some requirements (also called grid codes) to be fulfilled before connecting the wind turbine to the grid [65]. A key requirement for plant operation is that the power factor at the PCC must remain between 0.95 leading and 0.9 lagging [41]. The reason for this ruling is that reactive power capability for a wind plant is a significant additional cost compared to conventional units consisting of synchronous generators which possess inherent reactive power capability. Another significant focus of the grid codes has been on the active and reactive power control capability of the wind turbines so as to support the control of frequency and voltage in the grid, respectively [65].

Reactive power is essential for the stable operation of the power system. It facilitates the flow of active power from the generation sources to the load centers and maintains the various bus voltages within prescribed limits [66]. Stable operation of power systems requires the availability of sufficient reactive power generation. Both static and dynamic reactive power sources play an important role in voltage controllability of the power system. Hence accurate evaluation of the reactive power capability of wind turbines is very critical to assess the voltage controllability of the power system containing wind turbines and to prevent the voltage violations in all nodes of the power system. A DFIG being the most dominant wind generator installed in

current wind farms has significant impacts in the current power system stability and control. Hence it is very important to analyze the reactive power capability of the DFIG.

4.2.2 Reactive Power Capability Limitations with DFIG

To determine the reactive power limits in DFIG, the electromechanical characteristics of the generator and the power converter have to be taken into consideration. Although, the DFIG wind turbines are able to control active and reactive power independently, the reactive power capability of those generators depend on the active power generated, the slip and the limitation due to following design parameters [34, 35]: 1) rotor voltage, 2) stator current, and 3) rotor current. The stator voltage is given by the grid which can be assumed fairly constant, and is not influenced by the wind turbine design. The stator current limit depends on the generator design, whereas the rotor voltage and rotor current limits depend on generator as well as power converter designs. The size of power converter is limited (about 25-30% of the total MVA rating). The rotor voltage limitation is essential for the rotor speed interval, because the required rotor voltage to provide a certain field is directly proportional to the slip. Hence, the rotor speed is limited by the rotor voltage limitation.

4.2.3 Mathematical Model of the DFIG System

In the following section, a mathematical model of the DFIG is used for the calculation and derivation of its reactive power capability in terms of the active vs reactive power curve (P - Q diagram). The fundamental idea is to set the boundaries

defined by the rotor current, the rotor voltage, and the stator current combined together as well as separately so as to study the effect of each of them separately at the end.

The DFIG steady state voltage equations in complex form are given by (4.14) and (4.15). All the variables are referred to the stator side.

$$V_{qds} = r_s I_{qds} + j\omega_e L_s I_{qds} + j\omega_e L_m I_{qdr} \tag{4.14}$$

$$V_{qdr} = r_r I_{qdr} + j(\omega_e - \omega_r) L_m I_{qds} + j(\omega_e - \omega_r) L_r I_{qdr} \tag{4.15}$$

where $V_{qds} = V_{qs} - jV_{ds}$, $V_{qdr} = V_{qr} - jV_{dr}$, $I_{qds} = I_{qs} - jI_{ds}$, $I_{qdr} = I_{qr} - jI_{dr}$, ω_e is the synchronous speed, $L_s = L_{ls} + L_m$ and $L_r = L_{lr} + L_m$.

The equivalent circuit diagram represented by (4.14) and (4.15) is shown in Figure 4.12.

From (4.14), we can write:

$$I_{qds} = \frac{V_{qds} - j\omega_e L_m I_{qdr}}{r_s + j\omega_e L_s} \tag{4.16}$$

From (4.16):

$$I_{qdr} = \frac{V_{qds} - (r_s + j\omega_e L_s) I_{qds}}{j\omega_e L_m} \tag{4.17}$$

From (4.15) and (4.16):

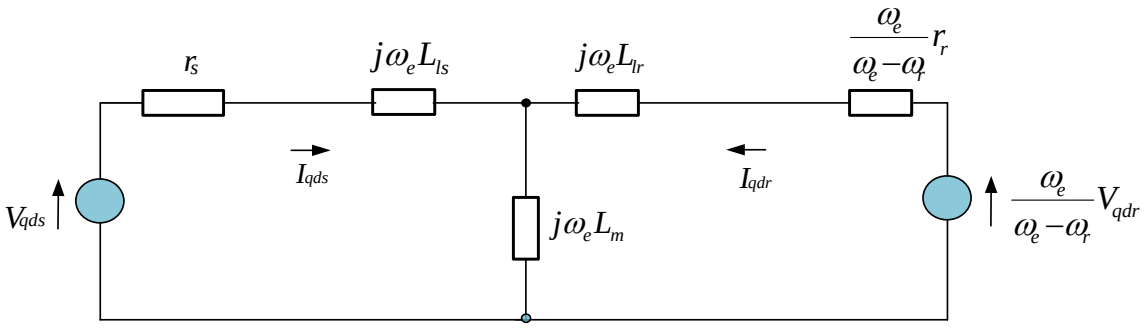

Figure 4.12 The DFIG steady state equivalent circuit

$$V_{qdr} = \left(r_r + \frac{\omega_e(\omega_e - \omega_r)L_m^2}{r_s + j\omega_e L_s} + j(\omega_e - \omega_r)L_r \right) I_{qdr} + \frac{j(\omega_e - \omega_r)L_m}{r_s + j\omega_e L_s} V_{qds} \tag{4.18}$$

Now we know the stator side supplied apparent power in DFIG is given as: (- sign is for generation mode)

$$S_s = P_s - jQ_s = -\frac{3}{2} V_{qds} I_{qds}^* \tag{4.19}$$

From Equations (4.16) and (4.19):

$$S_s = -\frac{3V_{qds}}{2} \left(\frac{V_{qds} - j\omega_e L_m I_{qdr}}{r_s + j\omega_e L_s} \right)^* \tag{4.20}$$

We know that:

$$P_s = \text{Real}[S_s] \tag{4.21}$$

Simplifying Equation (4.20) and separating into real and imaginary parts:

$$P_s = \frac{3}{2} \frac{1}{r_s^2 + (\omega_e L_s)^2} \left[-r_s(V_{qs}^2 + V_{ds}^2) - \omega_e r_s L_m (V_{ds} I_{qr} - V_{qs} I_{dr}) + \omega_e{}^2 L_s L_m (V_{qs} I_{qr} + V_{ds} I_{dr}) \right] \tag{4.22}$$

Similarly, the apparent power generated by rotor side in DFIG is given as:

$$S_r = P_r - jQ_r = -\frac{3}{2} V_{qdr} I_{qdr}^* \tag{4.23}$$

$$P_r = \text{Real}[S_r] \tag{4.24}$$

Substituting (4.18) into (4.23) and separating into real and imaginary parts gives:

$$P_r = -\frac{3}{2} \left[r_r(I_{qr}^2 + I_{dr}^2) + \frac{\omega_e(\omega_e - \omega_r) r_s L_m^2 (I_{qr}^2 + I_{dr}^2)}{r_s^2 + (\omega_e L_s)^2} + \frac{\omega_e(\omega_e - \omega_r) L_s L_m (V_{qs} I_{qr} + V_{ds} I_{dr})}{r_s^2 + (\omega_e L_s)^2} + \frac{(\omega_e - \omega_r) r_s L_m (V_{ds} I_{qr} - V_{qs} I_{dr})}{r_s^2 + (\omega_e L_s)^2} \right] \tag{4.25}$$

Hence the total power output of DFIG system is:

$$P_{Total} = P_s + P_r \tag{4.26}$$

4.2.4 Plotting PQ Diagram of DFIG for MPPT and Pitch Control Mode

Here the objective is to plot the optimum P-Q diagram of the DFIG system. The recommended way to study the reactive power capability of the DFIG machine is to use the optimization method subjected to the following equality constrints constraints and inequality constraints.Also the rotor speed (ω_r) and the total real the power output (P_{total}) of the DFIG should be varied according to the MPPT mode or Pitch control operation mode relation described at the beginning of the chapter.

The steady state stator voltage and rotor voltage equation in DFIG is given as:

$$V_{qs} = r_s I_{qs} + \omega_e L_s I_{ds} + \omega_e L_m I_{dr} \tag{4.27}$$

$$V_{ds} = r_s I_{ds} - \omega_e L_s I_{qs} - \omega_e L_m I_{qr} \tag{4.28}$$

$$V_{qr} = r_r I_{qr} + (\omega_e - \omega_r) L_m I_{ds} + (\omega_e - \omega_r) L_r I_{dr} \tag{4.29}$$

$$V_{dr} = r_r I_{dr} - (\omega_e - \omega_r) L_m I_{qs} - (\omega_e - \omega_r) L_r I_{qr} \tag{4.30}$$

In the DFIG, rotor side is connected to the grid through back-to-back power converters. In steady state, DC-link capacitor does not exchange any DC current, i.e.:

$$\frac{3}{4}\left(M_{qr} I_{qr} + M_{dr} I_{dr}\right) + \frac{3}{4}\left(M_{qf} I_{qf} + M_{df} I_{df}\right) = 0 \tag{4.31}$$

Using Kirchhoff's voltage law (KVL) across RL filter given by (4.11):

$$M_{qf} \frac{V_{dc}}{2} = r_f I_{qf} + \omega_e L_f I_{df} + V_{qs} \tag{4.32}$$

$$M_{df} \frac{V_{dc}}{2} = r_f I_{df} - \omega_e L_f I_{qf} + V_{ds} \tag{4.33}$$

where M_{qr} and M_{dr} are RSC modulation indexes, I_{qr} and I_{dr} are currents flowing into RSC, M_{qf} and M_{df} are GSC modulation indexes, and I_{qf} and I_{df} are currents flowing

out from GSC to grid. Here, it should be noted that during steady state, DC-link voltage V_{dc} is constant so $M_{qr} = \frac{2V_{qr}}{V_{dc}}$ and $M_{dr} = \frac{2V_{dr}}{V_{dc}}$.

The optimization should be done for the objective function given by (4.34) subjected under the equality constraints (4.27)-(4.33) and inequality constraints (4.35) - (4.37).

$$Q_{total} = Q_s + Q_f = \frac{3}{2}(V_{qs}I_{ds} - V_{ds}I_{qs}) + \frac{3}{2}(V_{qs}I_{df} - V_{ds}I_{qf}) \tag{4.34}$$

$$I_s \le I_{s\_rated} \tag{4.35}$$

$$I_r \le I_{r\_rated} \tag{4.36}$$

$$V_r \le V_{r\_rated} \tag{4.37}$$

The approach implemented in this particular study is to vary the total active power (P_{total}) with rotor speed varying proportional to power output in MPPT mode and power output is maintained at rated power in pitch control mode. The rotor current magnitude is set to its rated value ($|I_{qdr}| = |I_{r\_rated}|$) because it is typically the limiting factor for production of reactive power in DFIG (see Figure 4.14). The stator current and rotor voltage magnitudes are limited within the rated value, i.e. $|I_{qds}| \le |I_{s\_rated}|$ and $|V_{qdr}| \le |V_{r\_rated}|$. The corresponding reactive power (Q_{total}) is calculated and plotted against total active power. The approach used to get the P-Q diagram is explained in following steps:

- Step I

Since the V_s is reference grid voltage, we can write: $V_{qds} = V_s \angle \theta_s = V_s \angle 0$, hence

$V_{qs} = V_s \cos\theta_s = V_s$ and $V_{ds} = V_s \sin\theta_s = 0$. Similarly, $I_{qr} = I_r \cos\theta_{ir}$ and $I_{dr} = I_r \sin\theta_{ir}$.

Substituting V_{qs}, V_{ds}, I_{qr} and I_{dr} into Equation (4.26):

$$P_{Total} = \frac{3}{2}\frac{1}{r_s^2 + (\omega_e L_s)^2}\begin{bmatrix} -r_s V_s^2 + (2\omega_e - \omega_r) r_s L_m V_s I_r \sin\theta_{ir} + \omega_e \omega_r L_s L_m V_s I_r \cos\theta_{ir} - \\ r_r (r_s^2 + (\omega_e L_s)^2) I_r^2 - \omega_e (\omega_e - \omega_r) r_s L_m^2 I_r^2 \end{bmatrix} \quad (4.38)$$

- Step II

At boundary condition, we have: $I_r = \left| I_{r\_rated} \right|$.

From (4.27), we can get rotor current angle (θ_{ir}) at the boundary condition by varying the total power output of the DFIG from 0 to 1 pu. Equation (4.38) gives two rotor current angles (θ_{ir1} and θ_{ir2}), one for motoring mode and another for generating mode.

From (4.16):

$$I_{qds} = \frac{V_{qds} - j\omega_e L_m I_{qdr}}{r_s + j\omega_e L_s} \quad (4.39)$$

For known value of rotor current angles (θ_{ir1} *and* θ_{ir2}) from (4.38), we can get stator current magnitude and angles (θ_{is1} *and* θ_{is2}) using (4.39). If magnitude of I_{qds} is less than I_{s_rated}, then proceed to next step.

- Step III

Now from Equation (4.15):

$$V_{qdr} = r_r I_{qdr} + j(\omega_e - \omega_r) L_m I_{qds} + j(\omega_e - \omega_r)\, L_r I_{qdr} \quad (4.40)$$

Here I_r and I_s are known so after knowing their corresponding angles using (4.38) and (4.39), solve (4.40), if the magnitude of V_{qdr} is less than V_{r_rated}, calculate the corresponding reactive power.

In this study, GSC is assumed to be operating in unity power factor mode because of the following reasons:

1. This scenario gives the worst reactive power capability of DFIG. If GSC is supplying reactive power then the reactive power capability of DFIG system will be enhanced.
2. In the commercially available DFIG, the GSC is designed to operate at unity power factor [21, 22, 41].
3. The current (or MVA) rating of the GSC has to be increased significantly if GSC has to supply reactive power which is discussed in more detail in Chapter 5.

- Step IV

Hence, in this study, the stator supplied reactive power is equal to the total reactive power output from DFIG, i.e.

$$Q_{Total} = Q_s = imag\left[-\frac{3}{2} V_s \left(\frac{V_s - j\omega_e L_m I_r}{r_s + j\omega_e L_s} \right)^* \right] \tag{4.41}$$

Figures 4.13 (a) shows the P-Q diagram of DFIG system obtained by following above explained procedure and assuming the stator voltage (or grid voltage) to be 1 pu and rotor speed being the rated rotor speed (1.2 pu in this study). The 0.9 power factor (both leading and lagging) line is also included in the same plot. According to the Figure 4.13 (a), when the DFIG starts to generate more than 82 % of the rated power, the amount of reactive power that DFIG can supply, is not enough to maintain + 0.9 pf (leading) which is the requirement for interconnecting DFIG wind turbine to power grid according to grid code.

As shown in Figure 4.13 (b), when the wind turbine starts to operate in blade pitching mode where the active power output is maintained at rated power output of the DFIG, the reactive power capability of DFIG gets enhanced.

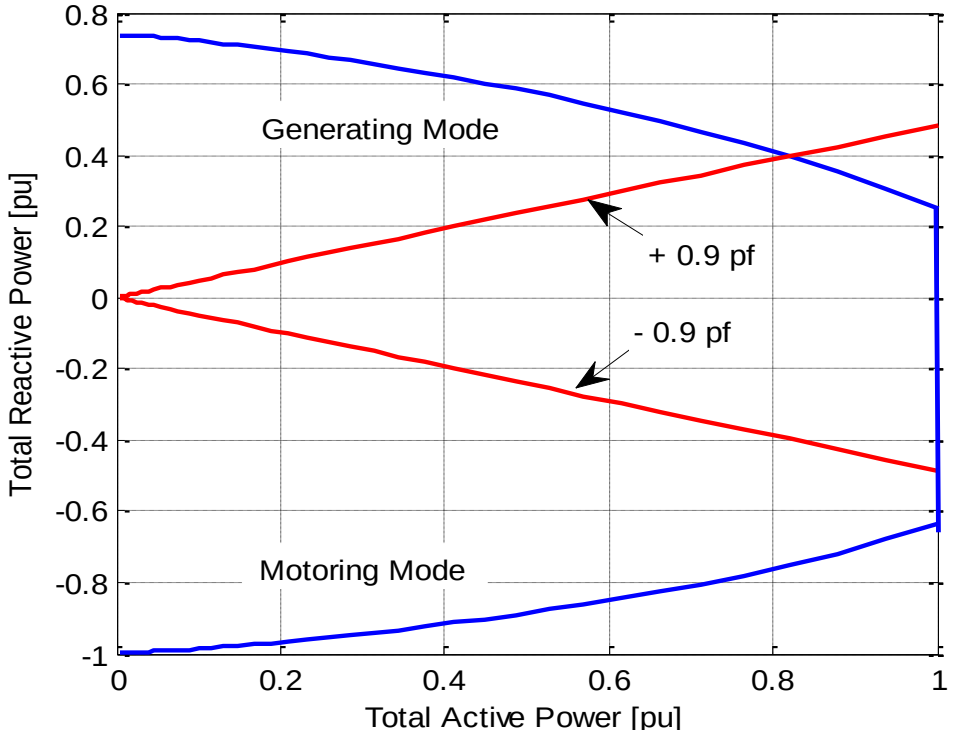

(a)

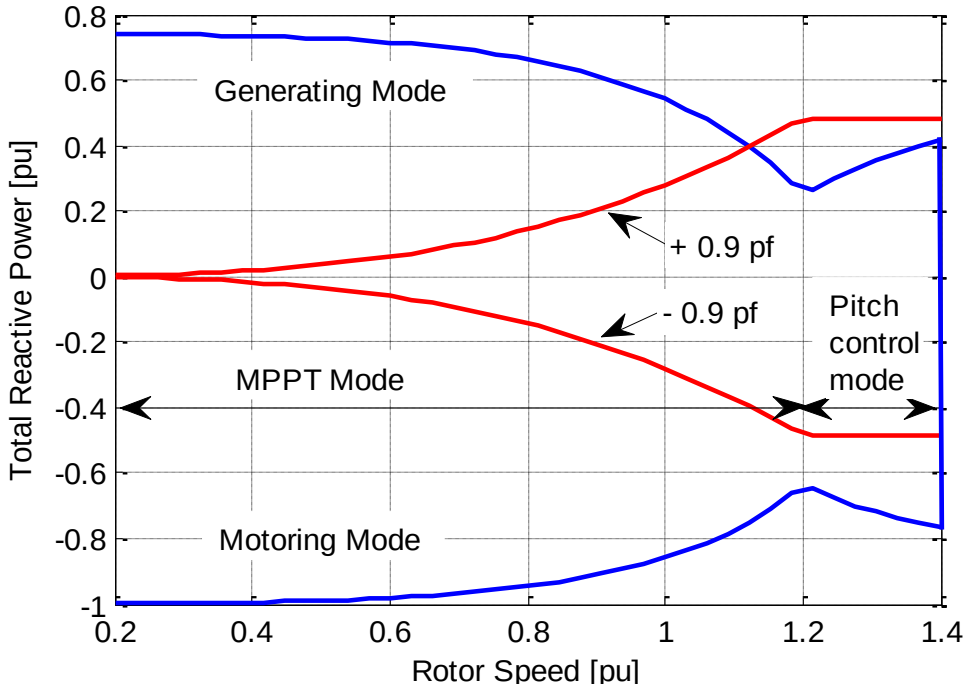

(b)

Figure 4.13 DFIG steady state reactive power capability curves: (a) active vs. reactive power (b) rotor speed vs. reactive power

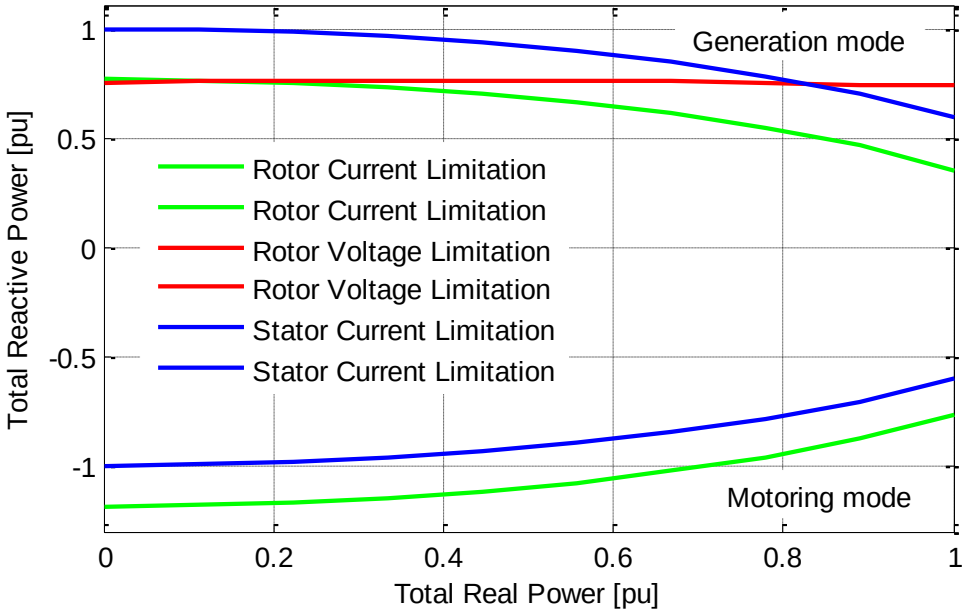

Figure 4.14 Comparison of three limiting quantities at rated rotor speed ($\omega_r = 1.2 \ \ pu$)

Figure 4.14 demonstrates that at low rotor speed, the rotor voltage limits the reactive power production capability (generating mode) and stator current limits the reactive power absorption capability. But at higher rotor speed, the rotor current limits the reactive power production capability whereas the stator current limits the reactive power absorption capability (motoring mode). The rotor voltage limitation in the motoring mode is not a problem and it falls beyond the range shown in the Figure 4.14.

Figure 4.15 shows that the reactive power capability of DFIG degrades with the reduced terminal voltage. Hence if the wind turbine is connected to weak grid where terminal voltage will be usually under-voltage, the wind turbine is unable to maintain the

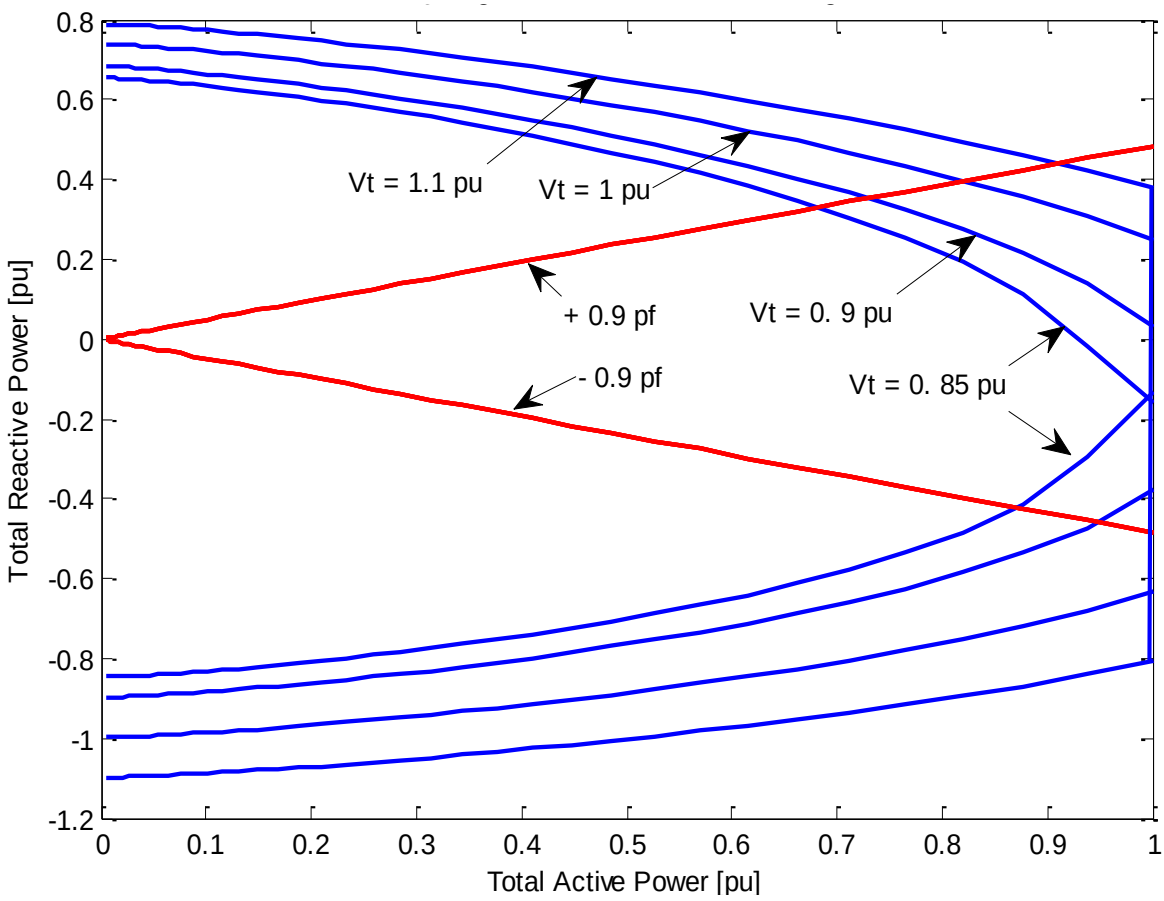

Figure 4.15 DFIG steady state reactive power capability curves at different DFIG terminal voltages

the required power factor demand at the PCC without having additional reactive power source even when the wind turbine is operating as low as 65 % of the rated power. However, if the grid voltage is over-voltage, the DFIG reactive power capability is enhanced. But this is not the appropriate way to operate DFIG because higher terminal voltage means higher stator voltage which might affect the generator. For instance, high voltage can damage the insulation system in the generator winding.

4.2.5 Plotting PQ Diagram of DFIG

In the previous section, process of plotting PQ diagram of DFIG operating in MPPT mode and pitch control mode is discussed. In this section, more generalized method of plotting PQ diagram of DFIG is presented where the rotor speed is varied independent of the powe output of the machine. Here the objective is to plot the PQ diagram of the DFIG system.

The steady state stator voltage and rotor voltage equation in DFIG is given as:

$$V_{qs} = r_s I_{qs} + \omega_e L_s I_{ds} + \omega_e L_m I_{dr} \tag{4.42}$$

$$V_{ds} = r_s I_{ds} - \omega_e L_s I_{qs} - \omega_e L_m I_{qr} \tag{4.43}$$

$$V_{qr} = r_r I_{qr} + (\omega_e - \omega_r) L_m I_{ds} + (\omega_e - \omega_r) L_r I_{dr} \tag{4.44}$$

$$V_{dr} = r_r I_{dr} - (\omega_e - \omega_r) L_m I_{qs} - (\omega_e - \omega_r) L_r I_{qr} \tag{4.45}$$

Since the V_s is reference grid voltage, we can write: $V_{qds} = V_s \angle \theta_s = V_s \angle 0$, hence $V_{qs} = V_s \cos\theta_s = V_s$ and $V_{ds} = V_s \sin\theta_s = 0$. Similarly, $V_{qr} = V_r \cos\theta_{vr}$, $V_{dr} = V_r \sin\theta_{Vr}$, $I_{qs} = I_s \cos\theta_{is}$, $I_{ds} = I_s \sin\theta_{is}$, $I_{qr} = I_r \cos\theta_{ir}$ and $I_{dr} = I_r \sin\theta_{ir}$.

In the DFIG, rotor side is connected to the grid through back-to-back power converters. In steady state, DC-link capacitor does not exchange any DC current, i.e.:

$$\frac{3}{4}\left(M_{qr} I_{qr} + M_{dr} I_{dr}\right) + \frac{3}{4}\left(M_{qf} I_{qf} + M_{df} I_{df}\right) = 0 \tag{4.46}$$

Using Kirchhoff's voltage law (KVL) across RL filter given by (4.11):

$$M_{qf} \frac{V_{dc}}{2} = r_f I_{qf} + \omega_e L_f I_{df} + V_{qs} \tag{4.47}$$

$$M_{df}\frac{V_{dc}}{2} = r_f I_{df} - \omega_e L_f I_{qf} + V_{ds} \tag{4.48}$$

where M_{qr} and M_{dr} are RSC modulation indexes, I_{qr} and I_{dr} are currents flowing into RSC, M_{qf} and M_{df} are GSC modulation indexes, and I_{qf} and I_{df} are currents flowing out from GSC to grid. Here, it should be noted that during steady state, DC-link voltage V_{dc} is constant so $M_{qr} = \frac{2V_{qr}}{V_{dc}}$ and $M_{dr} = \frac{2V_{dr}}{V_{dc}}$.

The stator side voltage is the grid voltage whose magnitude is also known. At the boundary of the PQ diagram, the rotor current, rotor voltage and stator current magnitude are equal to their rated values.

1) $I_s = I_{s\_rated}$
2) $I_r = I_{r\_rated}$
3) $V_r = V_{r\_rated}$

So, the overall system has seven equations (4.42) – (4.88) and seven unknowns which are: θ_{is}, θ_{vr}, θ_{ir}, M_{qf}, M_{df}, I_{qf} and I_{df}. By varying the rotor speed, active and reactive powers are calculated using:

$$P_s = \frac{3}{2}(V_{qs}I_{qs} + V_{ds}I_{ds}) \tag{4.49}$$

$$Q_s = \frac{3}{2}(V_{qs}I_{ds} - V_{ds}I_{qs}) \tag{4.50}$$

$$P_f = \frac{3}{2}(V_{qs}I_{qf} + V_{ds}I_{df}) \tag{4.51}$$

$$Q_f = \frac{3}{2}(V_{qs}I_{df} - V_{ds}I_{qf}) \tag{4.52}$$

$$P_{total} = P_s + P_f \tag{4.53}$$

$$Q_{total} = Q_s + Q_f \tag{4.54}$$

Varying the rotor speed within operation range of DFIG, P_{total} vs. Q_{total} can be plotted.

4.3 Connecting STATCOM at the PCC with DFIG-based WECS

It can be clearly seen in Figure 4.13 that the reactive power capability of DFIG is not enough to maintain required power factor at the PCC when the DFIG is operating at higher rotor speed (more than 1.1 pu and corresponding output active power being 0.82 pu). According to grid code requirement, WECS should be operating up to 0.9 lagging pf to support the stability of the connected power system. So to meet this requirement, we need extra reactive power source. Here STATCOM is proposed as a dynamic reactive power source because of its many advantages explained in detail in Chapter 5 compared to other reactive power sources. Here, the STATCOM is connected at the PCC as shown in Figure 4.16 and the power grid is modeled as an infinite bus, i.e. constant voltage

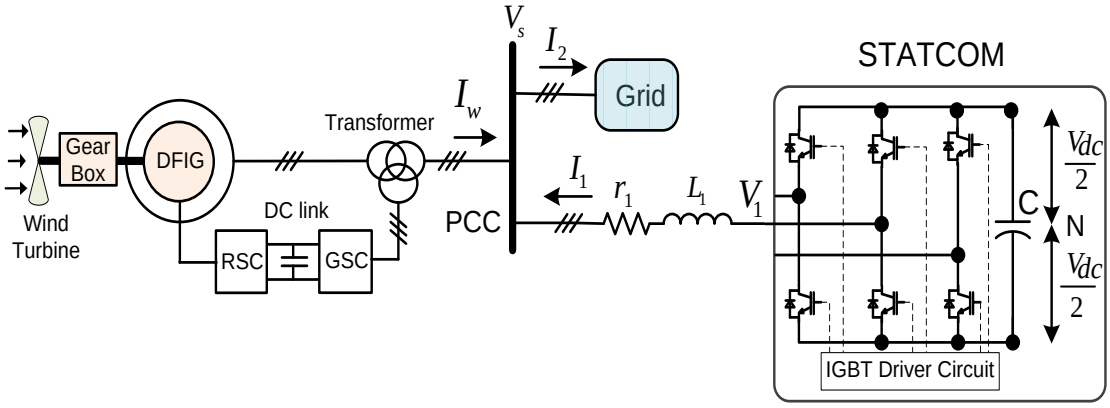

Figure 4.16 STATCOM connected to DFIG-based WECS at PCC

source, the reactive power required is provided by the combination of DFIG and STATCOM. The detail operation, modeling, and control of STATCOM are explained in Chapter 5.

4.3.1 Mathematical Model of the STATCOM

In this section, a mathematical model of the STATCOM during the steady state is used to derive the reactive power output expression from STATCOM and it is co-related with the DFIG reactive power capability to draw the reactive power capability curve of the combined STATCOM and DFIG system.

The steady state equations of the STATCOM connected to the power grid as shown in Figure 4.16 is obtained by applying KVL from STATCOM to the PCC as:

$$V_{q1} - V_{qs} = r_1 I_{q1} + \omega_e L_1 I_{d1} \tag{4.55}$$

$$V_{d1} - V_{ds} = r_1 I_{q1} - \omega_e L_1 I_{q1} \tag{4.56}$$

where V_{q1}, V_{d1}, V_{qs} and V_{ds} are q and d axis voltage at STATCOM terminal and PCC, respectively. I_{q1} and I_{d1} are the q and d axis current outputs from STATCOM. r_1 and L_1 are the resistance and inductance of the tie line connecting STATCOM to the PCC.

At steady state, DC-link current balance equation in STATCOM is:

$$\frac{3}{4}(M_{qs} I_{q1} + M_{ds} I_{d1}) = 0 \tag{4.57}$$

where M_{qs} and M_{ds} are q and d axis modulation indexes in STATCOM. We know that the STATCOM terminal voltages are given by: $V_{q1} = \frac{M_{qs} V_{dc}}{2}$ and $V_{d1} = \frac{M_{ds} V_{dc}}{2}$; V_{dc} being the DC-link voltage. Substituting V_{q1} and V_{d1} into (4.55) and (4.56):

$$\frac{M_{qs}V_{dc}}{2} - V_{qs} = r_1 I_{q1} + \omega_e L_1 I_{d1} \tag{4.58}$$

$$\frac{M_{ds}V_{dc}}{2} - V_{ds} = r_1 I_{d1} - \omega_e L_1 I_{q1} \tag{4.59}$$

If the amount of reactive power STATCOM is supplying to the system is known (Q_s^*) then:

$$Q_s^* = \frac{3}{2}(V_{qs} I_{d1} - V_{ds} I_{q1}) \tag{4.60}$$

Equations (4.47), (4.48), (4.49), and (4.50) are the required steady state equations. And M_{qs}, M_{ds}, I_{q1}, and I_{d1} are four unknowns so we can get the unique solution of the system, i.e. particular operating condition.

From Equations (4.48) and (4.49):

$$I_{q1} = \frac{r_1\left(\frac{M_{qs}V_{dc}}{2} - V_{qs}\right) - \omega_e L_1\left(\frac{M_{ds}V_{dc}}{2} - V_{ds}\right)}{r_1^2 + (\omega_e L_1)^2} \tag{4.61}$$

$$I_{d1} = \frac{\omega_e L_1\left(\frac{M_{qs}V_{dc}}{2} - V_{qs}\right) + r_1\left(\frac{M_{ds}V_{dc}}{2} - V_{ds}\right)}{r_1^2 + (\omega_e L_1)^2} \tag{4.62}$$

Substituting I_{q1} and I_{d1} from (4.11) and (4.12) to (4.57) and further simplification gives:

$$a(M_{qs}^2 + M_{ds}^2) - KM_{qs} - NM_{ds} = 0 \tag{4.63}$$

where $a = r_1 \frac{V_{dc}}{2}$, $K = r_1 V_{qs} - \omega L_1 V_{ds}$ and $N = r_1 V_{ds} + \omega L_1 V_{qs}$

Again, substituting I_{q1} and I_{d1} from (4.61) and (4.62) to (4.60) and further simplification gives:

$$M_{qs} = b - cM_{ds} \tag{4.64}$$

where $b = \dfrac{\dfrac{4Q_s^*}{3V_{dc}}(r_1^2 + (\omega_e L_1)^2) + \dfrac{2\omega_e L_1}{V_{dc}}(V_{qs}^2 + V_{ds}^2)}{\omega_e L_1 V_{qs} - r_1 V_{ds}}$ and $c = \dfrac{r_1 V_{qs} + \omega_e L_1 V_{ds}}{\omega_e L_1 V_{qs} - r_1 V_{ds}}$

Now substituting (4.64) into (4.63) gives:

$$a(c^2+1)M_{ds}^2 + (cK - N - 2abc)M_{ds} + ab^2 - bK = 0 \tag{4.65}$$

Solving (4.55) gives:

$$M_{ds1,2} = \frac{N + 2abc - cK \pm \sqrt{(cK - N - 2abc)^2 - 4ab(c^2+1)(ab-K)}}{2a(c^2+1)} \tag{4.66}$$

Substituting $M_{ds1,2}$ from (4.66) to (4.64) gives $M_{qs1,2}$ as follows:

$$M_{qs1,2} = b - c\frac{N + 2abc - cK \pm \sqrt{(cK - N - 2abc)^2 - 4ab(c^2+1)(ab-K)}}{2a(c^2+1)} \tag{4.67}$$

Only the +ve sign for $M_{ds1,2}$ and $M_{qs1,2}$ in (4.66) and (4.67) for some value of Q_s^* gives $M_x = \sqrt{M_{qs}^2 + M_{ds}^2} \le 1$ which is the feasible solution.

Hence M_{ds} and M_{qs} are given as:

$$M_{ds} = \frac{N + 2abc - cK + \sqrt{(cK - N - 2abc)^2 - 4ab(c^2+1)(ab-K)}}{2a(c^2+1)} \tag{4.68}$$

$$M_{qs} = b - c\frac{N + 2abc - cK + \sqrt{(cK - N - 2abc)^2 - 4ab(c^2+1)(ab-K)}}{2a(c^2+1)} \tag{4.69}$$

When the $r_1 = 0$ then (4.68) and (4.69) gives:

$$\begin{cases} M_{qs} = \dfrac{2}{V_{dc}}\left(\dfrac{2Q_s^*\omega_e L_1}{3V_s} + V_s\right) \\ M_{ds} = 0 \end{cases} \tag{4.70}$$

Since the q and d-axis modulation indexes can be only real values, i.e.:

$$(cK - N - 2abc)^2 - 4ab(c^2+1)(ab-K) \ge 0 \tag{4.71}$$

Solving (4.71) gives the condition for both modulations indexes to be always real as:

$$r_1 \le \frac{3}{4}\frac{V_s^{\,2}}{Q_s^*} \tag{4.72}$$

So, range of r_1 for which the solution given by (4.68) and (4.69) exists is $0 \le r_1 \le \frac{3}{4}\frac{V_s^{\,2}}{Q_s^*}$.

Based upon (4.72), since the steady state voltage is constant then when the resistance r_1 increases, maximum value of reactive power STATCOM can supply decreases. As shown in Figure 4.19, the maximumvalue of Q_s^* is 0.2 pu, and steady state voltage is 1 pu, using (4.72), r_1 can go upto 3.75 pu. The value of r_1 used in this study is 0.05 pu which satisfies (4.72). Figure 4.17 shows the maximum value of reactive power STATCOM can supply for various values of line resistance at different PCC voltages.

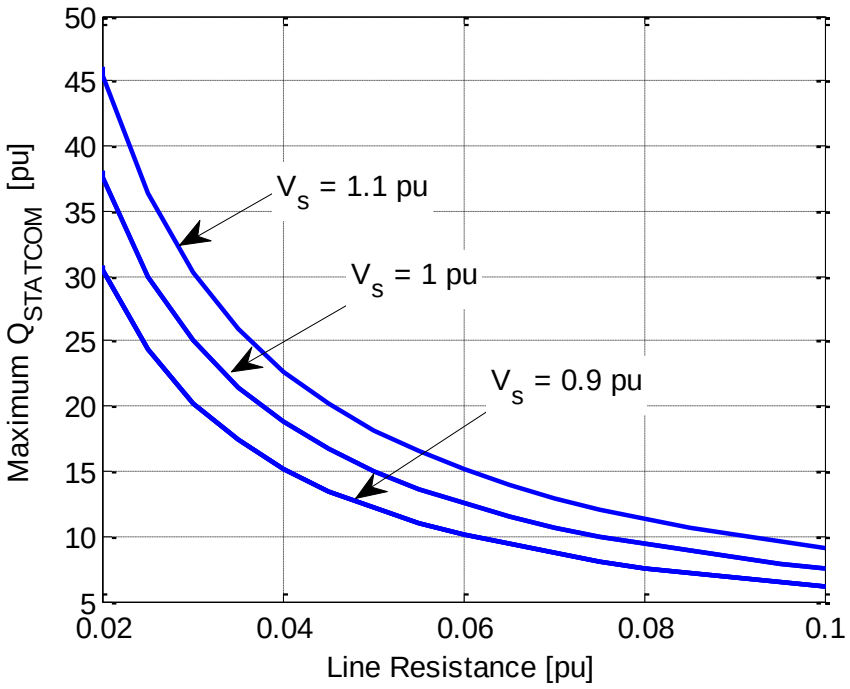

Figure 4.17 Maximum values of reactive power STATCOM can supply for various values of line resistance

Now, in the overall P_{total} - Q_{total} curve plotting, another one more condition should be satisfied, i.e. $\left|\sqrt{(M_{qs}^2 + M_{ds}^2)}\right| \leq 1$.

Here, $Q_{Total} = Q_{DFIG} + Q_{STATCOM}$.

The flowchart for drawing reactive power capability curve (P-Q diagram) of the DFIG wind turbine system with STATCOM at the PCC to meet the reactive power requirement (or power factor requirement) is shown in Figure 4.18.

The reactive power capability diagram of overall DFIG-based WECS with STATCOM connected at PCC is shown in Figure 4.19. When the DFIG does not have enough reactive power, STATCOM supplies the additional reactive power to maintain

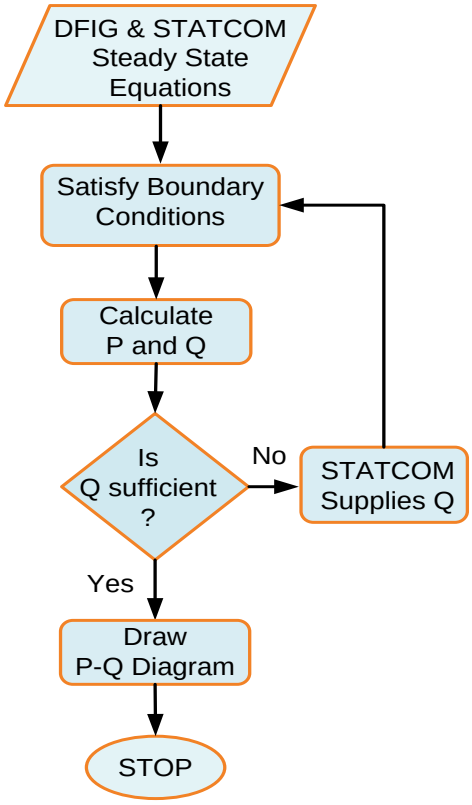

Figure 4.18 Flowchart for plotting PQ diagram of DFIG-based WECS with STATCOM

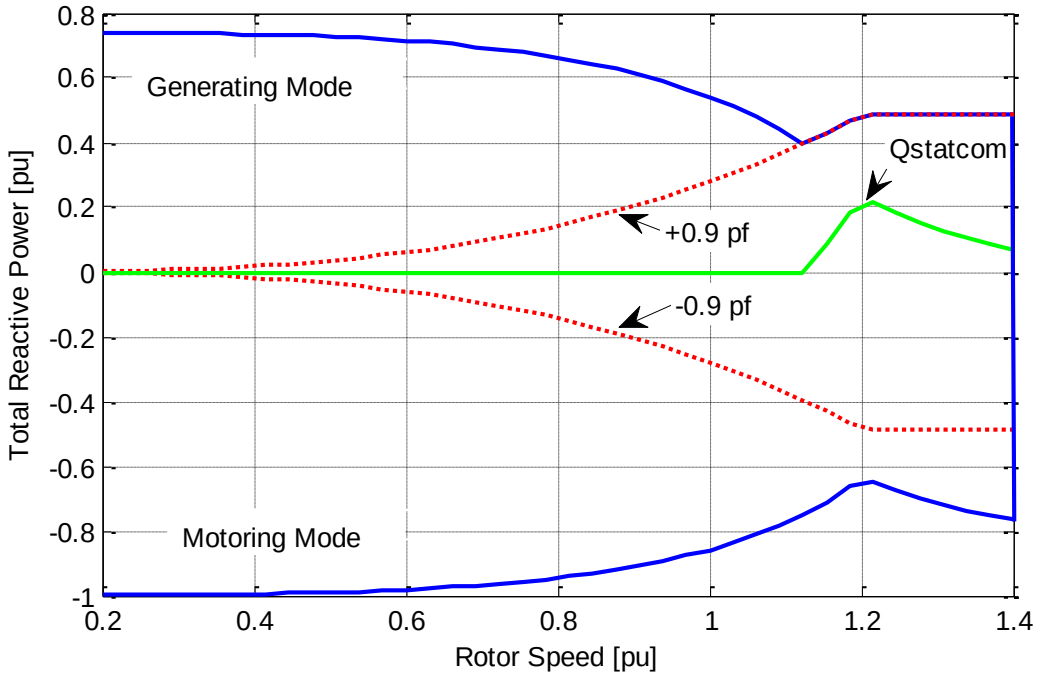

Figure 4.19 Reactive power capability diagram of overall DFIG-based WECS with STATCOM at various rotor speeds

0.9 pf during entire operation region of the DFIG to meet the grid code requirement. As depicted in Figure 4.19, STATCOM has to supply maximum of 0.2 pu reactive power, which gives the rating of the STATCOM required to fulfill the steady state reactive power (or power factor) requirement.

Therefore, in this chapter, steady state characteristics of the DFIG-based WECS are presented and the steady state reactive power capability of the DFIG is shown in the form of PQ diagram. It is observed that, DFIG has limited reactive power capability so installation of STATCOM at the PCC as an additional reactive power source to fulfill the reactive power requirement is proposed. In the Chapter 5, the use of STATCOM connected at the PCC to regulate the steady state voltage as well as improving the dynamic response of DFIG wind turbine system during grid side disturbance is discussed.

CHAPTER 5

VOLTAGE REGULATION IN DFIG-BASED WIND TURBINE SYSTEM USING STATCOM

5.1 Introduction

Most large size wind turbines are generally located at remote places or offshore because of the noise pollution created by wind turbines, large dimension of wind turbine and its ancillary components, better wind condition and impact on the scenery. Those areas typically have electrically weak power grids characterized by low short circuit ratios, low X/R ratio of the transmission line, and under-voltage conditions. Voltage instability problems occur in a power system that cannot supply the reactive power demand during disturbances like faults, heavy loading, and voltage swelling/sagging. In case of wind turbine system, the aerodynamic behavior of the wind turbine and variable nature of wind also causes its output voltage fluctuation. Voltage regulation refers to the task of keeping node voltages in the system within the tolerable bandwidth (normally 5% to 10%) in the whole power system. It is very important to notice that the particular bus voltage is local quantity and hence it is very difficult and costly to control the bus voltage at the remote node by the use of conventional power stations consisting of synchronous generators and synchronous condensers located elsewhere in the grid. It is because the reactive power flow in the system is associated with changes in voltage which in turn increases the power losses in the system. Hence it is necessary to install local voltage control devices in the transmission/distribution network even if the wind turbine itself has

voltage controlling capability because the wind turbines are usually located at a more distant location from the load center.

Voltage regulation can be maintained in the power system by supplying or absorbing the reactive power. Hence, the voltage regulation at a particular node in a power system is directly related to the reactive power capability of the devices directly connected to that node or present in the vicinity of that node. Although, the DFIG-based wind turbines are able to control active and reactive power independently, the reactive power capability of those generators is limited as discussed in Chapter 4. This problem is more severe in the case of DFIG wind turbines connected to weak power grids having under voltage condition as the reactive power capability gets even more degraded. Hence an additional local reactive power source is needed. Moreover, the power generation trend these days is shifting from the transmission network to the distribution grid, i.e. decentralization of power generation. As a result, it is becoming more difficult to control the voltage in the entire transmission network from conventional power stations only. Hence grid companies are installing dedicated local voltage control equipments like capacitor banks, FACTS devices and are demanding distributed generation equipments to have their own reactive power capability as a result there cannot be any exemption for wind turbines.

Furthermore, because of the increased penetration level of wind turbines in the power grid, utility companies are asking to fulfill certain criteria (grid codes) for the interconnection of wind turbines to the power grid. The grid codes mainly requires that wind turbines remain connected to the network during temporary disturbances in the network like voltage swelling and sagging, and step change in load. Wind turbines cannot

be a VAR neutral (or consumer). Now they must be able to provide reactive power and adjust their control according to the necessity of the system. To meet this requirement, the DFIG wind turbine system should be able to respond fast whenever there is disturbance in the system by supplying or absorbing reactive power. Hence, the added reactive power source should have good dynamic response.

FACTS devices are dynamic reactive power sources which are becoming more and more popular in power system application these days because of rapid advancement in high-current, high-power semiconductor device technology, digital control, and signals conditioning. In this study, a voltage source converter (VSC) PWM technique based STATCOM is modeled, its control system is designed and the use of STATCOM (a FACTS device) at the PCC is investigated for voltage regulation purpose in the DFIG wind turbine system. The voltage regulation study is done by creating three phase symmetrical fault and voltage swelling and sagging at the PCC where local load is also connected.

5.2 STATCOM

The IEEE definition of a STATCOM [66] is: “A static synchronous generator operated as a shunt connected static var compensator whose capacitive or inductive output current can be controlled independent of the AC system voltage”. Basically STATCOM is a FACTS device which is also known as electronic generator of reactive power. It consists of a VSC, a DC energy storage device (capacitor), and a coupling transformer which connects the VSC in shunt to the power network as shown in Figure

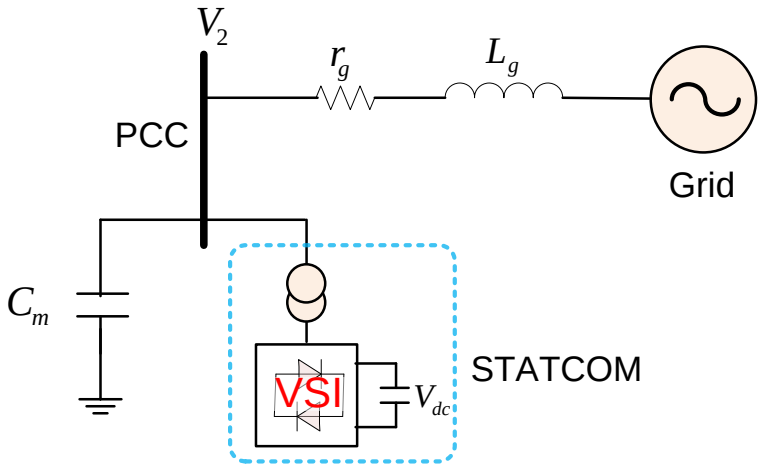

Figure 5.1 Single line diagram of the STATCOM connected to power grid

5.1. The VSC produces a set of controllable three-phase output voltages with the frequency of the AC power system. The charged capacitor provides a DC voltage to the VSC. It can continuously generate or absorb reactive power by varying the amplitude of the converter output voltage with respect to the line bus voltage so that a controlled current flows through the tie reactance (jX_s) between the STATCOM and the power grid. If the amplitude of the output voltage is increased above that of the line bus voltage, a leading current is produced, i.e. the STATCOM generates reactive power. Decreasing the amplitude of the output voltage below that of the line bus voltage, a lagging current results and the STATCOM absorbs the reactive power. If the amplitudes of both voltages are equal, no power exchange takes place. This enables the STATCOM to mitigate voltage fluctuations such as sags, swells, transient disturbances, and to provide voltage regulation.

5.2.1 Reasons for Choosing the STATCOM

Capacitors are usually connected to fixed speed wind turbines to enhance the system voltage because they are the sink of reactive power. Mechanically switched fixed shunt capacitors can enhance the system's voltage stability limit, but is not very sensitive to voltage changes, i.e. dynamic response of capacitors is not good.

STATCOM is the best option for dynamic compensation of reactive power because at voltages lower than the normal voltage range, it can generate more reactive power than other FACTS devices like Static Var Compensator (SVC) [67], which is very similar to STATCOM for functional compensation capability but its fundamental operating principle is different. A STATCOM functions as a shunt-connected synchronous voltage source whereas a SVC operates as a shunt-connected controlled reactive admittance. This difference accounts for the STATCOM's superior functional characteristics, better performance, and greater application flexibility than those attainable with a SVC [67]. The STATCOM is able to control its output current over the rated maximum capacitive or inductive range independently of AC system voltage, whereas the maximum attainable compensating current of the SVC decreases linearly with AC voltage. In addition, the STATCOM normally exhibits a faster response as it has no delay associated with the thyristor firing [42].

The output of the wind power plants and the total load vary continuously throughout the day. Reactive power compensation is required to maintain normal voltage levels in the power system. Reactive power imbalances, which can seriously affect the power system, can be minimized by connecting the STATCOM. The STATCOM can

also contribute to the low voltage ride through requirement because it can operate at full capacity even at lower voltages.

Moreover, the STATCOM can be connected to any voltage level in power system using coupling transformer of appropriate turn ratio. The STATCOM can be easily connected to an already installed wind turbine system which has a voltage regulation problem.

5.2.2 Location of the STATCOM

Simulation results show that STATCOM provides effective voltage support at the bus to which it is connected to. Hence, in this study, the STATCOM is placed at the PCC bus because of the following two reasons:

- The location of the reactive power support should be as close as possible to the point at which the support is needed because of the change in voltage and consequent power loss (I^2R loss) in transmission line associated with the reactive power flow.
- In the studied system, the effect of voltage change is most significant at this node.

5.2.3 STATCOM Output Power

For the balanced three-phase system, it is convenient to use the per-phase equivalent circuit as shown in Figure 5.2 to explain how the STATCOM output reactive power can be modulated by a VSC using the PWM technique. For simplicity, the resistances of the coupling transformer and filtering inductor are neglected.

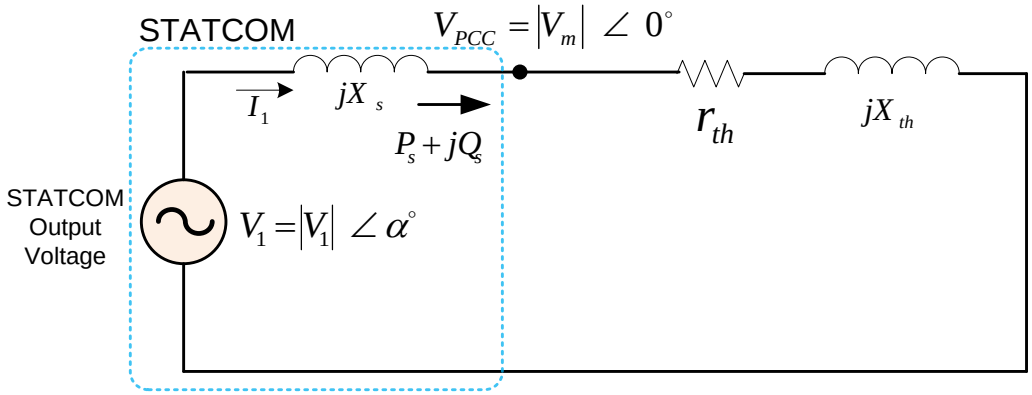

Figure 5.2 Single-phase equivalent circuit of a STATCOM connected to a power system

The complex power supplied by the STATCOM to the AC power system is given by the following equations [68]:

$$P_s = \frac{|V_1|\,|V_m|}{X_s}\sin\alpha \tag{5.1}$$

$$Q_s = -\frac{|V_m|^2}{X_s} + \frac{|V_1|\,|V_m|}{X_s}\cos\alpha \tag{5.2}$$

where V_m and V_1 are the voltages at the PCC and STATCOM output voltage, respectively and α is the STATCOM output voltage angle.

To simplify the analysis, let $|V_m|$=1 p.u. giving:

$$P_s = \frac{|V_1|}{X_s}\sin\alpha \tag{5.3}$$

$$Q_s = -\frac{1}{X_s} + \frac{|V_1|}{X_s}\cos\alpha \tag{5.4}$$

It is obvious from (5.3) and (5.4) that the STATCOM real power output and reactive power output can be controlled by either its output voltage magnitude $|V_1|$ or its phase angle α or both. In the design of a STATCOM controller, the reactive power output Q_s is of major concern to us since the negative of P_s simply gives us the real power that must be supplied by the AC bus to the STATCOM in order to cover the converter loss and transformer and filter loss (if present) [68].

5.2.4 Sensitivity Analysis

To see whether the voltage magnitude $|V_1|$ or phase angle α is more effective in controlling the STATCOM reactive power output, let's make a sensitivity analysis [68]:

$$\frac{\partial Q}{\partial |V_1|} = \frac{1}{X_s}\cos\alpha \tag{5.5}$$

$$\frac{\partial Q}{\partial \alpha} = -\frac{|V_1|}{X_s}\sin\alpha \tag{5.6}$$

In normal operation, $|V_1|$ is close to unity and $|\alpha|$ is very small because STATCOM generates only a small amount of active power to supply the losses in the terminal impedance. From (5.3), if P_s is small means α is small. So, $\cos\alpha \approx 1$, $\sin\alpha \approx 0$, and $\left|\frac{\partial Q}{\partial |V_1|}\right| >> \left|\frac{\partial Q}{\partial \alpha}\right|$. That implies that, the voltage magnitude $|V_1|$ is more effective than the phase angle α in controlling the reactive power output .Thus, it is desirable to control the voltage magnitude while trying to regulate the PCC bus voltage under disturbance conditions.

5.3 STATCOM Modeling and Controller Design

STATCOM is modeled as a PWM converter comprising of IGBT with a DC-link capacitor and a coupling transformer connected in shunt to the distribution network through a coupling transformer as shown in Figure 5.3. The objective of the STATCOM is to regulate the voltage magnitude swiftly at the PCC bus within a desired range by exchanging the reactive power with the distribution system. At the same time the converter in STATCOM should maintain constant DC-link voltage. A small filter capacitor C_m is also connected in shunt to the same bus for mitigating harmonics.

The dynamic equations of the STATCOM converter in qd-reference frame:

$$V_{q1} = r_s I_{q1} + L_s p I_{q1} + \omega_e L_s I_{d1} + V_{q2} = M_{q1} \frac{V_{dc}}{2} \tag{5.7}$$

$$V_{d1} = r_s I_{d1} + L_s p I_{d1} - \omega_e L_s I_{q1} + V_{d2} = M_{d1} \frac{V_{dc}}{2} \tag{5.8}$$

where V_{q1}, V_{d1}, V_{q2}, V_{d2} are the q and d-axis VSC output voltages and PCC bus voltages, respectively. I_{q1} and I_{d1} are the q and d-axis converter output currents, respectively. r_s and L_s are line resistance and inductance, respectively. M_{q1} and M_{d1} are q and d-axis modulation indexes of the converter, respectively. V_{dc} is the DC-link voltage and ω_e is the angular velocity of the synchronously rotating reference frame.

The STATCOM DC voltage dynamics in DC-link is given by:

$$C_{dc} p V_{dc} = -\frac{3}{4}(M_{q1} I_{q1} + M_{d1} I_{d1}) \tag{5.9}$$

And the voltage magnitude (V_m) at the PCC is given as:

$$V_m^2 = V_{q2}^2 + V_{d2}^2 \tag{5.10}$$

Differentiating (5.10) w.r.t. time,

$$pV_m^2 = 2V_{q2}pV_{q2} + 2V_{d2}pV_{d2} \tag{5.11}$$

Equation (5.11) gives the square of voltage magnitude dynamics at the PCC and thus the voltage magnitude will be: $V_m = \left|\sqrt{V_m^2}\right|$.

DC-voltage control:

Equation (5.9) can be rewritten as:

$$-\frac{4}{3}C_{dc}pV_{dc} = (M_{q1}I_{q1} + M_{d1}I_{d1}) = \sigma_{dc} = k_{dc}(V_{dc}^* - V_{dc}) \tag{5.12}$$

where k_{dc} is the PI controller for DC-voltage control given as: $k_{dc} = \left(k_{Pdc} + \frac{k_{Idc}}{p}\right)$. Then Equation (5.12) will be:

$$\frac{4}{3}C_{dc}pV_{dc} = \left(k_{Pdc} + \frac{k_{Idc}}{p}\right)V_{dc}^{\ *} - \left(k_{Pdc} + \frac{k_{Idc}}{p}\right)V_{dc} \tag{5.13}$$

$$\frac{V_{dc}}{V_{dc}^{\ *}} = \frac{\frac{3}{4C_{dc}}\left(pk_{Pdc} + k_{Idc}\right)}{p^2 + p\frac{3k_{Pdc}}{4C_{dc}} + \frac{3k_{Idc}}{4C_{dc}}} \tag{5.14}$$

Comparing denominator of (5.14) with Butterworth second order polynomial $p^2 + \sqrt{2}\omega_{0dc}p + \omega_{0dc}^2$, PI controller gains are obtained as:

$$k_{Pdc} = \frac{4}{3}\sqrt{2}\omega_{0dc}C_{dc} \tag{5.15}$$

$$k_{Idc} = \frac{4}{3}C_{dc}\omega_{0dc}^{\ 2} \tag{5.16}$$

where ω_{0dc} is the bandwidth of the DC-voltage controller.

Voltage magnitude control:

From Figure 5.3, the dynamic voltage equations at the PCC can be written as:

$$C_m\ pV_{q2} = I_{q1} - I_{q2} - C_m\omega_e V_{d2} \tag{5.17}$$

$$C_m\ pV_{d2} = I_{d1} - I_{d2} + C_m\omega_e V_{q2} \tag{5.18}$$

Substituting (5.17) and (5.18) into (5.11) gives:

$$\frac{C_m}{2}\, pV_m^2 = V_{q2}\left(I_{q1} - I_{q2}\right) + V_{d2}\left(I_{d1} - I_{d2}\right) = \sigma_m = k_m(V_m^{2*} - V_m^2) \tag{5.19}$$

where $k_m = \left(k_{Pm} + \frac{k_{\mathrm{Im}}}{p}\right)$ is the PI controller for voltage magnitude control. Substituting for k_m results in (5.20) and from which the transfer function is found as shown in (5.21).

$$\frac{C_m}{2}\, pV_m^2 = \left(k_{Pm} + \frac{k_{\mathrm{Im}}}{p}\right)V_m^{2^*} - \left(k_{Pm} + \frac{k_{\mathrm{Im}}}{p}\right)V_m^2 \tag{5.20}$$

$$\frac{V_m^2}{V_m^{2^*}} = \frac{\frac{2}{C_m}\left(pk_{Pm} + k_{\mathrm{Im}}\right)}{p^2 + p\frac{2k_{Pm}}{C_m} + \frac{2k_{\mathrm{Im}}}{C_m}} \tag{5.21}$$

Comparing the denominator of (5.21) with the Butterworth second order polynomial:

$$k_{Pm} = \sqrt{2}\omega_{0m}\frac{C_m}{2} \tag{5.22}$$

$$k_{\mathrm{Im}} = \frac{C_m}{2}\omega_{0m}{}^2 \tag{5.23}$$

where ω_{0m} is the bandwidth of the voltage controller.

Inner current control:

If we assume that:

$$r_s I_{q1} + L_s pI_{q1} = K_{1q}(I^*_{q1} - I_{q1}) = \sigma_{1q} \tag{5.24}$$

$$r_s I_{d1} + L_s pI_{d1} = K_{1d}(I^*_{d1} - I_{d1}) = \sigma_{1d} \tag{5.25}$$

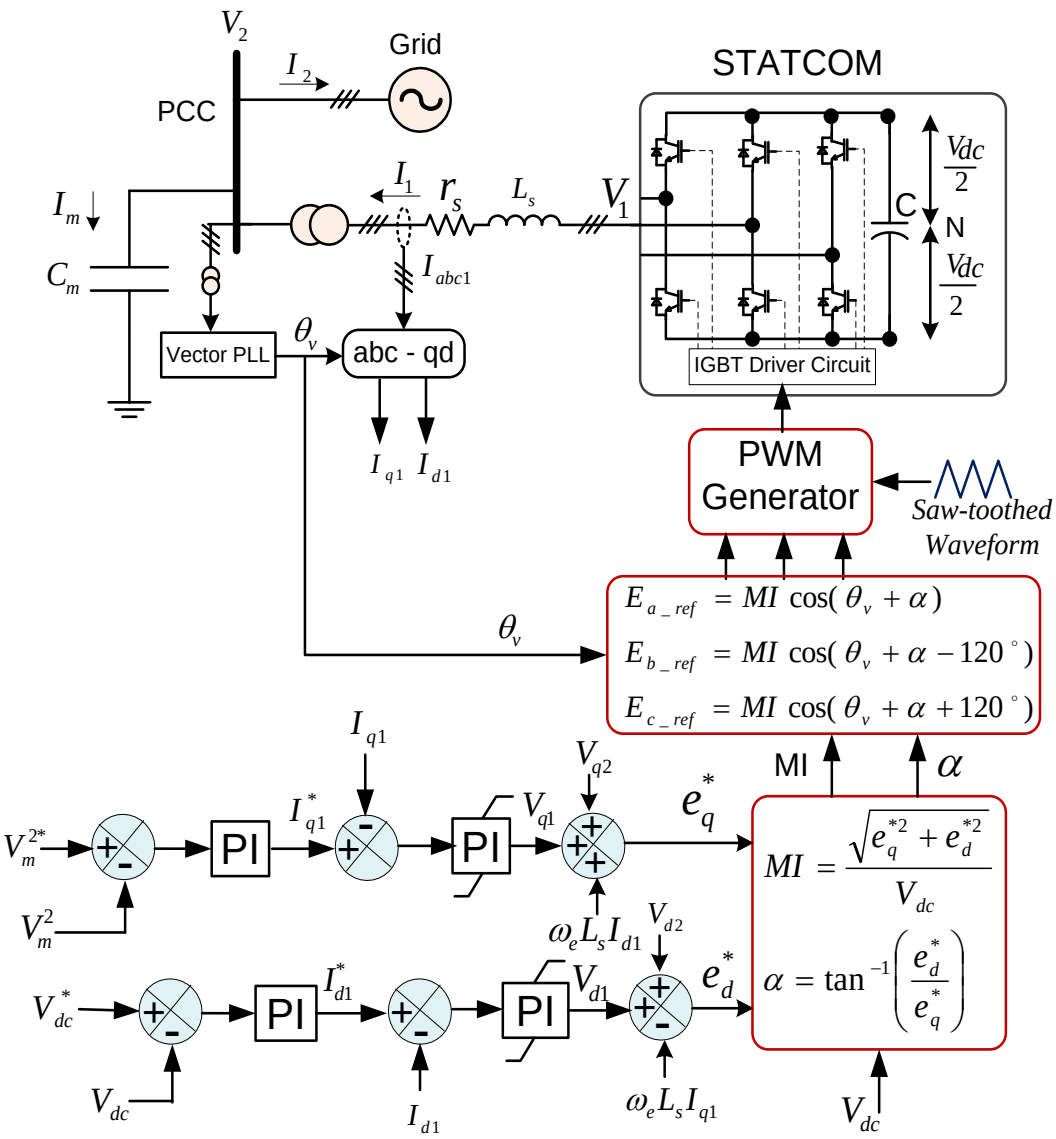

Figure 5.3 Proposed STATCOM controller

Then Equations (5.7) and (5.8) can be written as:

$$M_{q1} = (\sigma_{1q} + \omega_e L_s I_{d1} + V_{q2}) \frac{2}{V_{dc}} \tag{5.26}$$

$$M_{d1} = (\sigma_{1d} - \omega_e L_s I_{q1} + V_{d2}) \frac{2}{V_{dc}} \tag{5.27}$$

Equations (5.27) and (5.28) give modulation indexes which are the output of the converter. And K_{1q} and K_{1d} are PI current controllers for q and d-axis currents, respectively and $K_{1q} = K_{1d} = \left(k_{P1} + \frac{k_{I1}}{p} \right)$.

Equation (5.24) can be re-written as:

$$(r_s + sL_s)I_{q1} = \left(k_{P1} + \frac{k_{I1}}{p} \right) I_{q1}^{*} - \left(k_{P1} + \frac{k_{I1}}{p} \right) I_{q1} \tag{5.28}$$

$$\frac{I_{q1}}{I_{q1}^{*}} = \frac{\frac{1}{L_s}(pk_{P1} + k_{I1})}{p^2 + p\frac{1}{L_s}(r_s + k_{P1}) + \frac{1}{L_s}k_{I1}} \tag{5.29}$$

Comparing denominator of (5.29) with the Butterworth second order polynomial gives:

$$k_{P1} = \sqrt{2}\omega_{0c}L_s - r_s \tag{5.30}$$

$$k_{I1} = L_s\omega_{0c}^{2} \tag{5.31}$$

where ω_{0c} is the bandwidth frequency of the current controller. Table 5.1 gives the PI controllers values used for the simulation study following above procedure. The switching frequency is taken as 1 kHz and the bandwidth of inner current controller is taken ten times that of outer loop controller, i.e.

Table 5.1 Parameters of the STATCOM and PI controller coefficients

r_s	0.25 Ω	C_{dc}	60 mF	k_{Pdc}	7.1	k_{Idc}	315.5
L_s	1 mH	C_m	0.2 mF	k_{Pm}	0.088	k_{Im}	0.394
				k_{P1}	0.638	k_{I1}	394.38

$\omega_{sw} = 2*\pi* f_{sw} = 6280\ rad/s$ and $\omega_{inner} = \frac{\omega_{sw}}{10}$; $\omega_{outer} = \frac{\omega_{inner}}{10}$

$\omega_{inner} = \omega_{oc} = 628\ rad/s$ and $\omega_{outer} = \omega_{odc} = \omega_{om} = 62.8\ rad/s$

From (5.15): $k_{Pdc} = \frac{4}{3}\sqrt{2}\omega_{0dc}C_{dc} = 7.1$ and from (5.16): $k_{Idc} = \frac{4}{3}C_{dc}\omega_{0dc}{}^{2} = 315.5$

From (5.22): $k_{Pm} = \sqrt{2}\omega_{0m}\frac{C_m}{2} = 0.088$ and from (5.23): $k_{\mathrm{Im}} = \frac{C_m}{2}\omega_{0m}{}^{2} = 0.394$

From (5.30): $k_{P1} = \sqrt{2}\omega_{0c}L_s - r_s = 0.638$ and from (5.31): $k_{I1} = \omega_{oc}^2 L_s = 394.38$

5.4 Voltage Control Capability and Converter Rating in the DFIG

It is known fact that the DFIG wind turbine system has voltage control capability utilizing the GSC. Unfortunately, this does not come for free. Voltage control requires a power electronic converter with a power rating that is higher than the rating for unity power factor operation. In order to get better insight about this fact the steady state analysis of the DFIG system is done where the amount of reactive power GSC supplies is plotted against the current that has to flow through the GSC or the current rating of the GSC required. The steady states equations of the DFIG system, presented in Chapter 4, used in this analysis; are given below:

$$V_{qs} = r_s I_{qs} + \omega_e L_s I_{ds} + \omega_e L_m I_{dr} \tag{5.32}$$

$$V_{ds} = r_s I_{ds} - \omega_e L_s I_{qs} - \omega_e L_m I_{qr} \tag{5.33}$$

$$V_{qr} = r_r I_{qr} + (\omega_e - \omega_r) L_m I_{ds} + (\omega_e - \omega_r) L_r I_{dr} \tag{5.34}$$

$$V_{dr} = r_r I_{dr} - (\omega_e - \omega_r) L_m I_{qs} - (\omega_e - \omega_r) L_r I_{qr} \tag{5.35}$$

$$T_m = \frac{3P}{4} L_m \left[I_{qr} I_{ds} - I_{dr} I_{qs} \right] \tag{5.36}$$

$$Q_s = \frac{3}{2} (V_{qs} I_{ds} - V_{ds} I_{qs}) = 0 \tag{5.37}$$

$$\frac{3}{4} \left(M_{qr} I_{qr} + M_{dr} I_{dr} \right) + \frac{3}{4} \left(M_{qf} I_{qf} + M_{df} I_{df} \right) = 0 \tag{5.38}$$

$$M_{qf} \frac{V_{dc}}{2} = r_f I_{qf} + \omega_e L_f I_{df} + V_{qs} \tag{5.39}$$

$$M_{df} \frac{V_{dc}}{2} = r_f I_{df} - \omega_e L_f I_{qf} + V_{ds} \tag{5.40}$$

$$Q_{GSC} = \frac{3}{2} (V_{qs} I_{df} - V_{ds} I_{qf}) \tag{5.41}$$

In this study, it is assumed that the grid voltage (V_{qs}, V_{ds}) and frequency (ω) are equal to their nominal values. The DFIG system is operating at rated speed, producing rated power output of 1 pu and reactive power exchange through stator side is zero. Reactive power supplied to the grid by GSC (Q_{GSC}) is varied from 0 pu (unity power factor operation) to 0.5 pu. The latter corresponds to the overall power factor of DFIG system to be approximately 0.9 which is the grid code requirement for interconnection of DFIG to the grid. As presented above, we have ten steady state Equations (5.32)-(5.41), and ten unknowns which are: I_{qs}, I_{ds}, I_{qr}, I_{dr}, I_{qf}, I_{df}, M_{qf}, M_{df}, M_{qr} and M_{dr}. Solving simultaneously in MATLAB, I_{qf} and I_{df} are obtained for the different values of reactive power GSC supplies. Then the magnitude of the GSC current is given as:

$$\left| I_f \right|^2 = I_{qf}^2 + I_{df}^2 \tag{5.42}$$

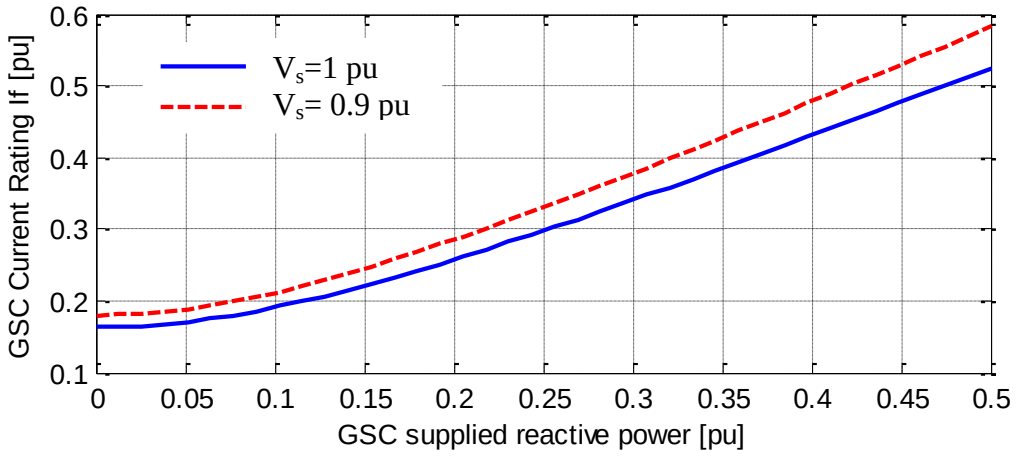

Figure 5.4 Converter phase current rating required for generating varying amount of reactive power Q_{GSC} in DFIG wind turbine system with two different terminal voltages

The obtained plot is shown in Figure 5.4 which shows that compared with unity power factor operation mode, the converter current rating is higher for reactive power generation. Full voltage control capability requires that reactive power can be both generated and consumed. The power rating of converter has to be increased significantly (more than 3 times according to Figure 5.4) to achieve the full voltage control capability in the DFIG system. Hence, connecting additional dynamic reactive power compensator at the PCC where reactive power is needed is a reasonable choice financially and technically; especially if the DFIG wind turbine is connected to weak power grid where turbine terminal voltage is usually under-voltage. As a result, the current rating of converter required to achieve full voltage controllability in the DFIG increases even more as shown in Figure 5.4.

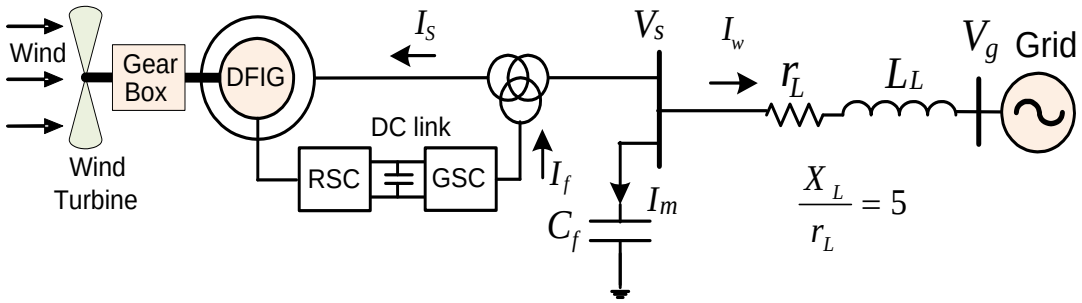

Figure 5.5 Schematic diagram of DFIG wind turbine connected to weak grid

5.5 Voltage Regulation of DFIG Wind Turbine Connected to Weak Grid

5.5.1 Test System

In this study, a simple test system is built in order to quantitatively investigate the voltage control capability of the DFIG wind turbine system. The test system shown in Figure 5.5 consists of a DFIG wind turbine which is connected through impedance (so as to model like a weak grid) to a strong grid represented by a constant voltage source. A small capacitor is connected at turbine terminal to filter the harmonics and stabilize the wind turbine terminal voltage. The nominal power output and voltage are 1.5 MW and 690 V, respectively.

5.5.2 Steady State Analysis

The steady state equations of DFIG represented by (5.32)-(5.41) are used for this analysis. The analysis is done for two distinct operation modes of the DFIG. During the steady state analysis, the shunt connected capacitor C_f is negelected because the terminal voltage is constant during steady state.

Mode I: Constant Terminal Voltage Operation:

In this operation mode, Equation (5.41) is modified to:

$$|V_s|^2 = V_{qs}^2 + V_{ds}^2 \tag{5.43}$$

And Using KVL from DFIG terminal bus to the grid bus:

$$V_{qs} - V_{qg} = r_L(I_{qf} - I_{qs}) + \omega_e L_L(I_{df} - I_{ds}) \tag{5.44}$$

$$V_{ds} - V_{dg} = r_L(I_{df} - I_{ds}) - \omega_e L_L(I_{qf} - I_{qs}) \tag{5.45}$$

We now have two more variables which are V_{qs} and V_{ds} which can be solved using two more steady state equations (5.44) and (5.45). V_{qg} and V_{dg} are grid voltages and are known.

Figure 5.6 shows the results of the steady state analysis of the DFIG wind turbine system. The GSC controls the terminal voltage to exactly 1 p.u. despite of the active power output variation from 0 to 1 p.u. by supplying reactive power as shown in Figure 5.6 (a). It should be noted that in the simulation study, GSC capacity is not limited. But the commercially available DFIG has limited power rating converter (30% of total wind turbine MVA) so reactive power supplying capability of those wind turbine is also limited as discussed in Chapter 4. Hence when the active power output level reaches 0.9 p.u. or above then the voltage controller (or GSC) in the DFIG cannot supply additional reactive power as a result the wind turbine terminal voltage drops below 1 p.u. Hence, additional reactive power source is required to be installed at the PCC to maintain the terminal voltage to 1 p.u.

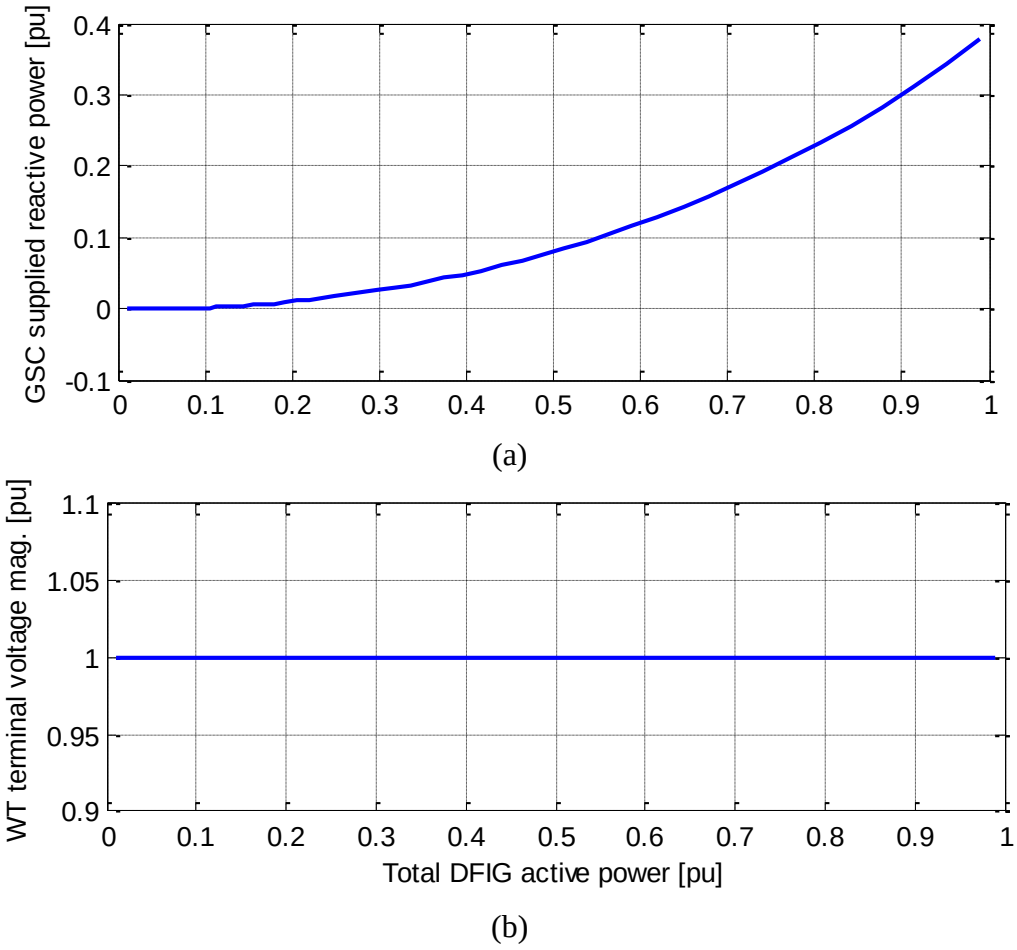

Figure 5.6 (a) Reactive power supplied by GSC and (b) DFIG terminal voltage

Mode II: Unity Power Factor Operation

Presently, the commercially available DFIG wind turbines are often controlled to operate in unity power factor operation mode [23]. For the steady state analysis of the DFIG system connected to power grid, Equations (5.32)-(5.41) and (5.44)-(5.45) are solved simultaneously in MATLAB. Figure 5.7 shows the results of the steady state analysis of the DFIG wind turbine system operating in unity power factor operation. The wind turbine reactive power output is set to zero despite of the active power output variation from zero to 1 p.u. As a result, the terminal voltage decreases gradually with the

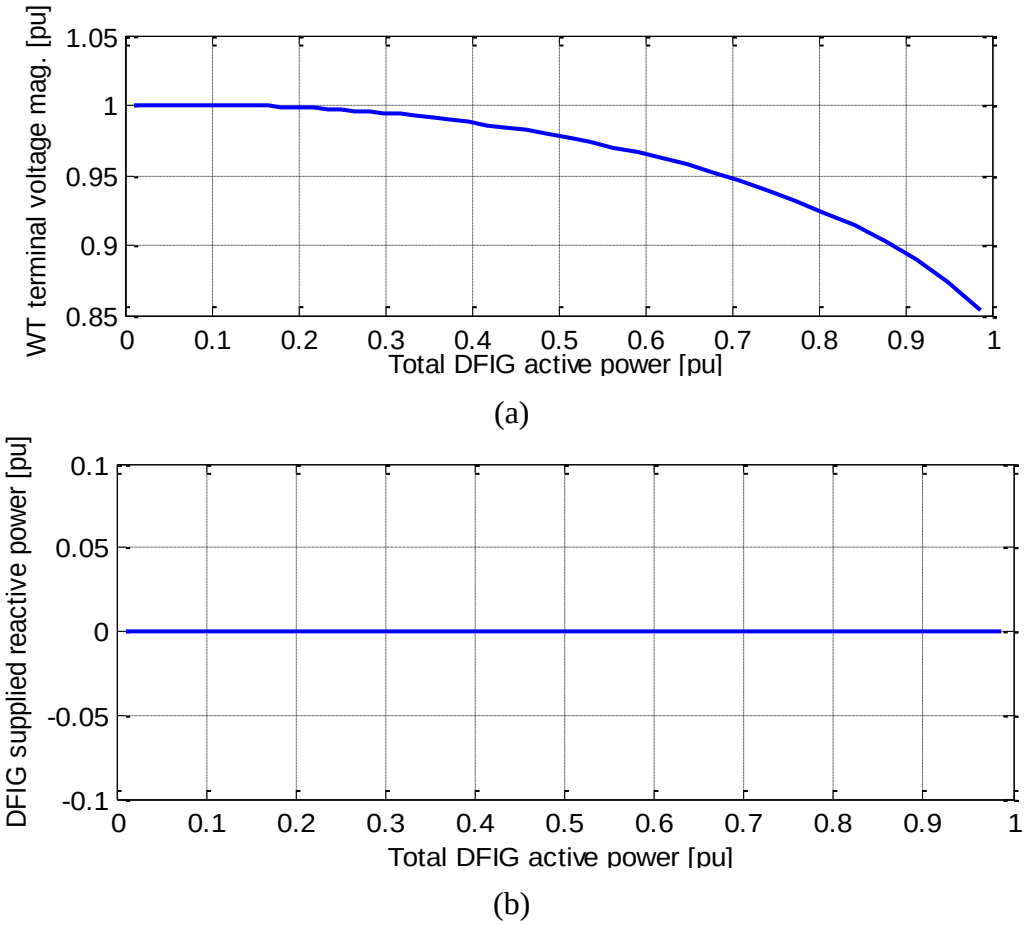

Figure 5.7 (a) DFIG terminal voltage and (b) reactive power generation by DFIG

increase in active power output owing to the high impedance of the grid connection as shown in Figure 5.7(a).

Hence, in both operation modes of the DFIG; additional reactive power source is needed. In this study, STATCOM is proposed to be installed at the PCC with the unity power factor operation mode of DFIG. In doing so, the terminal voltage can be maintained constant at 1 p.u. by supplying additional reactive power by the STATCOM as shown in Figure 5.8 and the DFIG can continuously generate active power only extracting maximum wind power available.

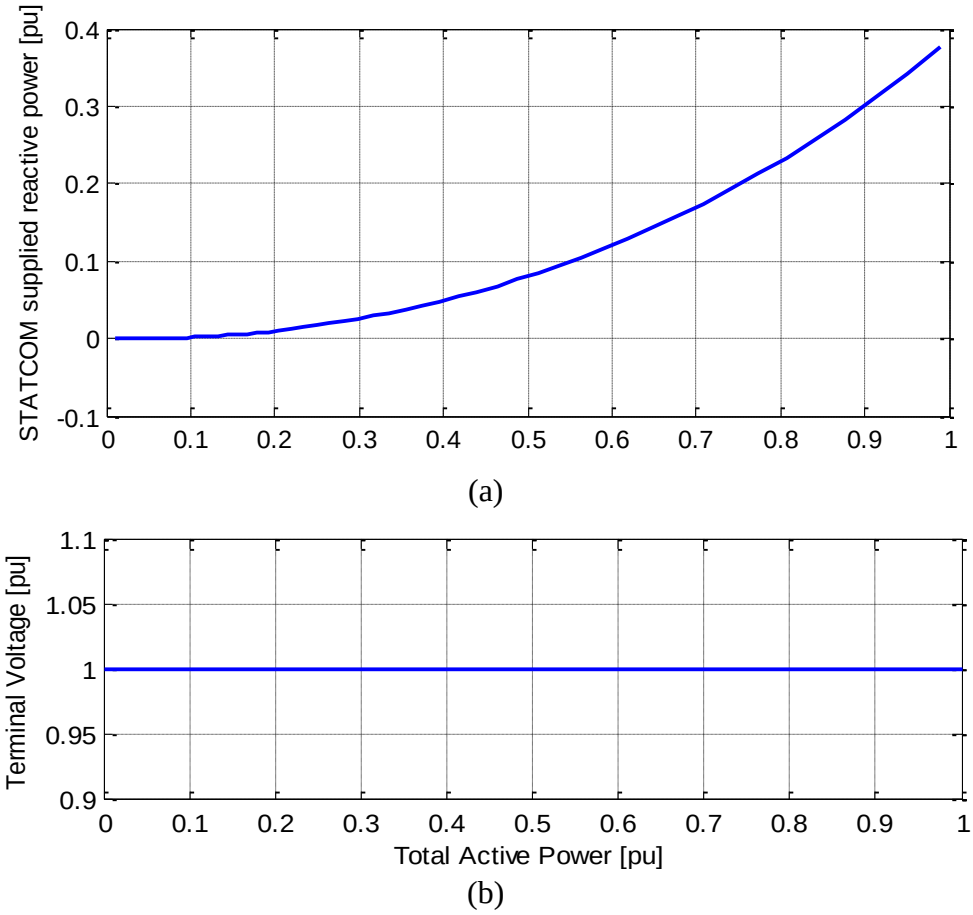

Figure 5.8 (a) Reactive power supplied by STATCOM and (b) DFIG terminal voltage

5.6 Disturbances Mitigation in the DFIG-based Wind Turbine System Using the STATCOM

With the increased penetration of wind in the power grid, the grid operators are forced to tighten their grid connection rules in order to limit the effects of wind power parks on power network quality and stability. Important issues are the steady state active and reactive power governing capability, continuously acting voltage control, and disturbance tolerant system like voltage sagging and voltage swelling. This means, the grid codes demand that wind farms stay connected to the grid and stabilize the grid voltage in case of disturbances in the grid [69].

5.6.1 Test System

Figure 5.9 demonstrates the single line diagram of the test system studied in this study. A 1.5 MW DFIG wind turbine system is connected to the distribution network at the PCC bus where a STATCOM is connected to regulate the terminal voltage. Three different types of loads, a linear RL load, a constant load (P, Q) and a nonlinear load (P_{non}, Q_{non}) are also connected in shunt to the same PCC bus. The rated wind speed of 12 m/s is inputted to the turbine so as to generate rated active power output during the entire study period. The GSC is always supplying its optimum reactive power (0.3 pu, i.e. equal to 30% of total power rating of DFIG). The distribution network is modeled as weak (X_g / R_g = 5). The models of the different loads used are given as:

For the linear RL loads, voltage equation is:

$$V_{qdPCC} = r_L I_{qdL} + L_L p I_{qdL} - j\omega_e L_L I_{qdL} \tag{5.46}$$

where r_L and L_L is the resistance and inductance of the RL load, respectively. V_{qdPCC} is the PCC voltage.

The filter capacitor current is given by:

$$I_{qdw} - I_{qdL} - I_{qdLL} - I_{qdnL} = C_m \ pV_{qdPCC} - j\omega_e C_m \ V_{qdPCC} \tag{5.47}$$

where C_m is the filter capacitor, I_{qdw} is the current supplied by the DFIG wind turbine system, I_{qdL}, I_{qdLL} and I_{qdnL} are currents drawn by RL load, linear load and non-linear load, respectively.

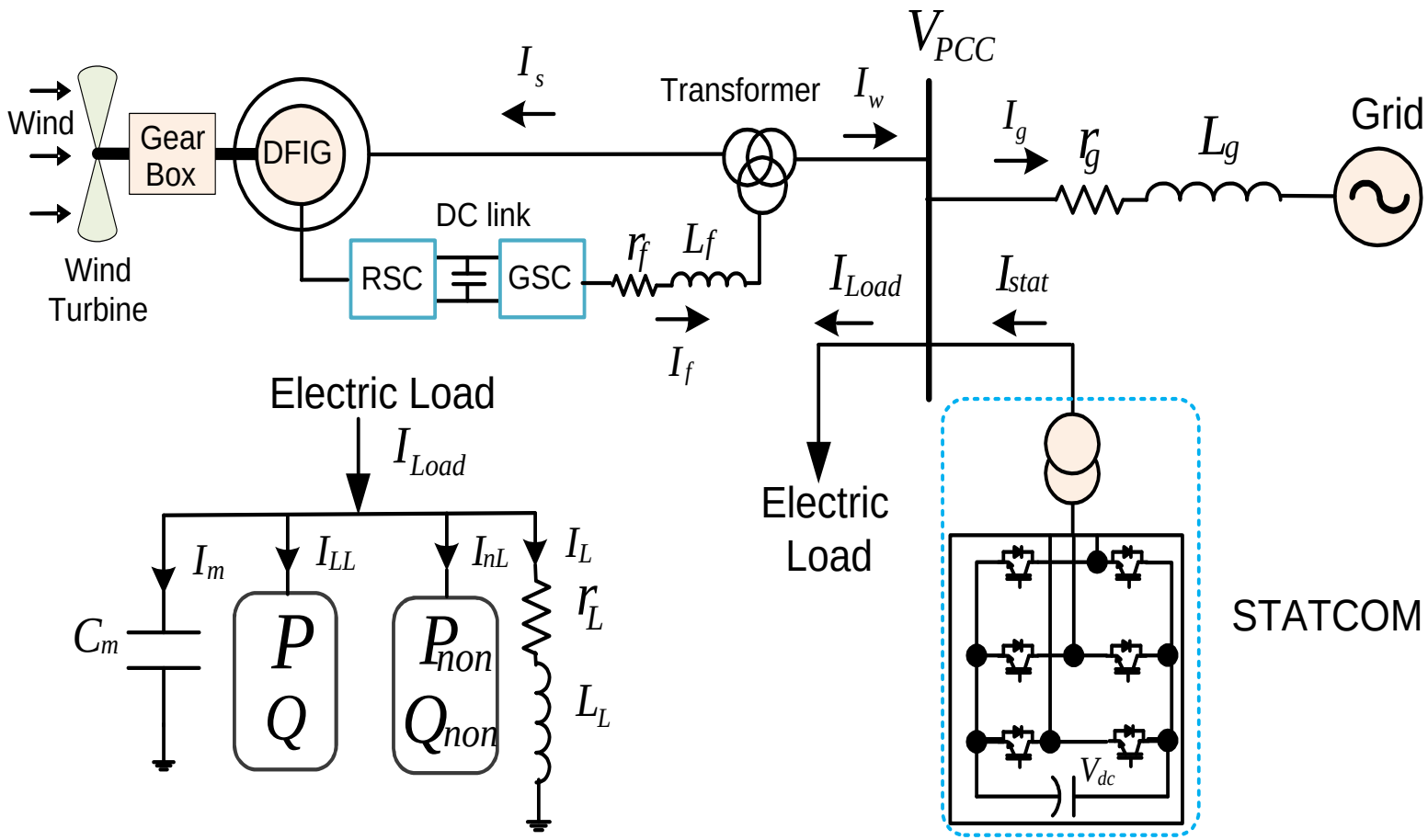

Figure 5.9 Single line diagram of the studied power network

A non-linear electrical load is a load on the electrical system that draws a non-sinusoidal current waveform from the connected supply. Computer, fax machine, printer, electronic lighting ballast, variable-speed drive etc. are the typical examples of non-linear electrical loads. The non-linear loads have non-linear relationship with the voltage magnitude and system frequency. In this study, non-linear loads are modeled as [70]:

$$\begin{cases} P_{non} = P_o\left(\dfrac{V_{m\_PCC}}{V_0}\right)^a\left(\dfrac{\omega}{\omega_0}\right)^b \\ Q_{non} = Q_o\left(\dfrac{V_{m\_PCC}}{V_0}\right)^a\left(\dfrac{\omega}{\omega_0}\right)^b \end{cases} \tag{5.48}$$

where P_o and Q_o are base active and reactive powers of non-linear loads, respectively. V_{m_PCC} and ω are local voltage magnitude and frequency, respectively. V_0 and ω_0 are nominal voltage magnitude and frequency of the distribution system, respectively. a and b are load-voltage and load-frequemcy dependence factors, respectively. In this study a=b=3 is taken.

The active and reactive powers consumed by the constane load are given as:

$$\begin{cases} P = \dfrac{3}{2}(V_{q\_PCC}I_{qLL} + V_{d\_PCC}I_{dLL}) \\ Q = \dfrac{3}{2}(V_{q\_PCC}I_{dLL} - V_{d\_PCC}I_{qLL}) \end{cases} \tag{5.49}$$

Hence, from (5.49), the constant load current equations are:

$$\begin{cases} I_{qLL} = \dfrac{2}{3}\dfrac{PV_{q\_PCC} - QV_{d\_PCC}}{V_{q\_PCC}^2 + V_{d\_PCC}^2} \\ I_{dLL} = \dfrac{2}{3}\dfrac{PV_{d\_PCC} + QV_{q\_PCC}}{V_{q\_PCC}^2 + V_{d\_PCC}^2} \end{cases} \tag{5.49(a)}$$

Similarly, the non-linear load current equations are:

$$\begin{cases} I_{qnL} = \dfrac{2}{3}\dfrac{P_{non}V_{q\_PCC} - Q_{non}V_{d\_PCC}}{V_{q\_PCC}^2 + V_{d\_PCC}^2} \\ I_{dnL} = \dfrac{2}{3}\dfrac{P_{non}V_{d\_PCC} + Q_{non}V_{q\_PCC}}{V_{q\_PCC}^2 + V_{d\_PCC}^2} \end{cases} \tag{5.50}$$

Now the below section describes the control of RSC and GSC in the DFIG wind turbine.

5.6.2 Design of the RSC Controller

The RSC control scheme consists of two cascaded vector control structure with inner current control loops which regulates independently the d-axis and q-axis rotor currents, i.e. I_{dr} and I_{qr}, according to some synchronously rotating reference frame. The outer control loop regulates the stator active power (or DFIG rotor speed) and reactive power (or DFIG terminal voltage) independently. The stator voltage orientation (SVO) control principle for a DFIG is described in [31], where the q-axis of the rotating reference frame is aligned to the stator voltage i.e V_{ds} = 0 and V_{qs} = V_s. From (3.15) and (3.16), the stator side flux can be controlled using PI controller. In this study, the q-axis flux is regulated to zero ($\lambda_{qs} = 0$) and ($\lambda_{ds} = \lambda_s$) for the de-coupled control of active and reactive power as described below:

$$\begin{cases} p\lambda_{qs} + \dfrac{r_s}{\sigma L_s}\lambda_{qs} = -\omega_e\lambda_{ds} + \dfrac{r_s L_m}{\sigma L_s L_r}\lambda_{qr} + V_{qs} \\ \sigma_{\lambda qs} = -\omega_e\lambda_{ds} + \dfrac{r_s L_m}{\sigma L_s L_r}\lambda_{qr} + V_{qs} \\ \lambda_{ds}^{*} = \dfrac{1}{\omega_e}\left(\dfrac{r_s L_m}{\sigma L_s L_r}\lambda_{qr} + V_{qs} - \sigma_{\lambda qs}\right) \end{cases} \tag{5.51}$$

$$\begin{cases} p\lambda_{ds} + \dfrac{r_s}{\sigma L_s}\lambda_{ds} = \omega_e \lambda_{qs} + \dfrac{r_s L_m}{\sigma L_s L_r}\lambda_{dr} + V_{ds} \\ \sigma_{\lambda ds} = \omega_e \lambda_{qs} + \dfrac{r_s L_m}{\sigma L_s L_r}\lambda_{dr} + V_{ds} \\ \lambda_{qs}^* = \dfrac{1}{\omega_e}\left(\sigma_{\lambda ds} - \dfrac{r_s L_m}{\sigma L_s L_r}\lambda_{qr} - V_{qs}\right) \end{cases} \tag{5.52}$$

where $\sigma_{\lambda qs} = p\lambda_{qs} + \dfrac{r_s}{\sigma L_s}\lambda_{qs} = \left(k_{P\lambda s} + \dfrac{k_{I\lambda s}}{p}\right)(\lambda_{qs}^* - \lambda_{qs})$ and $\sigma_{\lambda ds} = p\lambda_{ds} + \dfrac{r_s}{\sigma L_s}\lambda_{ds} = \left(k_{P\lambda s} + \dfrac{k_{I\lambda s}}{p}\right)(\lambda_{ds}^* - \lambda_{ds})$ are the outputs from the PI controllers as shown in Figure 5.10.

The PI parameters are determined by comparing with the Butterworth polynomial which is described in the below section, are given as:

$$\begin{cases} k_{P\lambda s} = \sqrt{2}\omega_0 - \dfrac{r_s}{\sigma L_s} \\ k_{I\lambda s} = {\omega_0}^2 \end{cases} \tag{5.53}$$

Now, neglecting frictional losses, rotor speed dynamics is given as:

$$p\omega_r = \frac{P}{2J}(T_m - T_e) \tag{5.54}$$

where T_m is the mechanical torque from the wind turbine. When the wind speed (V_w) is

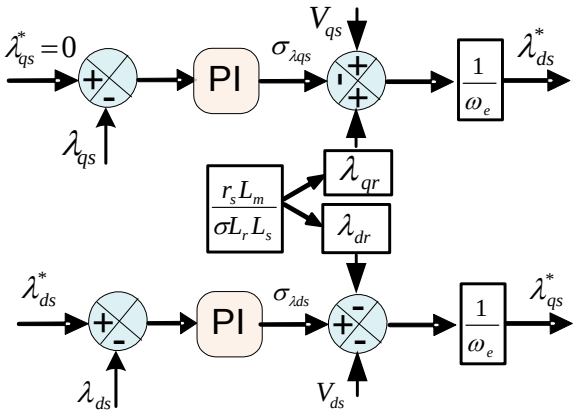

Figure 5.10 Stator fluxes control using PI controllers

less than the rated speed, then the T_m is given as:

$$T_m = k_{opt} V_w{}^2 \tag{5.55(a)}$$

where $k_{opt} = \frac{R}{2\lambda_{opt}} \rho\, A\, C_{p\_opt}$ = constant and if the wind speed (V_w) is more than the rated speed, then the T_m is given as:

$$T_m = \frac{P_{rated}}{\omega_{rated}} \tag{5.55(b)}$$

where P_{rated} is rated power of the wind turbine and ω_{rated} is the rated speed of the wind turbine.

Equation (5.54) can be re-written as:

$$\frac{2J}{P} p\omega_r = (T_m - T_e) = \sigma_{wr} = k_{wr}(\omega_r^* - \omega_r) \tag{5.56}$$

where k_{wr} is the PI controller for rotor speed controller, given as: $k_{wr} = \left(k_{Pwr} + \frac{k_{Iwr}}{p} \right)$

Then (5.54) will be:

$$\begin{cases} \frac{2J}{P} p\omega_r = \left(k_{Pwr} + \frac{k_{Iwr}}{p} \right) \omega_r{}^* - \left(k_{Pwr} + \frac{k_{Iwr}}{p} \right) \omega_r \\ \frac{\omega_r}{\omega_r{}^*} = \frac{\frac{P}{2J}\left(p k_{Pwr} + k_{Iwr} \right)}{p^2 + p\frac{P k_{Pwr}}{2J} + \frac{P k_{Iwr}}{2J}} \end{cases} \tag{5.57}$$

Now, comparing denominator of (5.57) with Butterworth second order polynomial $p^2 + \sqrt{2}\omega_{0wr} p + \omega_{0wr}^2$, PI controller gains are obtained as:

$$\begin{cases} k_{Pwr} = \sqrt{2}\omega_{0wr} \frac{2J}{P} \\ k_{Iwr} = \frac{2J}{P} \omega_{0wr}{}^2 \end{cases} \tag{5.58}$$

where ω_{0wr} is the bandwidth frequency of the speed controller.

Using λ_{qs} = 0, the electromechanical torque and q-axis stator current is given by (5.59) and (5.60) as:

$$T_e = \frac{3}{2}\frac{P}{2}\lambda_{ds} I_{qs} \tag{5.59}$$

$$I_{qs} = -\frac{L_m}{L_s} I_{qr} \tag{5.60}$$

$$T_e = \frac{3}{2}\frac{P}{2}\lambda_{ds}(-\frac{L_m}{L_s}) I_{qr} \tag{5.61}$$

$$I_{qr} = (\sigma_{wr} - T_m)\frac{4}{3P}\frac{L_s}{L_m \lambda_{ds}} \tag{5.62}$$

Similarly,

$$I_{ds} = \frac{\lambda_{ds}}{L_s} - \frac{L_m}{L_s} I_{dr} \tag{5.63}$$

Now, the stator active power can be written as:

$$P_s = \frac{3}{2}\left(V_{qs} I_{qs} + V_{ds} I_{ds}\right) = -\frac{3}{2}\frac{L_m}{L_s} V_{qs} I_{qr} \tag{5.64}$$

Now, the stator supplied reactive power is given as:

$$Q_s = \frac{3}{2}(V_{qs} I_{ds} - V_{ds} I_{qs}) = \frac{3}{2} V_{qs} I_{ds} \tag{5.65}$$

Substituting V_{qs} in (5.65) gives:

$$Q_s = \frac{3}{2}(r_s I_{qs} + \omega_e \lambda_{ds} + p\lambda_{qs}) I_{ds} \tag{5.66}$$

Assuming constant stator flux, neglecting the stator resistance and substituting I_{ds} from Equation (3.10) gives:

$$Q_s = \frac{3}{2}\frac{\omega_e}{\sigma L_s}\left(\lambda_{ds}^2 - \frac{L_m}{L_r}\lambda_{ds}\lambda_{dr}\right) \tag{5.67}$$

Differentiating (5.67) w.r.t. time gives:

$$pQ_s = -\frac{3}{2}\frac{\omega_e}{\sigma L_s}\frac{L_m}{L_r}\lambda_{ds}p\lambda_{dr} \tag{5.68}$$

From (5.68) and (3.4) gives (5.69) and solving λ_{qr} in terms of I_{qr} gives (5.70)

$$pQ_s = -\frac{3}{2}\frac{\omega_e}{\sigma L_s}\frac{L_m}{L_r}\lambda_{ds}\left(V_{dr} - r_r I_{dr} + (\omega_e - \omega_r)\lambda_{qr}\right) \tag{5.69}$$

$$pQ_s = -\frac{3}{2}\frac{\omega_e}{\sigma L_s}\frac{L_m}{L_r}\lambda_{ds}\left(V_{dr} - r_r I_{dr} + (\omega_e - \omega_r)\sigma L_r I_{qr}\right) \tag{5.70}$$

$$\nabla pQ_s = \sigma_{Qs} = k_{Qs}(Q_s^* - Q_s) \tag{5.71}$$

where $\nabla = \frac{2\sigma L_s L_r}{3\omega_e L_m}$ and k_{Qs} is the PI controller for stator side reactive power controller, given as: $k_{Qs} = \left(k_{PQs} + \frac{k_{IQs}}{p}\right)$. So, (5.71) can be re-written as:

$$\nabla pQ_s = \left(k_{PQs} + \frac{k_{IQs}}{p}\right)Q_s^* - \left(k_{PQs} + \frac{k_{IQs}}{p}\right)Q_s \tag{5.72}$$

$$\frac{Q_s}{Q_s^*} = \frac{\frac{1}{\nabla}\left(pk_{PQs} + k_{IQs}\right)}{p^2 + p\frac{k_{PQs}}{\nabla} + \frac{k_{IQs}}{\nabla}} \tag{5.73}$$

Similarly, comparing denominator of (5.73) with Butterworth second order polynomial $p^2 + \sqrt{2}\omega_{Qs}p + \omega_{Qs}^2$, PI controller gains are obtained as:

$$k_{PQs} = \sqrt{2}\omega_{0Qs}\Delta \tag{5.74}$$

$$k_{IQs} = \Delta\omega_{Qs}^{\ 2} \tag{5.75}$$

From (5.70) and (5.71) gives:

$$I_{dr}^{*} = \frac{1}{r_r}\left(V_{dr} + (\omega_e - \omega_r)\sigma L_r I_{qr} - \frac{\sigma_{Q_s}}{\lambda_{ds}} \right) \tag{5.76}$$

It can be seen from Equations (5.64) and (5.76) that, P_s and Q_s are proportional to I_{qr} and I_{dr}, respectively. The mutual coupling term $(\omega_e - \omega_r)\sigma L_r I_{qr}$ in (5.76) is very small so its effect is negligible. The rotor current can be regulated by means of rotor voltages. The relation between rotor current and rotor voltage is obtained by substituting values of λ_{dr} and λ_{qr} from (3.7) and (3.8) in Equations (3.3) and (3.4), respectively, and further simplification yields:

$$V_{qr} = r_r I_{qr} + \sigma L_r p I_{qr} + \omega_{so}\left(\frac{L_m}{L_s}\lambda_{ds} + \sigma L_r I_{dr} \right) \tag{5.77}$$

$$V_{dr} = r_r I_{dr} + \sigma L_r p I_{dr} - \omega_{so}\sigma L_r I_{qr} \tag{5.78}$$

where $\omega_{so} = (\omega_e - \omega_r)$ and $\sigma = 1 - \frac{L_m^{\,2}}{L_s L_r}$

In the Equations (5.77) and (5.78), there is the term including I_{dr} in the q-axis equation and there is the term including I_{qr} in the d-axis equation. So these two equations are coupled and the traditional linear controllers cannot be used. However, through the exact linearization method, these equations can be linearized by putting the terms other than the currents control to one side.

$$r_r I_{qr} + \sigma L_r p I_{qr} = V_{qr} - \omega_{so}\left(\frac{L_m}{L_s}\lambda_{ds} + \sigma L_r I_{dr} \right) \tag{5.79}$$

$$r_r I_{dr} + \sigma L_r p I_{dr} = V_{dr} + \omega_{so}\sigma L_r I_{qr} \tag{5.80}$$

Let's assume:

$$\sigma_{qr} = r_r I_{qr} + \sigma L_r p I_{qr} \tag{5.81}$$

$$\sigma_{dr} = r_r I_{dr} + \sigma L_r p I_{dr} \tag{5.82}$$

The idea here is to use the linear controllers that include integrations to calculate the derivative terms. And the nonlinear equations become linear when all the nonlinear terms are moved to the other side of the equations. Then the q and d-axis voltages are calculated as:

$$V_{qr}^{*} = \sigma_{qr} + \omega_{so}\left(\frac{L_m}{L_s}\lambda_{ds} + \sigma L_r I_{dr}\right) \tag{5.83}$$

$$V_{dr}^{*} = \sigma_{dr} - \omega_{so}\sigma L_r I_{qr} \tag{5.84}$$

Using the inner current control loop has a significant advantage for the protection of the DFIG. It can naturally protect the system from over-current since current limiters can be easily inserted in the control system shown in Figure 5.10.

Since the general PI controllers are widely used and proved to be effective, they are also applied in the following analysis [63]. For I_{qr} current control loop from (5.79):

$$V_{qr}^{'} = r_r I_{qr} + \sigma L_r p I_{qr} = (r_r + p\sigma L_r) I_{qr} \tag{5.85}$$

$$V_{qr}^{'} = \left(k_{qp} + \frac{k_{qi}}{p}\right)\left(I_{qr}^{*} - I_{qr}\right) \tag{5.86}$$

$$(r_r + p\sigma L_r) I_{qr} = \left(k_{qp} + \frac{k_{qi}}{p}\right) I_{qr}^{*} - \left(k_{qp} + \frac{k_{qi}}{p}\right) I_{qr} \tag{5.87}$$

Then the transfer functions between the reference and actual currents are changed to the following:

$$\frac{I_{qr}}{I_{qr}^{*}} = \frac{pk_{qp} + k_{qi}}{p^2\sigma L_r + p(r_r + k_{qp}) + k_i} = \frac{\frac{1}{\sigma L_r}\left(pk_{qp} + k_{qi}\right)}{p^2 + p\frac{1}{\sigma L_r}(r_r + k_{qp}) + \frac{1}{\sigma L_r}k_{qi}} \tag{5.88}$$

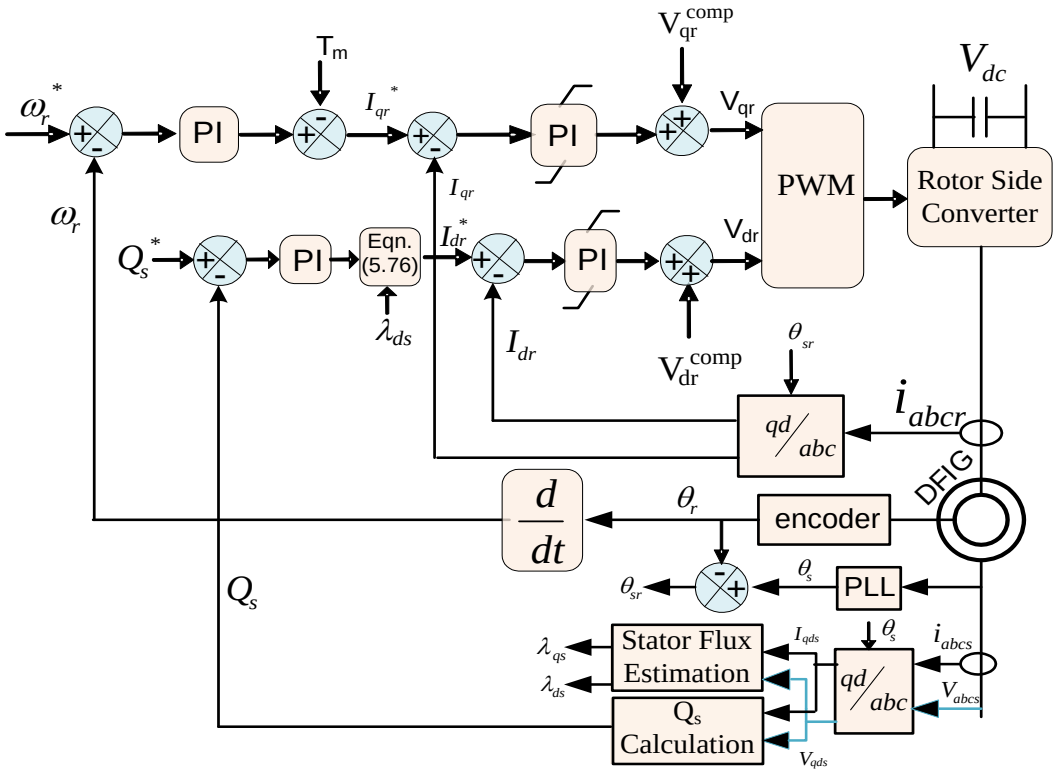

Figure 5.11 Block diagram of RSC control system: $V_{dr}^{comp} = -\omega_{so}\sigma L_r I_{qr}$

and $V_{qr}^{comp} = \omega_{so}(\frac{L_m}{L_s}\lambda_{ds} + \sigma L_r I_{dr})$

Similar process can be repeated for I_{dr} current control loop from (5.80). The PI parameters are determined by comparing the coefficients in the denominator of (5.88) with the Butterworth second order polynomial.

$$k_{qp} = k_{dp} = \sqrt{2}\omega_0\sigma L_r - r_r \tag{5.89}$$

$$k_{qi} = k_{di} = \sigma L_r \omega_0^{\,2} \tag{5.90}$$

Here ω_0 is the bandwidth of the current controller. The values of Kp and KI for RSC is shown in Table 5.2. The overall vector control scheme of the RSC is shown in Figure 5.11.

5.6.3 Design of the GSC Controller

Figure 5.12 shows the general vector control scheme of the GSC where control of DC-link voltage V_{dc} and reactive power exchange between GSC and power grid is achieved by controlling current in synchronous reference frame [54].

Now, DC voltage dynamics in DC-link is given by:

$$C\ pV_{dc} = \frac{3}{4}\left(M_{dr}I_{dr} + M_{qr}I_{qr}\right) + \frac{3}{4}\left(M_{df}I_{df} + M_{qf}I_{qf}\right) \tag{5.91}$$

where C is the DC-link capacitance, M_{dr} and M_{qr} are q and d-axis modulation indexes of RSC and M_{df} and M_{qf} are q and d-axis modulation indexes of GSC, respectively. Hence, (5.91) can be re-written as (5.92) which can be solved to get I_{qf} given by (5.93).

$$C\ pV_{dc} = \frac{3}{4}\left(M_{dr}I_{dr} + M_{qr}I_{qr}\right) + \frac{3}{4}\left(M_{df}I_{df} + M_{qf}I_{qf}\right) = \sigma_{dc} \tag{5.92}$$

Equation (5.91) can be re-written as:

$$C\ pV_{dc} = \sigma_{dc} = k_{dc}(V_{dc}^{*} - V_{dc}) \tag{5.93}$$

where k_{dc} is the PI controller for DC-voltage control given as: $k_{dc} = \left(k_{Pdc} + \frac{k_{Idc}}{p}\right)$. Then (5.93) will be:

$$C\ pV_{dc} = \left(k_{Pdc} + \frac{k_{Idc}}{p}\right)V_{dc}^{\ *} - \left(k_{Pdc} + \frac{k_{Idc}}{p}\right)V_{dc} \tag{5.94}$$

$$\frac{V_{dc}}{V_{dc}^{\ *}} = \frac{\frac{1}{C_{dc}}\left(pk_{Pdc} + k_{Idc}\right)}{p^2 + p\frac{k_{Pdc}}{C_{dc}} + \frac{k_{Idc}}{C_{dc}}} \tag{5.95}$$

Comparing denominator of (5.95) with Butterworth second order polynomial $p^2 + \sqrt{2}\omega_{0dc}p + \omega_{0dc}^2$, PI controller gains are obtained as:

$$k_{Pdc} = \sqrt{2}\omega_{0dc}C_{dc} \tag{5.96}$$

$$k_{Idc} = C_{dc}\omega_{0dc}{}^2 \tag{5.97}$$

where ω_{0dc} is the bandwidth frequency of the DC-voltage controller. From (5.92):

$$I_{qf}^{*} = \frac{4}{3}\frac{1}{M_{qf}}\left(\sigma_{dc} - \frac{3}{4}\left(M_{dr}I_{dr} + M_{qr}I_{qr}\right)\right) - \frac{M_{df}}{M_{qf}}I_{df} \tag{5.98}$$

Using KVL across the RL filter gives:

$$V_{qf} = r_f I_{qf} + L_f pI_{qf} + \omega_e L_f I_{df} + \frac{V_{qs}}{N} = M_{qf}\frac{V_{dc}}{2} \tag{5.99}$$

$$V_{df} = r_f I_{df} + L_f pI_{df} - \omega_e L_f I_{qf} = M_{df}\frac{V_{dc}}{2} \tag{5.100}$$

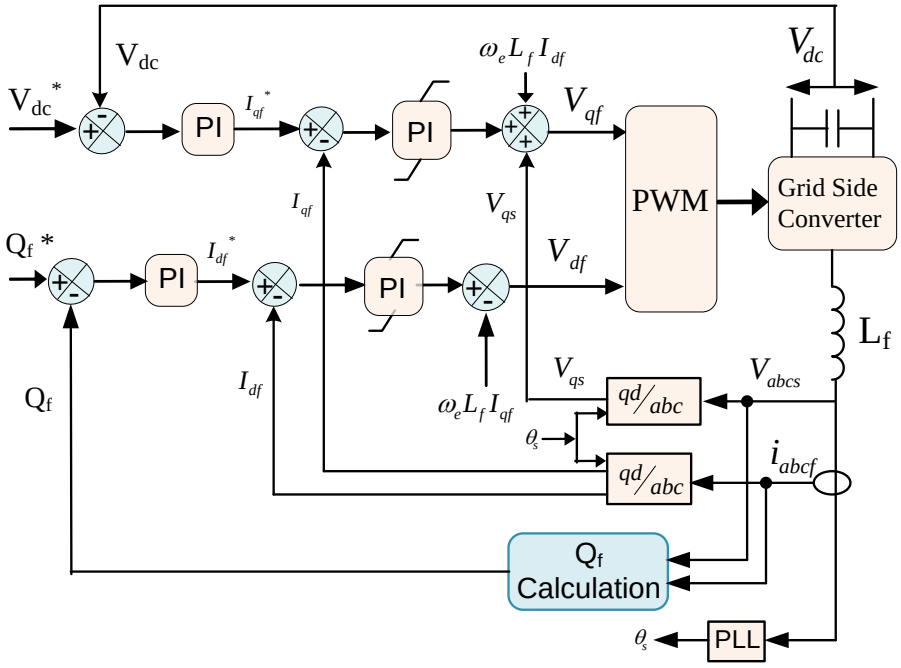

Figure 5.12 Block diagram of GSC control system

Since the q-axis of the rotating reference frame is aligned to the stator voltage i.e $V_{ds} = 0$ and $V_{qs} = V_s$. So, the GSC supplied reactive power to the grid is controlled using d-axis current.

$$Q_f = \frac{3}{2N} V_s I_{df} \tag{5.101}$$

where N is the transformer turns ratio connected between GSC and stator.

$$pQ_f = \frac{3V_s}{2N} pI_{df} \tag{5.102}$$

Substituting (5.100) in (5.102) gives:

$$pQ_f = \frac{3V_s}{2N} \frac{1}{L_f} (V_{df} - r_f I_{df} + \omega_e L_f I_{qf}) \tag{5.103}$$

$$\Gamma pQ_f = (V_{df} - r_f I_{df} + \omega_e L_f I_{qf}) = \sigma_{Qf} \tag{5.104}$$

where $\Gamma = \frac{2NL_f}{3V_s}$

$$\Gamma pQ_f = \sigma_{Qf} = k_{Qf} (Q_f^* - Q_f) \tag{5.105}$$

where k_{Qf} is the PI controller for reactive power supplied by GSC given as:

$k_{Qf} = \left(k_{PQf} + \frac{k_{IQf}}{p} \right)$. Then (5.105) will be:

$$\Gamma pQ_f = \left(k_{PQf} + \frac{k_{IQf}}{p} \right) Q_f^{\ *} - \left(k_{PQf} + \frac{k_{IQf}}{p} \right) Q_f \tag{5.106}$$

$$\frac{Q_f}{Q_f^{\ *}} = \frac{\frac{1}{\Gamma} \left(pk_{PQf} + k_{IQf} \right)}{p^2 + p \frac{k_{PQf}}{\Gamma} + \frac{k_{IQf}}{\Gamma}} \tag{5.107}$$

Comparing denominator of (5.107) with Butterworth second order polynomial, i.e., $p^2 + \sqrt{2}\omega_{0Qf} p + \omega_{0Qf}^2$, PI controller gains are obtained as:

$$k_{PQf} = \sqrt{2}\omega_{0Qf}\Gamma \tag{5.108}$$

$$k_{IQf} = \Gamma\omega_{0Qf}{}^2 \tag{5.109}$$

where ω_{0Qf} is the bandwidth frequency of the reactive power controller. From (5.104):

$$I_{df}^* = \frac{1}{r_f}\left(V_{df} + \omega_e L_f I_{qf} - \sigma_{Qf}\right) \tag{5.110}$$

Equations (5.99) and (5.100) give the inner current control loop for the GSC control.

Inner current control:

If we assume:

$$r_f I_{qf} + L_f pI_{qf} = k_{qf}(I^*{}_{qf} - I_{qf}) = \sigma_{qf} \tag{5.111}$$

$$r_f I_{df} + L_f pI_{df} = k_{df}(I^*{}_{df} - I_{df}) = \sigma_{df} \tag{5.112}$$

Then (5.99) and (5.100) can be written as:

$$M_{qf} = (\sigma_{qf} + \omega_e L_f I_{df} + \frac{V_{qs}}{N})\frac{2}{V_{dc}} \tag{5.113}$$

$$M_{df} = (\sigma_{df} - \omega_e L_f I_{qf})\frac{2}{V_{dc}} \tag{5.114}$$

Equations (5.113) and (5.114) give modulation indexes which are the output of the converter. And k_{qf} and k_{df} are PI current controllers for q and d-axis currents, respectively and $k_{qf} = k_{df} = \left(k_{P1} + \frac{k_{I1}}{p}\right)$. Then, (5.111) can be re-written as:

$$\frac{I_{qf}}{I_{qf}^{*}} = \frac{\frac{1}{L_f}(pk_{P1} + k_{I1})}{p^2 + p\frac{1}{L_f}(r_f + k_{P1}) + \frac{1}{L_f}k_{I1}} \tag{5.115}$$

Comparing denominator of (5.115) with the Butterworth second order polynomial gives:

$$k_{P1} = \sqrt{2}\omega_{0c}L_f - r_f \tag{5.116}$$

$$k_{I1} = L_f \omega_{0c}^{\ 2} \tag{5.117}$$

where ω_{0c} is the bandwidth frequency of the current controller.

5.6.4 Phase Locked Loop (PLL)

A PLL is designed to define the reference angle for qd transformation so that the stator voltage can be aligned along the q-axis and is included in the overall model of the system to make the designed system more realistic. Figure 5.13 shows the 3-phase PLL which takes the input as the measured DFIG terminal voltage V_s and transforms it to qd-reference frame. PLL aligns the stator side voltage to q-axis by comparing d-axis load voltage with zero reference voltage. The voltage error signal is passed through the PI

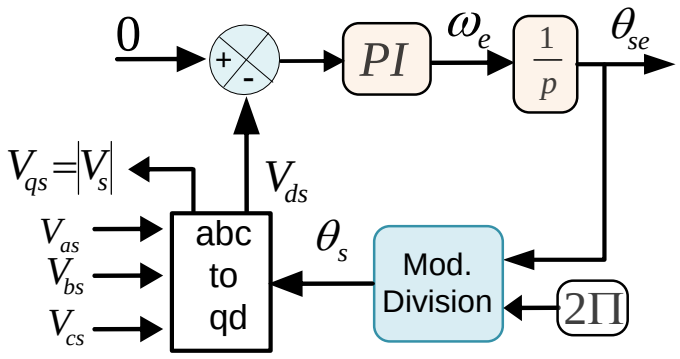

Figure 5.13 Block diagram of PLL control

controller to obtain the angular frequency of the terminal bus voltage. Hence, in the PLL system:

$$V_{ds} = -V_s \sin(\theta_i - \theta_s) \Rightarrow 0 = -V_s \sin(\theta_i - \theta_s) \tag{5.118}$$

$$\Rightarrow \theta_i = \theta_s \tag{5.119}$$

Now the error signal is given as: $e = 0 - V_{ds} = V_s \sin(\theta_i - \theta_s)$

If $(\theta_i - \theta_s)$ is very small, then we can write: $\sin(\theta_i - \theta_s) \approx (\theta_i - \theta_s)$

From the block diagram shown in Figure 5.13, $V_s(\theta_i - \theta_s)$ is the input to the controller and ω_e is the output from the controller hence:

$$V_s(\theta_i - \theta_s)K_{pll} = \omega_e \tag{5.120}$$

$$\frac{1}{V_s} p\theta_s = (\theta_i - \theta_s)K_{pll} = \sigma_\theta \tag{5.121}$$

where, $K_{pll} = k_{P\_pll} + \dfrac{k_{I\_pll}}{p}$

$$\frac{1}{V_s} p\theta_s = \left(k_{P\_pll} + \frac{k_{I\_pll}}{p}\right)\theta_i - \left(k_{P\_pll} + \frac{k_{I\_pll}}{p}\right)\theta_s \tag{5.122}$$

$$\frac{\theta_s}{\theta_i} = \frac{pV_s k_{P\_pll} + V_s k_{I\_pll}}{p^2 + pV_s k_{P\_pll} + V_s k_{I\_pll}} \tag{5.123}$$

Now comparing the denominator of (5.110) with the Butterworth second order polynomial $p^2 + \sqrt{2}\omega_{0\_pll} p + \omega_{0\_pll}^2$, the parameters of the controller are obtained as:

$$k_{P\_pll} = \frac{\sqrt{2}\omega_{0\_pll}}{V_s} \tag{5.124}$$

$$k_{I\_pll} = \frac{\omega_{0\_pll}^2}{V_s} \tag{5.125}$$

where ω_{0_pll} is the bandwidth frequency of the PLL controller.

Table 5.2 gives the PI controllers values used for the simulation study following above procedure. The switching frequency is taken as 1 kHz and the bandwidth of inner current controller is taken ten times that of outer loop controller, i.e.

$\omega_{sw} = 2*\pi* f_{sw} = 6280\ rad/\sec$ and $\omega_{inner} = \frac{\omega_{sw}}{10}$; $\omega_{outer} = \frac{\omega_{inner}}{10}$

$\omega_{inner} = \omega_0 = \omega_{oc} = 628\ rad/\sec$ and

$\omega_{outer} = \omega_{odc} = \omega_{oQs} = \omega_{oQf} = 62.8\ rad/\sec$, $\omega_{owr} = 0.628\ rad/\sec$

From (5.89): $k_{qp} = k_{dp} = \sqrt{2}\omega_0\sigma L_r - r_r = 1.76$ and from (5.90): $k_{qi} = k_{di} = \sigma L_r \omega_0^{\ 2} = 783.6$

From (5.57): $k_{Pwr} = \sqrt{2}\omega_{owr}\frac{2J}{P} = 8.26$ and from (5.58): $k_{Iwr} = \frac{2J}{P}\omega_{owr}^2 = 3.65$

From (5.96): $k_{Pdc} = \sqrt{2}\omega_{odc}C_{dc} = 5.32$ and from (5.97): $k_{Idc} = \omega_{odc}^2 C_{dc} = 236.63$

From (5.116): $k_{P1} = \sqrt{2}\omega_{oc}L_f - r_f = 1.77$ and from (5.117): $k_{I1} = \omega_{oc}^2 L_f = 788.76$

From (5.74): $k_{PQs} = \sqrt{2}\omega_{0Qs}\Delta = 0.00022$ and from (5.75): $= k_{IQs} = \Delta\omega_{Qs}^{\ 2} = 0.001$

Table 5.2 Parameters of the machine and PI controller coefficients

r_s	2.3 mΩ	C_{dc}	60 mF	k_{qp}/k_{dp}	1.76	k_{qi}/k_{di}	783.6
r_r	2 mΩ	L_f	2 mH	k_{Pwr}	8.26	k_{Iwr}	3.65
L_s	2.93 mH	r_f	2 mΩ	k_{Pdc}	5.32	k_{Idc}	236.63
L_r	2.97 mH	J	18.7	k_{P1}	1.77	k_{I1}	788.76
L_m	2.88 mH	P	4	k_{PQs}	0.00022	k_{IQs}	0.001
				k_{PQf}	0.00022	k_{IQf}	0.00093
V_s	563.38 V	N	1	k_{P_pll}	2.10	k_{I_pll}	1244.4

From (5.108): $k_{PQf} = \sqrt{2}\omega_{0Qf}\Gamma = 0.0002$ and from (5.109): $k_{IQf} = \Gamma\omega_{0Qf}^{\ 2} = 0.0093$

In PLL controller design, the switching frequency is taken as 2 kHz and the bandwidth of the PLL controller is taken as: $\omega_{sw} = 2*\pi*f_{sw} = 12{,}560\ rad/s$ and $\omega_0 = \frac{\omega_{sw}}{15} = 837.3\ rad/s$

From (5.124): $k_{P\_pll} = \frac{\sqrt{2}\omega_0}{V_s} = 2.10$ and from (5.125): $k_{I\_pll} = \frac{\omega_0^2}{V_s} = 1244.4$

5.6.5 Stator Flux Estimation

As shown in Figure 5.11, the stator side flux should be estimated as accurately as possible for the RSC control implementation. Therefore this section explains the stator flux estimation using the Low Pass Filter (LPF).

The stator flux in stationary reference frame is given as:

$$V_{qds}^s = r_s I_{qds}^s + p\lambda_{qds}^s \tag{5.126}$$

$$\lambda_{qds}^s = \int \left(V_{qds}^s - r_s I_{qds}^s\right) dt \tag{5.127}$$

Flux can be estimated using (5.127) but the pure integration $(1/s)$ involves the DC offsets and drifts [64]. To solve these problems, the pure integrator is replaced by a LPF. The estimated stator flux by the LPF can be given as:

$$\frac{\hat{\lambda}_{sl}}{V_e} = \frac{1}{p+a} \tag{5.128}$$

where $\hat{\lambda}_{sl}$ is the estimated stator flux by LPF, a = pole and $V_e = V_{qds} - r_s I_{qds}$ the phase lag and the gain of (5.128) can be given as:

$$\phi = -\tan^{-1}\frac{\hat{\omega}_e}{a} \tag{5.129}$$

$$M = \left|\frac{\hat{\lambda}_{sl}}{V_e}\right| = \frac{1}{\sqrt{a^2 + \hat{\omega}_e^2}} \tag{5.130}$$

where $\hat{\omega}_e$ is the estimated synchronous angular frequency given as [64]:

$$\hat{\omega}_e = \frac{(V_{qs} - r_s I_{qs})\lambda_{ds} - (V_{ds} - r_s I_{ds})\lambda_{qs}}{|\lambda_s|^2} \tag{5.131}$$

The LPF eliminates the saturation and reduces the effect of DC offsets but at the same time it brings the magnitude and phase angle error due to the cut off frequency of the LPF. Figure 5.14 shows the phase lag of $\hat{\lambda}_{sl}$ estimated by the LPF, and the phase lag of $\hat{\lambda}_{qds}$ estimated by the pure integrator. The phase lag of $\hat{\lambda}_{qds}$ is 90° and the gain is $1/\left|\hat{\omega}_e\right|$. However, the phase lag of the LPF is not 90° and the gain is not $1/\left|\hat{\omega}_e\right|$. Hence, an error will be produced by this effect of the LPF. When the machine frequency is lower than the cutoff frequency of the LPF, the error is more severe. In order to remove this

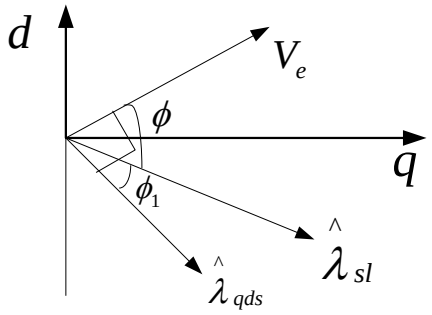

Figure 5.14 Vector diagram of the LPF and the pure integrator [64]

error, the LPF in (5.128) should have a very low cutting frequency. However, there still remains the drift problem due to the very large time constant of the LPF. For the exact estimation of the stator flux, the phase lag and the gain of $\hat{\lambda}_{sl}$ in (5.128) have to be 90° and $1/\left|\hat{\omega}_e\right|$, respectively. Furthurmore, to solve the drift problem, the pole should be located far from the origin.

Hence, the decrement in the gain of the LPF is compensated by multiplying a gain compensator, G in (5.132) and the phase lag is compensated by multiplying a phase compensator, P in (5.133) given as:

$$G = \frac{\sqrt{a^2 + \hat{\omega}_e^2}}{\left|\hat{\omega}_e\right|} \tag{5.132}$$

$$P = \exp(-j\phi_1) \tag{5.133}$$

$$\phi_1 = \tan^{-1}\frac{\hat{\omega}_e}{a} - \frac{\pi}{2} \tag{5.134}$$

$$\frac{\hat{\lambda}_{qds}}{V_e} = \frac{1}{p+a}\frac{\sqrt{a^2 + \hat{\omega}_e^2}}{\left|\hat{\omega}_e\right|}\exp(-j\phi_1) \tag{5.135}$$

The cutoff frequency in LPF cannot be located at fixed point far from the origin. If the pole is varied proportionally to the machine speed, the proportion of the machine frequency to the cutoff frequency of the LPF is constant. If the proportion is large, the estimation error will be very small. Consequently, the pole is determined to be varied proportionally to the motor speed as (5.136). Therefore, the pole is located close to the origin in very low speed range and far from the origin in high speed range.

$$a = \frac{\left|\hat{\omega}_e\right|}{K} \tag{5.136}$$

where K = constant. Finally, the complete equation for stator flux estimator can be derived as:

$$\frac{\hat{\lambda}_{qds}}{V_e} = \frac{1}{p + (\hat{\omega}_e / K)} \frac{\sqrt{(\hat{\omega}_e / K)^2 + \hat{\omega}_e^2}}{\left|\hat{\omega}_e\right|} \exp(-j\phi_1) \tag{5.137}$$

where $\exp(-j\phi_1) = \cos(\phi_1) - j\sin(\phi_1)$, $\cos(\phi_1) = \dfrac{\left|\hat{\omega}_e\right|}{\sqrt{(\hat{\omega}_e / K)^2 + \hat{\omega}_e^2}}$ and $\sin(\phi_1) = \dfrac{\hat{\omega}_e / K}{\sqrt{(\hat{\omega}_e / K)^2 + \hat{\omega}_e^2}}$

Simplifying (5.137) and separating into real and imaginary parts gives:

$$\hat{\lambda}_{qs} = \frac{1}{p + (\hat{\omega}_e / K)} \frac{\sqrt{(\hat{\omega}_e / K)^2 + \hat{\omega}_e^2}}{\left|\hat{\omega}_e\right|} \left\{\cos\phi_1 (V_{qs} - r_s I_{qs}) + \sin\phi_1 (V_{ds} - r_s I_{ds})\right\} \tag{5.138}$$

$$\hat{\lambda}_{ds} = \frac{1}{p + (\hat{\omega}_e / K)} \frac{\sqrt{(\hat{\omega}_e / K)^2 + \hat{\omega}_e^2}}{\left|\hat{\omega}_e\right|} \left\{\cos\phi_1 (V_{ds} - r_s I_{ds}) - \sin\phi_1 (V_{qs} - r_s I_{qs})\right\} \tag{5.139}$$

Figure 5.15 shows the overall block diagram of the system to estimate stator side flux using LPF and estimated synchronous speed of the machine. Figure 5.16 depicts the schematic diagram of the DFIG wind turbine and STATCOM control structure. Similarly, Figure 5.17 shows the q-axis and d-axis stator flux estimated by stator flux estimator and estimated synchronous speed of the machine. At t = 3 sec., a step change in rotor speed from 392 rad/s to 400 rad/s is applied as a result there is some oscillation in estimated values of flux and speed but finally it gets settled. The estimated flux is very close to the one obtained from pure integration using K = 0.001.

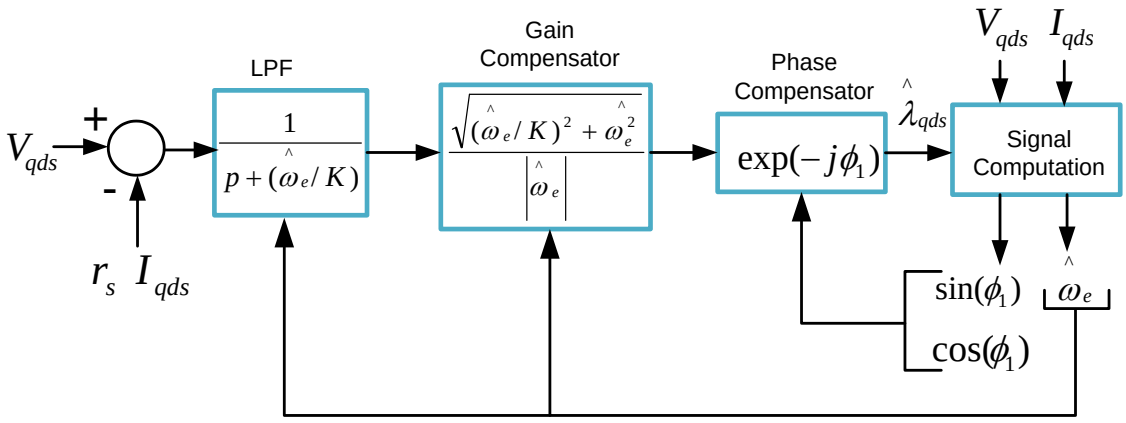

Figure 5.15 Overall block diagram of the stator flux estimation using LPF [64]

Figure 5.18 shows the plot of reference angle given by PLL to align the stator voltage along the q-axis. Figure 5.19 depicts the angular synchronous frequency of the system measured by the PLL and estimated by the stator flux estimator.

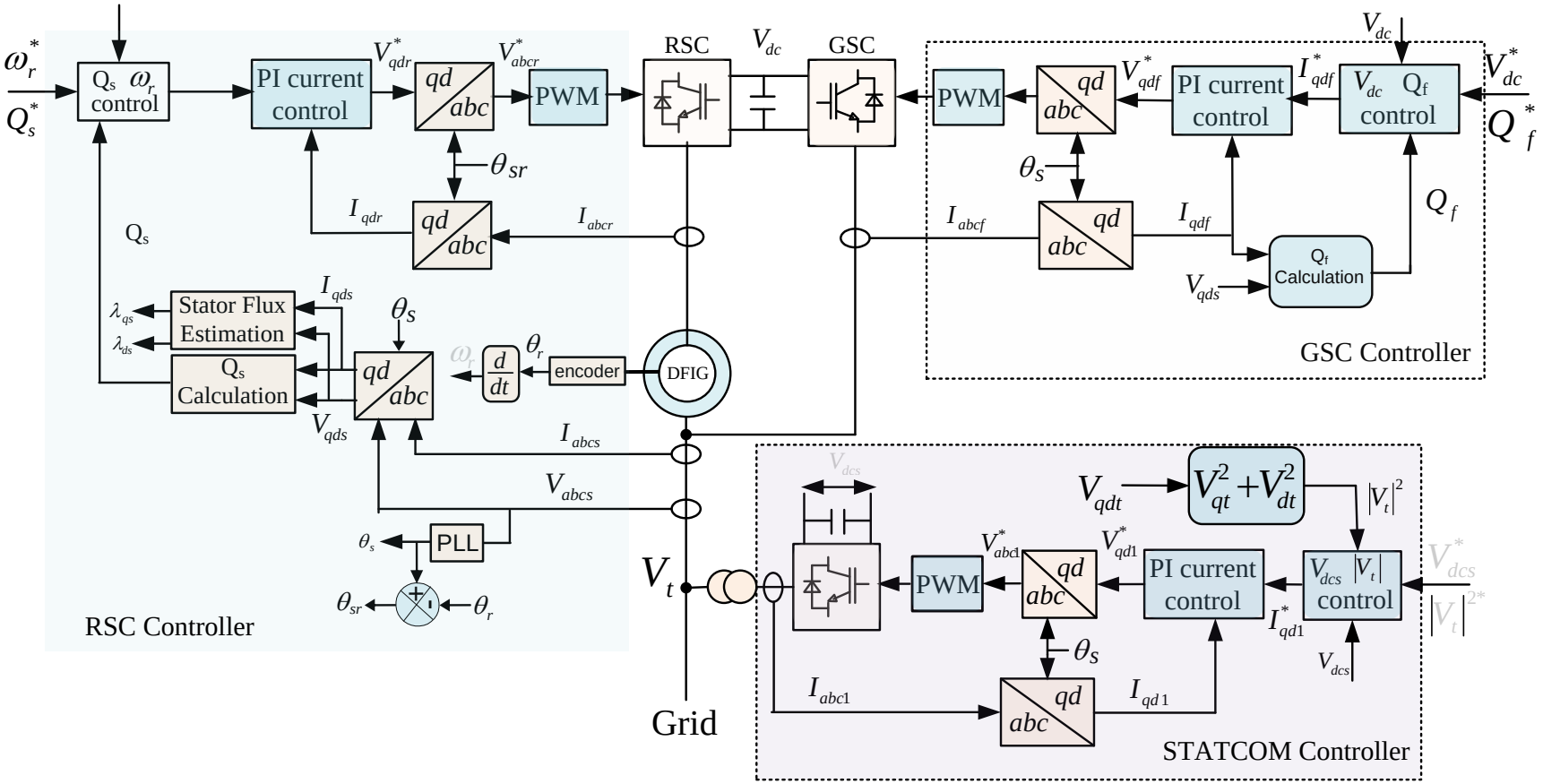

Figure 5.16 Schematic diagram of the DFIG wind turbine and STATCOM control strucure

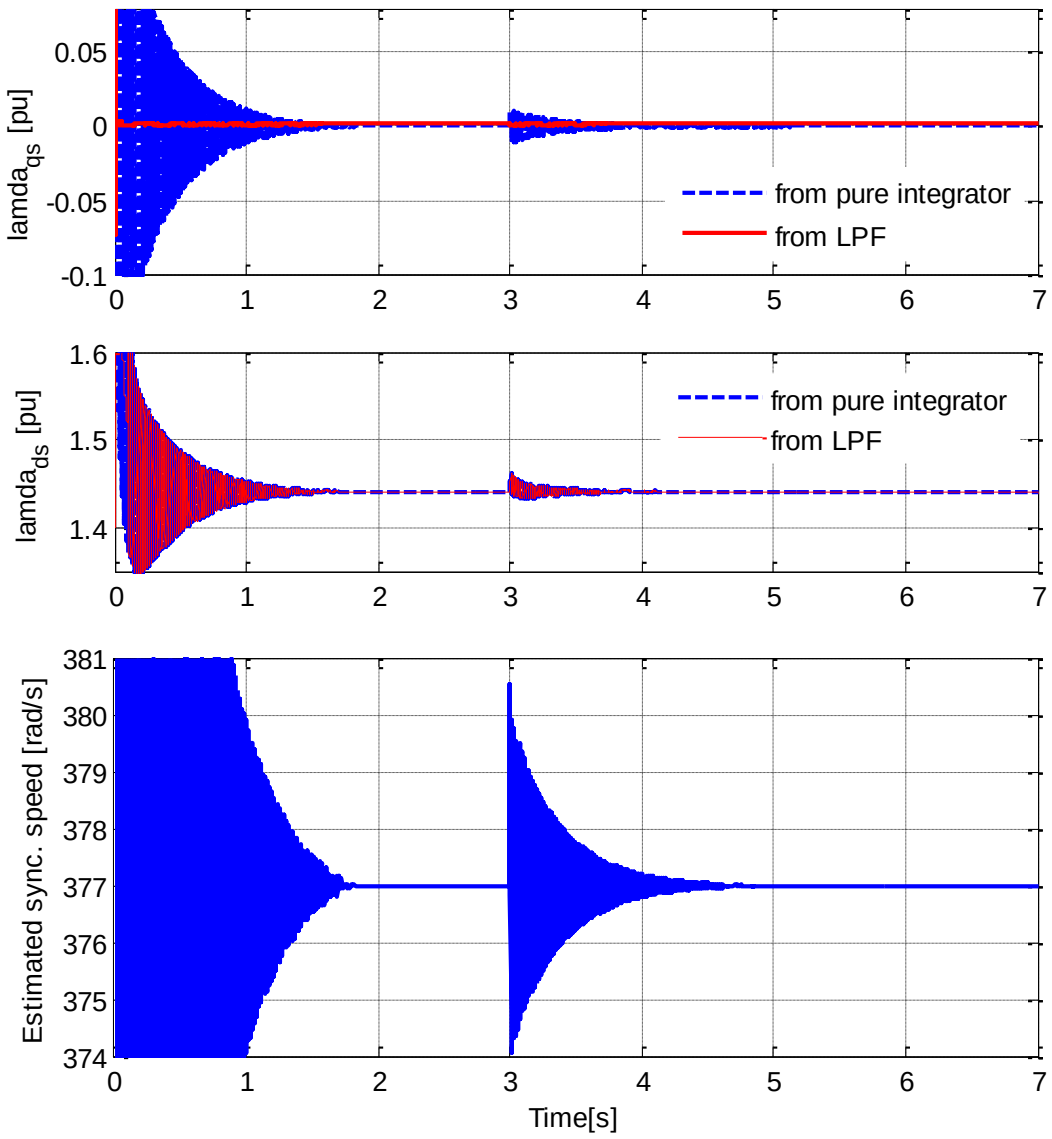

Figure 5.17 Flux and synchronous speed estimation using LPF

Now with all those above described models of the STATCOM, DFIG, loads and their controls are implemented in MATLAB/Simulink software. Voltage swelling and

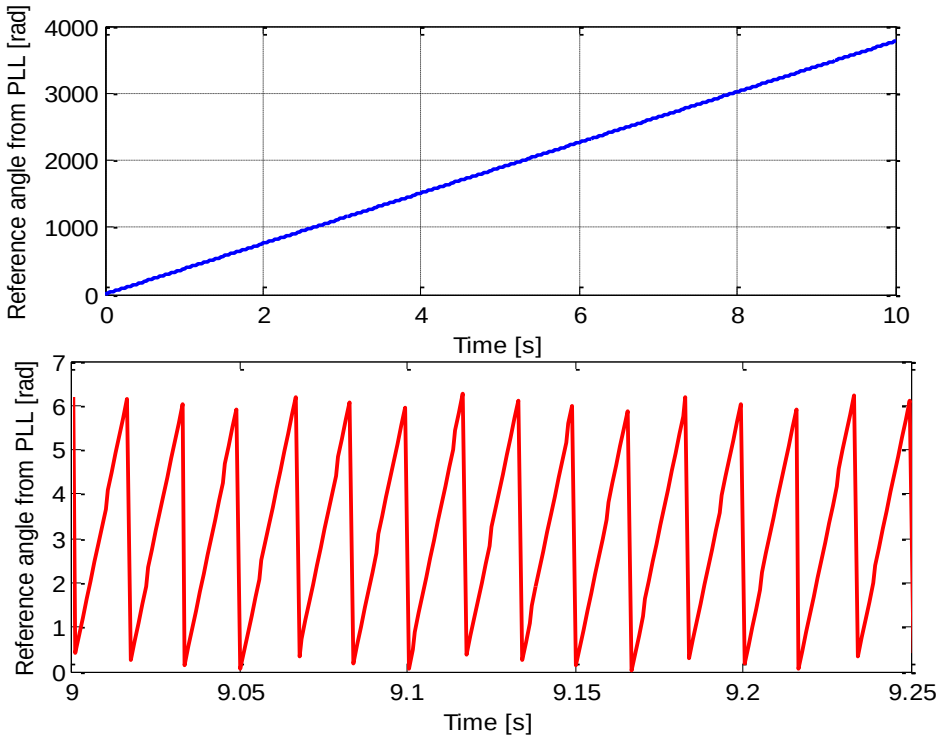

Figure 5.18 Reference angle output from PLL, θ_{se} (top) and θ_s (bottom)

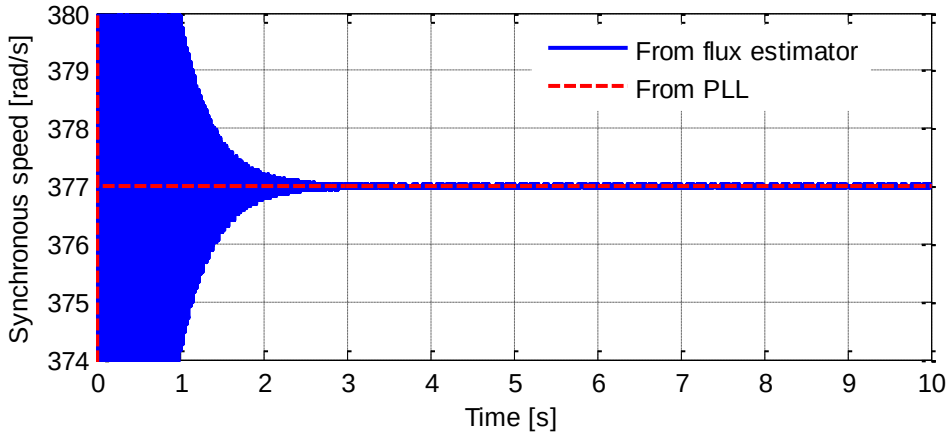

Figure 5.19 The angular synchronous frequency of the DFIG system measured by PLL and the stator flux estimator

voltage sagging study is performed to assesss the effectiveness of the implemented control system which is described in the below.

5.6.6 Voltage Swelling Study

Voltage swelling is the brief increases in voltage over the time range from milliseconds to few seconds. Among the grid disturbances, the voltage swell is a critical event that can be caused by abrupt switching off large loads or switching on capacitive load or damaged/loose neutral connection in the power system. Here the symmetrical voltage swelling of 22 % is created by step increase in capacitive constant load (-ve Q) at t = 5 sec. for 1 sec. duration. All the other loads remain same. In the absence of the STATCOM, when the capacitive load is increased instantly, the weak grid cannot respond quickly by absorbing additional reactive power and the DFIG output power is already regulated to its optimum value so voltage at the PCC increases as shown in Figure 5.20 (a). With the STATCOM connected at the PCC, same voltage swelling is created again but this time STATCOM responds quickly by absorbing additional reactive power; as a result, the voltage at the PCC is regulated close to 1 pu with small overshoot shown in Figure 5.20 (a) and Figure 5.20 (b). Figure 5.21 shows the modulation indexes of the STATCOM converter, RSC and GSC. Since the DFIG is operated at rated power with GSC supplying reactive power upto its rated capacity, the modulation index magnitude M_{xf} is close to 1. This also proves that GSC is operating at close to its maximum capacity.

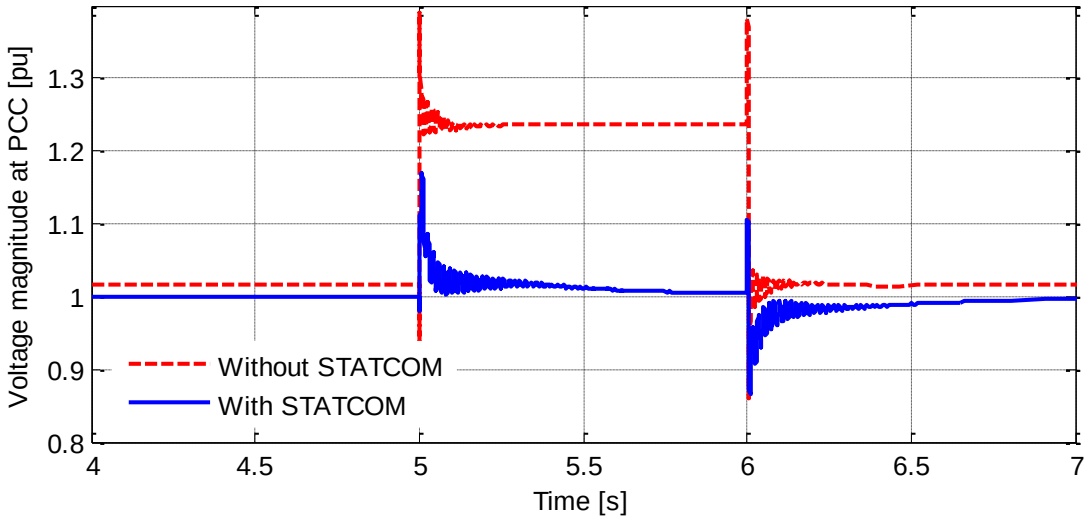

(a)

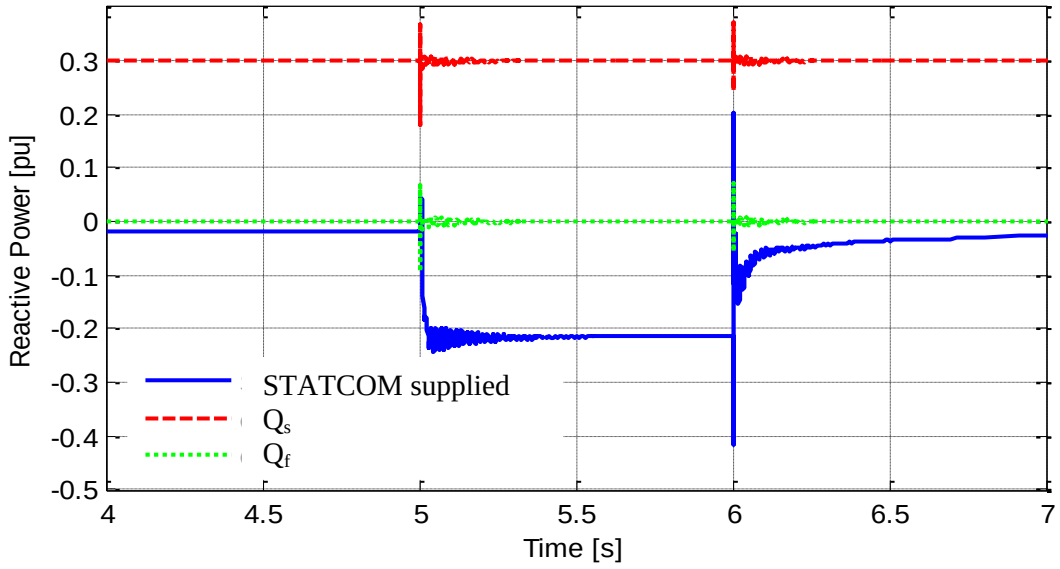

(b)

Figure 5.20 Simulation results of the PCC voltage at the DFIG wind turbine with and without STATCOM during 22 % symmetrical voltage swell: (a) PCC voltage magnitude, (b) Reactive power supplied by STATCOM, GSC, and RSC

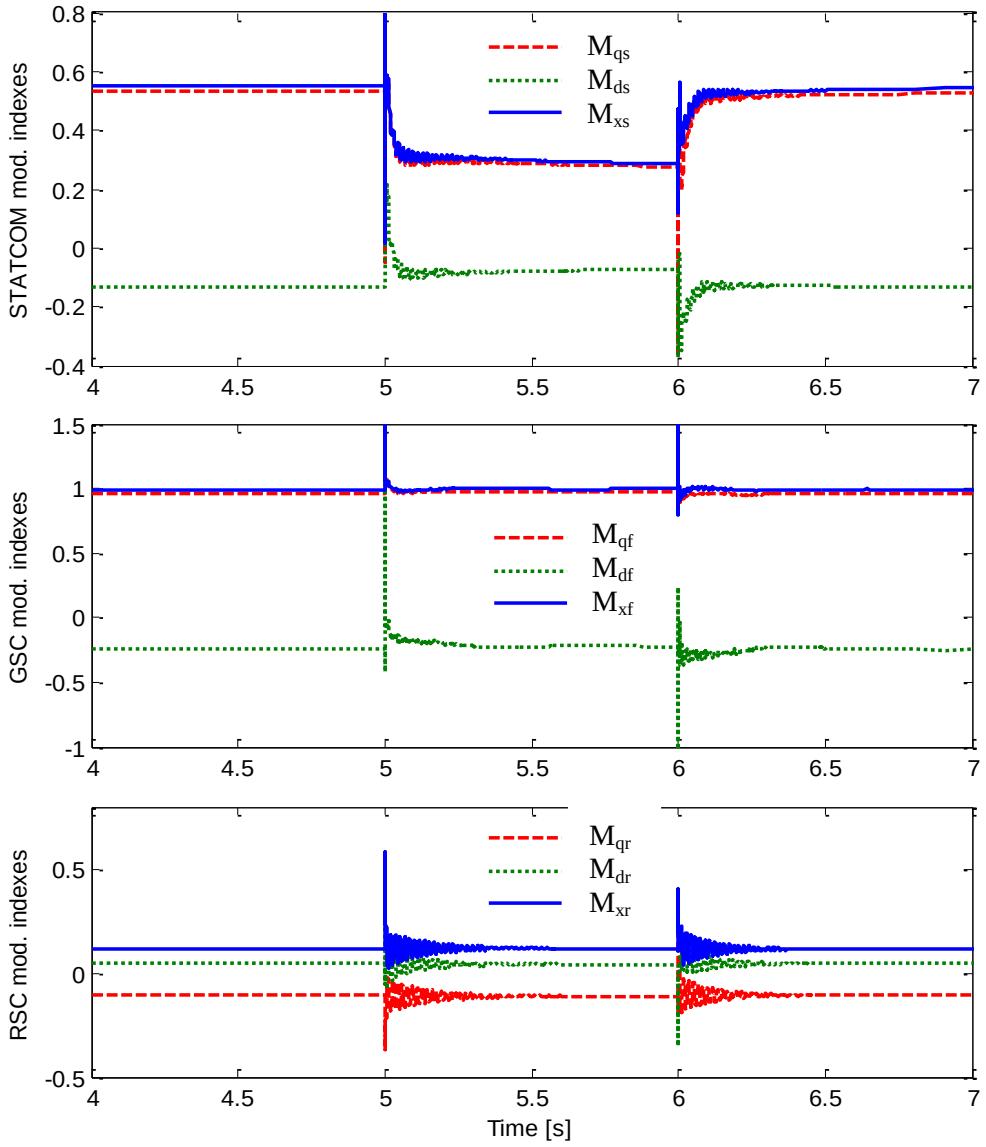

Figure 5.21 STATCOM converter, GSC and RSC modulation indexes during symmetrical voltage swelling by 22%

5.6.7 Voltage Sagging Study

Voltage sagging is the momentary reduction in voltage over the time range from milliseconds to few seconds. The voltage sagging is the most common type of grid disturbance which is caused by abrupt switching on large inductive loads like electrical

heater, motor starting or abrupt increase in source impedance typically caused by loose connection. In this study, the symmetrical voltage sagging of 18 % is created by step increase in inductive constant load (+ve Q) at t = 5 sec. for 1 sec. duration. All the other loads remain constant. In the absence of the STATCOM, when the inductive load is increased instantly, the weak grid cannot respond quickly by supplying required surplus reactive power and the DFIG output power is already regulated to its optimum value. As a result, the voltage at the PCC drops as shown in Figure 5.22 (a). When the STATCOM

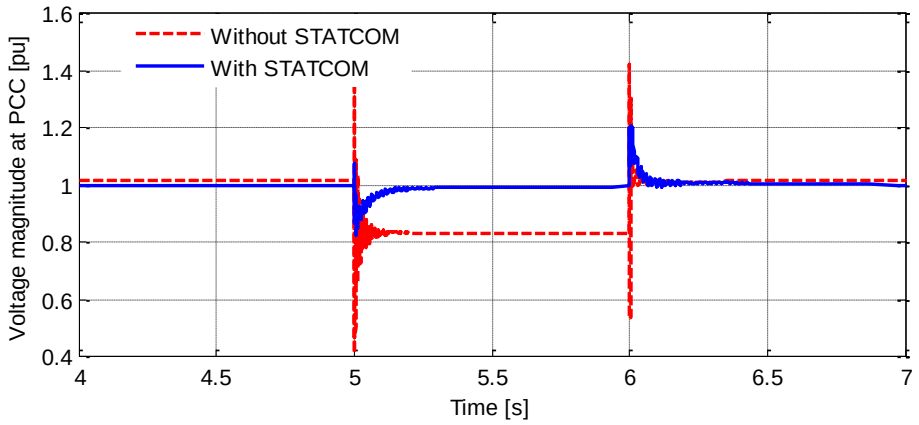

(a)

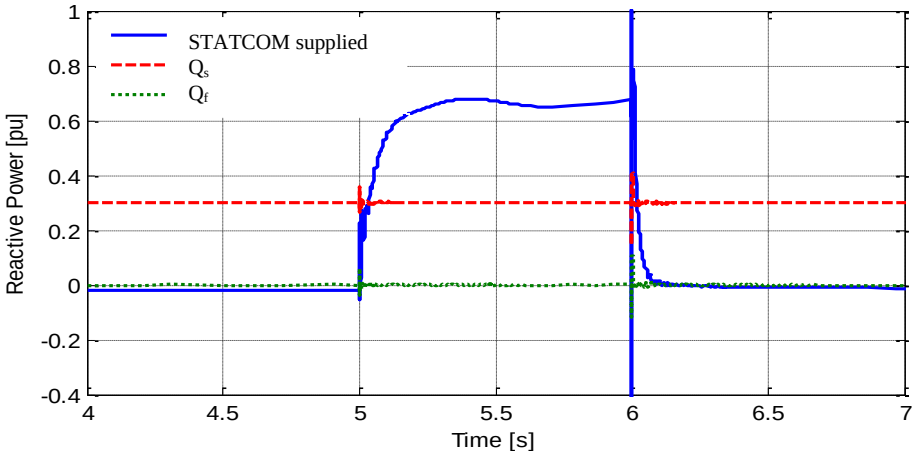

(b)

Figure 5.22 Simulation results of the PCC voltage at the DFIG wind turbine with and without STATCOM during 18 % symmetrical voltage sag: (a) PCC voltage magnitude, (b) Reactive power supplied by STATCOM, GSC, and RSC

is connected at the PCC and the same voltage sagging is created; in that case, STATCOM responds quickly by supplying additional reactive power. As a result, the voltage at the PCC is regulated closely to 1 p.u. with small overshoot shown in Figure 5.22 (b). Figure 5.23 shows the modulation indexes of the STATCOM converter, RSC and GSC. Since the DFIG is operated at rated power with GSC supplying reactive power upto its rated capacity, the modulation index magnitude M_{xf} is close to 1. This also proves that GSC is operating at its maximum capacity.

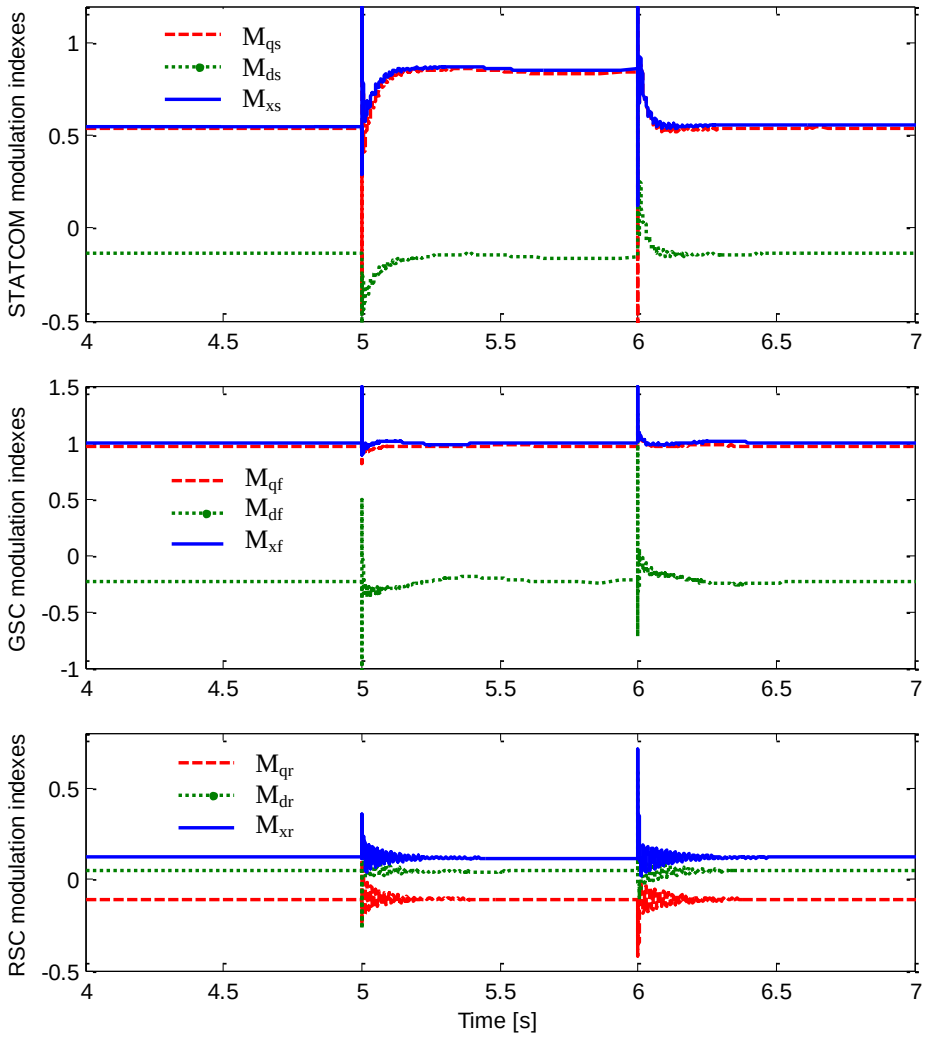

Figure 5.23 STATCOM converter, GSC, and RSC modulation indexes during symmetrical voltage sagging by 18%

5.7 Transfer Functions of STATCOM, RSC and GSC Controllers

In the above mentioned controller design for STATCOM, RSC and GSC, each controllers are designed separately and finally combined together. This procedure is only valid when the controlled variables are independent of each other i.e. they should be mutually decoupled. To check whether they are independent of each other or not, the transfer functions of the STATCOM, RSC and GSC are derived in this section.

In the STATCOM control, from (5.19):

$$\sigma_{vm} = k_{vm}(V_m^{2*} - V_m^2) = V_{q2}\left(I_{q1}^* - I_{q2}\right) + V_{d2}\left(I_{d1} - I_{d2}\right) \tag{5.140}$$

Similarly, from (5.12):

$$\sigma_{dcs} = k_{dcs}(V_{dcs}^* - V_{dcs}) = (M_{q1}I_{q1} + M_{d1}I_{d1}^*) \tag{5.141}$$

Solving (5.140) and (5.141) gives:

$$\begin{bmatrix} I_{q1}^* \\ I_{d1}^* \end{bmatrix} = \underbrace{\begin{bmatrix} \dfrac{1}{\tau V_{q2}} & -\dfrac{V_{d2}}{\tau M_{d1} V_{q2}} \\ -\dfrac{M_{q1}}{\tau V_{q2} M_{d1}} & \dfrac{\tau M_{d1} V_{q2} + M_{q1} V_{d2}}{\tau V_{q2} M_{d1}^2} \end{bmatrix}}_{L} \begin{bmatrix} \sigma_{vm} \\ \sigma_{dcs} \end{bmatrix} + \underbrace{\begin{bmatrix} \dfrac{V_{d2}}{\tau V_{q2}} I_{d2} + \dfrac{1}{\tau} I_{q2} \\ -\dfrac{M_{q1} V_{d2}}{\tau V_{q2} M_{d1}} I_{d2} - \dfrac{M_{q1}}{\tau M_{d1}} I_{q2} \end{bmatrix}}_{M} \tag{5.142}$$

where $\tau = \dfrac{M_{d1}V_{q2} + M_{q1}V_{d2}}{V_{q2}M_{d1}}$.

From (5.19)

$$\frac{C_m}{2} pV_m^2 = V_{q2}\left(I_{q1} - I_{q2}\right) + V_{d2}\left(I_{d1} - I_{d2}\right) \tag{5.143}$$

From (5.12)

$$-\frac{4}{3} C_{dc} pV_{dcs} = (M_{q1}I_{q1} + M_{d1}I_{d1}) \tag{5.144}$$

Solving (5.143) and (5.144) gives:

$$\begin{bmatrix} I_{q1} \\ I_{d1} \end{bmatrix} = \underbrace{\begin{bmatrix} \dfrac{pC_m}{2\tau V_{q2}} & \dfrac{4pC_{dc}V_{d2}}{3\tau M_{d1}V_{q2}} \\ -\dfrac{pC_m M_{q1}}{2\tau V_{q2}M_{d1}} & -\dfrac{4pC_{dc}}{3}\dfrac{\tau M_{d1}V_{q2}+M_{q1}V_{d2}}{\tau V_{q2}M_{d1}^2} \end{bmatrix}}_{N} \begin{bmatrix} V_m^2 \\ V_{dcs} \end{bmatrix} + \underbrace{\begin{bmatrix} \dfrac{V_{d2}}{\tau V_{q2}} I_{d2} + \dfrac{1}{\tau} I_{q2} \\ -\dfrac{M_{q1}V_{d2}}{\tau V_{q2}M_{d1}} I_{d2} - \dfrac{M_{q1}}{\tau M_{d1}} I_{q2} \end{bmatrix}}_{M} \tag{5.145}$$

From (5.24):

$$\left(\hat{r}_s + p\hat{L}_s\right) I_{q1} = k_{1q} I_{q1}^{\ *} - k_{1q} I_{q1} \tag{5.146}$$

From (5.25):

$$\left(\hat{r}_s + p\hat{L}_s\right) I_{d1} = k_{1d} I_{d1}^{\ *} - k_{1d} I_{d1} \tag{5.147}$$

where ($\hat{}$) shows the measured value. Combining (5.146) and (5.147):

$$\begin{bmatrix} I_{q1}^{\ *} \\ I_{d1}^{\ *} \end{bmatrix} = \underbrace{\begin{bmatrix} \dfrac{\hat{r}_s + p\hat{L}_s + k_{1q}}{k_{1q}} & 0 \\ 0 & \dfrac{\hat{r}_s + p\hat{L}_s + k_{1d}}{k_{1d}} \end{bmatrix}}_{P} \begin{bmatrix} I_{q1} \\ I_{d1} \end{bmatrix} \tag{5.148}$$

From (5.142), (5.145) and (5.148) gives:

$$L \begin{bmatrix} \sigma_{vm} \\ \sigma_{dcs} \end{bmatrix} + M = PN \begin{bmatrix} V_m^2 \\ V_{dcs} \end{bmatrix} + PM$$

$$\begin{bmatrix} \dfrac{1}{\tau V_{q2}} & -\dfrac{V_{d2}}{\tau M_{d1}V_{q2}} \\ -\dfrac{M_{q1}}{\tau V_{q2}M_{d1}} & \dfrac{\tau M_{d1}V_{q2}+M_{q1}V_{d2}}{\tau V_{q2}M_{d1}^2} \end{bmatrix} \begin{bmatrix} \sigma_{vm} \\ \sigma_{dcs} \end{bmatrix} + \begin{bmatrix} \dfrac{V_{d2}}{\tau V_{q2}} I_{d2} + \dfrac{1}{\tau} I_{q2} \\ -\dfrac{M_{q1}V_{d2}}{\tau V_{q2}M_{d1}} I_{d2} - \dfrac{M_{q1}}{\tau M_{d1}} I_{q2} \end{bmatrix} =$$

$$\gamma \begin{bmatrix} \dfrac{pC_m}{2\tau V_{q2}} & \dfrac{4pC_{dc}V_{d2}}{3\tau M_{d1}V_{q2}} \\ -\dfrac{pC_m M_{q1}}{2\tau V_{q2}M_{d1}} & -\dfrac{4pC_{dc}}{3}\dfrac{\tau M_{d1}V_{q2}+M_{q1}V_{d2}}{\tau V_{q2}M_{d1}^2} \end{bmatrix} \begin{bmatrix} V_m^2 \\ V_{dcs} \end{bmatrix} + \gamma \begin{bmatrix} \dfrac{V_{d2}}{\tau V_{q2}} I_{d2} + \dfrac{1}{\tau} I_{q2} \\ -\dfrac{M_{q1}V_{d2}}{\tau V_{q2}M_{d1}} I_{d2} - \dfrac{M_{q1}}{\tau M_{d1}} I_{q2} \end{bmatrix} \tag{5.149}$$

where, $\hat{\gamma} = \dfrac{\hat{r}_s + p\hat{L}_s + k_{1d}}{k_{1d}} = \dfrac{\hat{r}_s + p\hat{L}_s + k_{1q}}{k_{1q}}$

Solving (5.149) gives:

$$V_m^2 = \hat{\zeta}\ k_{vm}V_m^{2*} + \hat{\zeta}(1-\hat{\gamma})V_{d2}I_{d2} + \hat{\zeta}(1-\hat{\gamma})I_{q2} \tag{5.150}$$

where $\hat{\zeta} = \dfrac{1}{\tau V_{q2}\left\{\hat{\gamma}\dfrac{pC_m}{2} + k_{vm}\right\}}$.

$$V_{dcs} = \frac{k_{dcs}}{\hat{\delta}}V_{dcs}^* \tag{5.151}$$

where $\hat{\delta} = k_{dcs} - \dfrac{4}{3}pC_{dc}\hat{\gamma}$.

If the actual and measured parameters are same then:

Solving (5.149) gives:

$$V_m^2 = \zeta\ k_{vm}V_m^{2*} + \zeta(1-\gamma)V_{d2}I_{d2} + \zeta(1-\gamma)I_{q2} \tag{5.150(a)}$$

where, $\zeta = \dfrac{1}{\tau V_{q2}\left\{\gamma\dfrac{pC_m}{2} + k_{vm}\right\}}$ and

$$\gamma = \frac{r_s + pL_s + k_{1d}}{k_{1d}} = \frac{r_s + pL_s + k_{1q}}{k_{1q}}$$

$$V_{dcs} = \frac{k_{dcs}}{\delta}V_{dcs}^* \tag{5.151(a)}$$

where $\delta = k_{dcs} - \dfrac{4}{3}pC_{dc}\gamma$.

In the DFIG, from the flux control:

$$\begin{cases} \sigma_{\lambda qs} = -\omega_e \lambda_{ds} + \dfrac{r_s L_m}{\sigma L_s L_r} \lambda_{qr} + V_{qs} \\ \sigma_{\lambda qs} = -\omega_e \lambda_{ds} + \dfrac{r_s L_m}{\sigma L_s L_r} (\sigma L_r I_{qr} + \dfrac{L_m}{L_s} \lambda_{qs}) + V_{qs} \\ \sigma_{\lambda qs} = -\omega_e \lambda_{ds} + \dfrac{r_s L_m}{L_s} I_{qr} + \dfrac{r_s L_m^2}{\sigma L_s^2 L_r} \lambda_{qs} + V_{qs} \\ K_{\lambda s}(\lambda_{qs}^* - \lambda_{qs}) = -\omega_e \lambda_{ds} + r_s \left(\dfrac{p8J\omega_r - 4PT_m}{3P^2 \lambda_{ds}} \right) + \dfrac{r_s L_m^2}{\sigma L_s^2 L_r} \lambda_{qs} + V_{qs} \end{cases} \tag{5.152}$$

$$\lambda_{qs} = \frac{\sigma L_s^2 L_r (3P^2 K_{\lambda s} \lambda_{qs}^* + 3P^2 \lambda_{ds} - 3P^2 V_{qs})}{3 r_s L_m^2 P^2 + 3P^2 \sigma L_s^2 L_r K_{\lambda s}} - \frac{\sigma L_s^2 L_r r_s (p8J\omega_r - 4PT_m)}{\lambda_{ds}(3 r_s L_m^2 P^2 + 3P^2 \sigma L_s^2 L_r K_{\lambda s})} \tag{5.153}$$

Similarly,

$$\begin{cases} \sigma_{\lambda ds} = \omega_e \lambda_{qs} + \dfrac{r_s L_m}{\sigma L_s L_r} \lambda_{dr} + V_{ds} \\ \sigma_{\lambda ds} = \omega_e \lambda_{qs} + \dfrac{r_s L_m}{\sigma L_s L_r} (\dfrac{L_m}{L_s} \lambda_{ds} + L_r \sigma I_{dr}) + V_{ds} \\ \sigma_{\lambda ds} = \omega_e \lambda_{qs} + \dfrac{r_s L_m^2}{\sigma L_s^2} \lambda_{ds} + \dfrac{r_s L_m}{L_s} I_{dr} + V_{ds} \\ K_{\lambda s}(\lambda_{ds}^* - \lambda_{ds}) = \omega_e \lambda_{qs} + \dfrac{r_s L_m^2}{\sigma L_s^2} \lambda_{ds} - \dfrac{2r_s}{3} \dfrac{Q_s}{\omega_e \lambda_{ds}} + V_{ds} \end{cases} \tag{5.154}$$

$$\lambda_{ds} = \frac{K_{\lambda s} \lambda_{ds}^* - \omega_e \lambda_{qs} + \dfrac{2r_s}{3} \dfrac{Q_s}{\omega_e \lambda_{ds}} - V_{ds}}{\left(K_{\lambda s} + \dfrac{r_s L_m^2}{\sigma L_s^2} \right)} \tag{5.155}$$

From (5.153) and (5.155), it is clear that the relations between control variable ($\lambda_{ds}, \lambda_{qs}$) and reference variable (λ_{ds}^*, λ_{qs}^*) are non-linear. Hence, transfer function cannot be obtained. Therefore, in the later part of the transfer function derivation, the stator fluxes are assumed constant as a result the relationship between control variables and reference variable is linear.

In the RSC, from (5.54):

$$\sigma_{wr} = k_{wr}(\omega_r^* - \omega_r) = (T_m - T_e) \tag{5.156}$$

$$\sigma_{wr} = T_m + \frac{3P}{4}\frac{\hat{L}_m}{\hat{L}_s}\lambda_{ds} I^*_{qr} \tag{5.157}$$

$$I^*_{qr} = (\sigma_{wr} - T_m)\frac{4\hat{L}_s}{3P\hat{L}_m\lambda_{ds}} \tag{5.158}$$

where ($\hat{}$) shows the measured value. Similarly, from (5.71):

$$\sigma_{Qs} = k_{Qs}(Q_s^* - Q_s)_s = \lambda_{ds}\left(V_{dr} - \hat{r}_r I_{dr} + \hat{\omega}_{so}\hat{\sigma}\hat{L}_r I_{qr}\right) \tag{5.159}$$

$$\sigma_{Qs} = \lambda_{ds}\left(\hat{r}_r I_{dr} + p\hat{\sigma}\hat{L}_r I_{dr} - \hat{\omega}_{so}\hat{\sigma}\hat{L}_r I_{qr} - \hat{r}_r I_{dr} + \hat{\omega}_{so}\hat{\sigma}\hat{L}_r I_{qr}\right) \tag{5.160}$$

$$I_{dr}^* = \frac{\sigma_{Qs}}{p\hat{\sigma}\hat{L}_r\lambda_{ds}} \tag{5.161}$$

From (5.158) and (5.161):

$$\begin{bmatrix} I_{qr}^* \\ I_{dr}^* \end{bmatrix} = \underbrace{\begin{bmatrix} \frac{4\hat{L}_s}{3P\hat{L}_m\lambda_{ds}} & 0 \\ 0 & \frac{1}{p\hat{\lambda}_{ds}\hat{\sigma}\hat{L}_r} \end{bmatrix}}_{C}\begin{bmatrix} \sigma_{wr} \\ \sigma_{Qs} \end{bmatrix} + \underbrace{\begin{bmatrix} -\frac{4\hat{L}_s T_m}{3P\hat{L}_m\lambda_{ds}} \\ 0 \end{bmatrix}}_{D} \tag{5.162}$$

Here, the mechanical torque from the wind turbine is considered as a disturbance to the

Similarly, from (5.51):

$$p\omega_r = \frac{P}{2J}(T_m - T_e) \tag{5.163}$$

$$p\omega_r = \frac{P}{2J}(T_m + \frac{3P}{4}\frac{L_m}{L_s}\lambda_{ds} I_{qr}) \tag{5.164}$$

$$I_{qr} = \frac{p8J}{3P^2}\frac{L_s\omega_r}{L_m\lambda_{ds}} - \frac{4T_mL_s}{3PL_m\lambda_{ds}} \tag{5.165}$$

From (5.70):

$$pQ_s = -\frac{3}{2}\frac{\omega_e}{\sigma L_s}\frac{L_m}{L_r}\lambda_{ds}\left(V_{dr} - r_rI_{dr} + \omega_{so}\sigma L_rI_{qr}\right) \tag{5.166}$$

$$pQ_s = -\frac{3}{2}\frac{\omega_e}{\sigma L_s}\frac{L_m}{L_r}\lambda_{ds}\left(r_rI_{dr} + p\sigma L_rI_{dr} - \omega_{so}\sigma L_rI_{qr} - r_rI_{dr} + \omega_{so}\sigma L_rI_{qr}\right) \tag{5.167}$$

$$I_{dr} = -\frac{2Q_sL_s}{3\omega_eL_m\lambda_{ds}} \tag{5.168}$$

Combining (5.165) and (5.168) gives:

$$\begin{bmatrix} I_{qr} \\ I_{dr} \end{bmatrix} = \underbrace{\begin{bmatrix} \frac{p8JL_s}{3PL_m\lambda_{ds}} & 0 \\ 0 & -\frac{2L_s}{3\omega_eL_m\lambda_{ds}} \end{bmatrix}}_{E}\begin{bmatrix} \omega_r \\ Q_s \end{bmatrix} + \underbrace{\begin{bmatrix} -\frac{4L_sT_m}{3PL_m\lambda_{ds}} \\ 0 \end{bmatrix}}_{D} \tag{5.169}$$

From (5.87):

$$\left(\hat{r}_r + p\hat{\sigma}\hat{L}_r\right)I_{qr} = k_{iqr}{I_{qr}}^* - k_{iqr}I_{qr} \tag{5.170}$$

From (5.88):

$$\left(\hat{r}_r + p\hat{\sigma}\hat{L}_r\right)I_{dr} = k_{idr}{I_{dr}}^* - k_{idr}I_{dr} \tag{5.171}$$

Combining (5.170) and (5.171):

$$\begin{bmatrix} {I_{qr}}^* \\ {I_{dr}}^* \end{bmatrix} = \underbrace{\begin{bmatrix} \frac{\hat{r}_r + p\hat{\sigma}\hat{L}_r + k_{iqr}}{k_{iqr}} & 0 \\ 0 & \frac{\hat{r}_r + p\hat{\sigma}\hat{L}_r + k_{idr}}{k_{idr}} \end{bmatrix}}_{K}\begin{bmatrix} I_{qr} \\ I_{dr} \end{bmatrix} \tag{5.172}$$

Substituting (5.162) and (5.169) in (5.172) gives:

$$C\begin{bmatrix}\sigma_{wr}\\ \sigma_{Qs}\end{bmatrix}+D=KE\begin{bmatrix}\omega_r\\ Q_s\end{bmatrix}+KD \tag{5.173}$$

$$\begin{bmatrix}\dfrac{4\hat{L}_s}{3P\hat{L}_m\lambda_{ds}} & 0\\ 0 & \dfrac{1}{p\lambda_{ds}\hat{\sigma}\hat{L}_r}\end{bmatrix}\begin{bmatrix}k_{wr}(\omega_r^*-\omega_r)\\ k_{Qs}(Q_s^*-Q_s)\end{bmatrix}+\begin{bmatrix}-\dfrac{4\hat{L}_s T_m}{3P\hat{L}_m\lambda_{ds}}\\ 0\end{bmatrix}$$
$$=\begin{bmatrix}\dfrac{\hat{r}_r+p\hat{\sigma}\hat{L}_r+k_{iqr}}{k_{iqr}}\dfrac{p8JL_s}{3PL_m\lambda_{ds}} & 0\\ 0 & -\dfrac{\hat{r}_r+p\hat{\sigma}\hat{L}_r+k_{idr}}{k_{idr}}\dfrac{2L_s}{3\omega_e L_m\lambda_{ds}}\end{bmatrix}\begin{bmatrix}\omega_r\\ Q_s\end{bmatrix}+\begin{bmatrix}-\dfrac{\hat{r}_r+p\hat{\sigma}\hat{L}_r+k_{iqr}}{k_{iqr}}\dfrac{4L_s T_m}{3PL_m\lambda_{ds}}\\ 0\end{bmatrix} \tag{5.174}$$

Solving (5.174) gives:

$$\omega_r=\frac{\hat{k}_2}{\hat{k}_1}\omega_r^*+\frac{\hat{k}_3}{\hat{k}_1}T_m \tag{5.175}$$

where $\hat{k}_1=\dfrac{2pJL_s}{L_m\lambda_{ds}}\dfrac{\hat{r}_r+p\hat{\sigma}\hat{L}_r+k_{iqr}}{k_{iqr}}+\dfrac{\hat{L}_s k_{wr}}{\hat{L}_m\lambda_{ds}}$, $\hat{k}_2=\dfrac{k_{wr}\hat{L}_s}{\hat{L}_m\lambda_{ds}}$ and $\hat{k}_3=\dfrac{\hat{r}_r+p\hat{\sigma}\hat{L}_r+k_{iqr}}{k_{iqr}}\dfrac{L_s}{L_m\lambda_{ds}}-\dfrac{\hat{L}_s}{\hat{L}_m\lambda_{ds}}$.

Similarly,

$$Q_s=\frac{\hat{k}_4}{\hat{k}_5}Q_s^* \tag{5.176}$$

where $\hat{k}_4=\dfrac{k_{Qs}}{p\lambda_{ds}\hat{\sigma}\hat{L}_r}$ and $\hat{k}_5=\dfrac{k_{Qs}}{p\lambda_{ds}\hat{\sigma}\hat{L}_r}-\dfrac{\hat{r}_r+p\hat{\sigma}\hat{L}_r+k_{idr}}{k_{idr}}\dfrac{2L_s}{3\omega_e L_m\lambda_{ds}}$

If the measured parameters are assumed to be equal to the actual quantities, solving (5.174) gives:

$$\omega_r=\frac{k_2}{k_1}\omega_r^*+\frac{k_3}{k_1}T_m \tag{5.177}$$

where $k_1=\dfrac{2pJL_s}{L_m\lambda_{ds}}\dfrac{r_r+p\sigma L_r+k_{iqr}}{k_{iqr}}+\dfrac{L_s k_{wr}}{L_m\lambda_{ds}}$, $k_2=\dfrac{k_{wr}L_s}{L_m\lambda_{ds}}$ and $k_3=\dfrac{r_r+p\sigma L_r+k_{iqr}}{k_{iqr}}\dfrac{L_s}{L_m\lambda_{ds}}-\dfrac{L_s}{L_m\lambda_{ds}}$.

Similarly,

$$Q_s = \frac{k_4}{k_5} Q_s^* \tag{5.178}$$

where $k_4 = \frac{k_{Qs}}{p\lambda_{ds}\sigma L_r}$ and $k_5 = \frac{k_{Qs}}{p\lambda_{ds}\sigma L_r} - \frac{r_r + p\sigma L_r + k_{idr}}{k_{idr}} \frac{2L_s}{3\omega_e L_m \lambda_{ds}}$.

Here it should be noted that the inner current controller parameters are same for q and d-axis currents, i.e. $k_{iqr} = k_{idr}$.

Similarly, in the GSC, from (5.93):

$$\sigma_{dc} = k_{dc}(V_{dc}^* - V_{dc}) = \frac{3}{4}(M_{qr} I_{qr} + M_{dr} I_{dr}) + \frac{3}{4}\left(M_{df} I_{df} + M_{qf} I_{qf}\right) \tag{5.179}$$

$$I_{qf}^* = \frac{1}{M_{qf}}\left(\frac{4}{3}(\sigma_{dc} - \frac{3}{4}(M_{qr} I_{qr} + M_{dr} I_{dr})) - M_{df} I_{df}\right) \tag{5.180}$$

where $\frac{3}{4}(M_{qr} I_{qr} + M_{dr} I_{dr})$ is the dc-current supplied from RSC to the GSC and $M_{qr} = \frac{2V_{qr}^*}{V_{dc}}$ and $M_{dr} = \frac{2V_{dr}^*}{V_{dc}}$. And we also know from (5.77) and (5.78) that-

$$V_{qr}^* = k_{Iqr}(I_{qr}^* - I_{qr}) + \omega_{so}\left(\frac{L_m}{L_s}\lambda_{ds} + \sigma L_r I_{dr}\right) \tag{5.181}$$

$$V_{dr}^* = k_{Idr}(I_{dr}^* - I_{dr}) - \omega_{so}\sigma L_r I_{qr} \tag{5.182}$$

Using (5.162), (5.169), (5.181) and (5.182), the DC-link current is expressed as:

$$\frac{3}{4}(M_{qr} I_{qr} + M_{dr} I_{dr}) = \frac{3}{2V_{dc}}\left[\begin{array}{l} k_{Iqr}k_{wr}\frac{p8JL_s}{3P^2 L_m \lambda_{ds}}(\omega_r^*\omega_r - \omega_r^2) - \frac{4T_m L_s}{3PL_m\lambda_{ds}} k_{Iqr}k_{wr}(\omega_r^* - \omega_r) + \frac{\omega_{so} p8J\omega_r}{3P^2} \\ -\frac{\omega_{so}4T_m}{3P} + \frac{2L_s k_{Idr}k_{Qs}}{3p\sigma L_r \omega_e L_m \lambda_{ds}^2}(Q_s Q_s^* - Q_s^2) - \frac{4L_s^2 k_{Idr}}{9\omega_e{}^2 L_m^2 \lambda_{ds}^2} \end{array}\right] \tag{5.183}$$

Here, λ_{ds} is regulated to constant value using flux control. Hence, it is clear from (5.183) that the DC-current flowing in ac/dc/ac converter has a non-linear relationship between control variables like ω_r, Q_s and V_{dc}. So it can be concluded that decoupled control of Q_f, Q_s, ω_r and V_{dc} can be done if DC-link current is taken as a disturbance for the GSC control. Now, from (5.105):

$$\begin{cases} \sigma_{Qf} = (V_{df} - \hat{r}_f I_{df} + \hat{\omega}_e \hat{L}_f I_{qf}) \\ \sigma_{Qf} = (\hat{r}_f I_{df} + p\hat{L}_f I_{df} - \hat{\omega}_e \hat{L}_f I_{qf} - \hat{r}_f I_{df} + \hat{\omega}_e \hat{L}_f I_{qf}) \\ I_{df}^* = \dfrac{\sigma_{Qf}}{p\hat{L}_f} \end{cases} \tag{5.184}$$

From (5.184) and (5.180):

$$I_{qf}^* = \frac{1}{M_{qf}}\left(\frac{4}{3}(\sigma_{dc} - \frac{3}{4}(M_{qr}I_{qr} + M_{dr}I_{dr})) - M_{df}\frac{\sigma_{Qf}}{p\hat{L}_f}\right) \tag{5.185}$$

Combining (5.184) and (5.185):

$$\begin{bmatrix} I_{qf}^* \\ I_{df}^* \end{bmatrix} = \underbrace{\begin{bmatrix} \dfrac{4}{3M_{qf}} & -\dfrac{M_{df}}{p\hat{L}_f M_{qf}} \\ 0 & \dfrac{1}{p\hat{L}_f} \end{bmatrix}}_{O} \begin{bmatrix} \sigma_{dc} \\ \sigma_{Qf} \end{bmatrix} + \underbrace{\begin{bmatrix} -\dfrac{1}{M_{qf}}(M_{qr}I_{qr} + M_{dr}I_{dr}) \\ 0 \end{bmatrix}}_{P} \tag{5.186}$$

From (5.91):

$$pC V_{dc} = \frac{3}{4}(M_{qr}I_{qr} + M_{dr}I_{dr}) + \frac{3}{4}\left(M_{df}I_{df} + M_{qf}I_{qf}\right) \tag{5.187}$$

$$I_{qf} = \frac{4}{3M_{qf}}(pC V_{dc} - \frac{3}{4}(M_{qr}I_{qr} + M_{dr}I_{dr})) - \left(\frac{M_{df}}{M_{qf}}I_{df}\right) \tag{5.188}$$

From (5.103):

$$pQ_f = \frac{3V_{qs}}{2L_f}(V_{df} - r_f I_{df} + \omega_e L_f I_{qf}) \tag{5.189}$$

$$\begin{cases} pQ_f = \dfrac{3V_{qs}}{2L_f}(r_f I_{df} + pL_f I_{df} - \omega_e L_f I_{qf} - r_f I_{df} + \omega_e L_f I_{qf}) \\ I_{df} = \dfrac{2Q_f}{3V_{qs}} \end{cases} \tag{5.190}$$

Substituting (5.190) into (5.188):

$$I_{qf} = \frac{4}{3M_{qf}}(pC\,V_{dc} - \frac{3}{4}(M_{qr}I_{qr} + M_{dr}I_{dr})) - \left(\frac{2M_{df}}{3M_{qf}}\frac{Q_f}{V_{qs}}\right) \tag{5.191}$$

Combining (5.190) and (5.191)

$$\begin{bmatrix} I_{qf} \\ I_{df} \end{bmatrix} = \underbrace{\begin{bmatrix} \dfrac{4}{3M_{qf}}pC & -\dfrac{2M_{df}}{3V_{qs}M_{qf}} \\ 0 & \dfrac{2}{3V_{qs}} \end{bmatrix}}_{Q} \begin{bmatrix} V_{dc} \\ Q_f \end{bmatrix} + \underbrace{\begin{bmatrix} -\dfrac{1}{M_{qf}}(M_{qr}I_{qr} + M_{dr}I_{dr}) \\ 0 \end{bmatrix}}_{R} \tag{5.192}$$

From (5.111):

$$\left(\hat{r}_f + p\hat{L}_f\right)I_{qf} = k_{iqf}I_{qf}^* - k_{iqf}I_{qf} \tag{5.193}$$

From (5.112):

$$\left(\hat{r}_f + p\hat{L}_f\right)I_{df} = k_{idf}I_{df}^* - k_{idf}I_{df} \tag{5.194}$$

Combining (5.193) and (5.194) gives:

$$\begin{bmatrix} I_{qf}^* \\ I_{df}^* \end{bmatrix} = \underbrace{\begin{bmatrix} \dfrac{\hat{r}_f + p\hat{L}_f + k_{iqf}}{k_{iqf}} & 0 \\ 0 & \dfrac{\hat{r}_f + p\hat{L}_f + k_{idf}}{k_{idf}} \end{bmatrix}}_{F} \begin{bmatrix} I_{qf} \\ I_{df} \end{bmatrix} \tag{5.195}$$

Substituting (3.186) and (5.192) in (5.195):

$$O\begin{bmatrix}\sigma_{dc}\\ \sigma_{Qf}\end{bmatrix}+P=FQ\begin{bmatrix}V_{dc}\\ Q_f\end{bmatrix}+FR \tag{5.196}$$

$$\begin{bmatrix}\frac{4}{3M_{qf}} & -\frac{M_{df}}{\hat{p}\hat{L}_f M_{qf}}\\ 0 & \frac{1}{\hat{p}\hat{L}_f}\end{bmatrix}\begin{bmatrix}k_{dc}(V_{dc}^*-V_{dc})\\ k_{Qf}(Q_f^*-Q_f)\end{bmatrix}+\begin{bmatrix}-\frac{(M_{qr}I_{qr}+M_{dr}I_{dr})}{M_{qf}}\\ 0\end{bmatrix}$$

$$=\begin{bmatrix}\frac{4pC}{3M_{qf}}\frac{\hat{r}_f+p\hat{L}_f+k_{iqf}}{k_{iqf}} & -\frac{2M_{df}}{3V_{qs}M_{qf}}\frac{\hat{r}_f+p\hat{L}_f+k_{iqf}}{k_{iqf}}\\ 0 & \frac{\hat{r}_f+p\hat{L}_f+k_{idf}}{k_{idf}}\frac{2}{3V_{qs}}\end{bmatrix}\begin{bmatrix}V_{dc}\\ Q_f\end{bmatrix}+\begin{bmatrix}-\frac{(M_{qr}I_{qr}+M_{dr}I_{dr})}{M_{qf}}\frac{\hat{r}_f+p\hat{L}_f+k_{iqf}}{k_{iqf}}\\ 0\end{bmatrix} \tag{5.197}$$

Solving (5.197) gives:

$$V_{dc}=\frac{k_{dc}}{\hat{\tau}_1}V_{dc}^*-\frac{3}{4}\frac{\hat{\gamma}_f-1}{\hat{\tau}_1}(M_{qr}I_{qr}+M_{dr}I_{dr}) \tag{5.198}$$

where $\hat{\gamma}_f=\frac{\hat{r}_f+p\hat{L}_f+k_{idf}}{k_{idf}}$ and $\hat{\tau}_1=pC\hat{\gamma}_f+k_{dc}$. Similarly,

$$Q_f=\frac{\hat{\eta}_1}{\hat{\eta}_2}Q_f^* \tag{5.199}$$

where $\hat{\eta}_1=\frac{k_{Qf}}{\hat{p}\hat{L}_f}$ and $\hat{\eta}_2=\hat{\gamma}_f\frac{2}{3V_{qs}}+\frac{k_{Qf}}{\hat{p}\hat{L}_f}$

If the measured quantities are assumed to be equal to the actual quantities, solving (5.197) gives:

$$V_{dc}=\frac{k_{dc}}{\tau_1}V_{dc}^*-\frac{3}{4}\frac{\gamma_f-1}{\tau_1}(M_{qr}I_{qr}+M_{dr}I_{dr}) \tag{5.200}$$

where $\gamma_f = \dfrac{r_f + sL_f + k_{idf}}{k_{idf}}$ and $\tau_1 = pC\gamma_f + k_{dc}$.

Similarly,

$$Q_f = \frac{\eta_1}{\eta_2} Q_f^* \tag{5.201}$$

where $\eta_1 = \dfrac{k_{Qf}}{sL_f}$ and $\eta_2 = \gamma_f \dfrac{2}{3V_{qs}} + \dfrac{k_{Qf}}{pL_f}$

Here it should be noted that the inner current controller parameters are same for q and d-axis currents, i.e. $k_{iqf} = k_{idf}$.

Combining (5.150), (5.151), (5.175), (5.176), (5.198) and (5.199) gives:

$$\begin{bmatrix} V_m^2 \\ V_{dcs} \\ \omega_r \\ Q_s \\ V_{dc} \\ Q_f \end{bmatrix} = \underbrace{\begin{bmatrix} \hat{k}_{11} & 0 & 0 & 0 & 0 & 0 \\ 0 & \hat{k}_{22} & 0 & 0 & 0 & 0 \\ 0 & 0 & \hat{k}_{33} & 0 & 0 & 0 \\ 0 & 0 & 0 & \hat{k}_{44} & 0 & 0 \\ 0 & 0 & 0 & 0 & \hat{k}_{55} & 0 \\ 0 & 0 & 0 & 0 & 0 & \hat{k}_{66} \end{bmatrix}}_{\hat{A}} \begin{bmatrix} V_m^{2*} \\ V_{dcs}^* \\ \omega_r^* \\ Q_s^* \\ V_{dc}^* \\ Q_f^* \end{bmatrix} + \begin{bmatrix} \hat{\mu}_{11} \\ 0 \\ \hat{\mu}_{33} T_m \\ 0 \\ 0 \\ 0 \end{bmatrix} + \begin{bmatrix} 0 \\ 0 \\ 0 \\ 0 \\ \hat{\mu}_{55} \\ 0 \end{bmatrix} \tag{5.202}$$

where $\hat{k}_{11} = \hat{\zeta} k_{vm}$, $\hat{k}_{22} = \dfrac{k_{dcs}}{\hat{\delta}}$, $\hat{k}_{33} = \dfrac{\hat{k}_2}{\hat{k}_1}$, $\hat{k}_{44} = \dfrac{\hat{k}_4}{\hat{k}_5}$, $\hat{k}_{55} = \dfrac{\hat{k}_{dc}}{\hat{\tau}_1}$, $\hat{k}_{66} = \dfrac{\hat{\eta}_1}{\hat{\eta}_2}$,

$\hat{\mu}_{11} = \hat{\zeta}(1-\hat{\gamma}) V_{d2} I_{d2} + \hat{\zeta}(1-\hat{\gamma}) I_{q2}$, $\hat{\mu}_{33} = \dfrac{\hat{k}_3}{\hat{k}_1}$ and

$$\hat{\mu}_{55} = \frac{3}{2V_{dc}} \frac{\hat{\gamma}_f - 1}{\hat{\tau}_1} \left[\begin{array}{l} k_{Iqr} k_{wr} \dfrac{p8JL_s}{3P^2 L_m \lambda_{ds}} (\omega_r^* \omega_r - \omega_r^2) - \dfrac{4T_m L_s}{3PL_m \lambda_{ds}} k_{Iqr} k_{wr} (\omega_r^* - \omega_r) + \dfrac{\omega_{so} p8J\omega_r}{3P^2} \\ - \dfrac{\omega_{so} 4T_m}{3P} + \dfrac{2L_s k_{Idr} k_{Qs}}{3p\sigma L_r \omega_e L_m \lambda_{ds}^2} (Q_s Q_s^* - Q_s^2) - \dfrac{4L_s^2 k_{Idr}}{9\omega_e^2 L_m^2 \lambda_{ds}^2} \end{array} \right]$$

Combining (5.150(a)), (5.151(a)), (5.177), (5.178), (5.200) and (5.201) gives:

$$\begin{bmatrix} V_m^2 \\ V_{dcs} \\ \omega_r \\ Q_s \\ V_{dc} \\ Q_f \end{bmatrix} = \underbrace{\begin{bmatrix} k_{11} & 0 & 0 & 0 & 0 & 0 \\ 0 & k_{22} & 0 & 0 & 0 & 0 \\ 0 & 0 & k_{33} & 0 & 0 & 0 \\ 0 & 0 & 0 & k_{44} & 0 & 0 \\ 0 & 0 & 0 & 0 & k_{55} & 0 \\ 0 & 0 & 0 & 0 & 0 & k_{66} \end{bmatrix}}_{A} \begin{bmatrix} V_m^{2*} \\ V_{dcs}^* \\ \omega_r^* \\ Q_s^* \\ V_{dc}^* \\ Q_f^* \end{bmatrix} + \begin{bmatrix} \mu_{11} \\ 0 \\ \mu_{33} T_m \\ 0 \\ 0 \\ 0 \end{bmatrix} + \begin{bmatrix} 0 \\ 0 \\ 0 \\ 0 \\ \mu_{55} \\ 0 \end{bmatrix} \quad (5.203)$$

where $k_{11} = \zeta\, k_{vm}$, $k_{22} = \dfrac{k_{dcs}}{\delta}$, $k_{33} = \dfrac{k_2}{k_1}$, $k_{44} = \dfrac{k_4}{k_5}$, $k_{55} = \dfrac{k_{dc}}{\tau_1}$, $k_{66} = \dfrac{\eta_1}{\eta_2}$,

$\mu_{11} = \zeta(1-\gamma)V_{d2}I_{d2} + \zeta(1-\gamma)I_{q2}$, $\mu_{33} = \dfrac{k_3}{k_1}$ and

$$\mu_{55} = \frac{3}{2V_{dc}} \frac{\gamma_f - 1}{\tau_1} \begin{bmatrix} k_{Iqr} k_{wr} \dfrac{p8JL_s}{3P^2 L_m \lambda_{ds}} (\omega_r^* \omega_r - \omega_r^2) - \dfrac{4T_m L_s}{3PL_m \lambda_{ds}} k_{Iqr} k_{wr} (\omega_r^* - \omega_r) + \dfrac{\omega_{so} p8J\omega_r}{3P^2} \\ -\dfrac{\omega_{so} 4T_m}{3P} + \dfrac{2L_s k_{Idr} k_{Qs}}{3p\sigma L_r \omega_e L_m \lambda_{ds}^2} (Q_s Q_s^* - Q_s^2) - \dfrac{4L_s^2 k_{Idr}}{9\omega_e{}^2 L_m^2 \lambda_{ds}^2} \end{bmatrix}$$

As shown in (5.202) and (5.203), the transfer function matrices $\hat{A}$ and A are both diagonal which verifies that all the six controlled quantities are independent of each other regardless of error in parameter estimation. That means, the controller design can be done independent of each other and combined them together for the overall control and there exists a non-linear relation through the DC-link voltage control which can be considered as disturbance for the GSC control.

Hence, in this chapter, the modeling and controller design of STATCOM is shown. The support provided by the STATCOM to regulate steady state voltage and to improve dynamic response of the DFIG wind turbine system during disturbances in the grid side is explained clearly with the help of simulation results. The dynamic voltage regulation during voltage swelling and voltage sagging and its mitigation using STATCOM is discussed and is well supported by the simulation results.

CHAPTER 6

DFIG-BASED WIND TURBINE INTERFACED WITH SERIES COMPENSATED LINE

6.1 Introduction

The DFIG wind turbines are installed in remote areas and offshores because of the favorable wind available and no worries regarding noise pollution and scenery. So, those wind turbines are connected to power grid through a long transmission line. Usually those transmission lines are weak grids characterized by under voltage condition. As discussed in Chapter 5, the terminal voltage of a DFIG decreases with the increase in power output from wind turbine. The terminal voltage variation is because of the significant impedance of the transmission line.

The central idea of series compensation (SC) is to cancel part of the reactance of the transmission line by means of series capacitor. This increases the power transfer on the line. Series compensation is also used to enable power to be transmitted stably over a greater distance than is possible without compensation [46]. Moreover, series capcitor effectively reduces line reactance as a result line absorbs less reactive power, i.e. reactive power demand decreases. Hence, it helps in steady state voltage regulation. The most noticeable advantage of the SC is that series capacitor reactive generation increases with the current squared [46]. This means that a series capacitor has a self-regulating impact. In other words, it generates reactive power when it is most needed. The response of the SC is automatic and continuous.

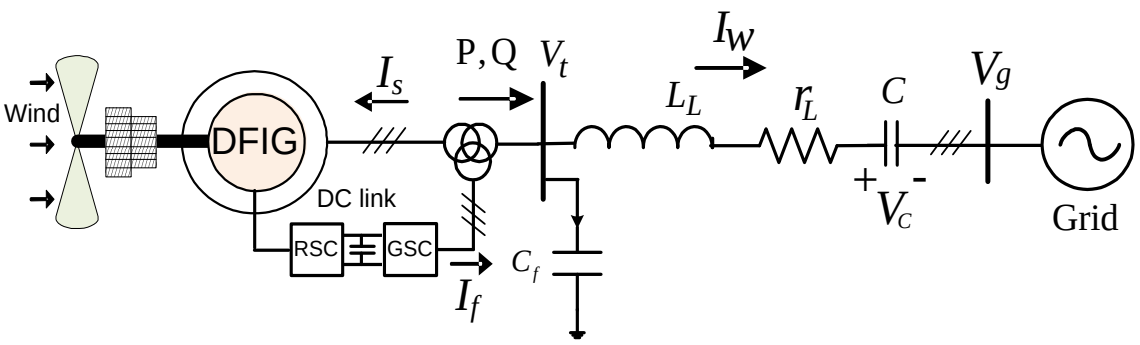

Figure 6.1 Schematic diagram of the studied DFIG-based wind turbine system connected to power grid through series compensated line

If a capacitor is connected in series with the transmission line as shown in Figure 6.1 then the net impedance of the transmission line reduces from $r_L + jX_L$ to $r_L + j(X_L - X_C)$.as a result the voltage variation also decreases. This chapter discusses the dynamic and steady state operation of a DFIG-based wind turbine interfaced with a series compensated line as shown in Figure 6.1.

6.2 Dynamic Modeling and Controller Design of the Overall System

The voltage dynamics at the DFIG terminal bus is given as:

$$C_f pV_{qt} + \omega_e C_f V_{dt} = I_{qf} - I_{qs} - I_{qw} \tag{6.1}$$

$$C_f pV_{dt} - \omega_e C_f V_{qt} = I_{df} - I_{ds} - I_{dw} \tag{6.2}$$

The state space matrix of equations (6.1)-(6.2) can be given by (6.3) as:

$$p\begin{bmatrix} V_{qt} \\ V_{dt} \end{bmatrix} = \begin{bmatrix} 0 & -\omega_e \\ \omega_e & 0 \end{bmatrix} \begin{bmatrix} V_{qt} \\ V_{dt} \end{bmatrix} + \begin{bmatrix} \dfrac{I_{qf} - I_{qs} - I_{qw}}{C_f} \\ \dfrac{I_{df} - I_{ds} - I_{dw}}{C_f} \end{bmatrix} \tag{6.3}$$

where V_{qt} and V_{dt} are the q and d-axis voltages at the DFIG terminal, respectively, the I_{qf} and I_{df} are the q and d-axis currents supplied by GSC, respectively, the I_{qs} and I_{ds} are the q and d-axis currents flowing to the stator side, respectively, the I_{qw} and I_{dw} are the q and d-axis currents through the transmission line, respectively, V_{qg} and V_{dg} are the q and d-axis voltages of the grid bus, respectively, and ω_e is the synchronous reference frame speed (377 rad/s).

The current flowing through the series compensated capacitor C is given as:

$$I_{qw} = C\ pV_{cq} + \omega_e C V_{cd} \tag{6.4}$$

$$I_{dw} = C\ pV_{cd} - \omega_e C V_{cq} \tag{6.5}$$

Using KVL from DFIG terminal bus to the grid bus:

$$V_{qt} - V_{qg} = r_L I_{qw} + L_L p I_{qw} + \omega_e L_L I_{dw} + V_{cq} \tag{6.6}$$

$$V_{dt} - V_{dg} = r_L I_{dw} + L_L p I_{dw} - \omega_e L_L I_{qw} + V_{cd} \tag{6.7}$$

The state space matrix of equations (6.4)-(6.7) can be written as follows:

$$p\begin{bmatrix} V_{cq} \\ V_{cd} \\ I_{qw} \\ I_{dw} \end{bmatrix} = \begin{bmatrix} 0 & -\omega_e & \frac{1}{C} & 0 \\ \omega_e & 0 & 0 & \frac{1}{C} \\ -\frac{1}{L_L} & 0 & -\frac{r_L}{L_L} & -\omega_e \\ 0 & -\frac{1}{L_L} & \omega_e & -\frac{r_L}{L_L} \end{bmatrix} \begin{bmatrix} V_{cq} \\ V_{cd} \\ I_{qw} \\ I_{dw} \end{bmatrix} + \begin{bmatrix} 0 \\ 0 \\ \frac{V_{qt} - V_{qg}}{L_L} \\ \frac{V_{dt} - V_{dg}}{L_L} \end{bmatrix} \tag{6.8}$$

where V_{cq} and V_{cd} are the q and d-axis voltages across the capacitor, respectively. The dynamic equations of the DFIG explained in Chapter 3 are given as:

$$\begin{bmatrix} \dot{\lambda}_{qs} \\ \dot{\lambda}_{ds} \\ \dot{\lambda}_{qr} \\ \dot{\lambda}_{dr} \end{bmatrix} = \begin{bmatrix} -\frac{r_s}{\sigma L_s} & -\omega_e & \frac{r_s L_m}{\sigma L_s L_r} & 0 \\ \omega_e & -\frac{r_s}{\sigma L_s} & 0 & \frac{r_s L_m}{\sigma L_s L_r} \\ \frac{r_r L_m}{\sigma L_s L_r} & 0 & \frac{r_r}{\sigma L_r} & (\omega_e - \omega_r) \\ 0 & \frac{r_r L_m}{\sigma L_s L_r} & (\omega_e - \omega_r) & -\frac{r_r}{\sigma L_r} \end{bmatrix} \begin{bmatrix} \lambda_{qs} \\ \lambda_{ds} \\ \lambda_{qr} \\ \lambda_{dr} \end{bmatrix} + \begin{bmatrix} 1 & 0 & 0 & 0 \\ 0 & 1 & 0 & 0 \\ 0 & 0 & 1 & 0 \\ 0 & 0 & 0 & 1 \end{bmatrix} \begin{bmatrix} V_{qs} \\ V_{ds} \\ V_{qr} \\ V_{dr} \end{bmatrix} \tag{6.9}$$

$$I_{qs} = \frac{1}{\sigma L_s}\lambda_{qs} - \frac{L_m}{\sigma L_s L_r}\lambda_{qr} \tag{6.10}$$

$$I_{ds} = \frac{1}{\sigma L_s}\lambda_{ds} - \frac{L_m}{\sigma L_s L_r}\lambda_{dr} \tag{6.11}$$

$$I_{qr} = -\frac{L_m}{\sigma L_s L_r}\lambda_{qs} + \frac{1}{\sigma L_r}\lambda_{qr} \tag{6.12}$$

$$I_{dr} = -\frac{L_m}{\sigma L_s L_r}\lambda_{ds} + \frac{1}{\sigma L_r}\lambda_{dr} \tag{6.13}$$

where leakage coefficient $\sigma = \frac{L_s L_r - L_m^2}{L_s L_r}$.

$$p\omega_r = \frac{P}{2J}(T_m - T_e - C_f \omega_r) \tag{6.14}$$

6.2.1 Design of the RSC Controller

The RSC control scheme consists of two cascaded vector control structure with inner current control loops which regulates independently the d-axis and q-axis rotor currents, i.e. I_{dr} and I_{qr}, according to some synchronously rotating reference frame. The outer control loop regulates the stator active power (or DFIG rotor speed) and reactive power (or DFIG terminal voltage) independently. The stator voltage orientation (SVO) control principle for a DFIG is described in [31], where the q-axis of the rotating

reference frame is aligned to the stator voltage i.e V_{ds} = 0 and V_{qs} = V_s. From (3.15) and (3.16), the stator side flux can be controlled using PI controller. In this study, the q-axis flux is regulated to zero ($\lambda_{qs}=0$) and ($\lambda_{ds}=\lambda_s$) for the de-coupled control of active and reactive power as described below:

$$\begin{cases} p\lambda_{qs}+\dfrac{r_s}{\sigma L_s}\lambda_{qs}=-\omega_e\lambda_{ds}+\dfrac{r_s L_m}{\sigma L_s L_r}\lambda_{qr}+V_{qs} \\ \sigma_{\lambda qs}=-\omega_e\lambda_{ds}+\dfrac{r_s L_m}{\sigma L_s L_r}\lambda_{qr}+V_{qs} \\ \lambda_{ds}^{*}=\dfrac{1}{\omega_e}\left(\dfrac{r_s L_m}{\sigma L_s L_r}\lambda_{qr}+V_{qs}-\sigma_{\lambda qs}\right) \end{cases} \tag{6.15}$$

$$\begin{cases} p\lambda_{ds}+\dfrac{r_s}{\sigma L_s}\lambda_{ds}=\omega_e\lambda_{qs}+\dfrac{r_s L_m}{\sigma L_s L_r}\lambda_{dr}+V_{ds} \\ \sigma_{\lambda ds}=\omega_e\lambda_{qs}+\dfrac{r_s L_m}{\sigma L_s L_r}\lambda_{dr}+V_{ds} \\ \lambda_{qs}^{*}=\dfrac{1}{\omega_e}\left(\sigma_{\lambda ds}-\dfrac{r_s L_m}{\sigma L_s L_r}\lambda_{qr}-V_{qs}\right) \end{cases} \tag{6.16}$$

where $\sigma_{\lambda qs}=p\lambda_{qs}+\dfrac{r_s}{\sigma L_s}\lambda_{qs}=\left(k_{P\lambda s}+\dfrac{k_{I\lambda s}}{p}\right)(\lambda_{qs}^{*}-\lambda_{qs})$ and

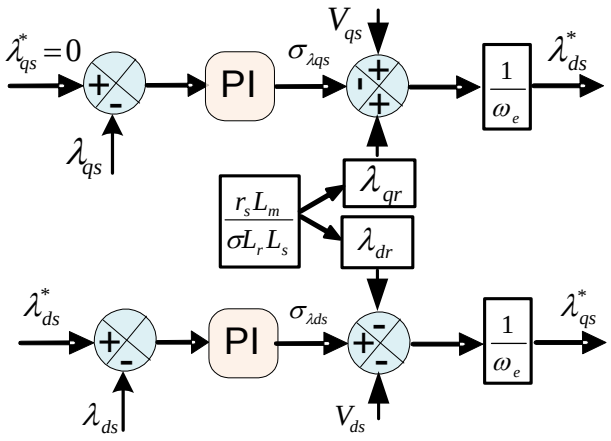

Figure 6.2 Stator fluxes control using PI controllers

$\sigma_{\lambda ds} = p\lambda_{ds} + \frac{r_s}{\sigma L_s}\lambda_{ds} = \left(k_{P\lambda s} + \frac{k_{I\lambda s}}{p}\right)(\lambda_{ds}^* - \lambda_{ds})$ are the outputs from the PI controllers as shown in Figure 6.2.

The PI parameters are determined by comparing with the Butterworth polynomial which is described in the below section, are given as:

$$\begin{cases} k_{P\lambda s} = \sqrt{2}\omega_0 - \frac{r_s}{\sigma L_s} \\ k_{I\lambda s} = \omega_0^{\,2} \end{cases} \tag{6.17}$$

Now, neglecting frictional losses, rotor speed dynamics is given as:

$$p\omega_r = \frac{P}{2J}(T_m - T_e) \tag{6.18}$$

where T_m is the mechanical torque from the wind turbine. When the wind speed (V_w) is less than the rated speed, then the T_m is given as:

$$T_m = k_{opt} V_w^{\,2} \tag{6.19}$$

where $k_{opt} = \frac{R}{2\lambda_{opt}} \rho\, A\, C_{p\_opt} = \text{constant}$ and if the wind speed (V_w) is more than the rated speed, then the T_m is given as:

$$T_m = \frac{P_{rated}}{\omega_{rated}} \tag{6.20}$$

where P_{rated} is rated power of the wind turbine and ω_{rated} is the rated speed of the wind turbine.

Equation (6.18) can be re-written as:

$$\frac{2J}{P} p\omega_r = (T_m - T_e) = \sigma_{wr} = k_{wr}(\omega_r^* - \omega_r) \tag{6.21}$$

where k_{wr} is the PI controller for rotor speed controller, given as: $k_{wr} = \left(k_{Pwr} + \frac{k_{Iwr}}{p} \right)$

Then (6.21) will be:

$$\frac{2J}{P} p\omega_r = \left(k_{Pwr} + \frac{k_{Iwr}}{p} \right) \omega_r^* - \left(k_{Pwr} + \frac{k_{Iwr}}{p} \right) \omega_r \tag{6.22}$$

$$\frac{\omega_r}{\omega_r^*} = \frac{\frac{P}{2J}\left(pk_{Pwr} + k_{Iwr} \right)}{p^2 + p\frac{Pk_{Pwr}}{2J} + \frac{Pk_{Iwr}}{2J}} \tag{6.23}$$

Now, comparing denominator of (6.23) with Butterworth second order polynomial, i.e. $p^2 + \sqrt{2}\omega_{0wr} p + \omega_{0wr}^2$, PI controller gains are obtained as:

$$\begin{cases} k_{Pwr} = \sqrt{2}\omega_{0wr} \frac{2J}{P} \\ k_{Iwr} = \frac{2J}{P} \omega_{0wr}{}^2 \end{cases} \tag{6.24}$$

where ω_{0wr} is the bandwidth frequency of the speed controller.

Using λ_{qs} = 0, the electromechanical torque and q-axis stator current is given by (6.25) as:

$$\begin{cases} T_e = \frac{3}{2} \lambda_{ds} I_{qs} \\ I_{qs} = -\frac{L_m}{L_s} I_{qr} \end{cases} \tag{6.25}$$

$$T_e = \frac{3}{2} \lambda_{ds} (-\frac{L_m}{L_s}) I_{qr} \tag{6.26}$$

$$I_{qr} = \left(\sigma_{wr} - T_m \right) \frac{2}{3} \frac{L_s}{L_m \lambda_{ds}} \tag{6.27}$$

Similarly,

$$I_{ds} = \frac{\lambda_{ds}}{L_s} - \frac{L_m}{L_s} I_{dr} \tag{6.28}$$

The stator side active power can be written as:

$$P_s = \frac{3}{2}\left(V_{qs} I_{qs} + V_{ds} I_{ds}\right) = -\frac{3}{2}\frac{L_m}{L_s} V_{qs} I_{qr} \tag{6.29}$$

The stator supplied reactive power is given as:

$$Q_s = \frac{3}{2}(V_{qs} I_{ds} - V_{ds} I_{qs}) = \frac{3}{2} V_{qs} I_{ds} \tag{6.30}$$

Substituting V_{qs} in (6.30) gives:

$$Q_s = \frac{3}{2}(r_s I_{qs} + \omega_e \lambda_{ds} + p\lambda_{qs}) I_{ds} \tag{6.31}$$

Assuming constant stator flux, neglecting the stator resistance and substituting I_{ds} from Equation (6.11) gives:

$$Q_s = \frac{3}{2}\frac{\omega_e}{\sigma L_s}\left(\lambda_{ds}^2 - \frac{L_m}{L_r}\lambda_{ds}\lambda_{dr}\right) \tag{6.32}$$

Differentiating (6.32) w.r.t. time gives:

$$pQ_s = -\frac{3}{2}\frac{\omega_e}{\sigma L_s}\frac{L_m}{L_r}\lambda_{ds} p\lambda_{dr} \tag{6.33}$$

From (6.33) and (3.4) gives (6.34) and solving λ_{qr} in terms of I_{qr} gives (6.35)

$$pQ_s = -\frac{3}{2}\frac{\omega_e}{\sigma L_s}\frac{L_m}{L_r}\lambda_{ds}\left(V_{dr} - r_r I_{dr} + (\omega_e - \omega_r)\lambda_{qr}\right) \tag{6.34}$$

$$pQ_s = -\frac{3}{2}\frac{\omega_e}{\sigma L_s}\frac{L_m}{L_r}\lambda_{ds}\left(V_{dr} - r_r I_{dr} + (\omega_e - \omega_r)\sigma L_r I_{qr}\right) \tag{6.35}$$

$$\nabla pQ_s = \sigma_{Qs} = k_{Qs}(Q_s^* - Q_s) \tag{6.36}$$

where $\nabla = \frac{2\sigma L_s L_r}{3\omega_e L_m}$ and k_{Qs} is the PI controller for stator side reactive power controller, given as: $k_{Qs} = \left(k_{PQs} + \frac{k_{IQs}}{p} \right)$. So, (6.36) can be re-written as:

$$\nabla p Q_s = \left(k_{PQs} + \frac{k_{IQs}}{p} \right) Q_s^* - \left(k_{PQs} + \frac{k_{IQs}}{p} \right) Q_s \tag{6.37}$$

$$\frac{Q_s}{Q_s^*} = \frac{\frac{1}{\nabla}\left(p k_{PQs} + k_{IQs} \right)}{p^2 + p\frac{k_{PQs}}{\nabla} + \frac{k_{IQs}}{\nabla}} \tag{6.38}$$

Similarly, comparing denominator of (6.37) with Butterworth second order polynomial, i.e. $p^2 + \sqrt{2}\omega_{Qs} p + \omega_{Qs}^2$, PI controller gains are obtained as:

$$\begin{cases} k_{PQs} = \sqrt{2}\omega_{0Qs}\Delta \\ k_{IQs} = \Delta {\omega_{Qs}}^2 \end{cases} \tag{6.39}$$

From (6.35) and (6.36) gives:

$$I_{dr}^* = \frac{1}{r_r}\left(V_{dr} + (\omega_e - \omega_r)\sigma L_r I_{qr} + \frac{\sigma_{Q_s}}{\lambda_{ds}} \right)$$

(6.40)

It can be seen from Equations (6.29) and (6.40) that, P_s and Q_s are proportional to I_{qr} and I_{dr}, respectively. The mutual coupling term $(\omega_e - \omega_r)\sigma L_r I_{qr}$ in (6.40) is very small so its effect is negligible. The rotor current can be regulated by means of rotor voltages. The relation between rotor current and rotor voltage is obtained by substituting values of λ_{dr} and λ_{qr} from (3.7) and (3.8) in Equations (3.3) and (3.4), respectively, and further simplification yields:

$$V_{qr} = r_r I_{qr} + \sigma L_r p I_{qr} + \omega_{so}\left(\frac{L_m}{L_s}\lambda_{ds} + \sigma L_r I_{dr}\right) \tag{6.41}$$

$$V_{dr} = r_r I_{dr} + \sigma L_r p I_{dr} - \omega_{so}\sigma L_r I_{qr} \tag{6.42}$$

where $\omega_{so} = (\omega_e - \omega_r)$ and $\sigma = 1 - \frac{L_m^{\ 2}}{L_s L_r}$

In the Equations (6.41) and (6.42), there is the term including I_{dr} in the q-axis equation and there is the term including I_{qr} in the d-axis equation. So these two equations are coupled and the traditional linear controllers cannot be used. However, through the exact linearization method, these equations can be linearized by putting the terms other than the currents control to one side.

$$r_r I_{qr} + \sigma L_r p I_{qr} = V_{qr} - \omega_{so}\left(\frac{L_m}{L_s}\lambda_{ds} + \sigma L_r I_{dr}\right) \tag{6.43}$$

$$r_r I_{dr} + \sigma L_r p I_{dr} = V_{dr} + \omega_{so}\sigma L_r I_{qr} \tag{6.44}$$

Lets assume:

$$\sigma_{qr} = r_r I_{qr} + \sigma L_r p I_{qr} \tag{6.45}$$

$$\sigma_{dr} = r_r I_{dr} + \sigma L_r p I_{dr} \tag{6.46}$$

The idea behind is to use the linear controllers that include integrations to calculate the derivative terms. And the nonlinear equations become linear when all the nonlinear terms are moved to the other side of the equations. Then the q and d-axis voltages are calculated as shown in Figure 6.3.

$$V_{qr}^{*} = \sigma_{qr} + \omega_{so}\left(\frac{L_m}{L_s}\lambda_{ds} + \sigma L_r I_{dr}\right) \tag{6.47}$$

$$V_{dr}^{*} = \sigma_{dr} - \omega_{so}\sigma L_r I_{qr} \tag{6.48}$$

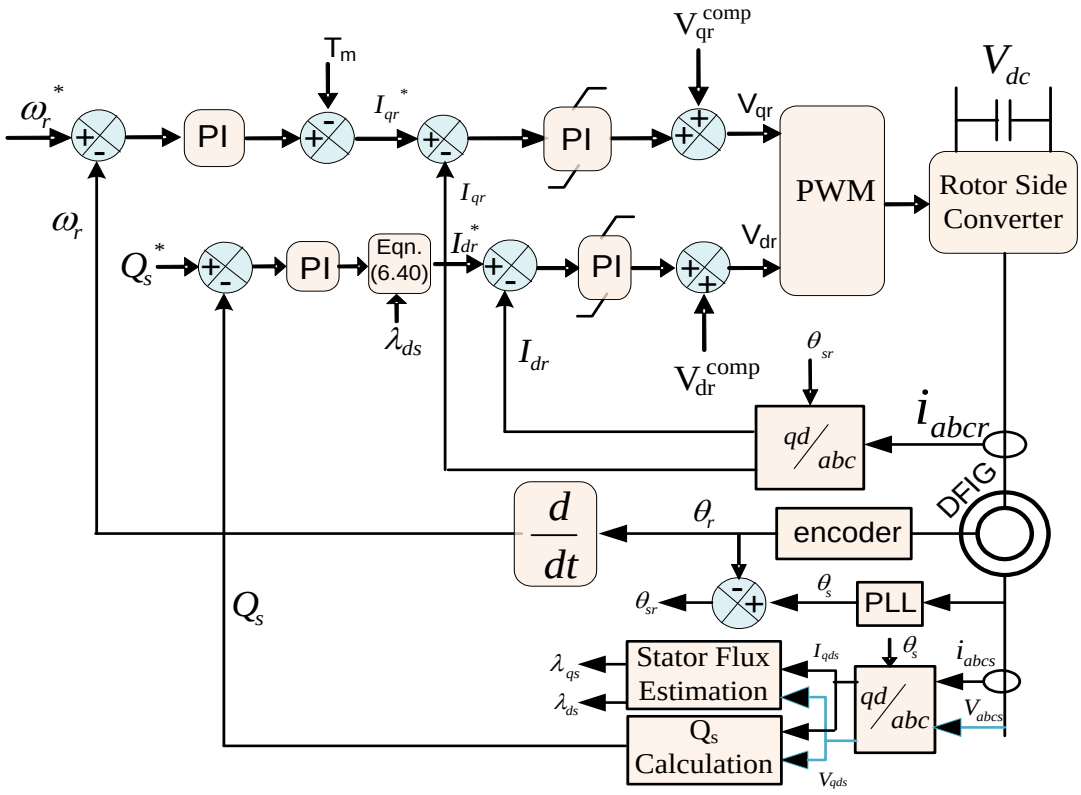

Figure 6.3 Block diagram of RSC control system: $V_{dr}^{comp} = -\omega_{so}\sigma L_r I_{qr}$

and $V_{qr}^{comp} = \omega_{so}\left(\frac{L_m}{L_s}\lambda_{ds} + \sigma L_r I_{dr}\right)$

Using the inner current control loop has a significant advantage for the protection of the DFIG. It can naturally protect the system from over-current since current limiters can be easily inserted in the control system shown in Figure 6.3.

Since the general PI controllers are widely used and proved to be effective, they are also applied in the following analysis [63]. For I_{qr} current control loop from (6.43):

$$V_{qr}^{'} = r_r I_{qr} + \sigma L_r p I_{qr} = (r_r + p\sigma L_r) I_{qr} \tag{6.49}$$

$$V_{qr}^{'} = \left(k_{qp} + \frac{k_{qi}}{p}\right)\left(I_{qr}^{*} - I_{qr}\right) \tag{6.50}$$

$$(r_r + p\sigma L_r)I_{qr} = \left(k_{qp} + \frac{k_{qi}}{p}\right)I_{qr}^{*} - \left(k_{qp} + \frac{k_{qi}}{p}\right)I_{qr} \tag{6.51}$$

Then the transfer functions between the reference and actual currents are changed to the following:

$$\frac{I_{qr}}{I_{qr}^{*}} = \frac{pk_{qp} + k_{qi}}{p^2\sigma L_r + p(r_r + k_{qp}) + k_i} = \frac{\frac{1}{\sigma L_r}\left(pk_{qp} + k_{qi}\right)}{p^2 + p\frac{1}{\sigma L_r}(r_r + k_{qp}) + \frac{1}{\sigma L_r}k_{qi}} \tag{6.52}$$

Similar process can be repeated for I_{dr} current control loop from (6.44).

The PI parameters are determined by comparing the coefficients in the denominator of (6.52) with the Butterworth second order polynomial.

$$k_{qp} = k_{dp} = \sqrt{2}\omega_0\sigma L_r - r_r \tag{6.53}$$

$$k_{qi} = k_{di} = \sigma L_r\omega_0^{\,2} \tag{6.54}$$

Here ω_0 is the bandwidth of the current controller. The values of k_p and k_I for RSC is shown in Table 6.1. The overall vector control scheme of the RSC is shown in Figure 6.3.

6.2.2 Design of the DFIG Terminal Voltage Controller

Here, the GSC is implemented to control the terminal voltage magnitude of the DFIG wind turbine. In addition to terminal voltage magnitude control, GSC also maintains constant dc-link voltage in the ac/dc/ac converter of the DFIG by controlling currents supplied by GSC.

Now the DC voltage dynamics in the DC-link is given by:

$$C_{dc}pV_{dc} = I_o + \frac{3}{4}\left(M_{df}I_{df} + M_{qf}I_{qf}\right) \tag{6.55}$$

where C_{dc} is the DC-link capacitance, $I_o = \frac{3}{4}\left(M_{dr}I_{dr} + M_{qr}I_{qr}\right)$ is the DC current from RSC towards GSC and M_{df}, M_{qf}, M_{dr} and M_{qr} are q and d-axis modulation indexes of GSC, and RSC respectively. Equation (6.55) can be re-written as:

$$C_{dc}pV_{dc} = \sigma_{dc} = k_{dc}(V_{dc}^{*} - V_{dc}) \tag{6.56}$$

where k_{dc} is the PI controller for DC-voltage control given as: $k_{dc} = \left(k_{Pdc} + \frac{k_{Idc}}{s}\right)$. Then (6.56) will be:

$$C_{dc}pV_{dc} = \left(k_{Pdc} + \frac{k_{Idc}}{p}\right)V_{dc}^{*} - \left(k_{Pdc} + \frac{k_{Idc}}{p}\right)V_{dc} \tag{6.57}$$

$$\frac{V_{dc}}{V_{dc}^{*}} = \frac{\frac{1}{C_{dc}}\left(pk_{Pdc} + k_{Idc}\right)}{p^2 + p\frac{k_{Pdc}}{C_{dc}} + \frac{k_{Idc}}{C_{dc}}} \tag{6.58}$$

Comparing denominator of (6.58) with Butterworth second order polynomial, i.e. $p^2 + \sqrt{2}\omega_{0dc}p + \omega_{0dc}^2$, PI controller gains are obtained as:

$$k_{Pdc} = \sqrt{2}\omega_{0dc}C_{dc} \tag{6.59}$$

$$k_{Idc} = C_{dc}\omega_{0dc}^{2} \tag{6.60}$$

where ω_{0dc} is the bandwidth frequency of the DC-voltage controller. (6.55) can be re-arranged as:

$$I_{df}^{*} = \frac{4}{3}\frac{1}{M_{df}}\left(\sigma_{dc} - I_o\right) - \frac{M_{qf}}{M_{df}}I_{qf} \tag{6.61}$$

From (6.61), it is clear that the DC voltage is regulated by regulating the d-axis current supplied by the GSC.

Dynamic voltage equations of the GSC in the qd-reference frame are:

$$V_{qf} = r_f I_{qf} + L_f pI_{qf} + \omega_e L_f I_{df} + V_{qt} = M_{qf} \frac{V_{dc}}{2} \tag{6.62}$$

$$V_{df} = r_f I_{df} + L_f pI_{df} - \omega_e L_f I_{qf} + V_{dt} = M_{df} \frac{V_{dc}}{2} \tag{6.63}$$

where V_{qf} and V_{df} are the q and d-axis GSC output voltages and r_f and L_f are RL filter resistance and inductance, respectively after GSC.

Equation (6.1) can be re-arranged as:

$$pV_{qt} = \frac{1}{C_f}\left(I_{qf} - I_{qs} - I_{qw} - \omega_e C_f V_{dt}\right) \tag{6.64}$$

Equation (6.2) can be re-arranged as:

$$pV_{qt} = \frac{1}{C_f}\left(I_{df} - I_{ds} - I_{dw} + \omega_e C_f V_{qt}\right) \tag{6.65}$$

The voltage magnitude, V_t at the DFIG terminal is given as:

$$V_t^2 = V_{qt}^2 + V_{dt}^2 \tag{6.66}$$

Differentiating (6.66) w.r.t. time,

$$pV_t^2 = 2V_{qt} pV_{qt} + 2V_{dt} pV_{dt} \tag{6.67}$$

Equation (6.67) gives the square of voltage magnitude dynamics at the terminal. Then the voltage magnitude is:

$$V_{t\_mag} = \left|\sqrt{V_t^2}\right|. \tag{6.68}$$

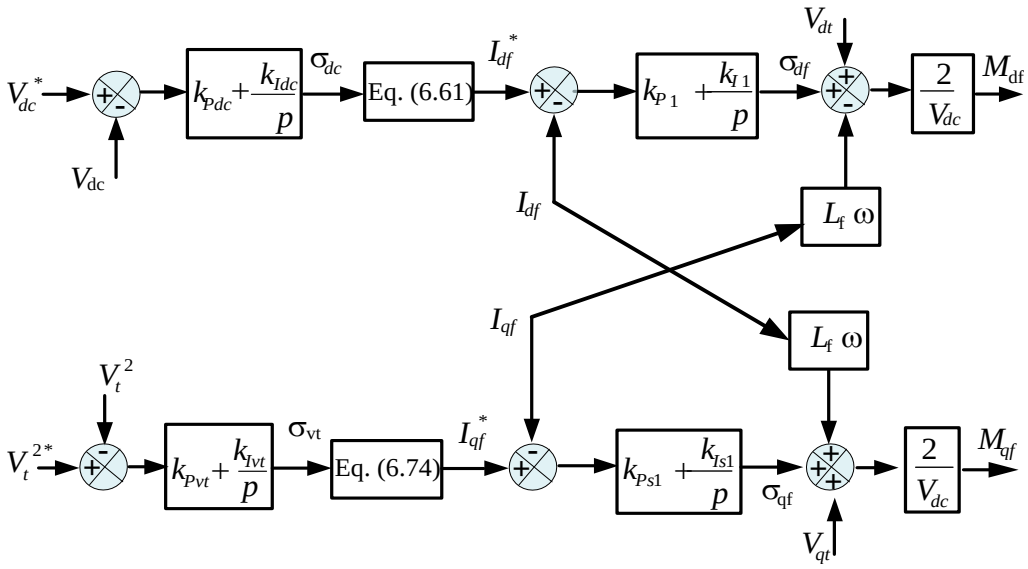

Figure 6.4 Block diagram of GSC control to regulate the DFIG terminal voltage

Substituting (6.64) and (6.65) in (6.68) gives:

$$\frac{C_f}{2} pV_t^2 = \left[V_{qt}\left(I_{qf} - I_{qs} - I_{qw}\right) + V_{dt}\left(I_{df} - I_{ds} - I_{dw}\right)\right] = k_{vt}(V_t^{2*} - V_t^2) = \sigma_{vt} \tag{6.69}$$

where $k_{vt} = \left(k_{Pvt} + \frac{k_{Ivt}}{p}\right)$ is the PI controller for voltage magnitude control. Then, (6.69)

can be written as:

$$\frac{C_f}{2} pV_t^2 = \left(k_{Pvt} + \frac{k_{Ivt}}{p}\right)V_t^{2^*} - \left(k_{Pvt} + \frac{k_{Ivt}}{p}\right)V_t^2 \tag{6.70}$$

$$\frac{V_t^2}{V_t^{2^*}} = \frac{\frac{2}{C_f}\left(pk_{Pvt} + k_{Ivt}\right)}{p^2 + p\frac{2k_{Pvt}}{C_f} + \frac{2k_{Ivt}}{C_f}} \tag{6.71}$$

Comparing denominator of (6.71) with the Butterworth second order polynomial:

$$k_{Pvt} = \sqrt{2}\omega_{0vt}\frac{C_f}{2} \tag{6.72}$$

$$k_{Ivt} = \frac{C_f}{2}{\omega_{0vt}}^2 \tag{6.73}$$

where ω_{0vt} is the bandwidth frequency of the voltage controller.

From (6.69), the reference q-axis current through GSC which regulates the voltage magnitude at the DFIG terminal is given as:

$$I_{qf}^{*} = \frac{1}{V_{qt}}\left[\sigma_{vt} - V_{dt}\left(I_{df} - I_{ds} - I_{dw}\right)\right] + I_{qs} + I_{qw} \tag{6.74}$$

Inner current control:

If we assume:

$$r_f I_{qf} + L_f pI_{qf} = k_{qf}(I^{*}{}_{qf} - I_{qf}) = \sigma_{qf} \tag{6.75}$$

$$r_f I_{df} + L_f pI_{df} = k_{df}(I^{*}{}_{df} - I_{df}) = \sigma_{df} \tag{6.76}$$

Then, (6.62) and (6.63) can be written as:

$$M_{qf} = (\sigma_{qf} + \omega_e L_f I_{df} + V_{qt})\frac{2}{V_{dc}} \tag{6.77}$$

$$M_{df} = (\sigma_{df} - \omega_e L_f I_{qf} + V_{dt})\frac{2}{V_{dc}} \tag{6.78}$$

Equations (6.77) and (6.78) give modulation indexes which are the output of the converter. And k_{qf} and k_{df} are PI current controllers for q and d-axis currents, respectively and $k_{qf} = k_{df} = \left(k_{P1} + \frac{k_{I1}}{p}\right)$.

Then, (6.75) can be re-written as:

$$\frac{I_{qf}}{I_{qf}^{*}} = \frac{\frac{1}{L_f}(pk_{P1} + k_{I1})}{p^2 + p\frac{1}{L_f}(r_f + k_{P1}) + \frac{1}{L_f}k_{I1}} \tag{6.79}$$

Comparing denominator of (6.79) with the Butterworth second order polynomial gives:

$$k_{P1} = \sqrt{2}\omega_{0c}L_f - r_f \tag{6.80}$$

$$k_{I1} = L_f \omega_{0c}^{\ 2} \tag{6.81}$$

where ω_{0c} is the bandwidth frequency of the current controller.

6.2.3 Phase Locked Loop (PLL)

A PLL is designed to obtain the reference angle for qd transformation so as to align the stator voltage along the q-axis and is included in the overall model of the system to make the design system more realistic. Figure 6.5 shows the 3-phase PLL which takes the input as the measured DFIG terminal voltage V_s and transforms it to qd-reference frame. PLL aligns the stator side voltage to q-axis by comparing d-axis load voltage with zero reference voltage. The voltage error signal is passed through the PI controller to obtain the angular frequency of the load bus voltage. Hence in the PLL system:

$$V_{ds} = -V_s \sin(\theta_i - \theta_s) \Rightarrow 0 = -V_s \sin(\theta_i - \theta_s) \tag{6.82}$$

$$\theta_i = \theta_s \tag{6.83}$$

Now the error signal is given as: $e = 0 - V_{ds} = V_s \sin(\theta_i - \theta_s)$

If $(\theta_i - \theta_s)$ is very small, then we can write: $\sin(\theta_i - \theta_s) \approx (\theta_i - \theta_s)$

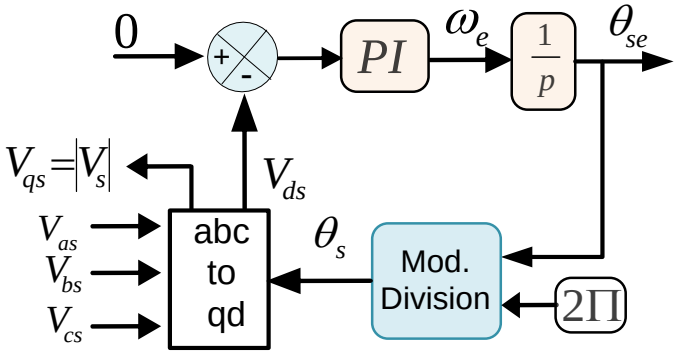

Figure 6.5 Block diagram of PLL control

From the block diagram shown in Figure 6.5, $V_s(\theta_i - \theta_s)$ is the input to the controller and ω_e is the output from the controller hence:

$$V_s(\theta_i - \theta_s)K_{pll} = \omega_e \tag{6.84}$$

$$\frac{1}{V_s} p\theta_s = (\theta_i - \theta_s)K_{pll} = \sigma_\theta \tag{6.85}$$

where, $K_{pll} = k_{P\_pll} + \frac{k_{I\_pll}}{p}$

$$\left(k_{P\_pll} + \frac{k_{I\_pll}}{p}\right)\theta_i - \left(k_{P\_pll} + \frac{k_{I\_pll}}{p}\right)\theta_s = \frac{1}{V_s} s\theta_s \tag{6.86}$$

$$\frac{\theta_s}{\theta_i} = \frac{pV_s k_{P\_pll} + V_s k_{I\_pll}}{p^2 + pV_s k_{P\_pll} + V_s k_{I\_pll}} \tag{6.87}$$

Now, comparing the denominator of (6.86) with the Butterworth second order polynomial, i.e. $p^2 + \sqrt{2}\omega_{0\_pll} p + \omega_{0\_pll}^2$, the parameters of the controller are given as:

$$\begin{cases} k_{P\_pll} = \dfrac{\sqrt{2}\omega_{0\_pll}}{V_s} \\ k_{I\_pll} = \dfrac{\omega_{0\_pll}^2}{V_s} \end{cases} \tag{6.88}$$

where ω_{0_pll} is the bandwidth frequency of the PLL controller.

Table 6.1 gives the PI controllers values used for the simulation study following above procedure. The switching frequency is taken as 1 kHz and the bandwidth of inner current controller is taken ten times that of outer loop controller i.e

$\omega_{sw} = 2 * \pi * f_{sw} = 6280 \ rad/s$ and $\omega_{inner} = \dfrac{\omega_{sw}}{10}$; $\omega_{outer} = \dfrac{\omega_{inner}}{10}$

$\omega_{inner} = \omega_0 = \omega_{oc} = 628 \ rad/s$; $\omega_{outer} = \omega_{odc} = \omega_{ovt} = 62.8 \ rad/s$ and $\omega_{owr} = 0.628 \ rad/s$

From (6.53): $k_{qp} = k_{dp} = \sqrt{2}\omega_0 \sigma L_r - r_r = 1.76$ and from (6.54): $k_{qi} = k_{di} = \sigma L_r \omega_0^{\ 2} = 783.6$

From (6.21): $k_{Pwr} = \sqrt{2}\omega_{owr}\dfrac{2J}{P} = 8.26$ and from (6.22): $k_{Iwr} = \dfrac{2J}{P}\omega_{owr}^2 = 3.65$

From (6.59): $k_{Pdc} = \sqrt{2}\omega_{odc}C_{dc} = 5.32$ and from (6.60): $k_{Idc} = \omega_{odc}^2 C_{dc} = 236.63$

Table 6.1 Parameters of the machine and PI controller coefficients

r_s	2.3 mΩ	C_{dc}	60 mF	k_{qp} / k_{dp}	1.76	k_{qi} / k_{di}	783.6
r_r	2 mΩ	L_f	2 mH	k_{Pwr}	8.26	k_{Iwr}	3.65
L_s	2.93 mH	r_f	2 mΩ	k_{Pdc}	5.32	k_{Idc}	236.63
L_r	2.97 mH	J	18.7	k_{P1}	1.77	k_{I1}	788.76
L_m	2.88 mH	P	4	k_{PQs}	0.00022	k_{IQs}	0.001
σ	0.669	C_f	5 mF	k_{PVt}	0.22	k_{IVt}	9.85
V_s	563.38 V			k_{P_pll}	2.10	k_{I_pll}	1244.4

From (6.80): $k_{P1} = \sqrt{2}\omega_{oc}L_f - r_f = 1.77$ and from (6.81): $k_{I1} = \omega_{oc}^2 L_f = 788.76$

From (6.38): $k_{PQs} = \sqrt{2}\omega_{0Qs}\Delta = 0.00022$ and from (6.39): $= k_{IQs} = \Delta\omega_{Qs}{}^2 = 0.001$

From (6.72): $k_{Pvt} = \sqrt{2}\omega_{0vt}\dfrac{C_f}{2} = 0.22$ and from (6.73): $k_{Ivt} = \dfrac{C_f}{2}\omega_{0vt}{}^2 = 9.85$

In PLL controller design, the switching frequency is taken as 2 kHz and the bandwidth of the PLL controller is taken as: $\omega_{sw} = 2*\pi*f_{sw} = 12{,}560\ rad/s$ and

$\omega_{0\_pll} = \dfrac{\omega_{sw}}{15} = 837.3\ rad/s$

From (6.88): $k_{P\_pll} = \dfrac{\sqrt{2}\omega_{0\_pll}}{V_s} = 2.10$ and from (6.88): $k_{I\_pll} = \dfrac{\omega_{0\_pll}^2}{V_s} = 1244.4$

6.2.4 Stator Flux Estimation

As shown in Figure 6.3, the stator side flux should be estimated as accurately as possible for the RSC control implementation. Therefore this section explains the stator flux estimation using Low Pass Filter (LPF).

The stator flux in stationary reference frame is given as:

$$V_{qds}^s = r_s I_{qds}^s + p\lambda_{qds}^s \tag{6.89}$$

$$\lambda_{qds}^s = \int \left(V_{qds}^s - r_s I_{qds}^s\right) dt \tag{6.90}$$

Flux can be estimated using (6.90) but the pure integration ($1/p$) involves the DC offsets and drifts [64]. To solve these problems, the pure integrator is replaced by a LPF. The estimated stator flux by the LPF can be given as:

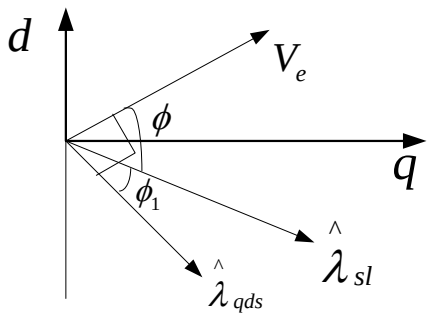

Figure 6.6 Vector diagram of the LPF and the pure integrator [64]

$$\frac{\hat{\lambda}_{sl}}{V_e} = \frac{1}{p+a} \tag{6.91}$$

where $\hat{\lambda}_{sl}$ is the estimated stator flux by LPF, a = pole and $V_e = V_{qds} - r_s I_{qds}$.

The phase lag and the gain of (6.91) can be given as:

$$\phi = -\tan^{-1}\frac{\hat{\omega}_e}{a} \tag{6.92}$$

$$M = \left|\frac{\hat{\lambda}_{sl}}{V_e}\right| = \frac{1}{\sqrt{a^2 + \hat{\omega}_e^2}} \tag{6.93}$$

where $\hat{\omega}_e$ is the estimated synchronous angular frequency given as [64]:

$$\hat{\omega}_e = \frac{(V_{qs} - r_s I_{qs})\lambda_{ds} - (V_{ds} - r_s I_{ds})\lambda_{qs}}{|\lambda_s|^2} \tag{6.94}$$

The LPF eliminates the saturation and reduces the effect of DC offsets but at the same time it brings the magnitude and phase angle error due to the cut off frequency of the LPF. Figure 6.6 shows the phase lag of $\hat{\lambda}_{sl}$ estimated by the LPF, and the phase lag

of $\hat{\lambda}_{qds}$ estimated by the pure integrator. The phase lag of $\hat{\lambda}_{qds}$ is 90° and the gain is $1/\left|\hat{\omega}_e\right|$. However, the phase lag of the LPF is not 90° and the gain is not $1/\left|\hat{\omega}_e\right|$. Hence, an error will be produced by this effect of the LPF. When the machine frequency is lower than the cutoff frequency of the LPF, the error is more severe. In order to remove this error, the LPF in (6.91) should have a very low cutting frequency. However, there still remains the drift problem due to the very large time constant of the LPF. For the exact estimation of the stator flux, the phase lag and the gain of $\hat{\lambda}_{sl}$ in (6.91) have to be 90° and $1/\left|\hat{\omega}_e\right|$, respectively. Furthurmore, to solve the drift problem, the pole should be located far from the origin.

Hence, the decrement in the gain of the LPF is compensated by multiplying a gain compensator, G in (6.95) and the phase lag is compensated by multiplying a phase compensator, P in (6.96) given as:

$$G = \frac{\sqrt{a^2 + \hat{\omega}_e^2}}{\left|\hat{\omega}_e\right|} \tag{6.95}$$

$$P = \exp(-j\phi_1) \tag{6.96}$$

$$\phi_1 = \tan^{-1}\frac{\hat{\omega}_e}{a} - \frac{\pi}{2} \tag{6.97}$$

$$\frac{\hat{\lambda}_{qds}}{V_e} = \frac{1}{p+a}\frac{\sqrt{a^2 + \hat{\omega}_e^2}}{\left|\hat{\omega}_e\right|}\exp(-j\phi_1) \tag{6.98}$$

The cutoff frequency in LPF cannot be located at fixed point far from the origin. If the pole is varied proportionally to the machine speed, the proportion of the machine frequency to the cutoff frequency of the LPF is constant. If the proportion is large, the estimation error will be very small. Consequently, the pole is determined to be varied proportionally to the motor speed as (6.99). Therefore, the pole is located close to the origin in very low speed range and far from the origin in high speed range.

$$a = \frac{\left|\hat{\omega}_e\right|}{K} \tag{6.99}$$

where K = constant.

The complete equation for stator flux estimator can be derived as:

$$\frac{\hat{\lambda}_{qds}}{V_e} = \frac{1}{p + (\hat{\omega}_e / K)} \frac{\sqrt{(\hat{\omega}_e / K)^2 + \hat{\omega}_e^2}}{\left|\hat{\omega}_e\right|} \exp(-j\phi_1) \tag{6.100}$$

where $\exp(-j\phi_1) = \cos(\phi_1) - j\sin(\phi_1)$, $\cos(\phi_1) = \dfrac{\left|\hat{\omega}_e\right|}{\sqrt{(\hat{\omega}_e / K)^2 + \hat{\omega}_e^2}}$ and $\sin(\phi_1) = \dfrac{\hat{\omega}_e / K}{\sqrt{(\hat{\omega}_e / K)^2 + \hat{\omega}_e^2}}$

Simplifying (6.100) and separating into real and imiginary parts gives:

$$\hat{\lambda}_{qs} = \frac{1}{p + (\hat{\omega}_e / K)} \frac{\sqrt{(\hat{\omega}_e / K)^2 + \hat{\omega}_e^2}}{\left|\hat{\omega}_e\right|} \left\{\cos\phi_1 (V_{qs} - r_s I_{qs}) + \sin\phi_1 (V_{ds} - r_s I_{ds})\right\} \tag{6.101}$$

$$\hat{\lambda}_{ds} = \frac{1}{p + (\hat{\omega}_e / K)} \frac{\sqrt{(\hat{\omega}_e / K)^2 + \hat{\omega}_e^2}}{\left|\hat{\omega}_e\right|} \left\{\cos\phi_1 (V_{ds} - r_s I_{ds}) - \sin\phi_1 (V_{qs} - r_s I_{qs})\right\} \tag{6.102}$$

Figure 6.7 shows the overall block diagram of the whole system to estimate stator side flux using LPF and synchronous speed of the machine. Figure 6.8 shows the

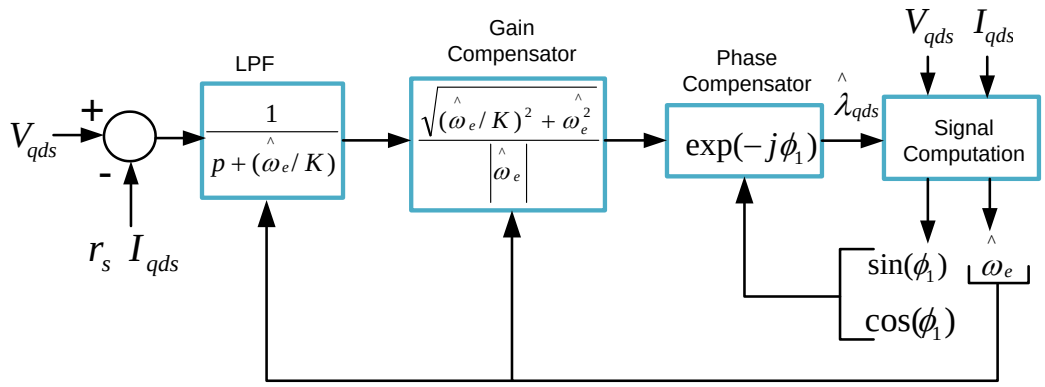

Figure 6.7 Overall block diagram of the stator flux estimation using LPF [64]

schematic diagram of the overall control system implemented in back to back converter of the DFIG system including stator side flux estimator using LPF.

6.3 Dynamic Simulation Results

First of all, the PLL and the stator flux estimator performance are discussed and the output from PLL and stator flux estimator is used for the control implementation of the GSC and RSC in DFIG. Figure 6.9 shows the plot of reference angle given by PLL to align the stator voltage along the q-axis. Figure 6.10 depicts the angular synchronous frequency of the system measured by the PLL and estimated by the stator flux estimator.

The estimated stator fluxes using pure integrater as well as LPF and synchronous angular speed of the machine is presented in Figure 6.11. At t=10 s, 15 s and 20 s, the compensation level of the series compensated line is changed, as a result the frequency and flux estimated by the stator flux estimator oscillates and finally settles quickly.

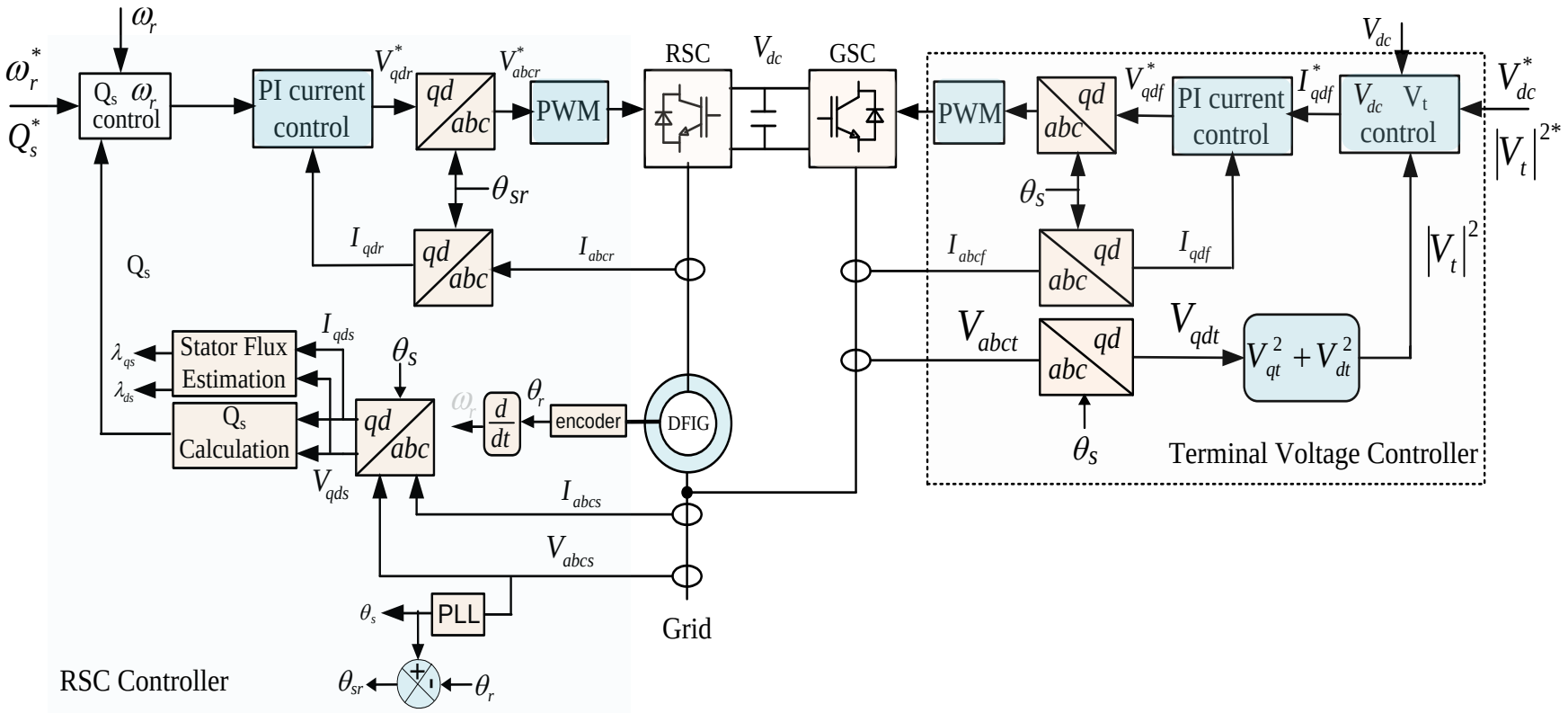

Figure 6.8 Schematic diagram of the implemented control structure of the DFIG wind turbine

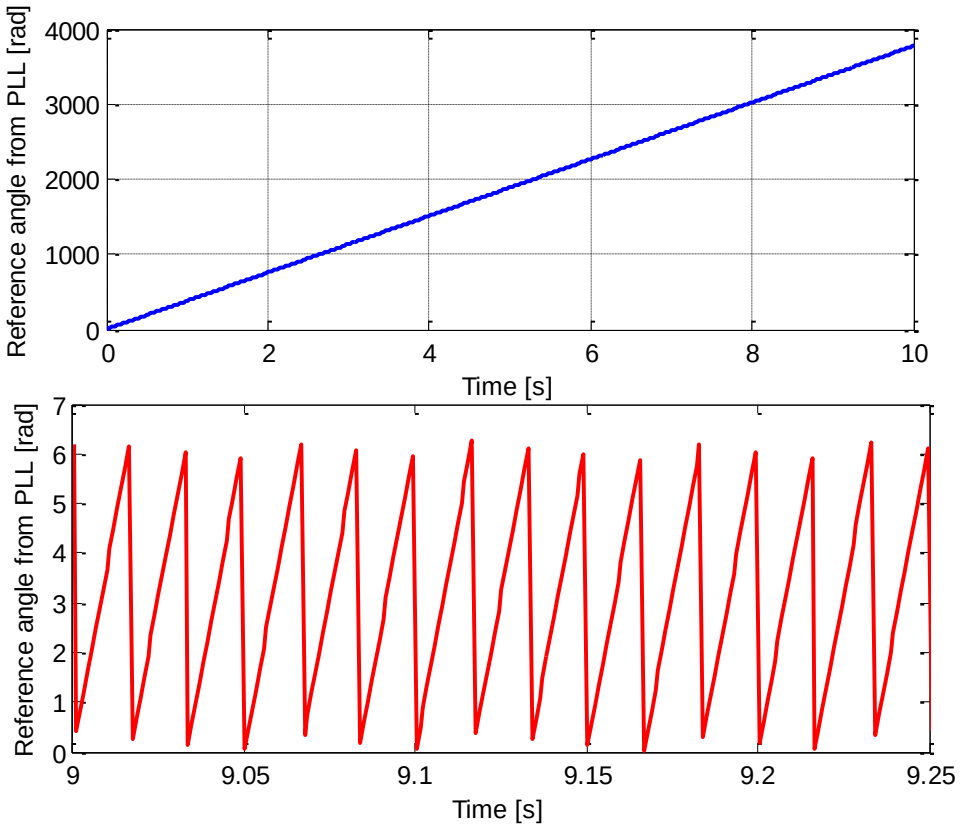

Figure 6.9 Reference angle output from PLL, θ_{se} (top) and reference angle after modular division by 2π, θ_s (bottom)

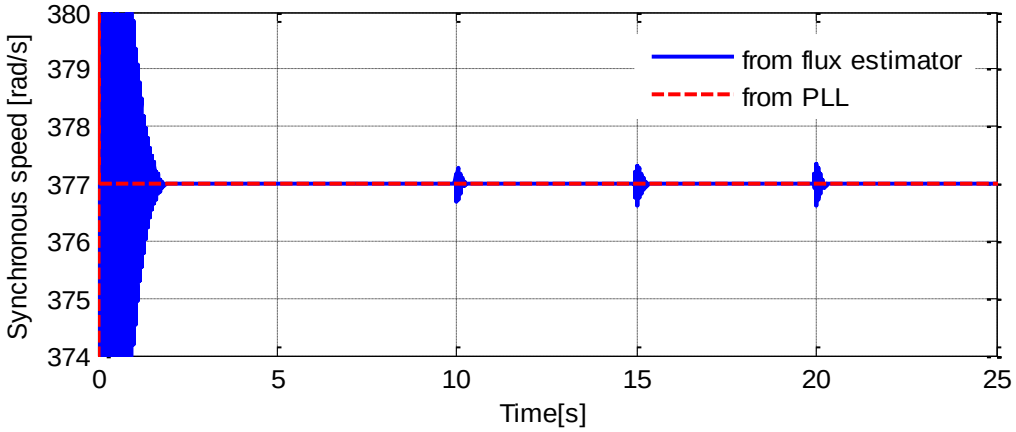

Figure 6.10 The angular synchronous frequency of the DFIG system measured by PLL and the stator flux estimator

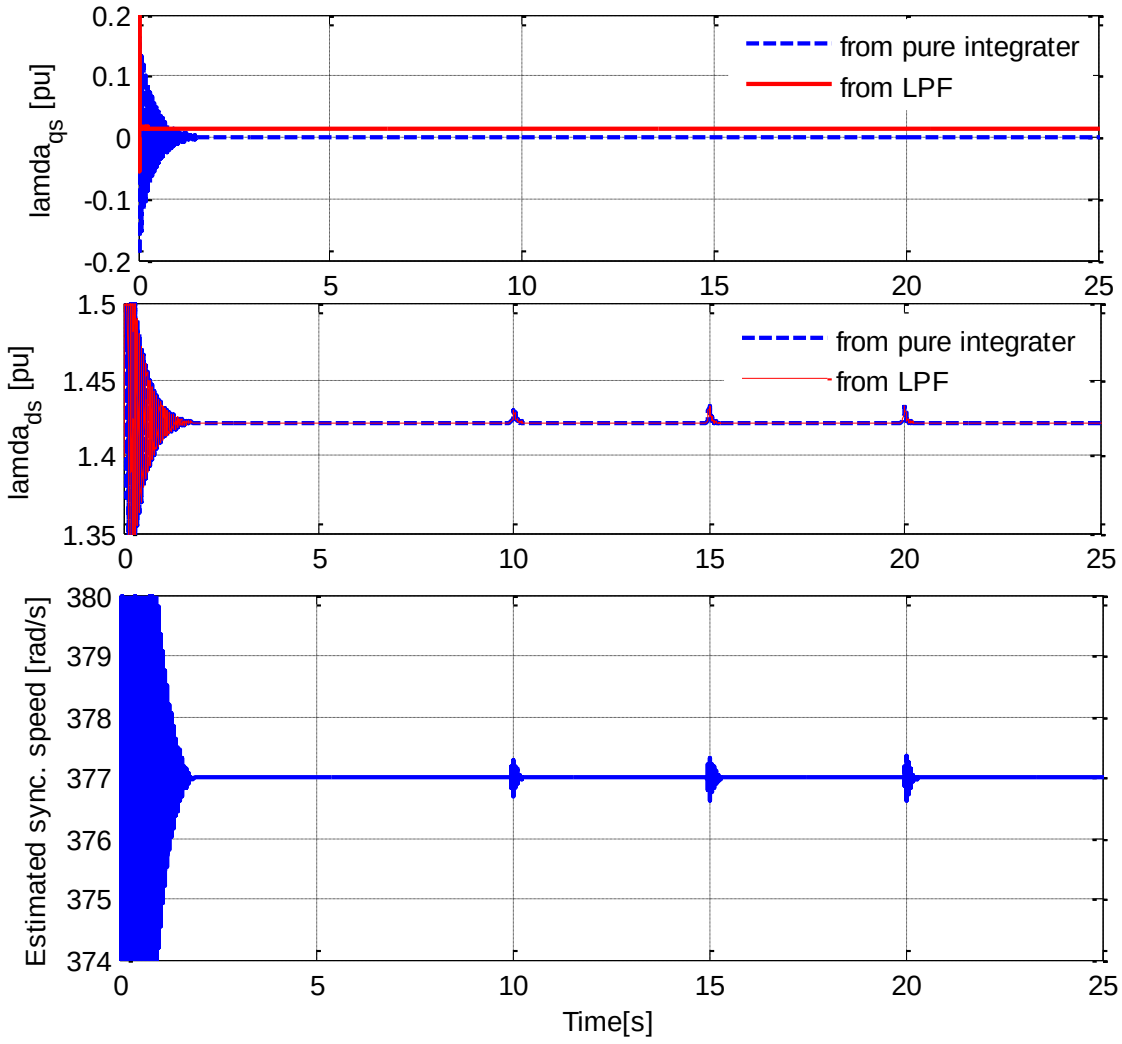

Figure 6.11 Estimated stator fluxes and synchronous speed of the machine

To assess the performance of the RSC and GSC controllers designed, four distinct case studies are done.

Case I: Constant wind speed

In this case, the wind speed to the DFIG is maintained constant at 11.5 m/s and the series compensation level is varied to analyze the effect of increasing compensation

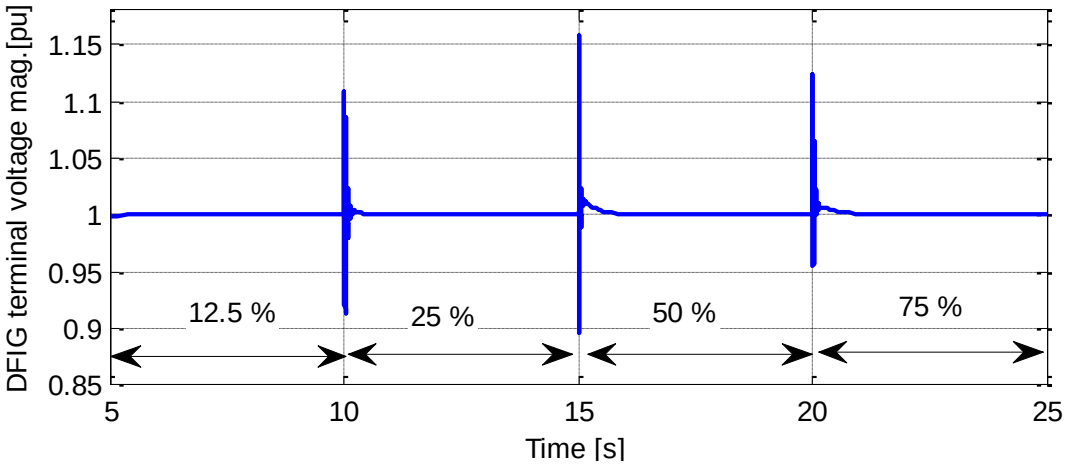

Figure 6.12 DFIG terminal voltage at various compensation levels

level. As shown in Figure 6.13(c), as the compensation level increases, the reactive power consumption in the transmission line decreases. As a result, the reactive power demand requirement to maintain constant terminal voltage reduces. The series compensation also helps to increase the power transfer capability in the transmission line as depicted in Figure 6.14(a). With the increase in compensation level, the voltage across series capacitor increases (see Figure 6.14(c)) as a result more reactive power will be supplied to the grid shown in Figure 6.14(b).

Case II: Varying wind speed with 50% compensation level

In this case, the wind speed to the DFIG is varied from 6 to 12 m/s and 50% series compensation level is maintained to analyze the effect of varying output power from DFIG. As shown in Figure 6.16(c), as the wind speed increases, the power output from

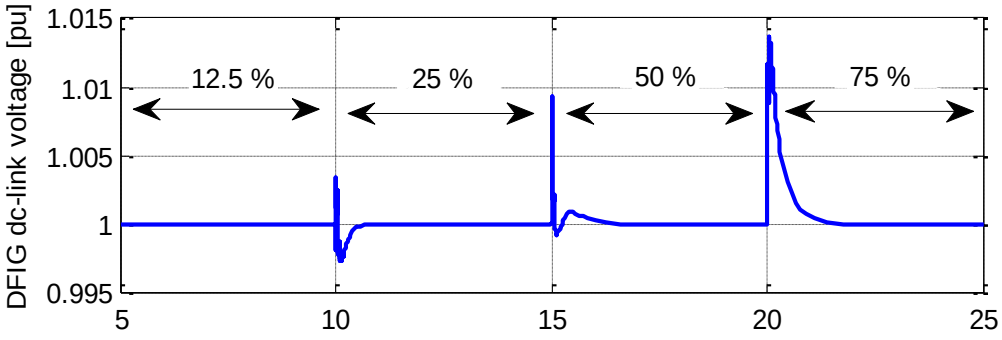

(a)

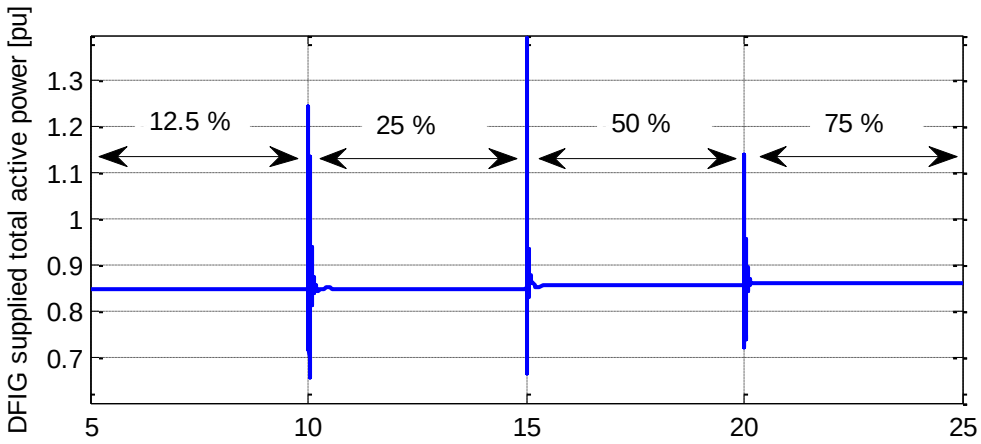

(b)

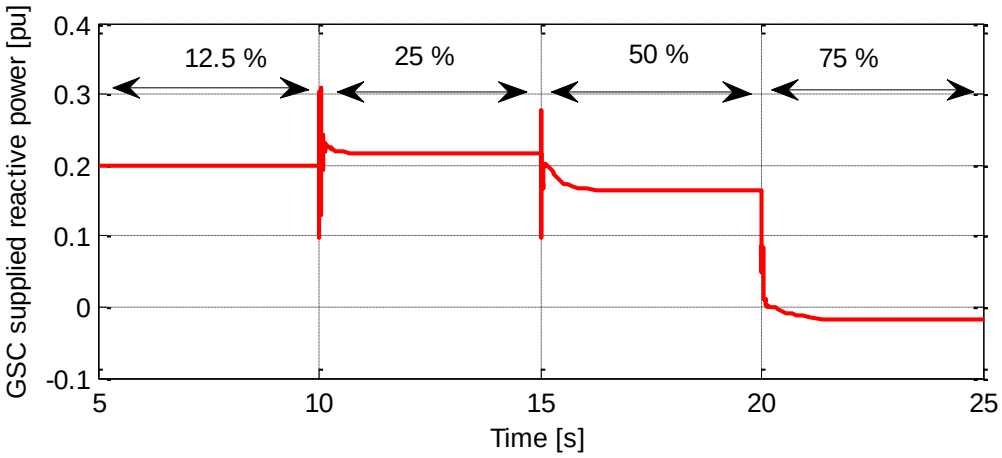

(c)

Figure 6.13 (a) DC-link voltage in DFIG, (b) DFIG supplied total active power and (c) GSC supplied reactive power at various compensation levels

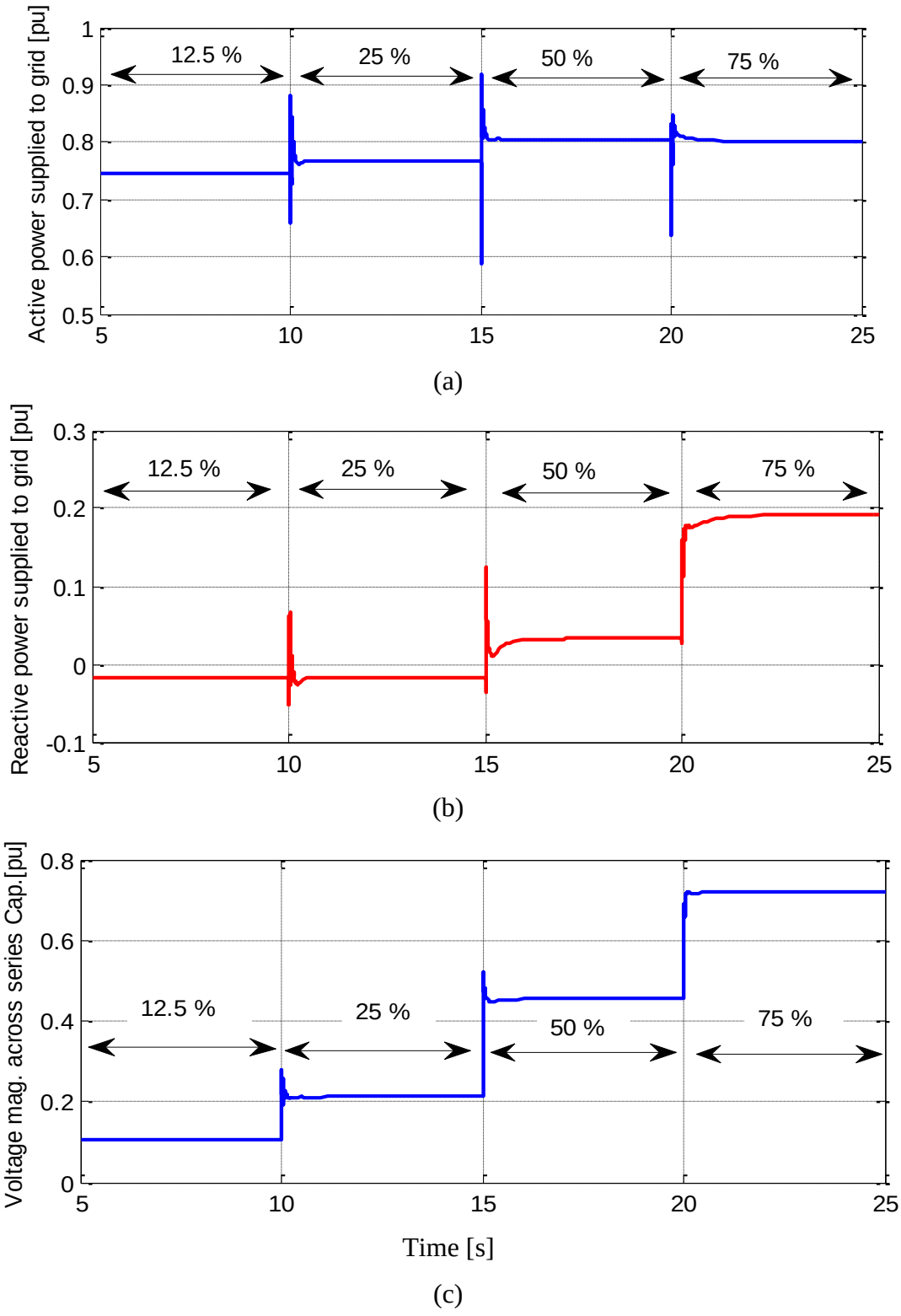

Figure 6.14 (a) Active power supplied to grid, (b) Reactive power supplied to grid and (c) Voltage across series capacitor at various compensation levels

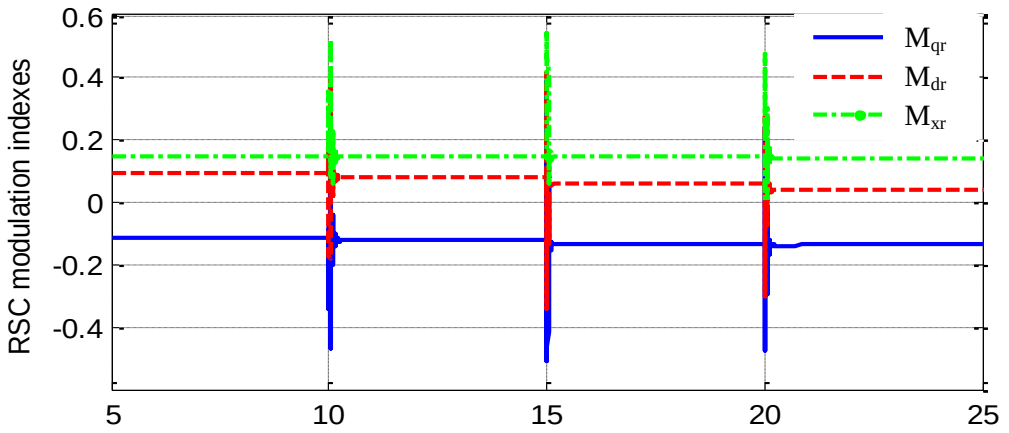

(a)

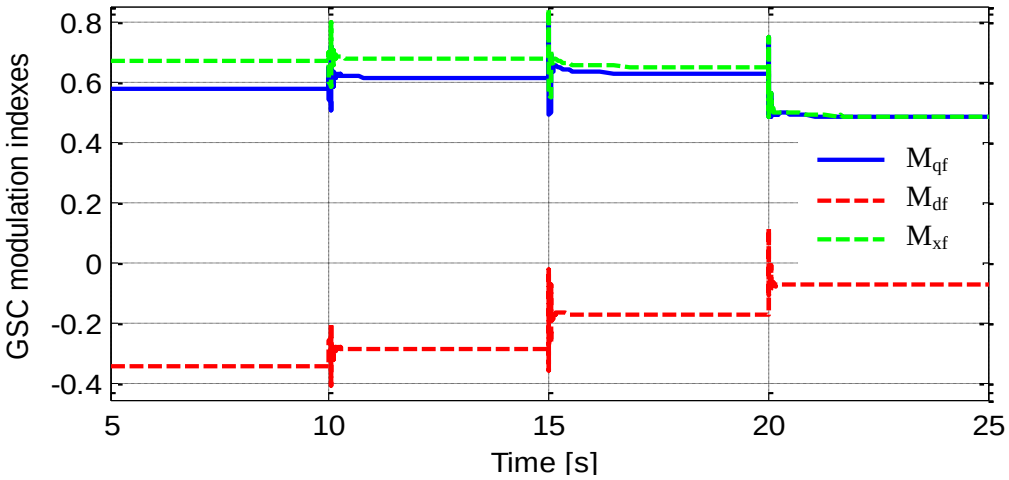

(b)

Figure 6.15 (a) RSC modulation indexes and (b) GSC modulation indexes

the DFIG increases and DFIG supplies reactive power proportional to active power output (see Figure 6.17 (a)) to maintain constant terminal voltage at DFIG terminal bus as portrayed in Figure 6.16(b). When the current in transmission line increases, the series capacitor generates more reactive power because at higher current through the capacitor, the voltage across the capacitor increases as shown in Figure 6.18(b) which shows the self voltage regulating behaviour of the series compensation.

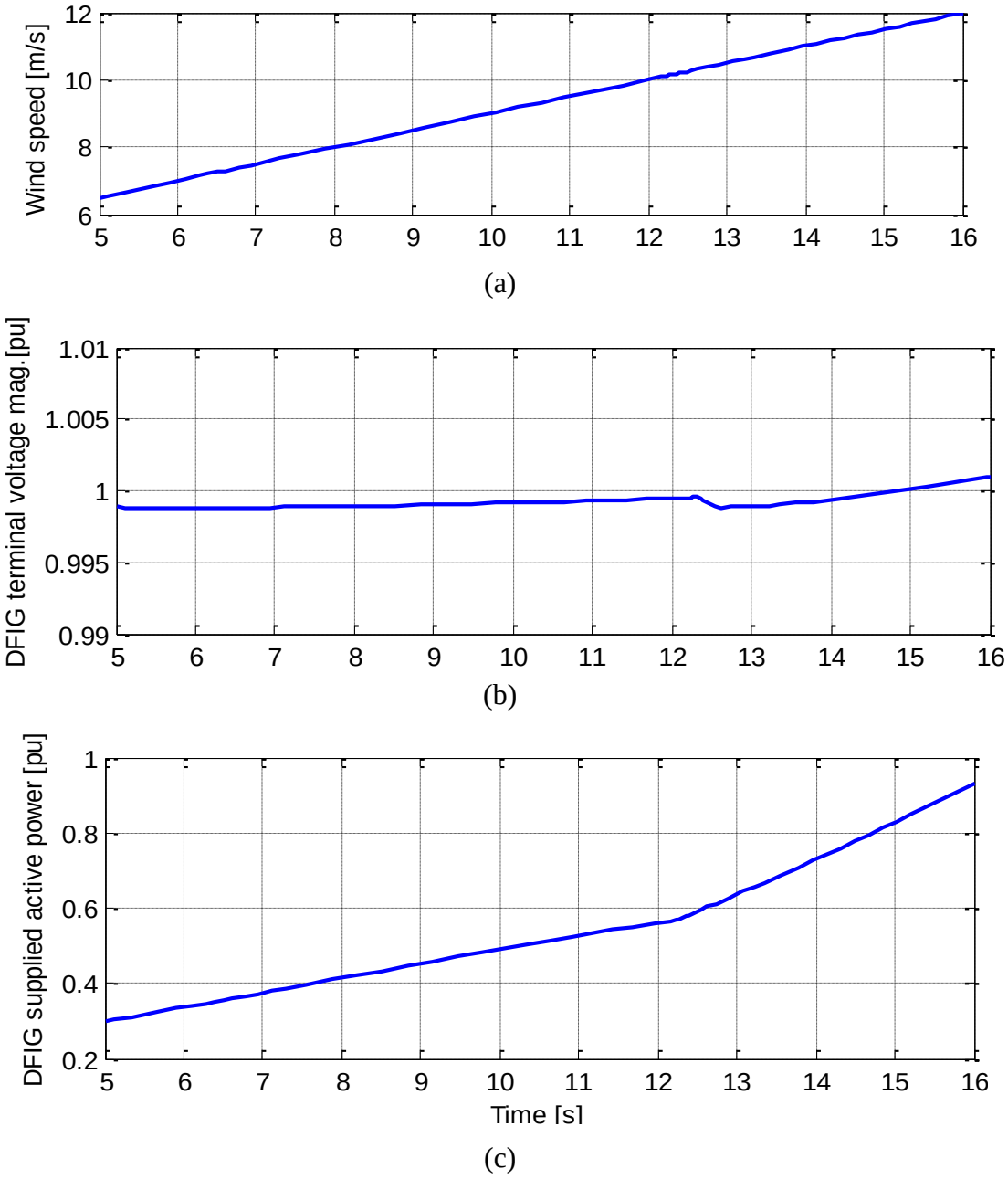

Figure 6.16 (a) Wind speed, (b) DFIG terminal voltage and (c) DFIG supplied active power during varying wind and 50% compensation level

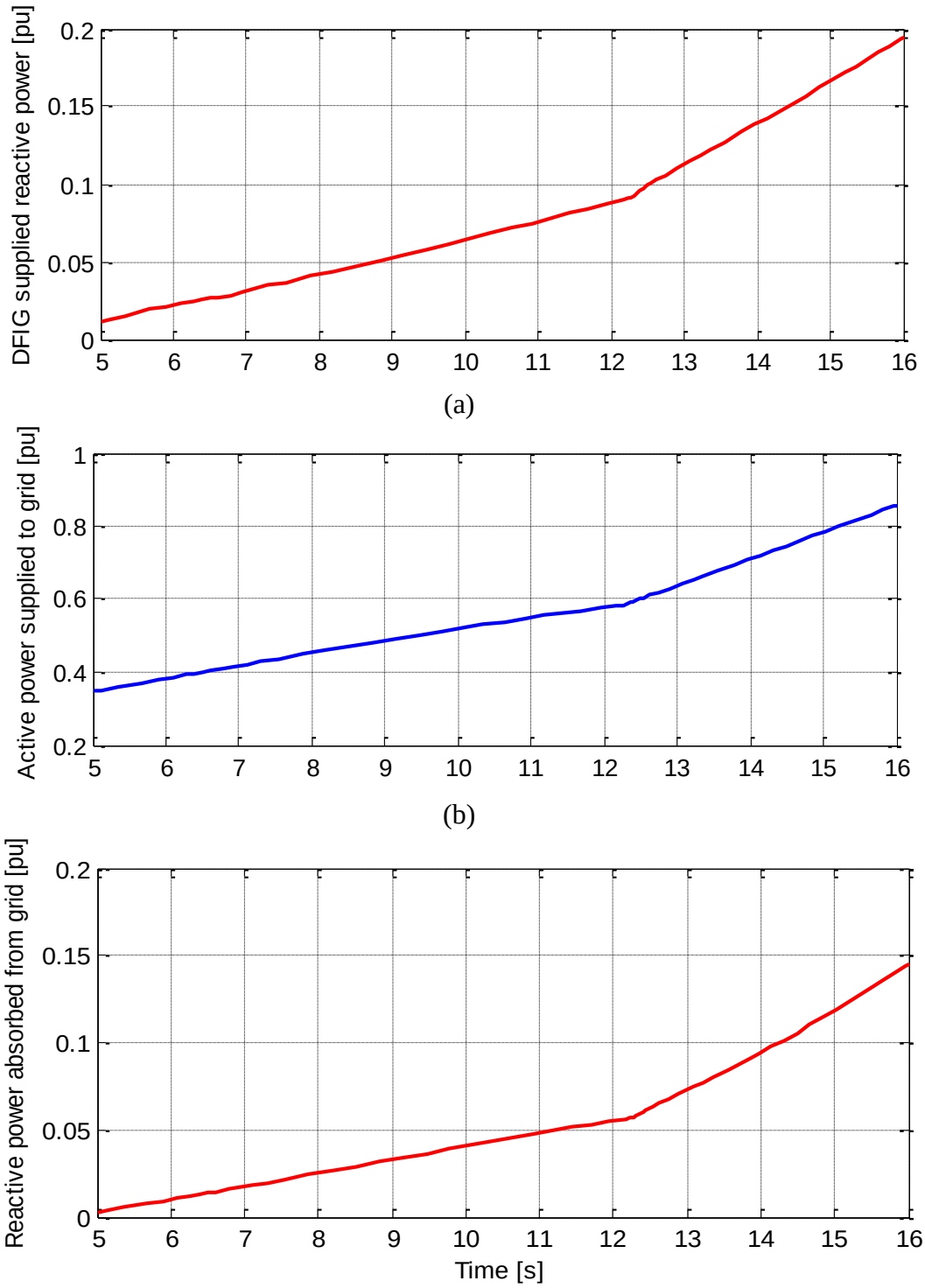

Figure 6.17 (a) DFIG supplied reactive power, (b) Active power supplied to grid and (c) Reactive power absorbed from the grid during varying wind and 50% compensation level

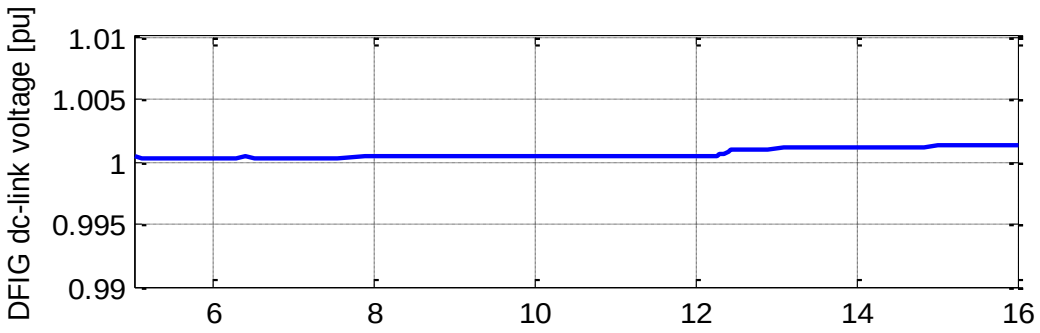

(a)

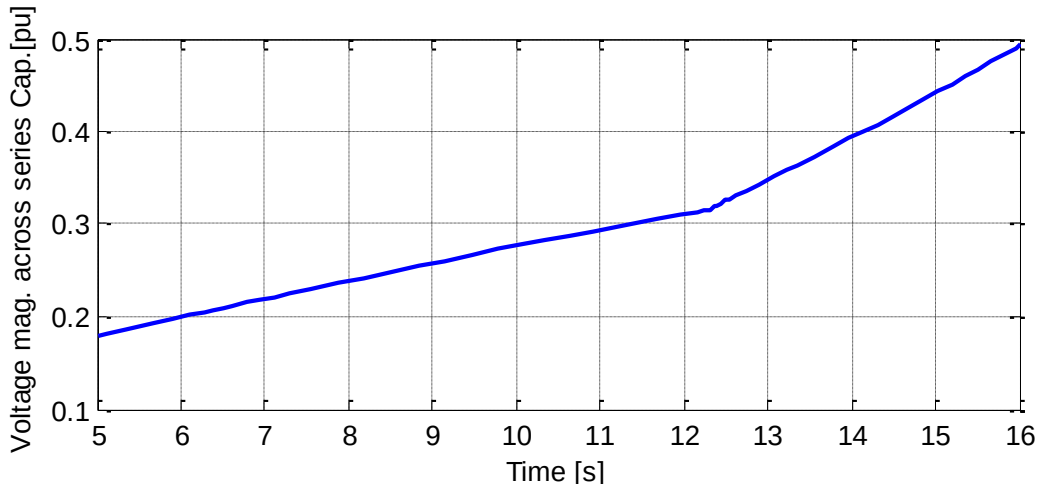

(b)

Figure 6.18 (a) DC-link voltage in DFIG and (b) Voltage magnitude across series capacitor during varying wind and 50% compensation level

The GSC regulates the DC-link voltage constant for the whole operation period. Similarly, the magnitude of modulation indexes in GSC and RSC are less than 1 as shown in Figure 6.19 during the entire operation period of the DFIG.

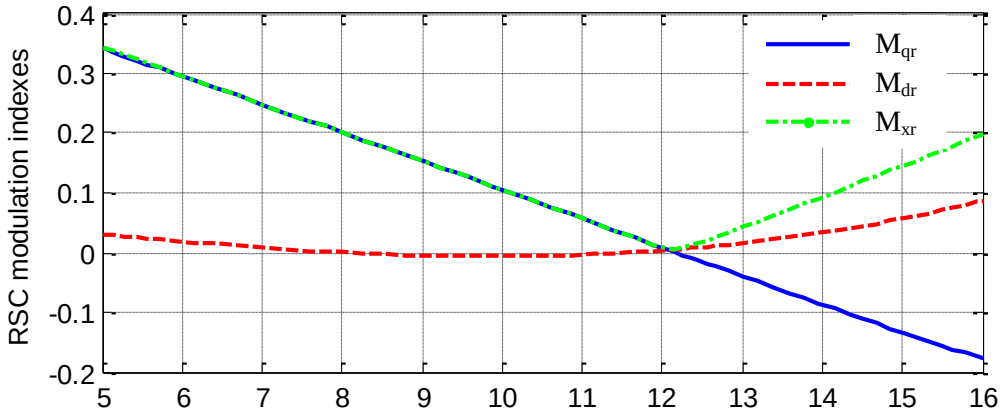

(a)

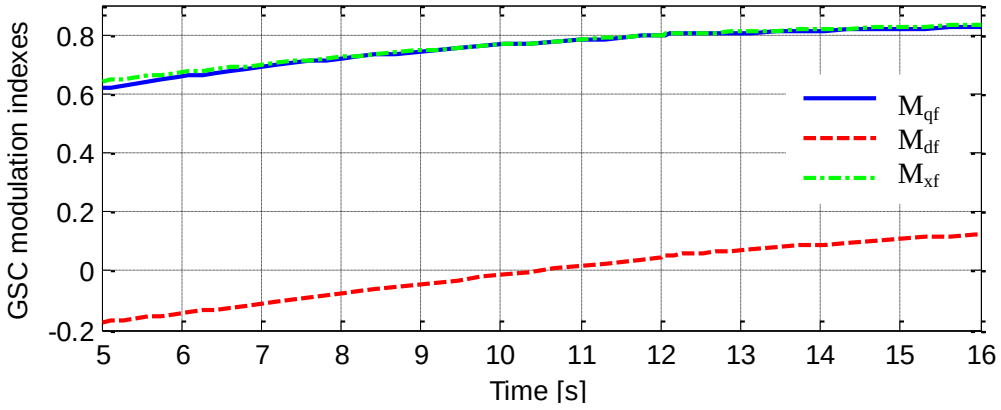

(b)

Figure 6.19 (a) RSC modulation indexes and (b) GSC modulation indexes

Case III: Wind speed profile with 50% compensation:

In this case, the wind speed profile is shown in Figure 6.20 (a) and 50% series compensation level is maintained to analyze the effect of wind speed fluctuation to the overall system performance.

The GSC regulates the DC-link voltage and the DFIG terminal voltage to their rated values eventhough the wind speed fluctuates as depicted in Figure 6.20(b) and 6.20(c) respectively. When the wind speed increases, the active power output from the

DFIG also increases propertionally and the GSC has to supply more reactive power to maintain the wind turbine terminal voltage constant.

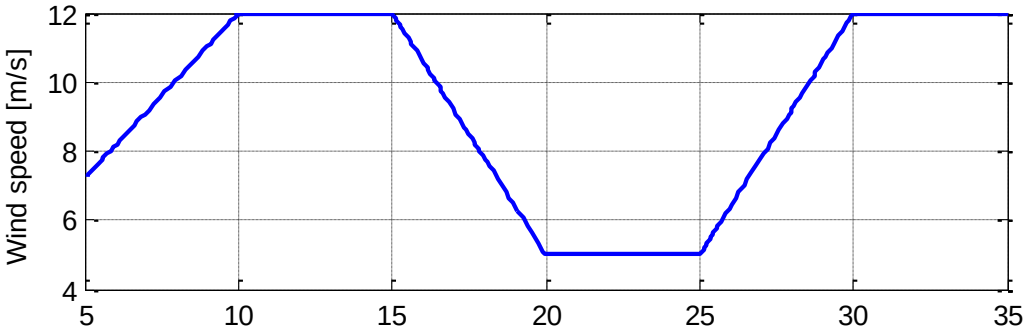

(a)

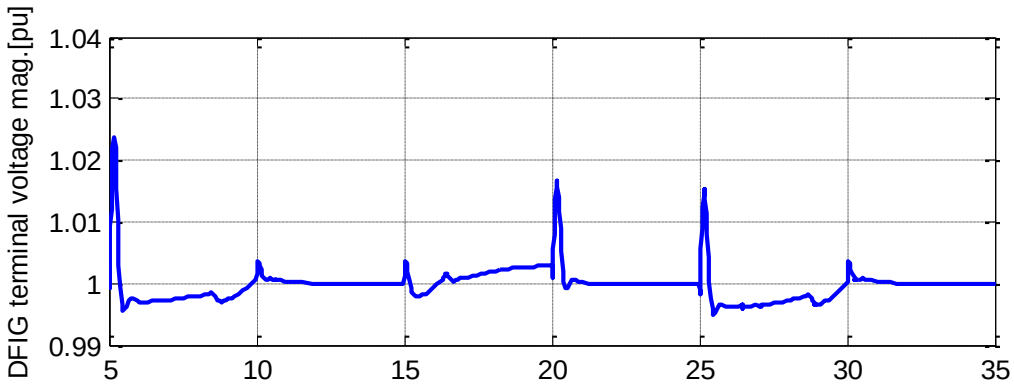

(b)

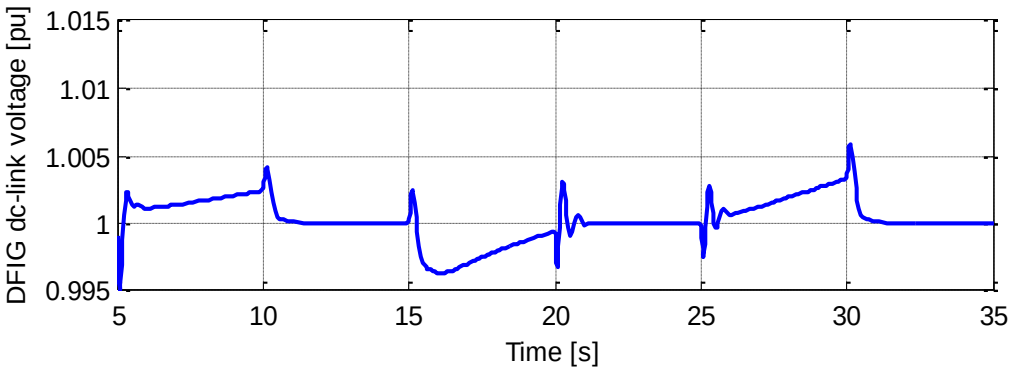

(c)

Figure 6.20 (a) Wind speed profile (b) DFIG terminal voltage and (c) DC-link voltage in DFIG

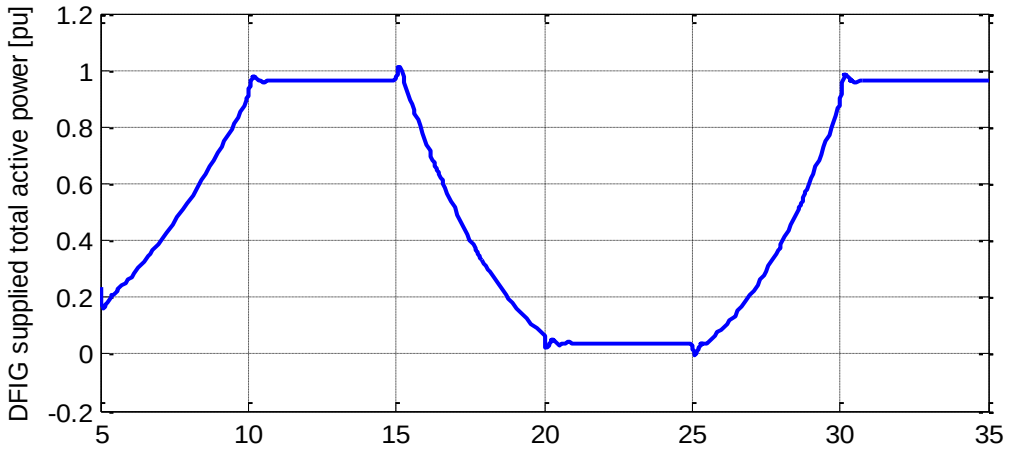

(a)

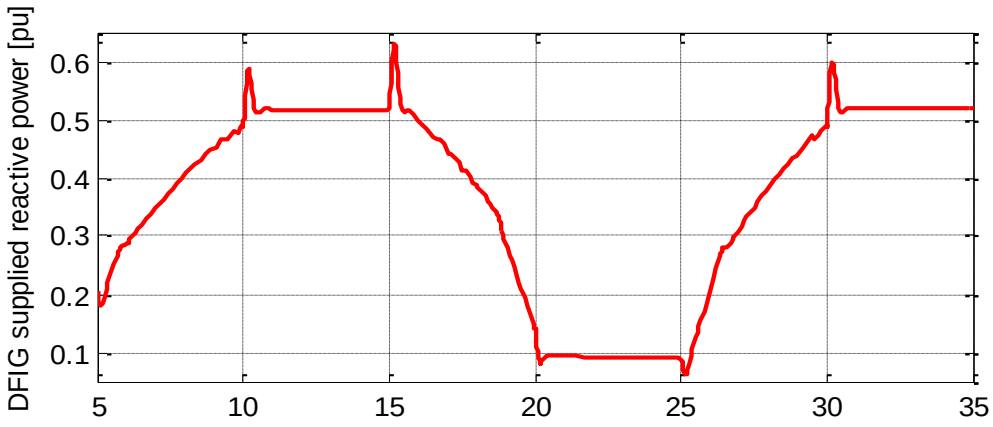

(b)

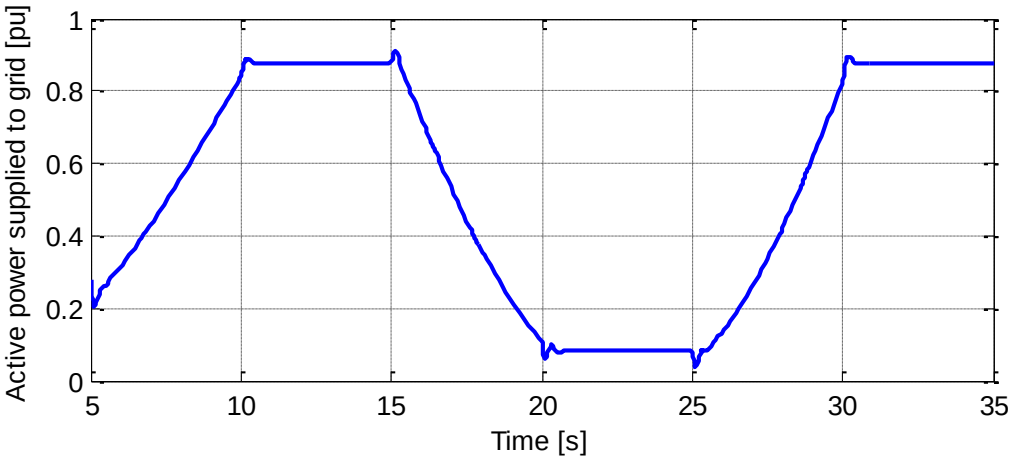

(c)

Figure 6.21 (a) DFIG generated active power (b) GSC generated reactive power and (c) Active power supplied to grid

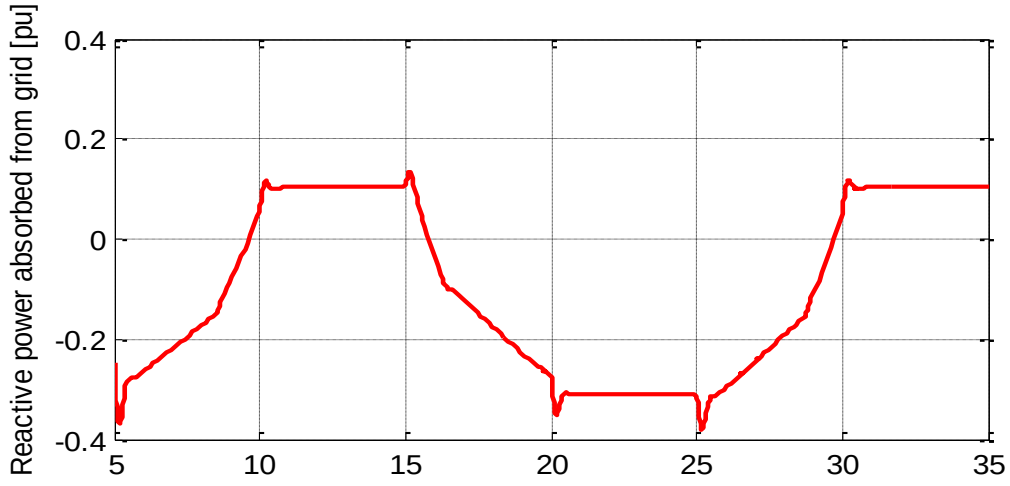

(a)

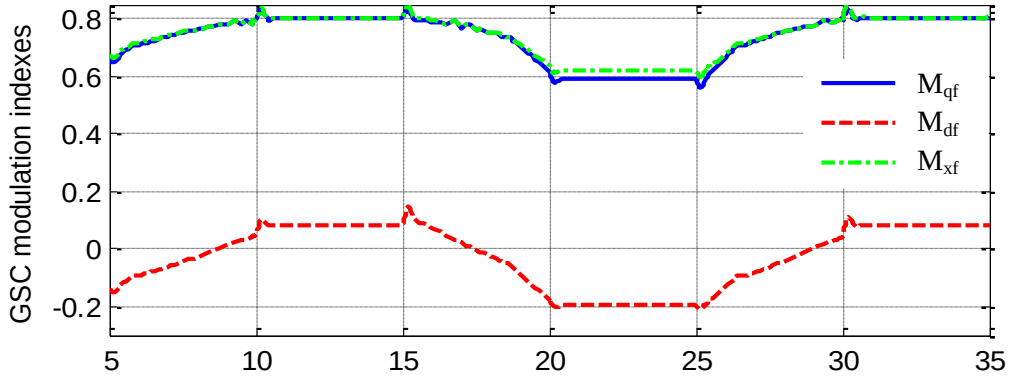

(b)

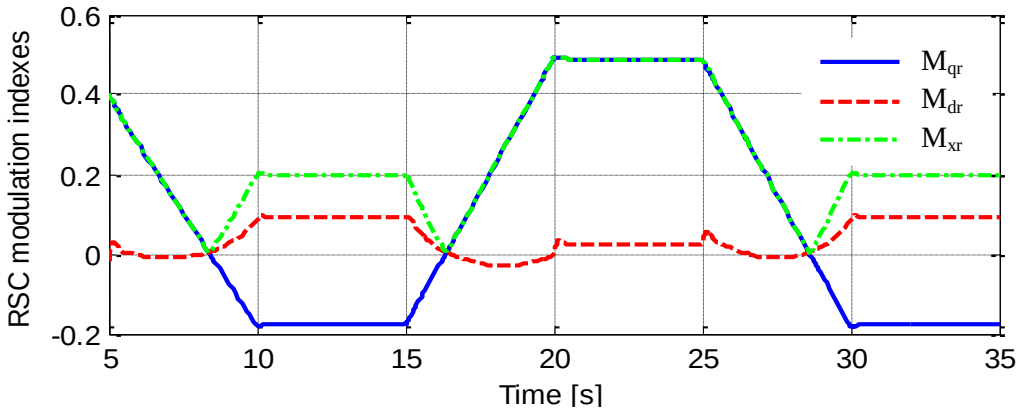

(c)

Figure 6.22 (a) Reactive power absorbed from the grid (b) GSC modulation indexes and (c) RSC modulation indexes

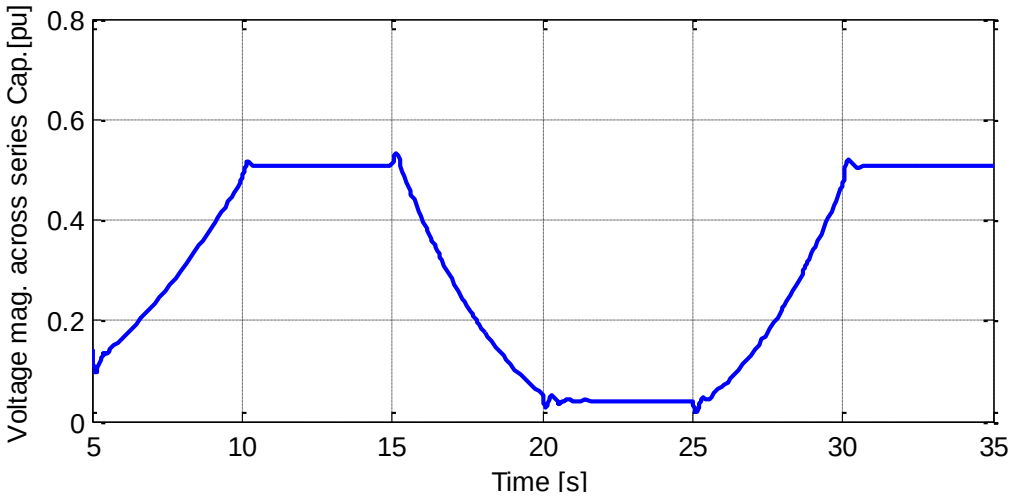

Figure 6.23 Voltage magnitude across series capacitor

Case IV: Wind speed profile with 25% compensation:

In this case, the wind speed profile is shown in Figure 6.24(a) and 25 % series compensation level is maintained to analyze the effect of varying wind speed to the overall system.

All the observations are similar to what is observed in case III. The only noticeable difference being the amount of reactive power GSC has to supply to maintain the wind turbine terminal voltage constant. From Figures 6.21(b) and 6.25(b), it can be concluded that as the compensation level increases, the reactive power consumed by the line reactance decreases so the GSC has to generate less reactive power to maintain constant wind turbine terminal voltage.

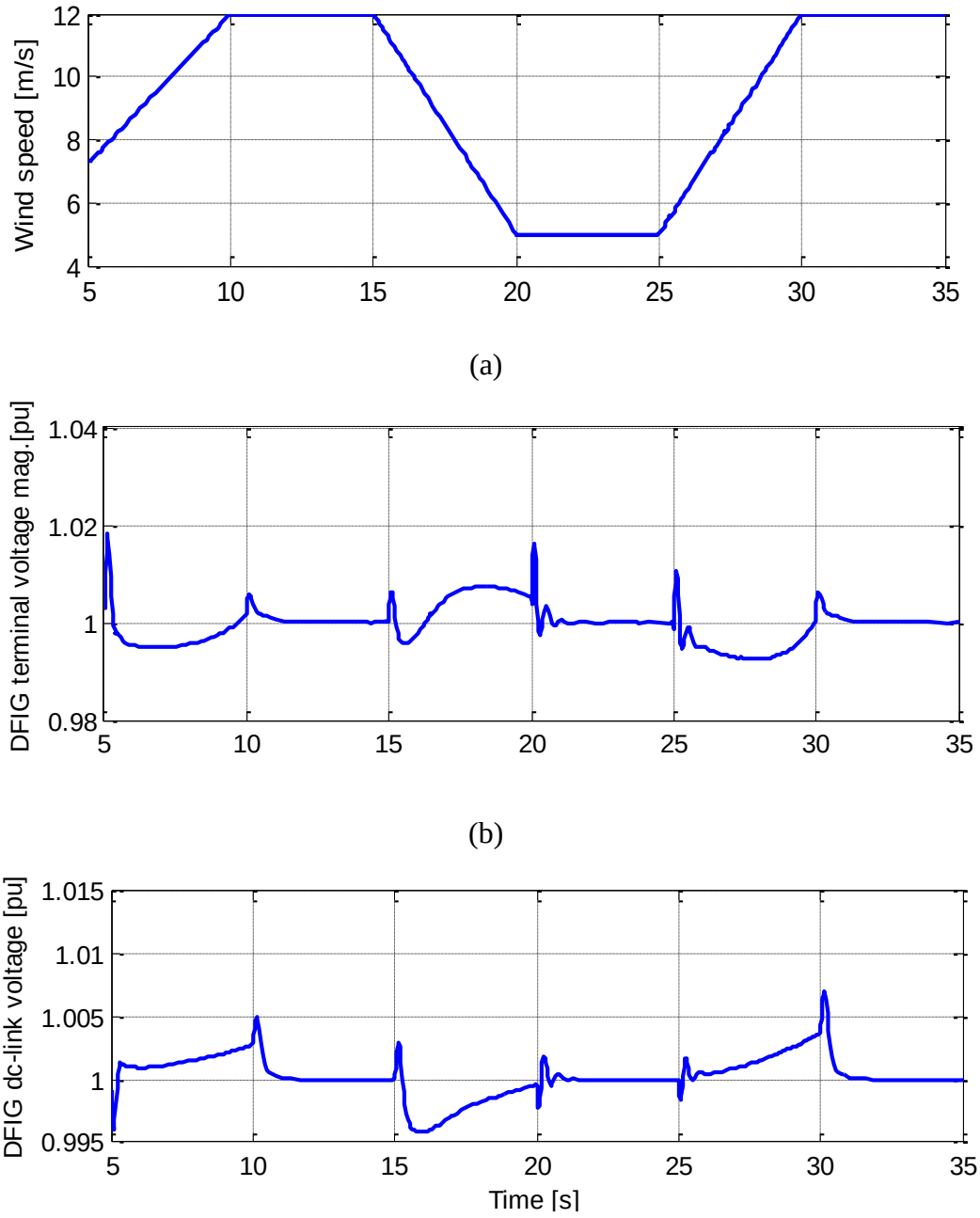

Figure 6.24 (a) Wind speed profile (b) DFIG terminal voltage and (c) DC-link voltage in DFIG

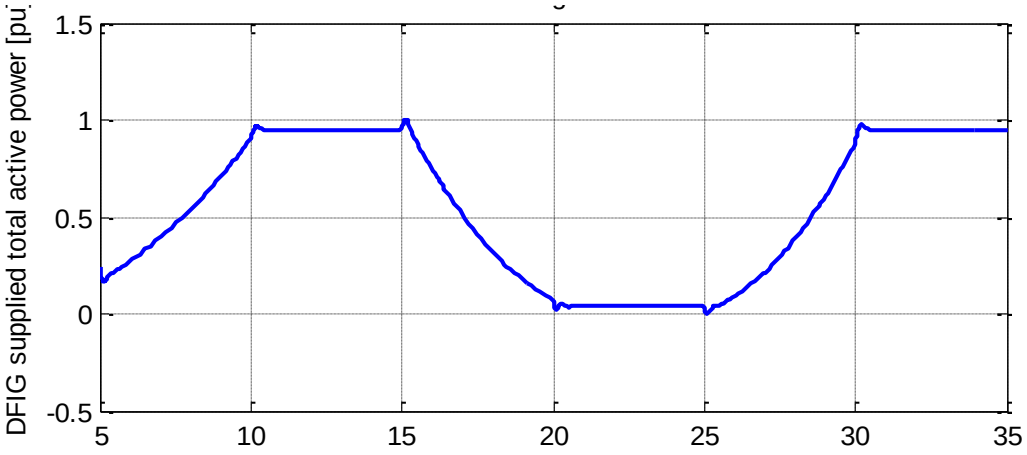

(a)

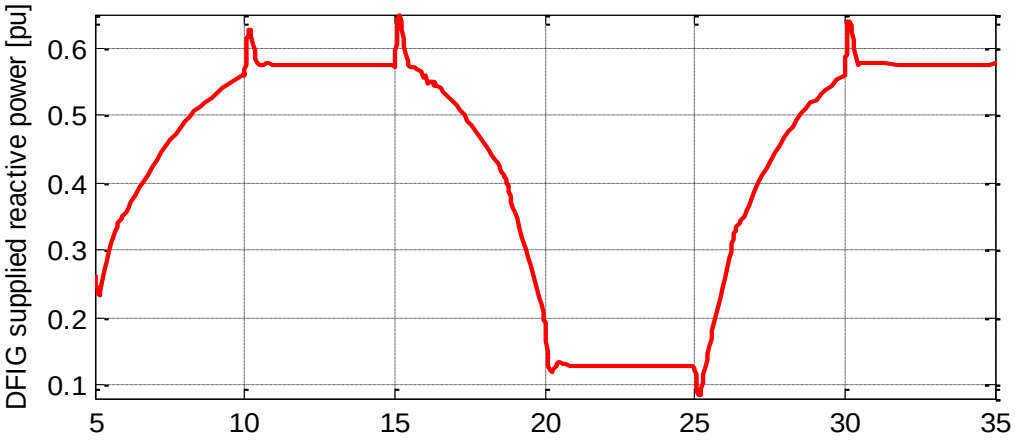

(b)

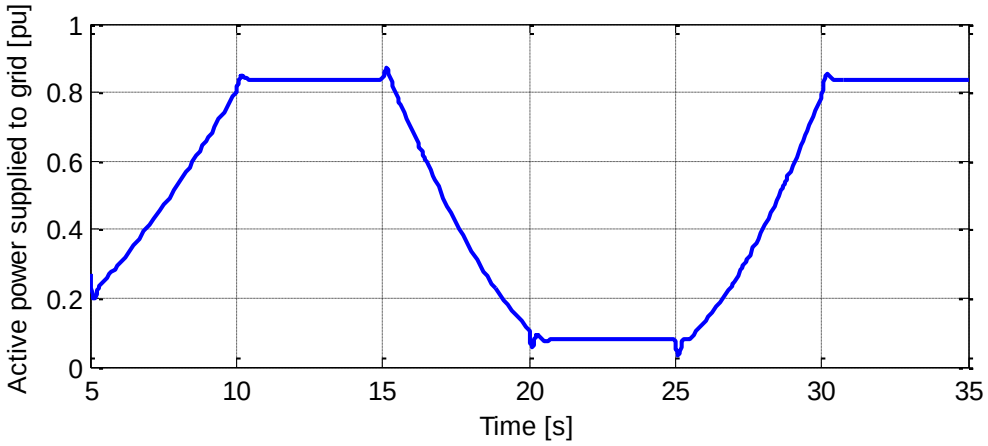

(c)

Figure 6.25 (a) DFIG generated active power (b) GSC generated reactive power and (c) Active power supplied to grid

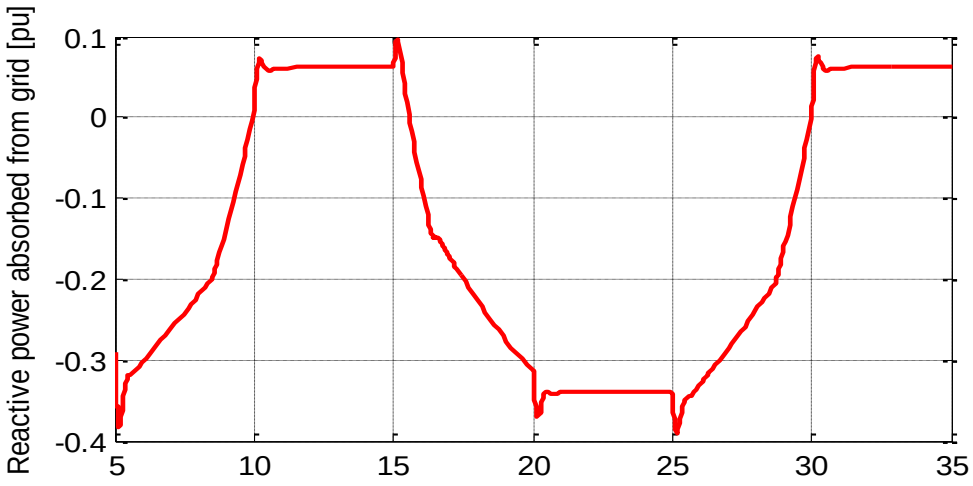

(a)

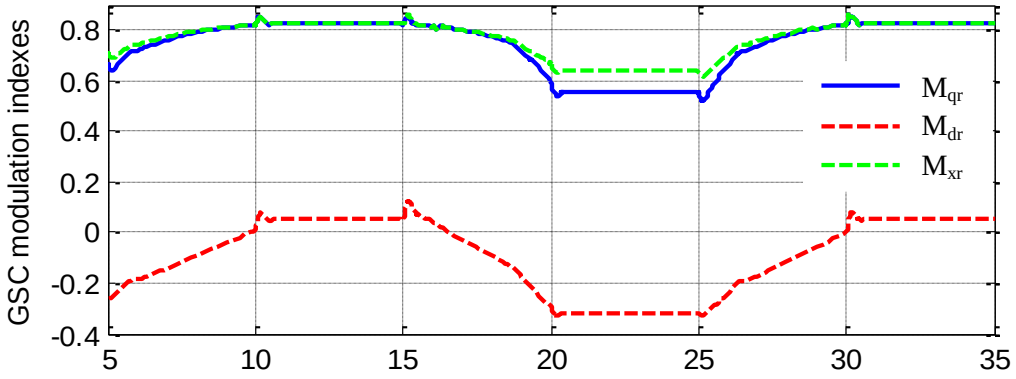

(b)

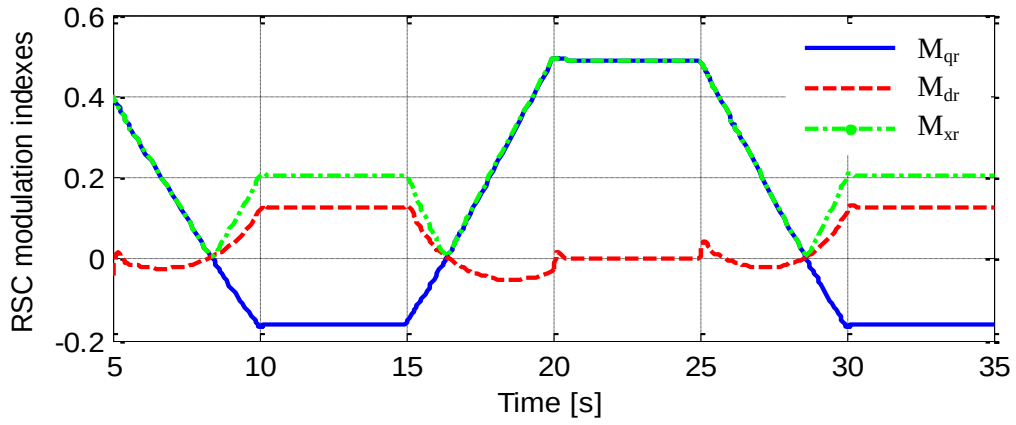

(c)

Figure 6.26 (a) Reactive power drawn from the grid (b) GSC modulation indexes and (c) RSC modulation indexes

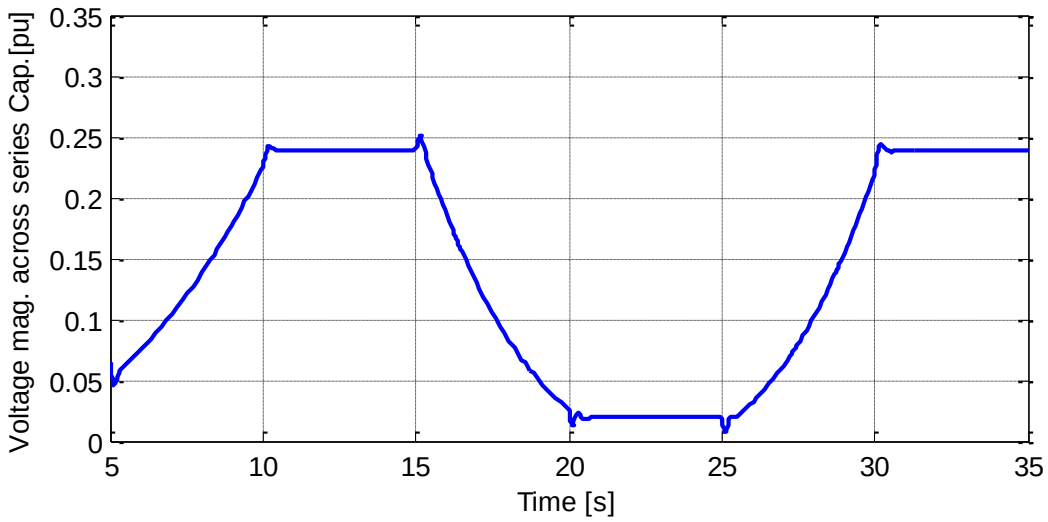

Figure 6.27 Voltage magnitude across series capacitor

Therefore, from the dynamic simulation study of the terminal voltage controller in the DFIG interfaced with series compensated line, it is observed that as the compensation level increases, the consumption of the reactive power in the transmission line decreases and the power carrying capability of the line increases. It is also noticed that as the loading of the line increases, the reactive power demand in the uncompensated line increases because the line consumes more reactive power but in case of the compensated line, series capacitor generates more reactive power at higher loading so reactive power demand doesnot increases significantly hence the GSC does not need to supply more reactive power to maintain constant terminal voltage magnitude at the wind turbine.

6.4 Series Compensated Power Grid

To study the effect of series compensation in the performance of the transmission line with regard to voltage regulation and power transmission capability enhancement, a test system model shown in Figure 6.28 is built. The bus-1 is generator terminal bus and the bus-2 is grid. The grid voltage is assumed to be known. The active power (P) injected to the system is varied at bus-1 so as to study the effect of active power loading in the line. The reactive power (Q) supplied to the system is also varied to study the effect of power factor variation on the voltage regulation of the bus-1. The steady state performance of this test system is studied by varying the series compensation level of the line for voltage regulation and power carrying capability enhancement of the line.

The steady state equations of the series compensated line are discussed here. The active (P) and reactive (Q) power injected at bus-1 is modeled by varying the q and d-axis current given by (6.103) and (6.104) which are derived as:

$$S = \frac{3}{2} V_{qdt} I_{qd1}^{*} \tag{6.103}$$

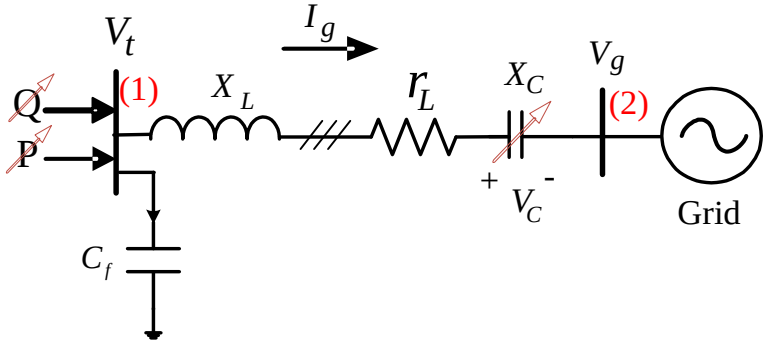

Figure 6.28 Schematic diagram of the series compensated two bus test power system

$$I_{qd1} = \frac{2}{3}\frac{S^*}{V_{qdt}^*} \tag{6.104}$$

where, $V_{qdt} = V_{qt} + jV_{dt}$, $I_{qd1} = I_{q1} + jI_{d1}$ and $S = P - jQ$ and I_{qd1} is current generated from the generator and V_{qdt} is the instantaneous voltages at bus-1 and $S = P - jQ$ is the apparent power injected at bus-1. The steady state bus-1 voltage in complex form is given as:

$$-j\omega_e C_f V_{qdt} = I_{qd1} - I_{qdg} \tag{6.105}$$

The steady state current flowing through the series compensated line is given as:

$$I_{qdg} = -j\omega_e C V_{cqd} \tag{6.106}$$

Using KVL from bus-1 to the bus-2:

$$V_{qdt} - V_{qdg} = r_L I_{qdg} - j\omega_e L_L I_{qdg} + V_{cqd} \tag{6.107}$$

Different power factor (pf) operation at the bus-1 is studied by relating active and reactive power supplied by the generator at bus-1 given as:

$$Q = \tan\left(\cos^{-1}(pf)\right) * P \tag{6.108}$$

Here, the objective is to vary the active and reactive power and study the voltage profile at bus-1 (V_{qdt}). Since we have four steady state equations and four unknowns which are: I_{qd1}, I_{qgd}, V_{qdt} and V_{cqd}.

From (6.107) and (6.107)

$$V_{qdt} - V_{qdg} = (r_L - j\omega_e L_L)(-j\omega_e C V_{cqd}) + V_{cqd} \tag{6.109}$$

$$V_{qdt} - V_{qdg} = (Z_{lc} - j\omega_e C\, r_L) V_{cqd} \tag{6.110}$$

where $Z_{lc} = (1 - \omega_e^{\,2} L_L C)$, from (6.105)

$$I_{qdg} = I_{qd1} + j\omega_e C_f V_{qdt} \tag{6.111}$$

From (6.104) and (6.111):

$$I_{qdg} = \frac{2}{3}\frac{S^*}{V_{qdt}^*} + j\omega_e C_f V_{qdt} \tag{6.112}$$

From (6.106) and (6.112):

$$\frac{2}{3}\frac{S^*}{V_{qdt}^*} + j\omega_e C_f V_{qdt} = -j\omega_e C V_{cqd} \tag{6.113}$$

$$V_{cqd} = \frac{2}{3\omega_e C}\frac{S^*}{V_{qdt}^*} - \frac{C_f V_{qdt}}{C} \tag{6.114}$$

From (6.110) and (6.114):

$$V_{qdt} - V_{qdg} = (Z_{lc} - j\omega_e C\, r_L)\left(j\frac{2}{3\omega_e C}\frac{S^*}{V_{qdt}^*} - \frac{C_f V_{qdt}}{C} \right) \tag{6.115}$$

$$V_{qdt}\left(1 + Z_{lc}\frac{C_f}{C} - j\omega_e C_f r_L\right) - V_{qdg} = \frac{2}{3}\frac{S^*}{V_{qdt}^*}\left(r_L + j\frac{Z_{lc}}{\omega_e C}\right) \tag{6.116}$$

$$V_{qdt}\left(1 + Z_{lc}\frac{C_f}{C} - j\omega_e C_f r_L\right) = \frac{2}{3}\frac{S^*}{\left|V_{qdt}\right|^2}\left(r_L + j\frac{Z_{lc}}{\omega_e C}\right)V_{qdt} + V_{qdg} \tag{6.117}$$

Separating (6.117) into real and imaginary parts gives:

$$\left(1 + Z_{lc}\frac{C_f}{C}\right)V_{qt} + \omega_e C_f r_L V_{dt} = \frac{2}{3\left|V_{qdt}\right|^2}\left\{\left(\mathrm{Pr}_L - \frac{QZ_{lc}}{\omega_e C}\right)V_{qt} - \left(\frac{PZ_{lc}}{\omega_e C} + Qr_L\right)V_{dt}\right\} + V_{qg} \tag{6.118}$$

$$\left(1 + Z_{lc}\frac{C_f}{C}\right)V_{dt} - \omega_e C_f r_L V_{qt} = \frac{2}{3\left|V_{qdt}\right|^2}\left\{\left(\mathrm{Pr}_L - \frac{QZ_{lc}}{\omega_e C}\right)V_{dt} + \left(\frac{PZ_{lc}}{\omega_e C} + Qr_L\right)V_{qt}\right\} + V_{dg} \tag{6.119}$$

Solving (6.118) and (6.119) simultaneously in MATLAB gives the V_{qt} and V_{dt} for various values of P and Q. Then the terminal voltage magnitude is calculated as:

$$\left|V_{qdt}\right|^2 = V_{qt}^2 + V_{dt}^2 \tag{6.120}$$

Case I: Unity power factor operation:

In this case, the reactive power supplied is zero as shown in Figure 6.29(a). In this operation mode, higher compensation level gives better voltage profile through out the variation of active power from zero to 100 % as shown in Figure 6.29(b). It is because the higher compensated line generates more reactive power as the current flowing in the line increases, i.e., self-regulation property of series compensated line.

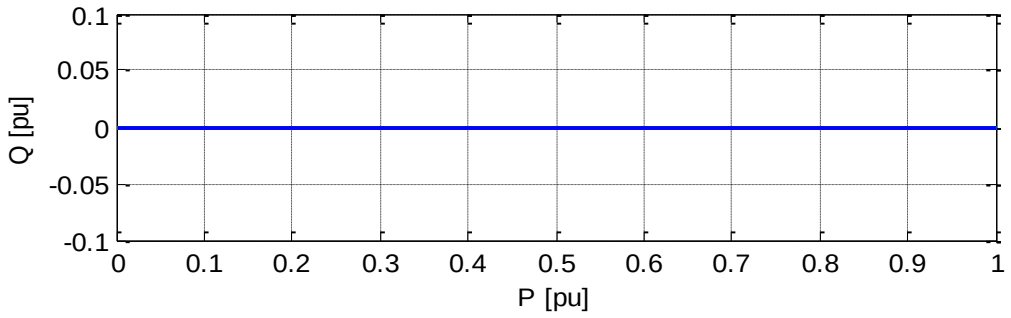

(a)

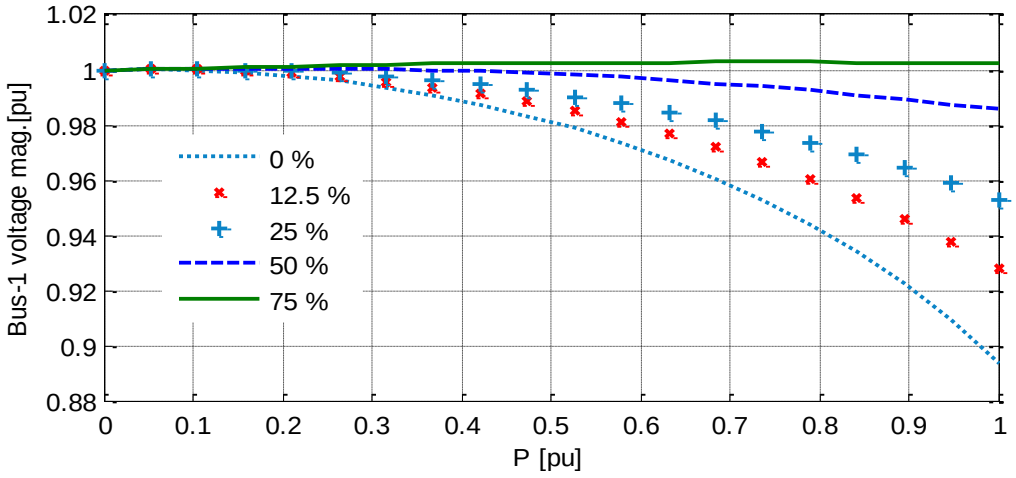

(b)

Figure 6.29 (a) Reactive power supplied at bus-1 and (b) Voltage magnitude at bus-1

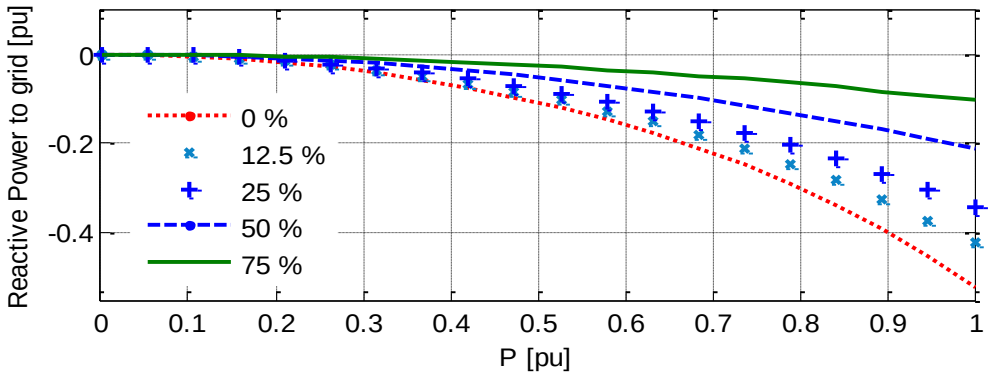

(a)

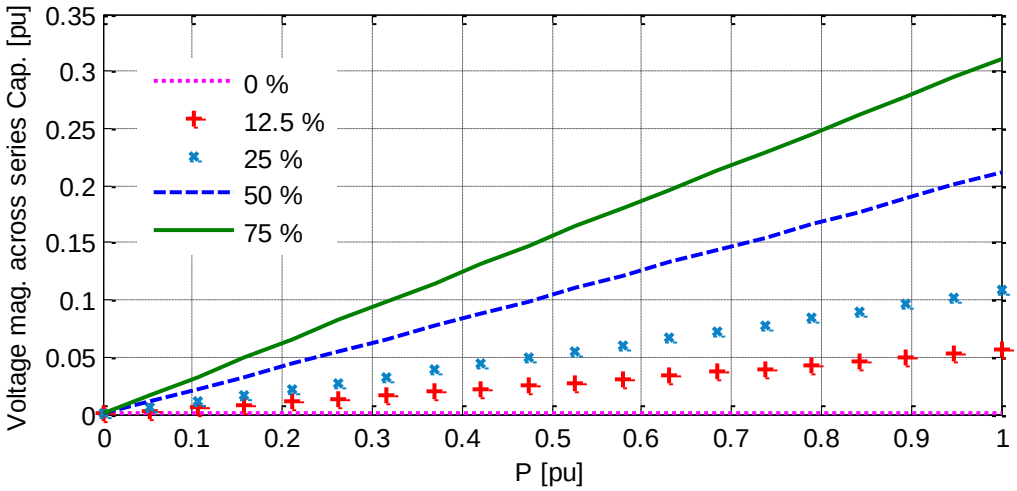

(b)

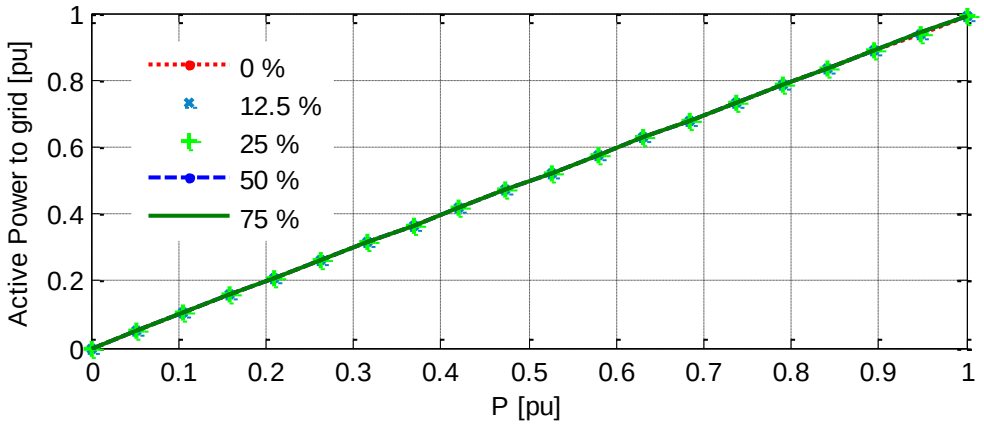

(c)

Figure 6.30 (a) Reactive power supplied to grid (-ve means absorption from grid), (b) Voltage across series capacitor and (c) Active power to grid

Case II: 0.8 leading power factor operation:

In this case, the reactive power is supplied to the transmission line proportional to the active power supplied at bus-1 as shown in Figure 6.31(a). In this operation mode, higher compensation level gives lower voltage profile as shown in Figure 6.31(b) because the line is over compensated, i.e. the net reactance of higher compensated line is more capacitive whereas less compensated line has net inductive impedance as a result the voltage difference between bus-1 and bus-2 can be high.

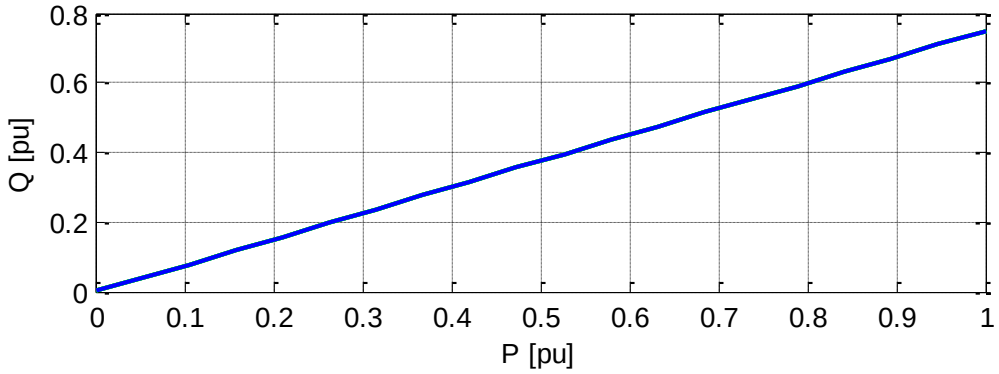

(a)

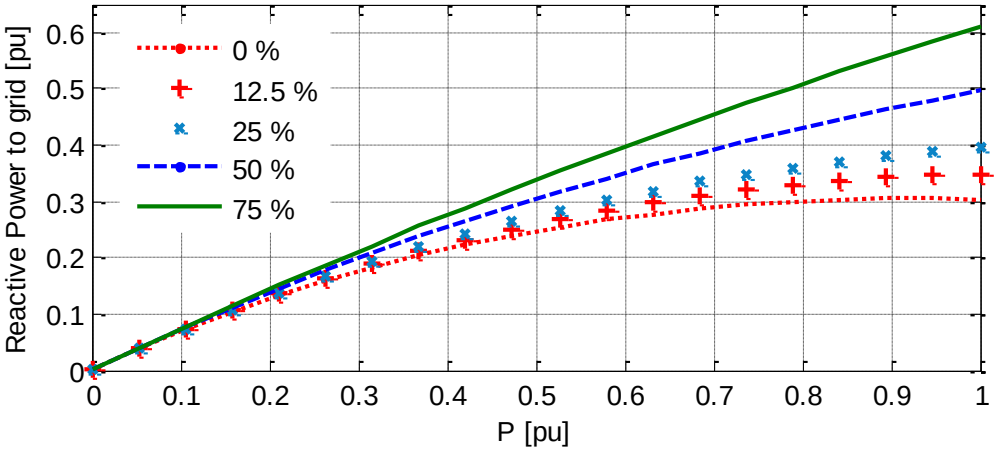

(b)

Figure 6.31 (a) Reactive power supplied at bus-1 (b) Reactive power supplied to grid

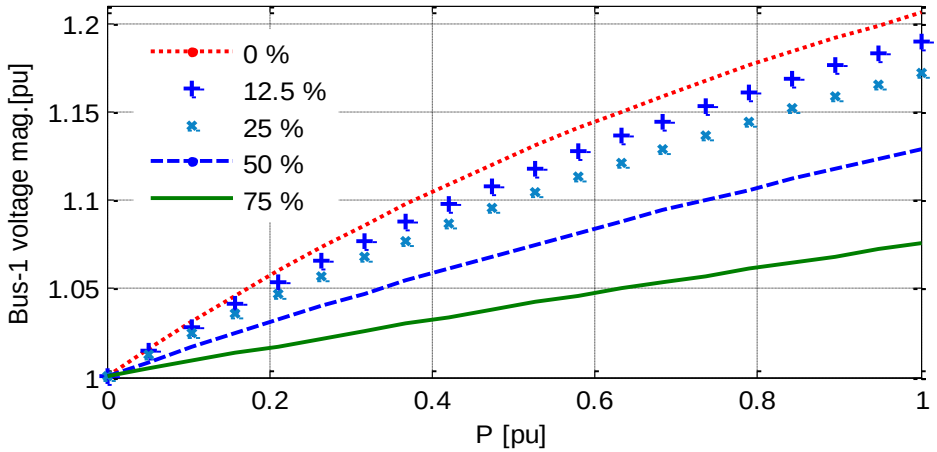

(a)

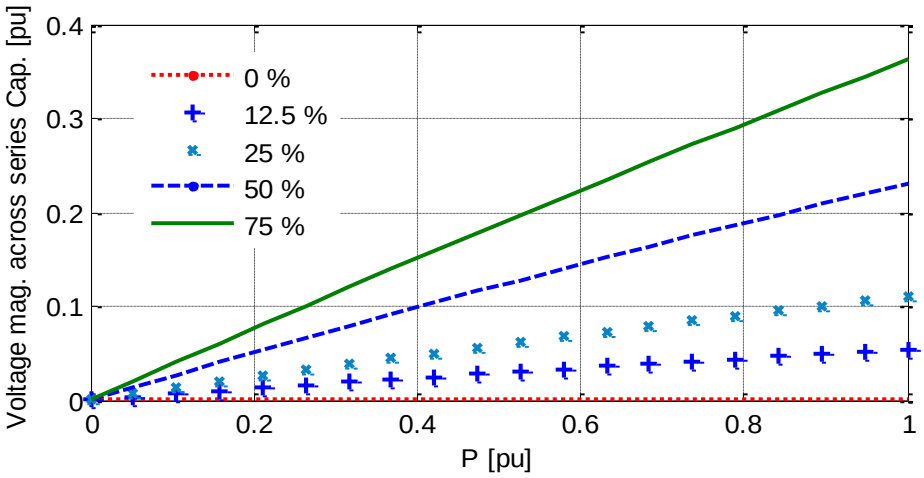

(b)

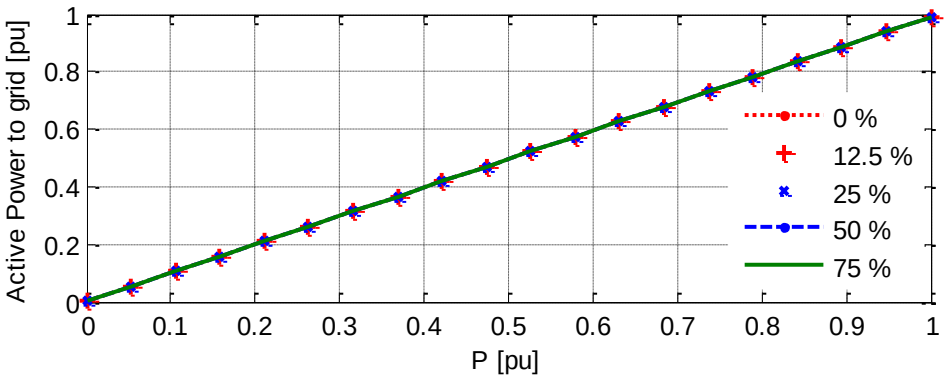

(c)

Figure 6.32 (a) Voltage magnitude at bus-1, (b) Voltage across series capacitor and (c) Active power to grid

Case III: 0.8 lagging power factor operation:

In this case, the reactive power is absorbed from the system proportional to the active power supplied at bus-1 as shown in Figure 6.33(a). In this operation mode, higher compensation level gives better voltage profile as the active power flowing in the line varies (see Figure 6.34(a)). It is because higher compensation means less net impedance of the line so the voltage difference between bus-1 and bus-2 cannot be high.

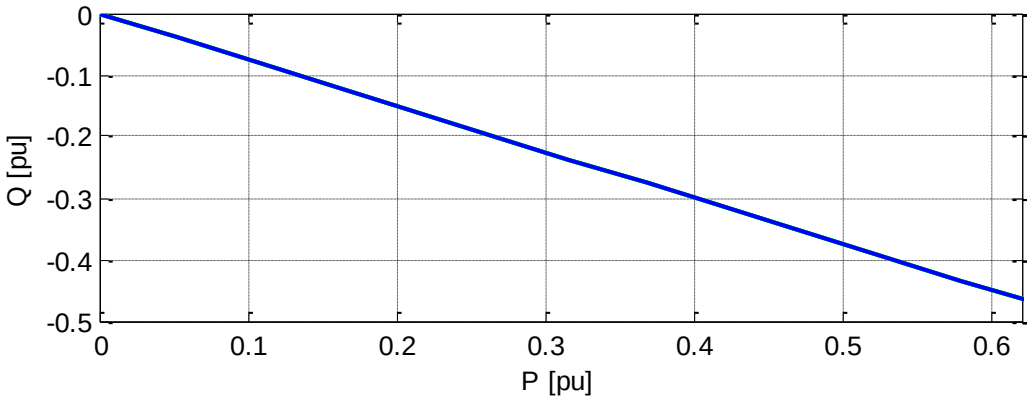

(a)

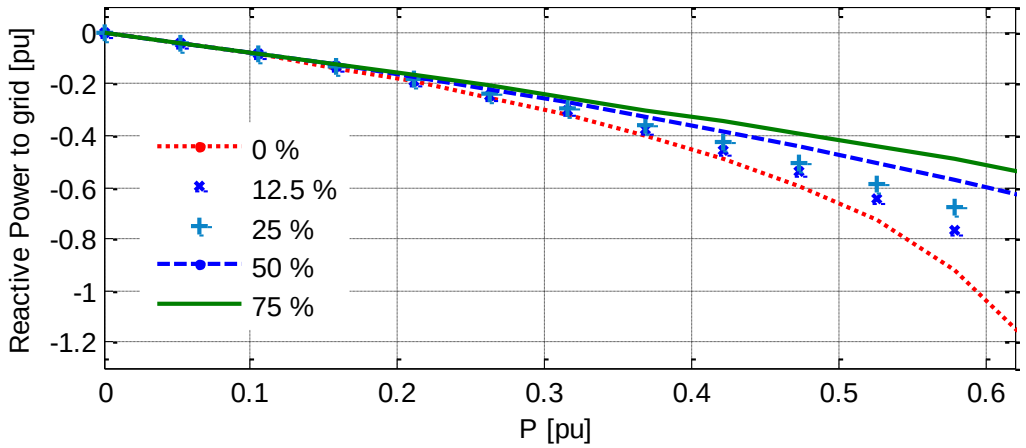

(b)

Figure 6.33 (a) Reactive power supplied at bus-1 and (b) Reactive power supplied to grid (-ve means absorbed from grid)

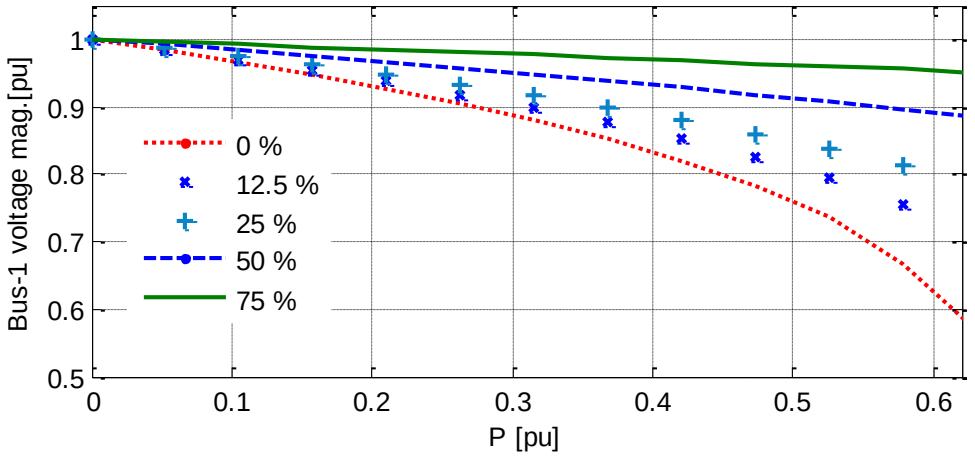

(a)

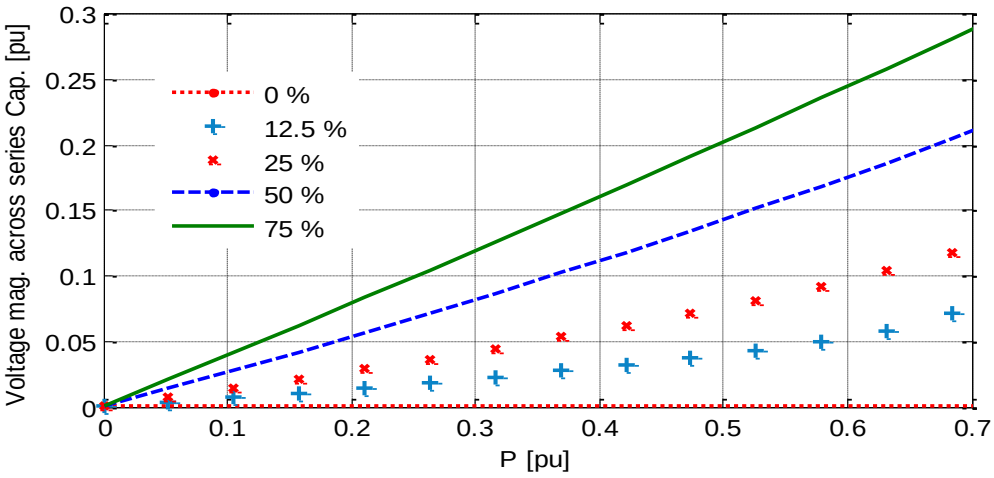

(b)

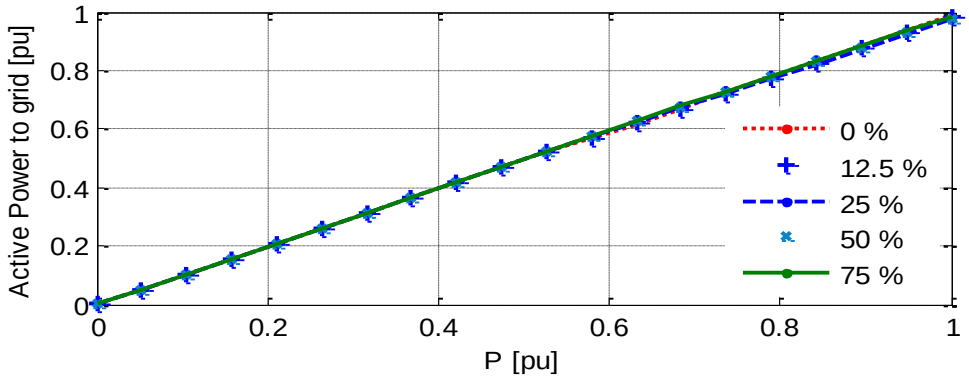

(c)

Figure 6.34 (a) Voltage magnitude at bus-1, (b) Voltage across capacitor and (c) Active power to grid

6.5 Steady State Analysis of the Overall System

The steady state equations of the DFIG system used in this analysis, presented in Chapter 4, are given below:

$$V_{qs} = r_s I_{qs} + \omega_e L_s I_{ds} + \omega_e L_m I_{dr} \tag{6.121}$$

$$V_{ds} = r_s I_{ds} - \omega_e L_s I_{qs} - \omega_e L_m I_{qr} \tag{6.122}$$

$$V_{qr} = r_r I_{qr} + (\omega_e - \omega_r) L_m I_{ds} + (\omega_e - \omega_r) L_r I_{dr} \tag{6.123}$$

$$V_{dr} = r_r I_{dr} - (\omega_e - \omega_r) L_m I_{qs} - (\omega_e - \omega_r) L_r I_{qr} \tag{6.124}$$

$$T_m = \frac{3P}{4} L_m \left[I_{qr} I_{ds} - I_{dr} I_{qs} \right] \tag{6.125}$$

$$T_m = \frac{R}{\lambda * Gear\ Ratio} \rho\, A V_w{}^2 C_p \tag{6.126}$$

$$w_r = \frac{\lambda V_w}{R} Gear\ Ratio \tag{6.127}$$

$$Q_s = \frac{3}{2}(V_{qs} I_{ds} - V_{ds} I_{qs}) = 0 \tag{6.128}$$

$$\frac{3}{4}\left(M_{qr} I_{qr} + M_{dr} I_{dr}\right) + \frac{3}{4}\left(M_{qf} I_{qf} + M_{df} I_{df}\right) = 0 \tag{6.129}$$

$$M_{qf} \frac{V_{dc}}{2} = r_f I_{qf} + \omega_e L_f I_{df} + V_{qs} \tag{6.130}$$

$$M_{df} \frac{V_{dc}}{2} = r_f I_{df} - \omega_e L_f I_{qf} + V_{ds} \tag{6.131}$$

$$Q_{GSC} = \frac{3}{2}(V_{qs} I_{df} - V_{ds} I_{qf}) = 0 \tag{6.132}$$

If the GSC is supplying/absorbing reactive power, Equation (6.132) should be changed accordingly.

The steady state equations of the series compensated line shown in Figure 6.1 are discussed here. The steady state DFIG terminal voltages are given as:

$$V_{dt} = \frac{1}{\omega_e C_f}\left(I_{qf} - I_{qs} - I_{qw}\right) \tag{6.133}$$

$$V_{qt} = -\frac{1}{\omega_e C_f}\left(I_{df} - I_{ds} - I_{dw}\right) \tag{6.134}$$

The steady state current flowing through the series compensated line is given as:

$$I_{qw} = \omega_e C V_{cd} \tag{6.135}$$

$$I_{dw} = -\omega_e C V_{qc} \tag{6.136}$$

Using KVL from DFIG terminal bus to the grid bus:

$$V_{qt} - V_{qg} = r_L I_{qw} + \omega_e L_L I_{dw} + V_{cq} \tag{6.137}$$

$$V_{dt} - V_{dg} = r_L I_{dw} - \omega_e L_L I_{qw} + V_{cd} \tag{6.138}$$

For studying the steady state operating characteristics of the DFIG wind turbine interfaced with the series compensated line, the steady state equations given by (6.121)-(6.138) are solved simultaneously in MATLAB. The wind speed is varied from cut-in speed to rated speed to get the total output power from DFIG wind turbine close to zero to 1 pu and the corresponding relevant quantities are plotted against varying power output from DFIG wind turbine for different values of C (series compensation level) as shown in Figures 6.35-6.43. The steady state voltage regulation as well as active power carrying capability of the series compensated line is studied for three distinct operation modes of the DFIG.

Case I: Unity power factor operation mode:

The DFIG is not supplying any reactive power to the system. The terminal voltages at different compensation levels is presented in Figure 6.36(a). The modulation indexes of the GSC and RSC as well as active power flowing through the ac/dc/ac converter is shown in Figure 6.37.

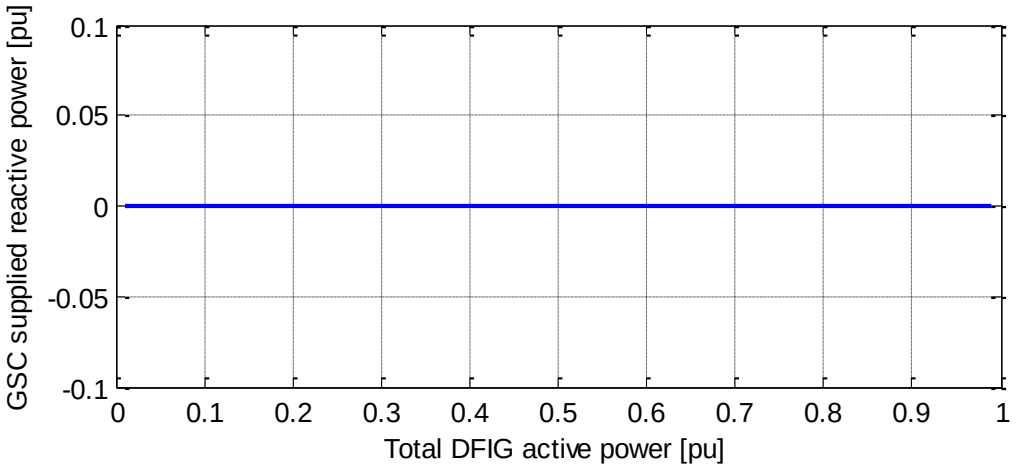

(a)

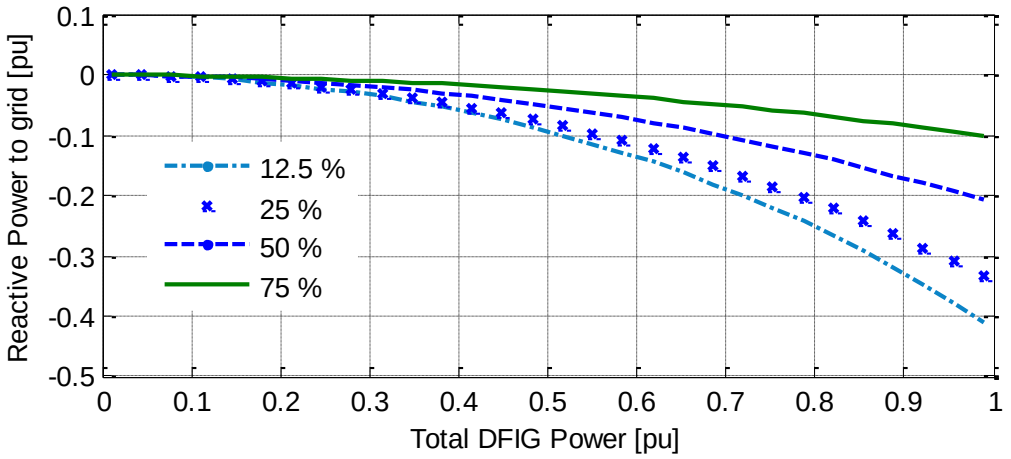

(b)

Figure 6.35 (a) Reactive power supplied at bus-1 and (b) Reactive power supplied to grid (-ve means absorbed from grid)

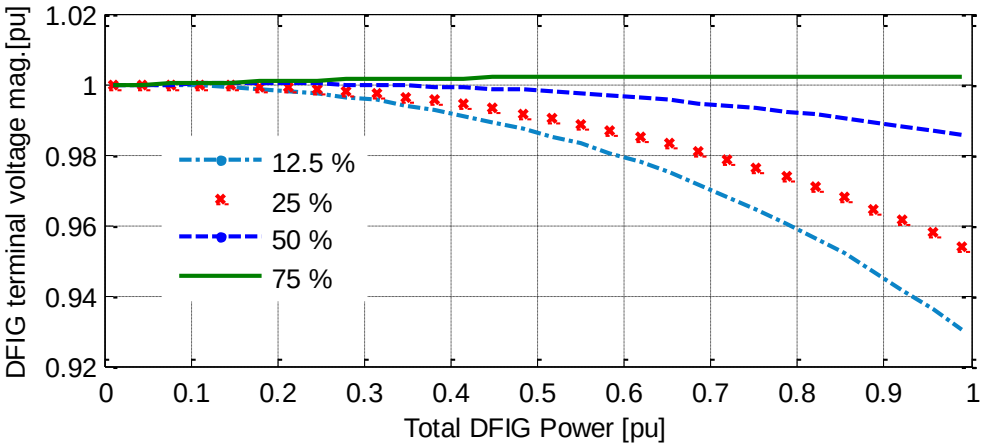

(a)

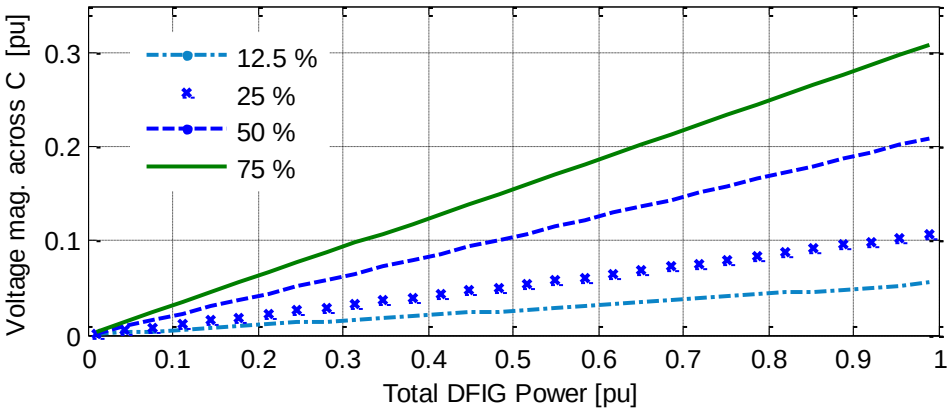

(b)

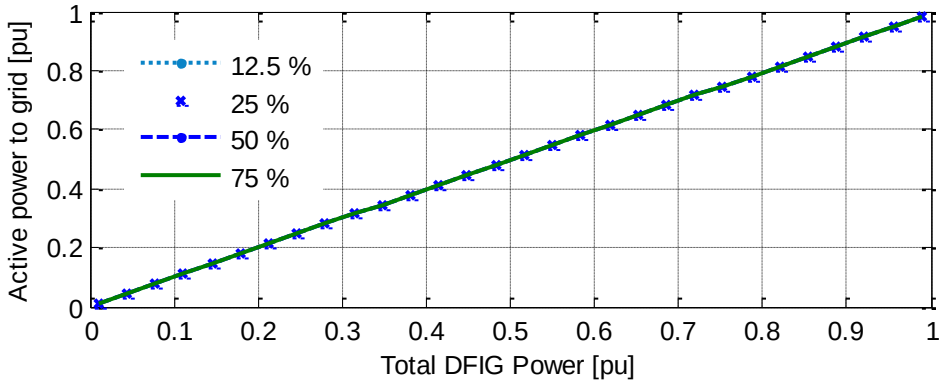

(c)

Figure 6.36 (a) Steady state DFIG wind turbine terminal voltage, (b) Voltage magnitude across series capacitor and (c) Active power supplied to grid

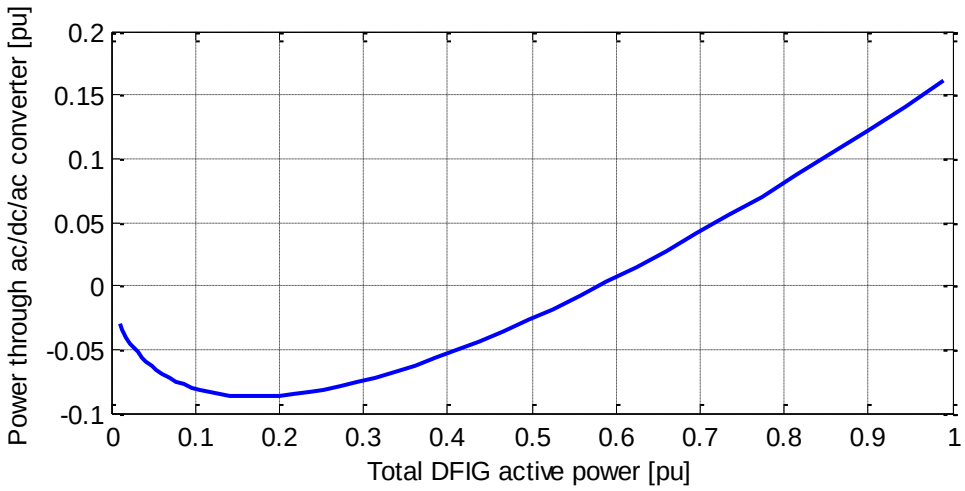

(a)

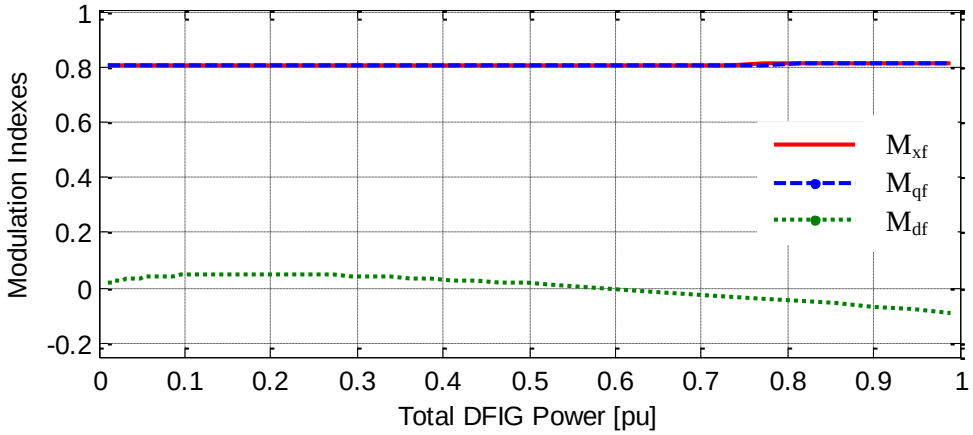

(b)

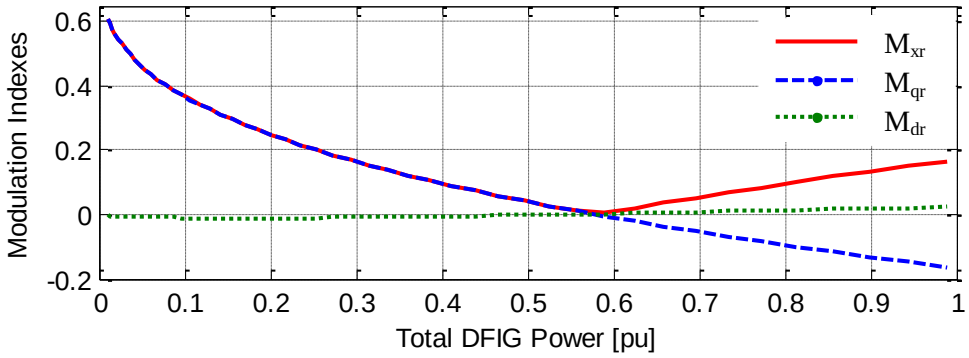

(c)

Figure 6.37 (a) Active power flowing through the ac/dc/ac converter, (b) GSC modulation indexes and (c) RSC modulation indexes

Case II: 0.95 leading power factor operation mode:

In this operation mode, the GSC in DFIG is supplying reactive power to the grid proportional to the active power output from the wind turbine as shown in Figure 6.38(a). Figure 6.39(a) shows the voltage profile of the DFIG terminal voltage while the power

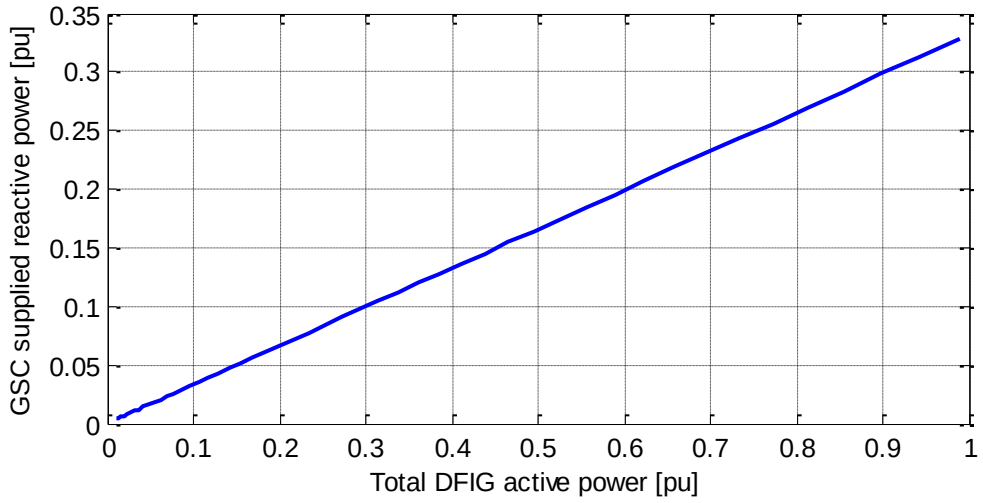

(a)

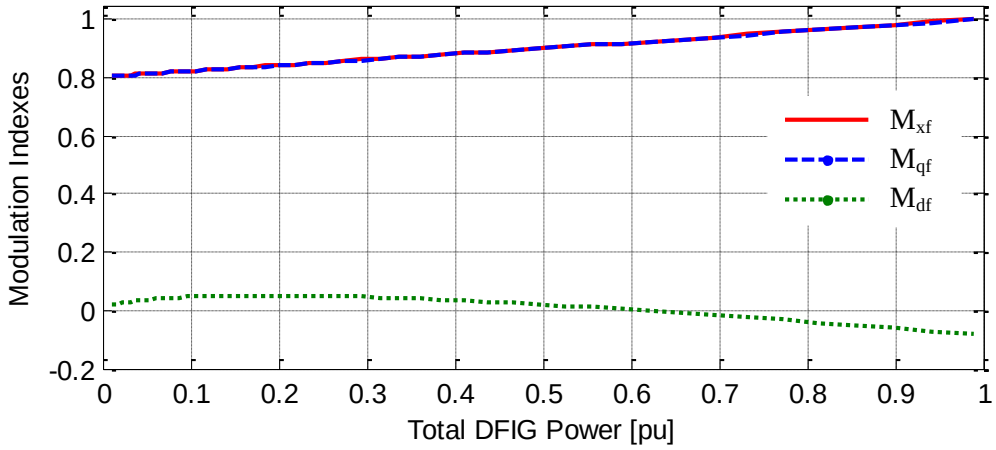

(b)

Figure 6.38 (a) Steady state GSC supplied reactive power and (b) GSC modulation indexes

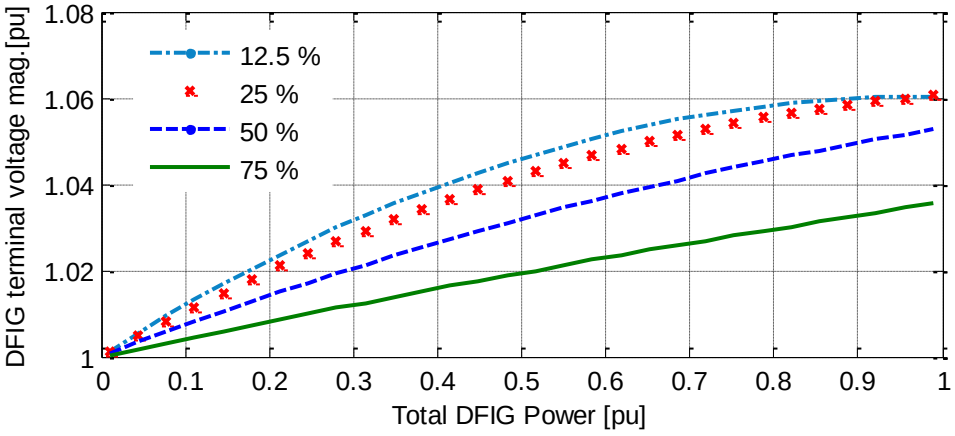

(a)

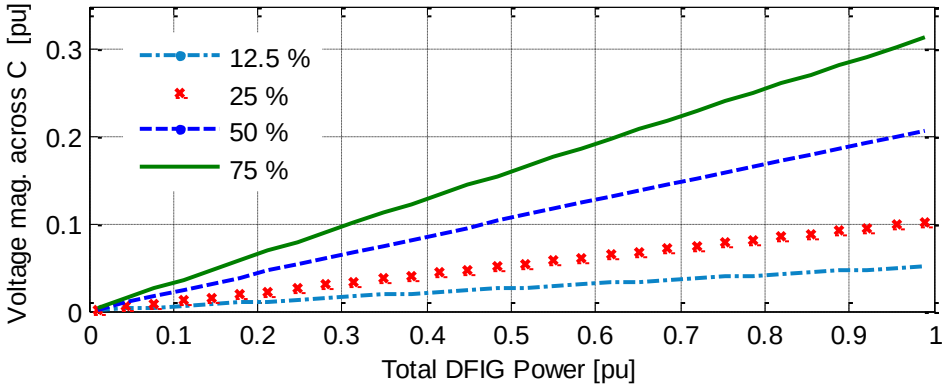

(b)

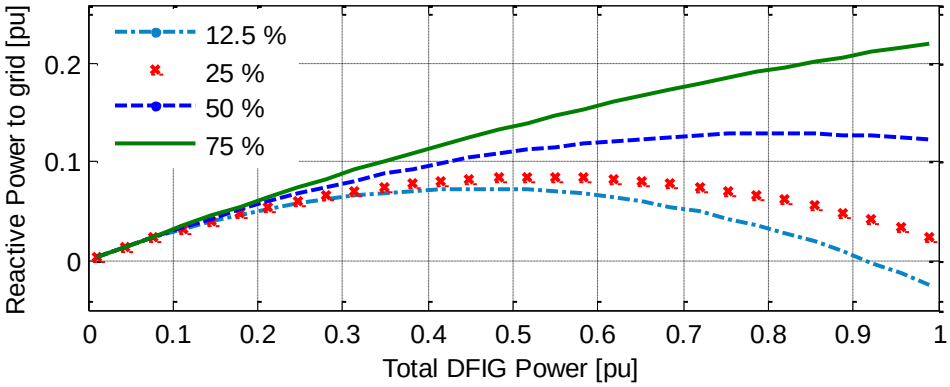

(c)

Figure 6.39 (a) DFIG terminal voltage magnitude (b) Voltage magnitude across the series capacitor and (c) Reactive power supplied to grid

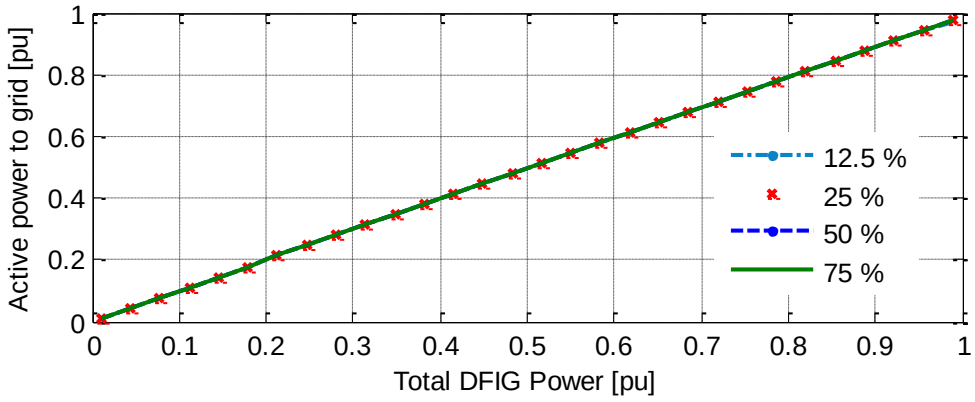

(a)

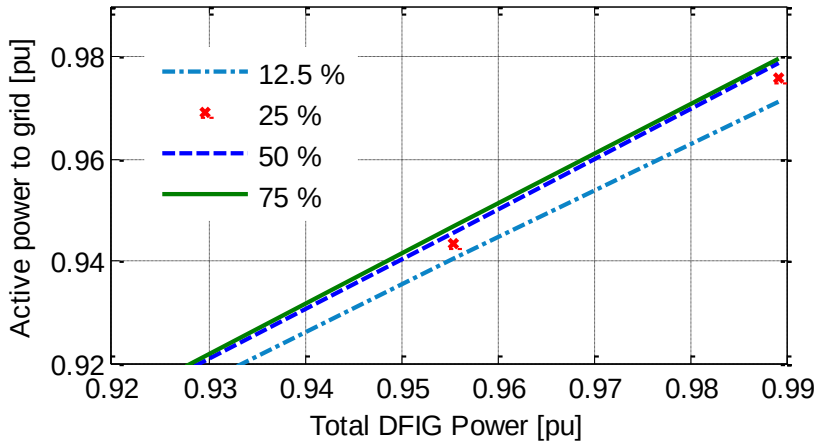

(b)

Figure 6.40 (a) Active power supplied to grid and (b) Zoomed view of active power supplied to grid

output from the wind turbine varies from 0 to 1 pu at various level of compensation in the line. Figure 6.40(b) clearly shows the enhancement in power carrying capability of the transmission line at higher series compensation level.

Case III: 0.95 lagging power factor operation mode:

In this operation mode, the GSC in DFIG is absorbing the reactive power from the system which is proportional to the active power output from the wind turbine as shown in Figure 6.41(a). Figure 6.42(a) shows the voltage profile of the DFIG terminal voltage.

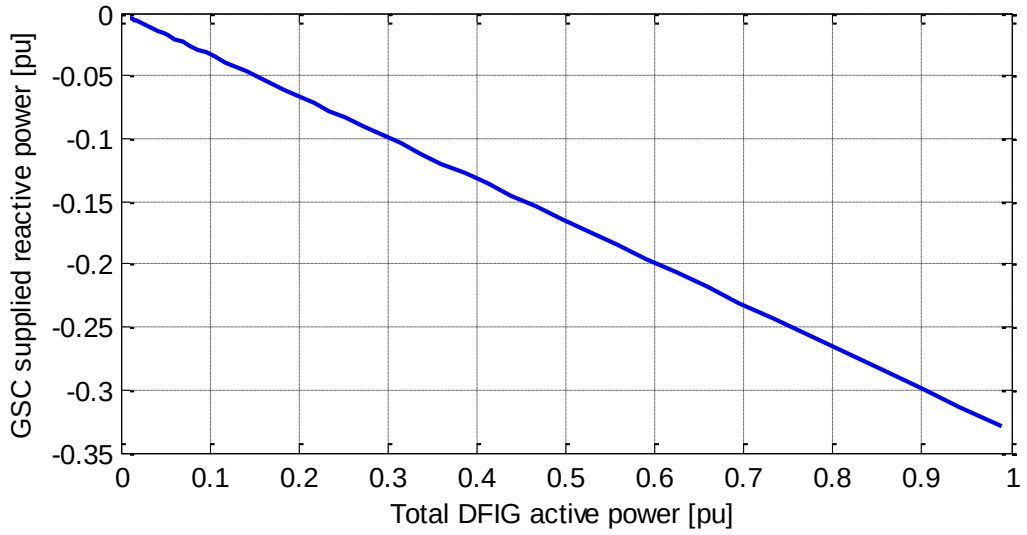

(a)

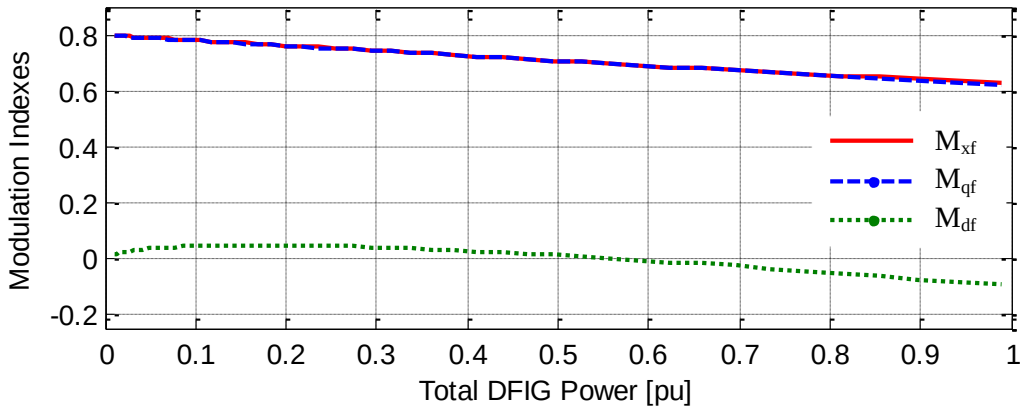

(b)

Figure 6.41 (a) Steady state GSC consumed reactive power and (b) GSC modulation indexes

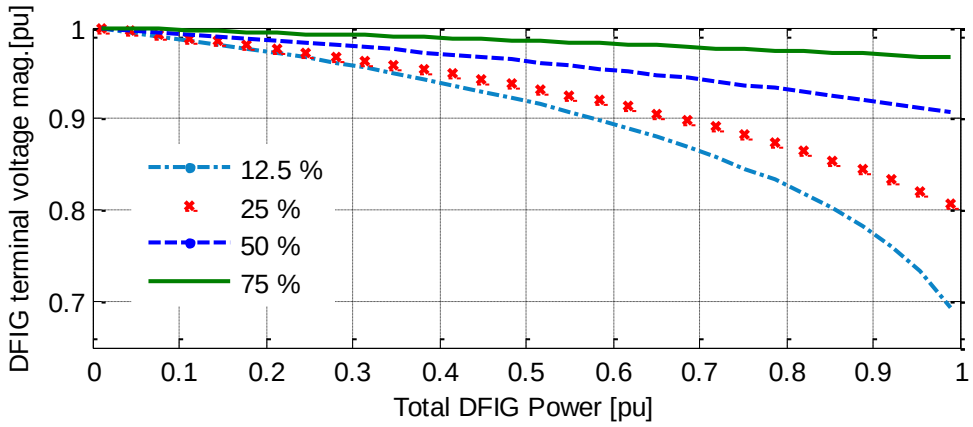

(a)

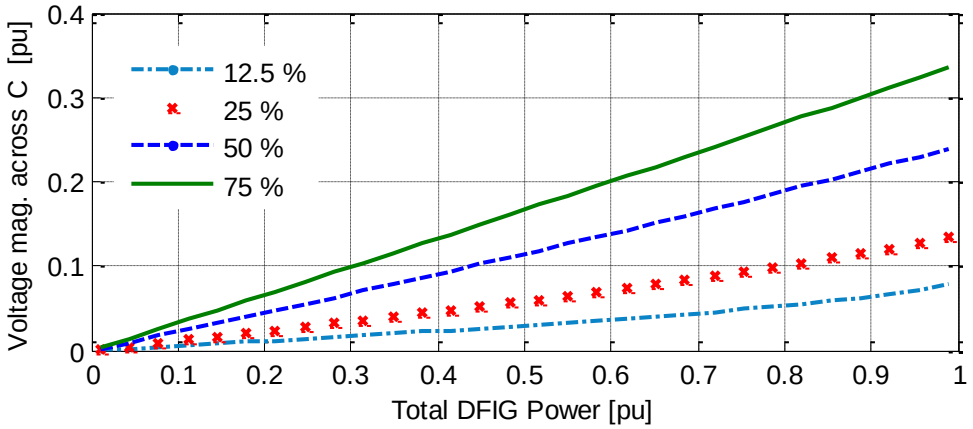

(b)

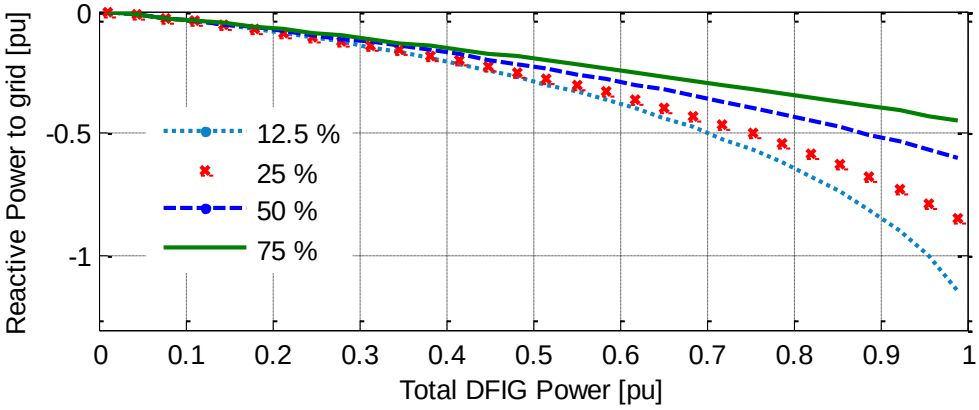

(c)

Figure 6.42 (a) DFIG terminal voltage magnitude (b) Voltage magnitude across the series capacitor and (c) Reactive power supplied to grid

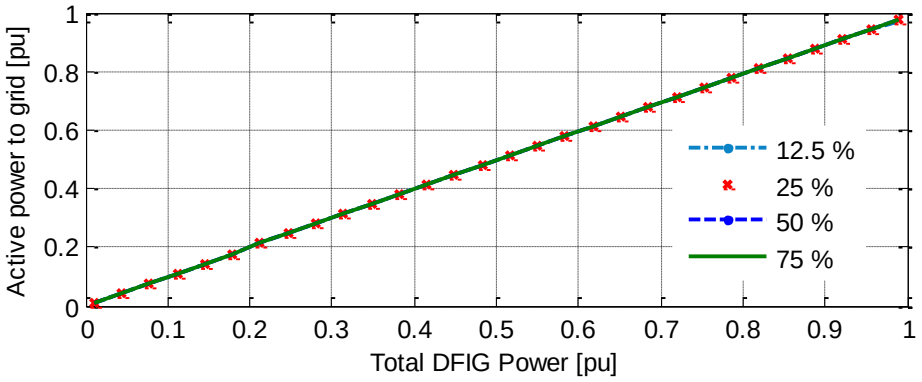

Figure 6.43 Active power supplied to grid

Hence, in this chapter, the effect of series compensation in the terminal voltage regulation of the DFIG wind turbine and the power transferring capability of the transmission line are studied through the dynamic simulation as well as steady state analysis. A two bus power system is used to analyze the effect of series compensation on the steady state voltage regulation as well as power carrying capability of the compensated line. It is clearly observed that as the compensation level increases, the reactive power consumption in the transmission line decreases. As a result, the demand of reactive power to maintain the constant terminal voltage at the DFIG wind turbine decreases. That means, smaller size GSC can be used in the DFIG turbine interconnected to power grid through the series compensated line. Series compensation gives better steady state terminal voltage profile when the DFIG is operating in unity power factor as well as lagging power factor mode. In case of leading power factor, the line will be overcompensated and the terminal voltage rises. As the compensation level increases, the amount of active power supplied to the grid through the same transmission line increases, i.e. power transferring capability of the line gets enhanced.

CHAPTER 7

AUTONOMOUS OPERATION OF DFIG WIND ENERGY CONVERSION UNIT WITH INTEGRATED ENERGY STORAGE

7.1 Introduction

In many remote areas, installation of the WECS is feasible for local electricity generation because of the availability of favorable wind condition. However, due to the absence of electrical power network, wind energy cannot be utilized easily because of its stochastic nature and uncontrollability. In such a case, a wind turbine has to be operated in standalone mode. Moreover, a grid connected wind generator can be operated in standalone mode to supply locally connected load because of problems with the grid or connection to the grid, which may also increase the reliability of the power supply system. Standalone operation mode of wind turbine requires more complex control strategy development than the grid connected operation mode. In the standalone system, variation in the connected load results in generation mismatch and leads to offer either an over generation (situation where generated power is more than connected load) or under generation (situation where generated power is less than connected load) situation. Over generation results in increase of frequency and voltage; whereas under generation results in decrease of frequency and voltage. As a result, system frequency and voltage might fall below or above the standard limit. Hence, in this operation mode, besides supplying demanded active and reactive powers to the connected load, the WECS should also control the electrical frequency of the system and magnitude of the voltage supplied to

the load. Since the wind speed fluctuates randomly, power output from wind turbine also changes. So, to increase the reliability and the stability of the autonomously operated wind turbine system, integration of properly sized energy storage system into the WECS is necessary. The energy storage system basically mitigates the power fluctuations and consequent power quality problems [47]. Among the different energy storage technologies available as discussed in Chapter 2, the battery storage system is the technically and commercially developed technology. Hence, integrated battery energy storage system is implemented in this study. And to control the voltage and frequency of the standalone operated system, traditional reactive power versus voltage (Q-V) and real power versus frequency (P-ω) droop techniques is used.

The DFIG with energy storage system in standalone operation mode can be taken as two sources of power. One is the DFIG with RSC and the other is storage system with LSC. The control of the RSC allows wind turbine to capture maximum power available in the wind. Control of RSC also enables the DFIG to control active and reactive power in the stator side independently. On the other hand, LSC with the storage system will regulate the system frequency and voltage magnitude. The DC-link voltage in ac/dc/ac converter remains almost constant, but the current flows through battery vary, so the battery can be considered as a load with a variable resistance

Hence, this chapter focuses on the modeling, control, and operation issues of DFIG-based WECS with integrated battery energy storage system operating in autonomous mode. Finally, the performance of proposed system is verified by dynamic and steady state simulation results. Hereafter the overall DFIG wind turbine system with integrated energy storage is called as 'DFIG Wind Energy Conversion Unit (WECU)'.

7.2 Studied System

Figure 7.1 shows the single line diagram of the studied system. The overall system consists of: 1) DFIG-based WECS whose main components are a wind turbine, a gear box, a DFIG, a back-to-back ac-dc-ac converter consisting of the RSC and the LSC, a battery bank connected in parallel with the dc-link capacitor of power converter and an RL filter connected after LSC. The DFIG-based WECS is connected to the load through load bus. 2) A three phase capacitor C_m connected at load bus primarily to mitigate switching voltage harmonics and voltage fluctuation in the load bus. And 3) Loads: three types of loads are connected to the system to make system more realistic which are: a linear RL load, a constant load and a nonlinear load which is related to voltage magnitude and frequency. The connected load is always assumed to be less than the sum of power generated by DFIG and battery energy storage system. The whole system is working autonomously.

7.3 Dynamic Model of the System Components

7.3.1 Wind Turbine Model

The turbine is the prime mover of the WECS that enables the conversion of kinetic energy of wind E_w into mechanical power P_m and eventually into electricity [62].

$$P_m = \frac{\partial E_w}{\partial t} \; C_p = \frac{1}{2} \rho \, A V_w^{\,3} \, C_p \tag{7.1}$$

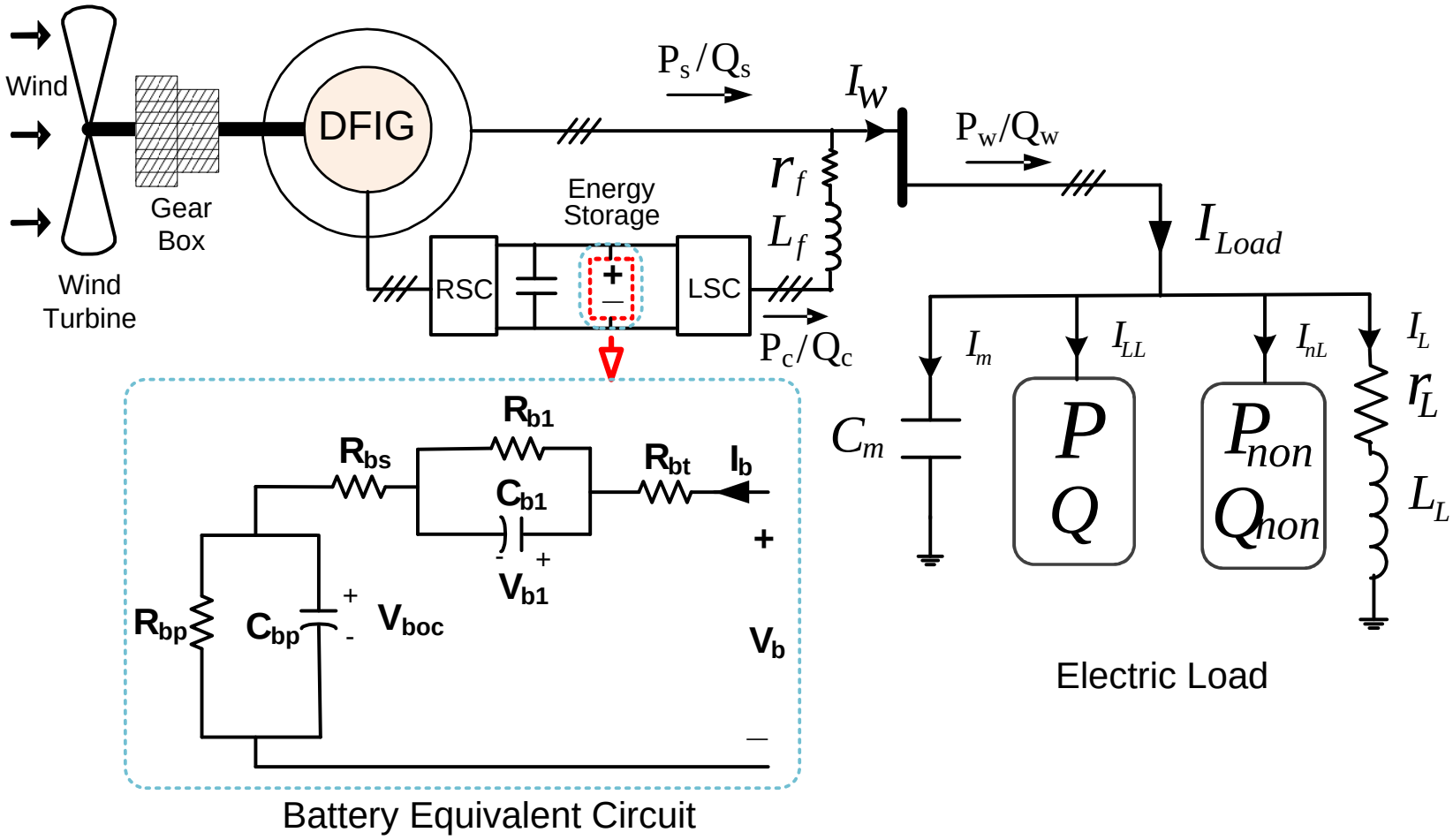

Figure 7.1 Schematic diagram of the studied system

where V_w is the wind speed at the center of the rotor (m/sec), ρ is the air density (kg/m^3), A is the frontal area of the wind turbine (m^2); R being the rotor radius. C_p is the performance coefficient which in turn depends upon turbine characteristics (blade pitch angle, β and tip speed ratio, λ) that is responsible for the losses in the energy conversion process. The numerical approximation of C_p used in this study is [62]:

$$C_p(\lambda,\beta) = 0.5176\left(\frac{116}{\lambda_i} - 0.4\beta - 5\right)e^{-21/\lambda_i} + 0.0068\lambda \tag{7.2}$$

where the TSR λ and $\lambda_i = f(\lambda,\beta)$ are given by [62]:

$$\lambda = \frac{\omega_t R}{V_w} \tag{7.3}$$

$$\frac{1}{\lambda_i} = \frac{1}{\lambda + 0.08\beta} - \frac{0.035}{\beta^3 + 1} \tag{7.4}$$

where ω_t is the turbine speed and R is the blade radius of the wind turbine.

7.3.2 DFIG Model

The dynamics of DF'IG is represented by a fourth-order state space model using the synchronously rotating reference frame (qd-frame), described in Chapter 3, are as follows:

$$\begin{bmatrix} \dot{\lambda}_{qs} \\ \dot{\lambda}_{ds} \\ \dot{\lambda}_{qr} \\ \dot{\lambda}_{dr} \end{bmatrix} = \begin{bmatrix} -\frac{r_s}{\sigma L_s} & -\omega_e & \frac{r_s L_m}{\sigma L_s L_r} & 0 \\ \omega_e & -\frac{r_s}{\sigma L_s} & 0 & \frac{r_s L_m}{\sigma L_s L_r} \\ \frac{r_r L_m}{\sigma L_s L_r} & 0 & \frac{r_r}{\sigma L_r} & (\omega_e - \omega_r) \\ 0 & \frac{r_r L_m}{\sigma L_s L_r} & (\omega_e - \omega_r) & -\frac{r_r}{\sigma L_r} \end{bmatrix} \begin{bmatrix} \lambda_{qs} \\ \lambda_{ds} \\ \lambda_{qr} \\ \lambda_{dr} \end{bmatrix} + \begin{bmatrix} 1 & 0 & 0 & 0 \\ 0 & 1 & 0 & 0 \\ 0 & 0 & 1 & 0 \\ 0 & 0 & 0 & 1 \end{bmatrix} \begin{bmatrix} V_{qs} \\ V_{ds} \\ V_{qr} \\ V_{dr} \end{bmatrix} \tag{7.5}$$

$$I_{qs} = \frac{1}{\sigma L_s}\lambda_{qs} - \frac{L_m}{\sigma L_s L_r}\lambda_{qr} \tag{7.6}$$

$$I_{ds} = \frac{1}{\sigma L_s}\lambda_{ds} - \frac{L_m}{\sigma L_s L_r}\lambda_{dr} \tag{7.7}$$

$$I_{qr} = -\frac{L_m}{\sigma L_s L_r}\lambda_{qs} + \frac{1}{\sigma L_r}\lambda_{qr} \tag{7.8}$$

$$I_{dr} = -\frac{L_m}{\sigma L_s L_r}\lambda_{ds} + \frac{1}{\sigma L_r}\lambda_{dr} \tag{7.9}$$

where leakage coefficient $\sigma = \frac{L_s L_r - L_m^2}{L_s L_r}$.

$$p\omega_r = \frac{P}{2J}(T_m - T_e - C_f \omega_r) \tag{7.10}$$

$$T_e = \frac{3}{2}\left[\lambda_{qs} I_{ds} - \lambda_{ds} I_{qs}\right] \tag{7.11}$$

7.3.3 Battery Model

The storage system plays a major role for controlling frequency and voltage in the standalone operation mode. The storage system is composed of a set of batteries connected in parallel and series connection. The equivalent circuit of the battery is shown in Figure 7.1, where V_b is the battery terminal voltage, R_{bt} is the equivalent resistance of series/parallel connected batteries and its value depends upon the connection conditions and amount of batteries. The parallel circuit of R_{b1} and C_{b1} is used to describe the energy and voltage during charging or discharging. R_{bp} is connected in parallel with C_{bp} to simulate the self-discharging of a battery. Since the self-discharging current of a battery is small, the resistance of R_{bp} is large. As the battery is an energy storage unit, its energy

Table 7.1 Battery Parameters [71]:

Parameter	Value	Parameter	Value
C_{b1}	1 F	C_{bp}	52600 F
R_{b1}	0.001 Ω	R_{bp}	10 kΩ
R_{bs}	0.013 Ω	R_{bt}	0.0167 Ω

is represented in kWh. When the capacitor is used to model the battery unit, the capacitance can be determined from the following relationship [71]:

$$C_{bp} = \frac{kWh\ x\ 7200\ x\ 10^3}{\left(V_{boc\_\max}^2 - V_{boc\_\min}^2\right)}\ F \tag{7.12}$$

where $V_{boc\_\max}$ and $V_{boc\_\min}$ are the maximum and minimum voltage across battery capacitance, respectively.

The dynamic model of the battery based on its structure in Figure 7.1 is represented as:

$$\begin{cases} C_{bp} p V_{boc} = I_b - \dfrac{V_{boc}}{R_{bp}} \\ C_{b1} p V_{b1} = I_b - \dfrac{V_{b1}}{R_{b1}} \end{cases} \tag{7.13}$$

$$I_b = \frac{V_b - V_{b1} - V_{boc}}{R_{bt} + R_{bs}} \tag{7.14}$$

7.3.4 Load Model

For the linear RL loads, voltage equation is:

$$V_{qdt} = r_L I_{qdL} + L_{qdL} p I_L - j\omega_e L_L I_{qdL} \tag{7.15}$$

where r_L and L_L is the resistance and inductance of the RL load, respectively.

The filter capacitor current is given by:

$$C_m\ pV_{qdt} - j\omega_e C_m V_{qdt} = I_{qdw} - I_{qdL} - I_{qdLL} - I_{qdnL} \tag{7.16}$$

where C_m is the filter capacitor, I_{qdw} is the current supplied by the DFIG wind turbine system and I_{qdL}, I_{qdLL} and I_{qdnL} are current drawn by RL load, linear load and non-linear load, respectively.

A non-linear electrical load is a load on the electrical system that draws a non-sinusoidal current waveform from the connected supply. Computer, fax machine, printer, electronic lighting ballast, variable-speed drive etc. are the typical examples of non-linear electrical loads. The non-linear loads have non-linear relationship with the voltage magnitude and system frequency. In this study, non-linear loads are modeled as [70]:

$$\begin{cases} P_{non} = P_o\left(\dfrac{V_{m\_PCC}}{V_0}\right)^a\left(\dfrac{\omega}{\omega_0}\right)^b \\ Q_{non} = Q_o\left(\dfrac{V_{m\_PCC}}{V_0}\right)^a\left(\dfrac{\omega}{\omega_0}\right)^b \end{cases} \tag{7.17}$$

where P_o and Q_o are base active and reactive powers of non-linear loads, respectively. V_{m_PCC} and ω are local voltage magnitude and frequency, respectively. V_0 and ω_0 are nominal voltage magnitude and frequency of the distribution system, respectively. a and b are load-voltage and load-frequemcy dependence factors, respectively. In this study a=b=3 is taken.

The active and reactive powers drawn by the constant load are given as:

$$\begin{cases} P = \dfrac{3}{2}(V_{qt}I_{qLL} + V_{dt}I_{dLL}) \\ Q = \dfrac{3}{2}(V_{qt}I_{dLL} - V_{dt}I_{qLL}) \end{cases} \tag{7.18}$$

Hence, the current drawn by the constant load can be expressed using (7.18) as:

$$\begin{cases} I_{qLL} = \dfrac{2}{3}\dfrac{PV_{qt} + QV_{dt}}{V_{qt}^2 + V_{dt}^2} \\ I_{dLL} = \dfrac{2}{3}\dfrac{PV_{dt} - QV_{qt}}{V_{qt}^2 + V_{dt}^2} \end{cases} \tag{7.18(a)}$$

Similarly, the non-linear load current equations are:

$$\begin{cases} I_{qnL} = \dfrac{2}{3}\dfrac{P_{non}V_{qt} + Q_{non}V_{dt}}{V_{qt}^2 + V_{dt}^2} \\ I_{dnL} = \dfrac{2}{3}\dfrac{P_{non}V_{dt} - Q_{non}V_{qt}}{V_{qt}^2 + V_{dt}^2} \end{cases} \tag{7.19}$$

7.4 Controller Design

7.4.1 Rotor Side Converter (RSC) Controller

The RSC control scheme consists of two cascaded vector control structure with inner current control loops which regulates independently the d-axis and q-axis rotor currents, i.e. I_{dr} and I_{qr}, according to some synchronously rotating reference frame. The outer control loop regulates the stator active power (or DFIG rotor speed) and reactive power independently. The stator voltage orientation (SVO) control principle for a DFIG is described in [31], where the q-axis of the rotating reference frame is aligned to the stator voltage, i.e V_{ds} = 0 and V_{qs} = V_s. From (3.15) and (3.16), the stator side flux can be controlled using PI controller. In this study, the q-axis flux is regulated to zero ($\lambda_{qs} = 0$) and ($\lambda_{ds} = \lambda_s$) for the de-coupled control of active and reactive power as described below:

$$\begin{cases} p\lambda_{qs} + \dfrac{r_s}{\sigma L_s}\lambda_{qs} = -\omega_e \lambda_{ds} + \dfrac{r_s L_m}{\sigma L_s L_r}\lambda_{qr} + V_{qs} \\ \sigma_{\lambda qs} = -\omega_e \lambda_{ds} + \dfrac{r_s L_m}{\sigma L_s L_r}\lambda_{qr} + V_{qs} \\ \lambda_{ds}^{*} = \dfrac{1}{\omega_e}\left(\dfrac{r_s L_m}{\sigma L_s L_r}\lambda_{qr} + V_{qs} - \sigma_{\lambda qs}\right) \end{cases} \tag{7.20}$$

$$\begin{cases} p\lambda_{ds} + \dfrac{r_s}{\sigma L_s}\lambda_{ds} = \omega_e \lambda_{qs} + \dfrac{r_s L_m}{\sigma L_s L_r}\lambda_{dr} + V_{ds} \\ \sigma_{\lambda ds} = \omega_e \lambda_{qs} + \dfrac{r_s L_m}{\sigma L_s L_r}\lambda_{dr} + V_{ds} \\ \lambda_{qs}^{*} = \dfrac{1}{\omega_e}\left(\sigma_{\lambda ds} - \dfrac{r_s L_m}{\sigma L_s L_r}\lambda_{qr} - V_{qs}\right) \end{cases} \tag{7.21}$$

where $\sigma_{\lambda qs} = p\lambda_{qs} + \dfrac{r_s}{\sigma L_s}\lambda_{qs} = \left(k_{P\lambda s} + \dfrac{k_{I\lambda s}}{p}\right)(\lambda_{qs}^{*} - \lambda_{qs})$ and $\sigma_{\lambda ds} = p\lambda_{ds} + \dfrac{r_s}{\sigma L_s}\lambda_{ds} = \left(k_{P\lambda s} + \dfrac{k_{I\lambda s}}{p}\right)(\lambda_{ds}^{*} - \lambda_{ds})$ are the outputs from the PI controllers as shown in Figure 7.2.

The PI parameters determined by comparing with the Butterworth polynomial, are given as:

$$\begin{cases} k_{P\lambda s} = \sqrt{2}\omega_0 - \dfrac{r_s}{\sigma L_s} \\ k_{I\lambda s} = \omega_0^{\,2} \end{cases} \tag{7.22}$$

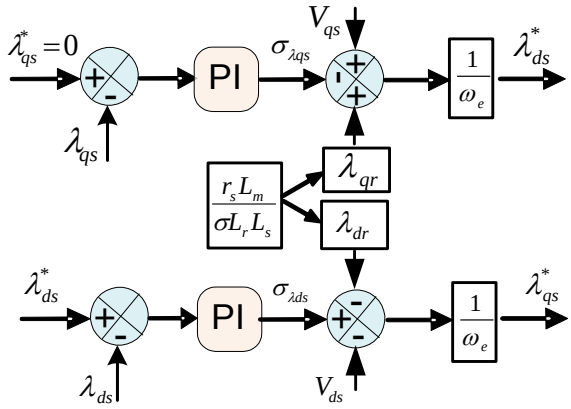

Figure 7.2 Stator fluxes control using PI controllers

Now, neglecting frictional losses, rotor speed dynamics is given from (7.10) as:

$$p\omega_r = \frac{P}{2J}(T_m - T_e) \tag{7.23}$$

where T_m is the mechanical torque from the wind turbine. When the wind speed (V_w) is less than the rated speed, then the T_m is given as:

$$T_m = k_{opt} V_w{}^2 \tag{7.24}$$

where $k_{opt} = \frac{R}{2\lambda_{opt}} \rho\, A\, C_{p\_opt}$ = constant and if the wind speed (V_w) is more than the rated speed, then the T_m is given as:

$$T_m = \frac{P_{rated}}{\omega_{rated}} \tag{7.25}$$

where P_{rated} is rated power of the wind turbine and ω_{rated} is the rated speed of the wind turbine. Equation (7.23) can be re-written as:

$$\frac{2J}{P} p\omega_r = (T_m - T_e) = \sigma_{wr} = k_{wr}(\omega_r^* - \omega_r) \tag{7.26}$$

where k_{wr} is the PI controller for rotor speed controller, given as: $k_{wr} = \left(k_{Pwr} + \frac{k_{Iwr}}{p}\right)$

Then (7.26) will be:

$$\frac{2J}{P} p\omega_r = \left(k_{Pwr} + \frac{k_{Iwr}}{p}\right)\omega_r{}^* - \left(k_{Pwr} + \frac{k_{Iwr}}{p}\right)\omega_r \tag{7.27}$$

$$\frac{\omega_r}{\omega_r{}^*} = \frac{\frac{P}{2J}\left(pk_{Pwr} + k_{Iwr}\right)}{p^2 + p\frac{Pk_{Pwr}}{2J} + \frac{Pk_{Iwr}}{2J}} \tag{7.28}$$

Now, comparing denominator of (7.28) with the Butterworth second order polynomial, i.e. $p^2 + \sqrt{2}\omega_{0wr} p + \omega_{0wr}^2$, PI controller gains are obtained as:

$$\begin{cases} k_{Pwr} = \sqrt{2}\omega_{0wr} \dfrac{2J}{P} \\ k_{Iwr} = \dfrac{2J}{P} {\omega_{0wr}}^2 \end{cases} \tag{7.29}$$

where ω_{0wr} is the bandwidth frequency of the speed controller.

Using λ_{qs} = 0, the electromechanical torque and q-axis stator current is given by (7.30) and (7.31) as:

$$T_e = \frac{3}{2}\lambda_{ds} I_{qs} \tag{7.30}$$

$$I_{qs} = -\frac{L_m}{L_s} I_{qr} \tag{7.31}$$

$$T_e = \frac{3}{2}\lambda_{ds}(-\frac{L_m}{L_s}) I_{qr} \tag{7.32}$$

$$I_{qr} = (\sigma_{wr} - T_m)\frac{2}{3}\frac{L_s}{L_m \lambda_{ds}} \tag{7.33}$$

Similarly,

$$I_{ds} = \frac{\lambda_{ds}}{L_s} - \frac{L_m}{L_s} I_{dr} \tag{7.34}$$

The stator side active power can be written as:

$$P_s = \frac{3}{2}(V_{qs} I_{qs} + V_{ds} I_{ds}) = -\frac{3}{2}\frac{L_m}{L_s} V_{qs} I_{qr} \tag{7.35}$$

The stator supplied reactive power is given as:

$$Q_s = \frac{3}{2}(V_{qs} I_{ds} - V_{ds} I_{qs}) = \frac{3}{2} V_{qs} I_{ds} \tag{7.36}$$

Substituting V_{qs} in (7.36) gives:

$$Q_s = \frac{3}{2}(r_s I_{qs} + \omega_e \lambda_{ds} + p\lambda_{qs}) I_{ds} \tag{7.37}$$

Assuming constant stator flux, neglecting the stator resistance and substituting I_{ds} from Equation (7.7) gives:

$$Q_s = \frac{3}{2}\frac{\omega_e}{\sigma L_s}\left(\lambda_{ds}^2 - \frac{L_m}{L_r}\lambda_{ds}\lambda_{dr}\right) \tag{7.38}$$

Differentiating (7.38) w.r.t. time gives:

$$pQ_s = -\frac{3}{2}\frac{\omega_e}{\sigma L_s}\frac{L_m}{L_r}\lambda_{ds} p\lambda_{dr} \tag{7.39}$$

From (7.5) and (3.4) gives (7.40) and solving λ_{qr} in terms of I_{qr} gives (7.41)

$$pQ_s = -\frac{3}{2}\frac{\omega_e}{\sigma L_s}\frac{L_m}{L_r}\lambda_{ds}\left(V_{dr} - r_r I_{dr} + (\omega_e - \omega_r)\lambda_{qr}\right) \tag{7.40}$$

$$pQ_s = -\frac{3}{2}\frac{\omega_e}{\sigma L_s}\frac{L_m}{L_r}\lambda_{ds}\left(V_{dr} - r_r I_{dr} + (\omega_e - \omega_r)\sigma L_r I_{qr}\right) \tag{7.41}$$

$$\nabla pQ_s = \sigma_{Qs} = k_{Qs}(Q_s^* - Q_s) \tag{7.42}$$

where $\nabla = \frac{2\sigma L_s L_r}{3\omega_e L_m}$ and k_{Qs} is the PI controller for stator side reactive power controller, given as: $k_{Qs} = \left(k_{PQs} + \frac{k_{IQs}}{p}\right)$. So, (7.42) can be re-written as:

$$\nabla pQ_s = \left(k_{PQs} + \frac{k_{IQs}}{p}\right)Q_s^* - \left(k_{PQs} + \frac{k_{IQs}}{p}\right)Q_s \tag{7.43}$$

$$\frac{Q_s}{Q_s^*} = \frac{\frac{1}{\nabla}\left(pk_{PQs} + k_{IQs}\right)}{p^2 + p\frac{k_{PQs}}{\nabla} + \frac{k_{IQs}}{\nabla}} \tag{7.44}$$

Similarly, comparing denominator of (7.44) with Butterworth second order polynomial, i.e. $p^2 + \sqrt{2}\omega_{Qs} p + \omega_{Qs}^2$, PI controller gains are obtained as:

$$\begin{cases} k_{PQs} = \sqrt{2}\omega_{0Qs}\Delta \\ k_{IQs} = \Delta{\omega_{Qs}}^2 \end{cases} \tag{7.45}$$

From (7.41) and (7.42) gives:

$$I_{dr}^{*} = \frac{1}{r_r}\left(V_{dr} + (\omega_e - \omega_r)\sigma L_r I_{qr} - \frac{\sigma_{Q_s}}{\lambda_{ds}} \right) \tag{7.46}$$

It can be seen from Equations (7.33) and (7.45) that, P_s and Q_s are proportional to I_{qr} and I_{dr}, respectively. The mutual coupling term $(\omega_e - \omega_r)\sigma L_r I_{qr}$ in (7.45) is very small so its effect is negligible. The rotor current can be regulated by means of rotor voltages. The relation between rotor current and rotor voltage is obtained by substituting values of λ_{dr} and λ_{qr} from (3.7) and (3.8) in Equations (3.3) and (3.4), respectively, and further simplification yields:

$$V_{qr} = r_r I_{qr} + \sigma L_r p I_{qr} + \omega_{so}\left(\frac{L_m}{L_s}\lambda_{ds} + \sigma L_r I_{dr} \right) \tag{7.47}$$

$$V_{dr} = r_r I_{dr} + \sigma L_r p I_{dr} - \omega_{so}\sigma L_r I_{qr} \tag{7.48}$$

where $\omega_{so} = (\omega_e - \omega_r)$ and $\sigma = 1 - \frac{{L_m}^2}{L_s L_r}$

In the Equations (7.47) and (7.48), there is the term including I_{dr} in the q-axis equation and there is the term including I_{qr} in the d-axis equation. So these two equations are coupled and the traditional linear controllers cannot be used. However, through the exact linearization method, these equations can be linearized by putting the terms other than the currents control to one side.

$$\begin{cases} r_r I_{qr} + \sigma L_r p I_{qr} = V_{qr} - \omega_{so}\left(\frac{L_m}{L_s}\lambda_{ds} + \sigma L_r I_{dr}\right) \\ r_r I_{dr} + \sigma L_r p I_{dr} = V_{dr} + \omega_{so}\sigma L_r I_{qr} \end{cases} \tag{7.49}$$

Let's assume:

$$\sigma_{qr} = r_r I_{qr} + \sigma L_r p I_{qr} \tag{7.50}$$

$$\sigma_{dr} = r_r I_{dr} + \sigma L_r p I_{dr} \tag{7.51}$$

The idea behind is to use the linear controllers that include integrations to calculate the derivative terms. And the nonlinear equations become linear when all the nonlinear terms are moved to the other side of the equations. Then the q and d-axis voltages are calculated as shown in Figure 7.3.

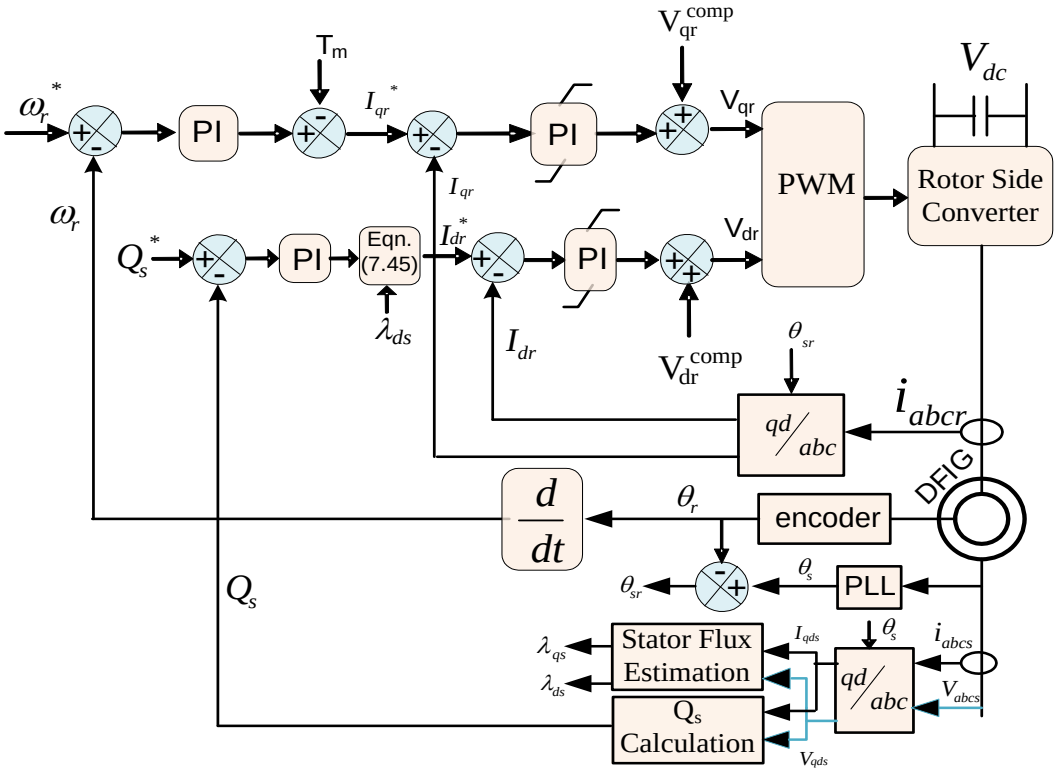

Figure 7.3 Block diagram of RSC control system: $V_{dr}^{comp} = -\omega_{so}\sigma L_r I_{qr}$

and $V_{qr}^{comp} = \omega_{so}\left(\frac{L_m}{L_s}\lambda_{ds} + \sigma L_r I_{dr}\right)$

$$V_{qr}^{*} = \sigma_{qr} + \omega_{so}\left(\frac{L_m}{L_s}\lambda_{ds} + \sigma L_r I_{dr}\right) \tag{7.52}$$

$$V_{dr}^{*} = \sigma_{dr} - \omega_{so}\sigma L_r I_{qr} \tag{7.53}$$

Using the inner current control loop has a significant advantage for the protection of the DFIG. It can naturally protect the system from over-current since current limiters can be easily inserted in the control system shown in Figure 7.3.

Since the general PI controllers are widely used and proved to be effective, they are also applied in the following analysis [63]. For I_{qr} current control loop from (7.48):

$$V_{qr}^{'} = r_r I_{qr} + \sigma L_r p I_{qr} = (r_r + p\sigma L_r) I_{qr} \tag{7.54}$$

$$V_{qr}^{'} = \left(k_{qp} + \frac{k_{qi}}{p}\right)\left(I_{qr}^{*} - I_{qr}\right) \tag{7.55}$$

$$(r_r + p\sigma L_r) I_{qr} = \left(k_{qp} + \frac{k_{qi}}{p}\right) I_{qr}^{*} - \left(k_{qp} + \frac{k_{qi}}{p}\right) I_{qr} \tag{7.56}$$

Then the transfer functions between the reference and actual currents are changed to the following:

$$\frac{I_{qr}}{I_{qr}^{*}} = \frac{pk_{qp} + k_{qi}}{p^2\sigma L_r + p(r_r + k_{qp}) + k_i} = \frac{\frac{1}{\sigma L_r}(pk_{qp} + k_{qi})}{p^2 + p\frac{1}{\sigma L_r}(r_r + k_{qp}) + \frac{1}{\sigma L_r}k_{qi}} \tag{7.57}$$

Similar process can be repeated for I_{dr} current control loop from (7.49).

The PI parameters are determined by comparing the coefficients in the denominator of (7.57) with the Butterworth second order polynomial.

$$k_{qp} = k_{dp} = \sqrt{2}\omega_0 \sigma L_r - r_r \tag{7.58}$$

$$k_{qi} = k_{di} = \sigma L_r \omega_0^{\ 2} \tag{7.59}$$

Here ω_0 is the bandwidth of the current controller. The values of k_p and k_I for RSC is shown in Table 7.1. The overall vector control scheme of the RSC is shown in Figure 7.3.

7.4.2 Load Side Converter (LSC) Controller

In the DFIG system shown in Figure 7.1, the real power P_c and reactive power Q_c are controlled by the LSC. In this autonomous operation mode, the real power control is used to regulate the network frequency and the reactive power control is employed to regulate the load bus voltage magnitude V_{tm}. The integrated battery energy storage system provides the system stability by adjusting frequency and voltage close to their nominal value when frequency and voltage deviates because of load demand and wind speed variation. In over generation situation, the controller will sink extra energy into the storage system up to the maximum charging limit. In an under generation situation, when load demand is higher than production, the storage system provides the additional energy.

Figure 7.4 shows the general vector control scheme of the LSC where control of dc-link voltage as well as system frequency and load bus voltage magnitude are achieved by controlling current in synchronous reference frame.

Applying KVL from LSC to the load bus -

$$V_{qL} = r_f I_{qf} + L_f p I_{qf} + \omega_e L_f I_{df} + V_{qt} \tag{7.60}$$

$$V_{dL} = r_f I_{df} + L_f p I_{df} - \omega_e L_f I_{qf} + V_{dt} \tag{7.61}$$

$$V_{qL} = M_{qL}\frac{V_{dc}}{2} \tag{7.62}$$

$$V_{dL} = M_{dL}\frac{V_{dc}}{2} \tag{7.63}$$

where V_{qt} and V_{dt} are the qd-voltages at load bus, respectively, V_{qL} and V_{dL} are the output voltages of LSC given by (7.62) and (7.63) and I_{qf} and I_{df} are the qd-currents supplied by LSC to the load bus, respectively. M_{qL} and M_{dL} are modulation indexes of LSC and V_{dc} is the DC-link voltage of the DFIG system. Substuting Equation (7.60) in (7.62) and (7.61) in (7.63) gives:

$$r_f I_{qf} + L_f pI_{qf} = M_{qL}\frac{V_{dc}}{2} - \omega_e L_f I_{df} - V_{qt} \tag{7.64}$$

$$r_f I_{df} + L_f pI_{df} = M_{dL}\frac{V_{dc}}{2} - \omega_e L_f I_{qf} - V_{dt} \tag{7.65}$$

$$r_f I_{qf} + L_f pI_{qf} = K_{qL}(I^*_{qf} - I_{qf}) = \sigma_{qL} \tag{7.66}$$

$$r_f I_{df} + L_f pI_{df} = K_{dL}(I^*_{df} - I_{df}) = \sigma_{dL} \tag{7.67}$$

Now DC-link voltage dynamics is given by:

$$C_{dc}pV_{dc} = I_r + \frac{3}{4}\left(M_{dL}I_{df} + M_{qL}I_{qf}\right) - I_b = \sigma_{dc} \tag{7.68}$$

where C_{dc} is the dc-link capacitance, $I_r = \frac{3}{4}\left(M_{dr}I_{dr} + M_{qr}I_{qr}\right)$ is the dc current from RSC towards LSC and I_b is the battery supplied current.

As shown in Figure 7.1, the battery storage system is connected in parallel with the DC-link. The battery charges and discharges according to the wind speed and connected load variation. When the battery charging/discharging happens, the DC-link

voltage tries to fluctuate. Since DC-link voltage is connected to back-to-back power converter of the DFIG system, it should be maintained constant within a narrow range of the maximum permissible dc-voltage ($V_{dc\text{-}max}$) and the minimum permissible dc-voltage ($V_{dc\text{-}min}$). Hence for the DC voltage control, the reference voltage ($V_{dc\text{-}ref}$) can be given as:

$$V_{dc-ref} = \begin{cases} V_{dc-\min}, if\ V_{dc} \le V_{dc-\min} \\ V_{dc-\max}, if\ V_{dc} \ge V_{dc-\max} \end{cases} \tag{7.69}$$

Equation (7.68) can be re-written as:

$$C_{dc} pV_{dc} = I_r + \frac{3}{4}\left(M_{dL} I_{df} + M_{qL} I_{qf}\right) - I_b = \sigma_{dc} = k_{dc}(V_{dc}^* - V_{dc}) \tag{7.70}$$

and Equation (7.70) can be re-written as:

$$I_{df} = \frac{1}{M_{dL}}\left(\frac{4}{3}\left(\sigma_{dc} - I_r + I_b\right) - M_{qL} I_{qf}\right) \tag{7.71}$$

The voltage magnitude (V_{tm}) at load bus is given as:

$$V_{tm}^2 = V_{qt}^2 + V_{dt}^2 \tag{7.72}$$

Differentiating (7.72) with respect to time,

$$pV_{tm}^2 = 2V_{qt} pV_{qt} + 2V_{dt} pV_{dt} \tag{7.73}$$

Equation (7.74) gives the square of voltage magnitude dynamics at the load bus. Thus the voltage magnitude is: $V_{tm} = \left|\sqrt{V_{tm}^2}\right|$.

Now applying KCL at the load bus,

$$I_{qw} - I_{qLL} - I_{qnL} - I_{qL} = C_m pV_{qt} + C_m \omega_e V_{dt} \tag{7.74}$$

$$pV_{qt} = \frac{1}{C_m}\left\{I_{qw} - I_{qLL} - I_{qnL} - I_{qL} - \omega_e V_{dt}\right\} \tag{7.75}$$

Similarly,

$$I_{dw} - I_{dLL} - I_{dnL} - I_{dL} = C_m pV_{dt} - C_m \omega_e V_{qt} \tag{7.76}$$

$$pV_{dt} = \frac{1}{C_m}\left\{I_{dw} - I_{dLL} - I_{dnL} - I_{dL} + \omega_e V_{qt}\right\} \tag{7.77}$$

where C_m is the filter capacitor, $I_{qw} = I_{qf} - I_{qs}$ and $I_{dw} = I_{df} - I_{ds}$ are the q and d axis currents supplied by DFIG wind turbine system and I_{qL}, I_{qLL}, I_{qnL}, I_{dL}, I_{dLL}, I_{dnL} are q and d axis currents drawn by RL load, linear load and non-linear load, respectively.

Inner current control loop:

From Equation.(7.66):

$$\sigma_{qL} = \left(k_{pqL} + \frac{k_{iqL}}{p}\right)\left(I_{qf}^{\ *} - I_{qf}\right) \tag{7.78}$$

$$\left(r_f + pL_f\right)I_{qf} = \left(k_{pqL} + \frac{k_{iqL}}{p}\right)I_{qf}^{\ *} - \left(k_{pqL} + \frac{k_{iqL}}{p}\right)I_{qf} \tag{7.79}$$

$$\frac{I_{qf}}{I_{qf}^{\ *}} = \frac{pk_{pqL} + k_{iqL}}{p^2 L_f + p(r_f + k_{pqL}) + k_{iqL}} = \frac{\frac{1}{L_f}\left(pk_{pqL} + k_{iqL}\right)}{p^2 + p\frac{1}{L_f}(r_f + k_{pqL}) + \frac{1}{L_f}k_{iqL}} \tag{7.80}$$

Comparing denominator of (7.80) with the Butterworth second order polynomial:

$p^2 + \sqrt{2}\omega_{0c} p + \omega_0^{\ 2}$, gives:

$$k_{pqL} = k_{pdL} = \sqrt{2}\omega_{0c} L_f - r_f \tag{7.81}$$

$$k_{iqL} = k_{idL} = L_f \omega_{0c}^{\ 2} \tag{7.82}$$

where ω_{0c} is the bandwidth of the current controller.

DC-voltage control loop:

From Equation (7.70):

$$C_{dc} pV_{dc} = \sigma_{dc} = k_{dc}(V_{dc}^{*} - V_{dc}) \tag{7.83}$$

$$C_{dc}pV_{dc} = \left(k_{pdc} + \frac{k_{idc}}{p}\right)V_{dc}^{*} - \left(k_{pdc} + \frac{k_{idc}}{p}\right)V_{dc} \tag{7.84}$$

$$\frac{V_{dc}}{V_{dc}^{*}} = \frac{pk_{pdc} + k_{idc}}{p^2C_{dc} + pk_{pdc} + k_{idc}} = \frac{\frac{1}{C_{dc}}\left(pk_{pdc} + k_{idc}\right)}{p^2 + p\frac{k_{pdc}}{C_{dc}} + \frac{k_{idc}}{C_{dc}}} \tag{7.85}$$

Comparing denominator of (7.85) with Butterworth second order polynomial gives:

$$k_{pdc} = \sqrt{2}\omega_{0dc}C_{dc} \tag{7.86}$$

$$k_{idc} = C_{dc}\omega_{0dc}^{2} \tag{7.87}$$

where ω_{0dc} is the bandwidth frequency of the DC-voltage controller.

Voltage magnitude control loop:

Substituting Equations (7.85) and (7.87) into (7.73) and further simplification yields:

$$\frac{C_m}{2}pV_{tm}^2 = V_{qt}\left(I_{qf} - I_{qs} - I_{qLL} - I_{qnL} - I_{qL}\right) + V_{dt}\left(I_{df} - I_{ds} - I_{dLL} - I_{dnL} - I_{dL}\right) = \sigma_m = k_m(V_m^{2*} - V_{tm}^2) \tag{7.88}$$

$$I_{qf} = \frac{1}{V_{qt}}\left\{\sigma_m - V_{dt}\left(I_{df} - I_{ds} - I_{dLL} - I_{dnL} - I_{dL}\right)\right\} + I_{qs} + I_{qLL} + I_{qnL} + I_{qL} \tag{7.89}$$

From Equation (7.79):

$$\frac{C_m}{2}pV_{tm}^2 = \sigma_{tm} = k_m(V_m^{2*} - V_{tm}^2) \tag{7.90}$$

$$\frac{C_m}{2}pV_{tm}^2 = \left(k_{Pm} + \frac{k_{\mathrm{Im}}}{p}\right)V_m^{2*} - \left(k_{Pm} + \frac{k_{\mathrm{Im}}}{p}\right)V_{tm}^2 \tag{7.91}$$

$$\frac{V_{tm}^2}{V_m^{2*}} = \frac{\frac{2}{C_m}\left(pk_{pm} + k_{im}\right)}{p^2 + p\frac{2k_{pm}}{C_m} + \frac{2k_{im}}{C_m}} \tag{7.92}$$

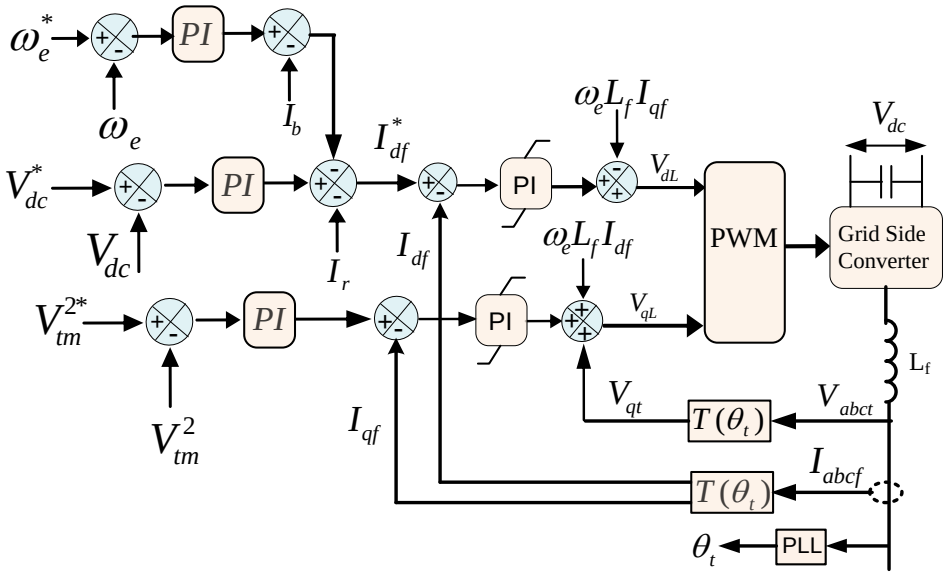

Figure 7.4 Block diagram of LSC controller

Comparing denominator of (7.92) with the Butterworth second order polynomial gives:

$$k_{Pm} = \sqrt{2}\frac{C_m}{2}\omega_{0m} \tag{7.93}$$

$$k_{\mathrm{Im}} = \frac{C_m}{2}{\omega_{0m}}^2 \tag{7.94}$$

where ω_{0m} is the bandwidth frequency of the voltage controller.

7.4.3 Phase Locked Loop (PLL) Design

A PLL is designed to define the reference frequency for qd transformation and included in the overall model of the system to make the design system more realistic. Figure 7.5 shows the 3-phase PLL which takes the input as the measured load bus voltage V_t and transforms it to qd-reference frame. PLL aligns the load voltage to q-axis by

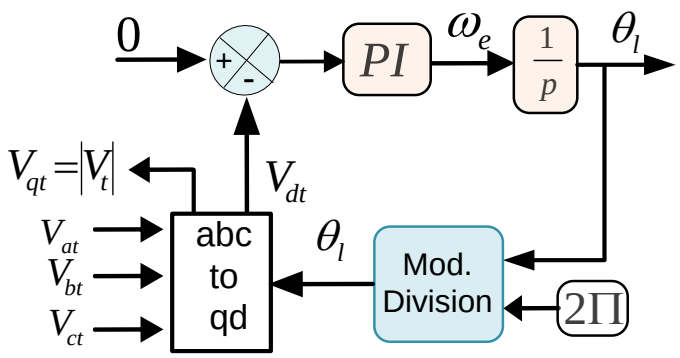

Figure 7.5 Block diagram of PLL control

comparing d-axis load voltage with zero reference voltage. The voltage error signal is passed through the PI controller to obtain the angular frequency of the load bus voltage. Hence in the PLL system:

$$V_{dt} = -V_t \sin(\theta_i - \theta_l) \Rightarrow 0 = -V_t \sin(\theta_i - \theta_l) \tag{7.95}$$

$$\theta_i = \theta_l \tag{7.96}$$

Now the error signal is given as: $e = 0 - V_{dt} = V_t \sin(\theta_i - \theta_l)$

If $(\theta_i - \theta_l)$ is very small, then we can write: $\sin(\theta_i - \theta_l) \approx (\theta_i - \theta_l)$

From the block diagram shown in Figure 7.5, $V_t(\theta_i - \theta_l)$ is the input to the controller and ω_l is the output from the controller hence:

$$V_t(\theta_i - \theta_l)K_{pll} = \omega_e \tag{7.97}$$

$$\Rightarrow \frac{1}{V_t} p\theta_l = (\theta_i - \theta_l)K_{pll} = \sigma_\theta \tag{7.98}$$

where, $K_{pll} = k_{P\_pll} + \frac{k_{I\_pll}}{p}$

$$\left(k_{P\_pll}+\frac{k_{I\_pll}}{p}\right)\theta_i-\left(k_{P\_pll}+\frac{k_{I\_pll}}{p}\right)\theta_l=\frac{1}{V_t}\,p\theta_l \;\Rightarrow \frac{\theta_l}{\theta_i}=\frac{pV_tk_{P\_pll}+V_tk_{I\_pll}}{p^2+pV_tk_{P\_pll}+V_tk_{I\_pll}},$$

(7.99)

Now comparing the denominator of (7.99) with the Butterworth second order polynomial, i.e. $p^2+\sqrt{2}\omega_0 p+\omega_0^2$, we can obtain the parameters of the controller as:

$$k_{P\_pll}=\frac{\sqrt{2}\omega_0}{V_t} \tag{7.100}$$

$$k_{I\_pll}=\frac{\omega_0^2}{V_t} \tag{7.101}$$

where ω_0 is the bandwidth frequency of the PLL controller. Table 7.2 gives the PI controllers values used for the simulation study following above procedure. The switching frequency is taken as 1 kHz and the bandwidth of inner current controller is taken ten times that of outer loop controller i.e

$\omega_{sw}=2*\pi*f_{sw}=6280\ rad/s$ and $\omega_{inner}=\frac{\omega_{sw}}{10}$; $\omega_{outer}=\frac{\omega_{inner}}{10}$

$\omega_{inner}=\omega_0=\omega_{oc}=628\ rad/s$; $\omega_{outer}=\omega_{odc}=\omega_{om}=62.8\ rad/s$ and $\omega_{owr}=0.628\ rad/s$

From (7.58): $k_{qp}=k_{dp}=\sqrt{2}\omega_0\sigma L_r-r_r\ =1.76$ and from (7.59): $k_{qi}=k_{di}=\sigma L_r\omega_0{}^2=783.6$

From (7.26): $k_{Pwr}=\sqrt{2}\omega_{owr}\frac{2J}{P}=8.26$ and from (7.27): $k_{Iwr}=\frac{2J}{P}\omega_{owr}^2=3.65$

From (7.43): $k_{PQs}=\sqrt{2}\omega_{0Qs}\Delta$ and from (7.44): $k_{IQs}=\Delta\omega_{Qs}{}^2$

From (7.86): $k_{pdc}=\sqrt{2}\omega_{odc}C_{dc}=0.53$ and from (7.87): $k_{idc}=\omega_{odc}^2C_{dc}=23.66$

From (7.93): $k_{Pm}=\sqrt{2}\omega_{om}\frac{C_f}{2}=0.22$ and from (7.94): $k_{\mathrm{Im}}=\omega_{om}^2\frac{C_f}{2}=3.94$

Table 7.2 PI controller parameters and machine parameters

r_s	2.3 mΩ	C_{dc}	6 mF	k_{qp}/k_{dp}	1.76	k_{qi}/k_{di}	783.6
r_r	2 mΩ	L_f	2 mH	k_{Pwr}	8.26	k_{Iwr}	3.65
L_s	2.93 mH	r_f	2 mΩ	k_{pdc}	0.53	k_{idc}	23.66
L_r	2.97 mH	J	18.7 kg.m^2	k_{Pm}	0.088	k_{Im}	3.94
L_m	2.88 mH	P	4	k_{P1}	1.77	k_{I1}	788.76
σ	0.669	C_f	2 mF				
V_t	563.38 V			k_{P_pll}	2.10	k_{I_pll}	1244.4

From (7.81): $k_{PqL} = \sqrt{2}\omega_{oc}L_f - r_f = 1.77$ and from (7.82): $k_{IqL} = \omega_{oc}^2 L_f = 788.76$

The switching frequency is taken as 2 kHz and the bandwidth of the PLL controller is taken as: $\omega_{sw} = 2*\pi* f_{sw} = 12{,}560\ rad/s$ and $\omega_0 = \frac{\omega_{sw}}{15} = 837.3\ rad/s$

From (7.100): $k_{P\_pll} = \frac{\sqrt{2}\omega_0}{V_t} = 2.10$ and from (7.101): $k_{I\_pll} = \frac{\omega_0^2}{V_t} = 1244.4$

7.4.4 Stator Flux Estimation

As shown in Figure 7.3, the stator side flux should be estimated as accurately as possible for the RSC control implementation. Therefore this section explains the stator flux estimation using Low Pass Filter (LPF).

The stator flux in stationary reference frame is given as:

$$V_{qds}^s = r_s I_{qds}^s + p\lambda_{qds}^s \tag{7.102}$$

$$\lambda_{qds}^s = \int \left(V_{qds}^s - r_s I_{qds}^s\right) dt \tag{7.103}$$

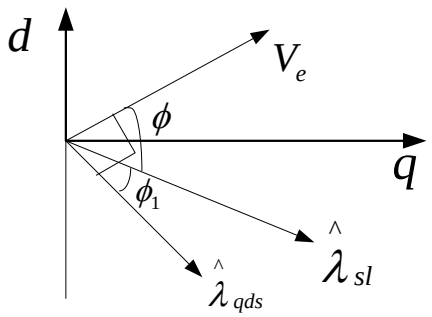

Figure 7.6 Vector diagram of the LPF and the pure integrator [64]

Flux can be estimated using (7.103) but the pure integration ($1/p$) involves the DC offsets and drifts [64]. To solve these problems, the pure integrator is replaced by a LPF. The estimated stator flux by the LPF can be given as:

$$\frac{\hat{\lambda}_{sl}}{V_e} = \frac{1}{p+a} \tag{7.104}$$

where $\hat{\lambda}_{sl}$ is the estimated stator flux by LPF, a = pole and $V_e = V_{qds} - r_s I_{qds}$.

The phase lag and the gain of (7.104) can be given as:

$$\phi = -\tan^{-1}\frac{\hat{\omega}_e}{a} \tag{7.105}$$

$$M = \left|\frac{\hat{\lambda}_{sl}}{V_e}\right| = \frac{1}{\sqrt{a^2 + \hat{\omega}_e^2}} \tag{7.106}$$

where $\hat{\omega}_e$ is the estimated synchronous angular frequency given as [64]:

$$\hat{\omega}_e = \frac{(V_{qs} - r_s I_{qs})\lambda_{ds} - (V_{ds} - r_s I_{ds})\lambda_{qs}}{|\lambda_s|^2} \tag{7.107}$$

The LPF eliminates the saturation and reduces the effect of DC offsets but at the same time it brings the magnitude and phase angle error due to the cut off frequency of the LPF. Figure 7.6 shows the phase lag of $\hat{\lambda}_{sl}$ estimated by the LPF, and the phase lag of $\hat{\lambda}_{qds}$ estimated by the pure integrator. The phase lag of $\hat{\lambda}_{qds}$ is 90° and the gain is $1/\left|\hat{\omega}_e\right|$. However, the phase lag of the LPF is not 90° and the gain is not $1/\left|\hat{\omega}_e\right|$. Hence, an error will be produced by this effect of the LPF. When the machine frequency is lower than the cutoff frequency of the LPF, the error is more severe. In order to remove this error, the LPF in (7.104) should have a very low cutting frequency. However, there still remains the drift problem due to the very large time constant of the LPF. For the exact estimation of the stator flux, the phase lag and the gain of $\hat{\lambda}_{sl}$ in (7.104) have to be 90° and $1/\left|\hat{\omega}_e\right|$, respectively. Furthurmore, to solve the drift problem, the pole should be located far from the origin.

Hence, the decrement in the gain of the LPF is compensated by multiplying a gain compensator, G in (7.108) and the phase lag is compensated by multiplying a phase compensator, P in (7.109) given as:

$$G = \frac{\sqrt{a^2 + \hat{\omega}_e^2}}{\left|\hat{\omega}_e\right|} \tag{7.108}$$

$$P = \exp(-j\phi_1) \tag{7.109}$$

$$\phi_1 = \tan^{-1}\frac{\hat{\omega}_e}{a} - \frac{\pi}{2} \tag{7.110}$$

$$\frac{\hat{\lambda}_{qds}}{V_e} = \frac{1}{p+a}\frac{\sqrt{a^2+\hat{\omega}_e^2}}{\left|\hat{\omega}_e\right|}\exp(-j\phi_1) \tag{7.111}$$

The cutoff frequency in LPF cannot be located at fixed point far from the origin. If the pole is varied proportionally to the machine speed, the proportion of the machine frequency to the cutoff frequency of the LPF is constant. If the proportion is large, the estimation error will be very small. Consequently, the pole is determined to be varied proportionally to the motor speed as (7.112). Therefore, the pole is located close to the origin in very low speed range and far from the origin in high speed range.

$$a = \frac{\left|\hat{\omega}_e\right|}{K} \tag{7.112}$$

where K = constant.

The complete equation for stator flux estimator can be derived as:

$$\frac{\hat{\lambda}_{qds}}{V_e} = \frac{1}{p+(\hat{\omega}_e/K)}\frac{\sqrt{(\hat{\omega}_e/K)^2+\hat{\omega}_e^2}}{\left|\hat{\omega}_e\right|}\exp(-j\phi_1) \tag{7.113}$$

where $\exp(-j\phi_1) = \cos(\phi_1) - j\sin(\phi_1)$, $\cos(\phi_1) = \dfrac{\left|\hat{\omega}_e\right|}{\sqrt{(\hat{\omega}_e/K)^2+\hat{\omega}_e^2}}$ and $\sin(\phi_1) = \dfrac{\hat{\omega}_e/K}{\sqrt{(\hat{\omega}_e/K)^2+\hat{\omega}_e^2}}$

Simplifying (7.113) and separating into real and imiginary parts gives:

$$\hat{\lambda}_{qs} = \frac{1}{p+(\hat{\omega}_e/K)}\frac{\sqrt{(\hat{\omega}_e/K)^2+\hat{\omega}_e^2}}{\left|\hat{\omega}_e\right|}\left\{\cos\phi_1(V_{qs}-r_sI_{qs}) + \sin\phi_1(V_{ds}-r_sI_{ds})\right\} \tag{7.114}$$

$$\hat{\lambda}_{ds} = \frac{1}{p+(\hat{\omega}_e/K)}\frac{\sqrt{(\hat{\omega}_e/K)^2+\hat{\omega}_e^2}}{\left|\hat{\omega}_e\right|}\left\{\cos\phi_1(V_{ds}-r_sI_{ds}) - \sin\phi_1(V_{qs}-r_sI_{qs})\right\} \tag{7.115}$$

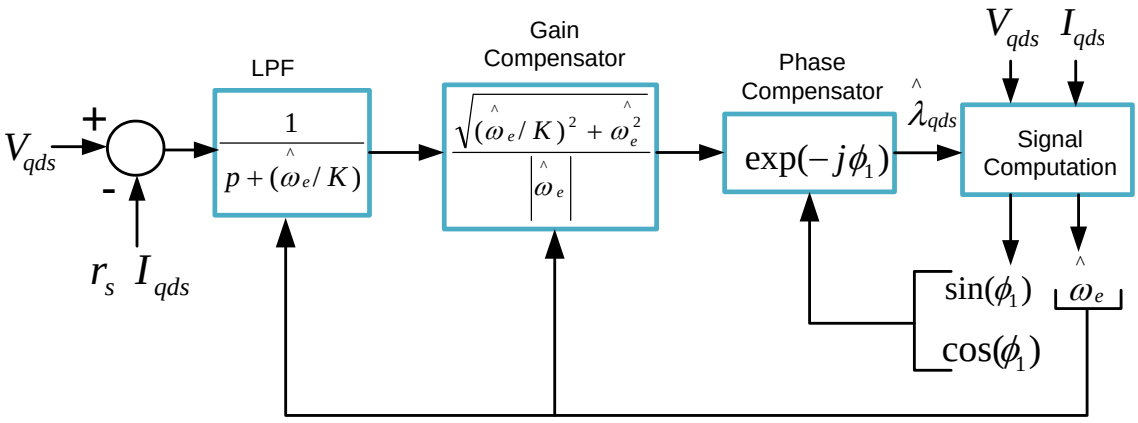

Figure 7.7 Overall block diagram of the stator flux estimation using LPF [64]

Figure 7.7 shows the overall block diagram of the whole system to estimate stator side flux using LPF and synchronous speed of the machine.

7.4.5 Droop Control

The droop control method is used to regulate the load frequency and voltage magnitude in the autonomous operation mode of DFIG wind turbine system with integrated energy storage. Droop control is given by [72]:

$$\omega_e^* = \omega_o - \kappa_{\omega-P} P \tag{7.116}$$

$$V_m^* = V_0 - \kappa_{V-Q} Q \tag{7.117}$$

where ω_o and V_0 are the nominal frequency and voltage of the system, respectively. $\kappa_{\omega-P}$, κ_{V-Q}, P and Q are active power droop coefficient, reactive power droop coefficient, output active power and output reactive power of LSC, respectively. The

active power droop coefficient depends on maximum change of tolerable frequency (taken 1% in this study) with maximum change in active power from LSC given as:

$$\kappa_{\omega-P} = \frac{\Delta\omega}{\Delta P_{\max}} \tag{7.118}$$

Similarly, reactive power droop coefficient depends on maximum change of tolerable voltage (taken 2% in this study) with maximum change in reactive power from LSC given as:

$$\kappa_{V-Q} = \frac{\Delta V}{\Delta Q_{\max}} \tag{7.119}$$

As shown in Figure 7.8, the instantaneous output active and reactive power from LSC are calculated using measured DFIG system supplied current (I_{qdw}) and the load bus voltage (V_{qdt}) in qd reference frame as follows:

$$\begin{cases} \hat{P}_L = \frac{3}{2}(V_{qt}I_{qw} + V_{dt}I_{dw}) \\ \hat{Q}_L = \frac{3}{2}(V_{qt}I_{qw} - V_{dt}I_{dw}) \end{cases} \tag{7.120}$$

To obtain average value and remove fluctuations in output active and reactive powers, both instantaneous powers are passed through a low pass filter with a cut out frequency of ω_c which is taken to be 10% of the nominal frequency [72].

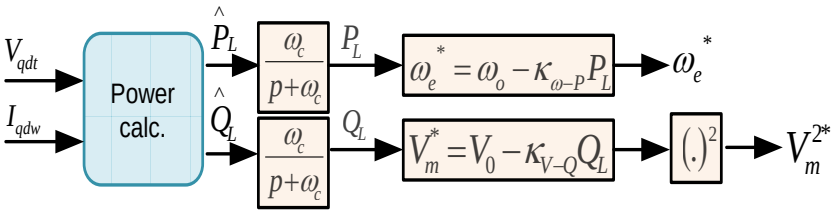

Figure 7.8 Block diagram showing droop control

$$\begin{cases} P_L = \dfrac{\omega_c}{p+\omega_c}\hat{P}_L \\ Q_L = \dfrac{\omega_c}{p+\omega_c}\hat{Q}_L \end{cases} \tag{7.121}$$

The outputs from the droop control are voltage magnitude and angular frequency which defines the reference for LSC.

7.4.6 Pitch Angle Control Scheme

The wind turbine blade pitch angle is controlled to regulate the output power from the wind turbine to match the load power demand and the power required to charge the embedded battery storage system. If the wind speed is high while the network load is small, pitch angle control is applied to reduce the output power from the DFIG so as to prevent the battery from being over-charged.

7.5 Battery Storage System and Converter Sizing

In case of the conventional DFIG, the RSC and LSC has to handle only fraction (25 - 30%) of total wind turbine power to control the whole generator. In autonomously operated DFIG wind turbine unit also, RSC is subjected to handle the rotor supplied power only like in conventional DFI. Hence the same size of RSC is needed. However, in this operation mode, the LSC requires larger rating to handle the sum of battery storage power and rotor supplied power.

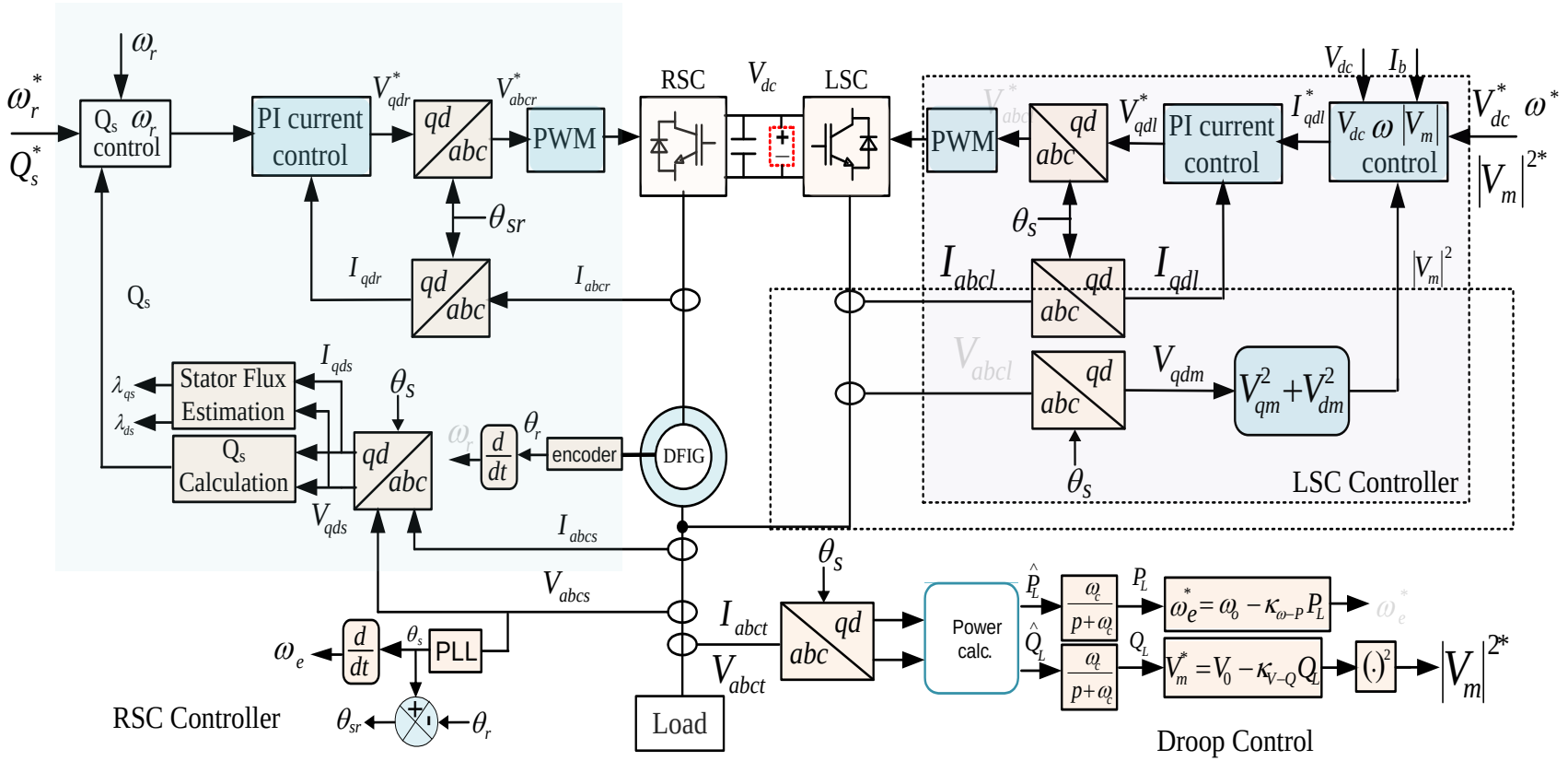

Figure 7.9 Schematic diagram of the autonomously operated DFIG wind turbine control structure

Moreover, the battery energy storage system must be sized properly to satisfy the technical requirements at the same time justifying the financial investment. Hence, the main factors to be considered in proper sizing include maximum and minimum load demand, wind speed profile on the plant site, and the economic analysis.

7.6 Frequency to the ac/dc/ac controllers in the DFIG

The droop control gives the reference frequency for the frequency control of DFIG wind turbine unit and the PLL measures the load bus frequency. Frequency control scheme shown in Figure 7.4 ensures that the PLL frequency tracks the reference frequency obtained from the droop control as shown in Figure 7.10. In this study, the frequency given by the droop controller (red thick line in Figure 7.10) is provided to the converters in the DFIG.

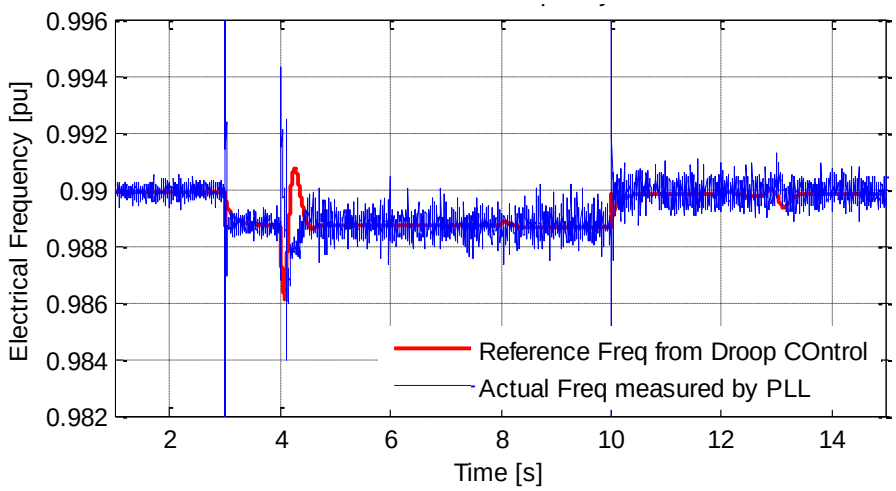

Figure 7.10 Waveforms of PLL and droop control output frequencies

7.7 Dynamic Simulation Results

To assess the effectiveness of the proposed control strategy, simulation studies are performed on a model of the system shown in Figure 7.1 in MATLAB/Simulink software environment. In this study, to show the charging and discharging of the battery storage system, the input wind speed of the DFIG system is varied in such a way that at minimum wind speed, the DFIG cannot supply enough power to the connected load. Hence, the battery storage system will supply the deficient power (discharging of battery) and at maximum wind speed, the DFIG will produce more than demanded power so the extra power will be stored to battery storage system (charging of the battery).

Case I: Low to medium wind speed operation

In this study, it is assumed that the storage system has enough capacity to store extra energy and to supply deficient energy as the wind speed varies. It is also assumed that the battery is assumed to be fully charged initially. The wind speed is varied as shown in Figure 7.11(a) and a step increase in load by 0.1 MW is introduced at t = 3 s, but the wind speed being the same (9.5 m/s). As a result, the frequency drops slightly (see Figure 7.14 (c)) according to droop control scheme and battery storage supplies the added 0.1 MW as shown in Figure 7.12 (b). At t = 4 s, when the wind speed suddenly drops from 9.5 m/s to 8.5 m/s, the DFIG wind turbine power output decreases so does the rotor speed but the connected load is same. In that case also the battery storage supplies the deficient active power as a result the frequency of the system remains constant with small transient oscillation. After t = 8 s, the wind speed starts increasing continuously so the battery supplied power decreases continuously till t = 10 s. At t = 11 s, active load

decreases by 0.1 MW hence the frequency of the system increases slightly. But the wind speed remains constant at 11 m/s. So after t = 9 s. (approximately), the amount of power generated by the DFIG wind turbine becomes more than the connected load. Hence, battery storage starts to store the extra power available. During the entire operation period, the load bus voltage magnitude is maintained constant with small oscillations during those disturbances in the system as shown in Figure 7.14(b). During charging and

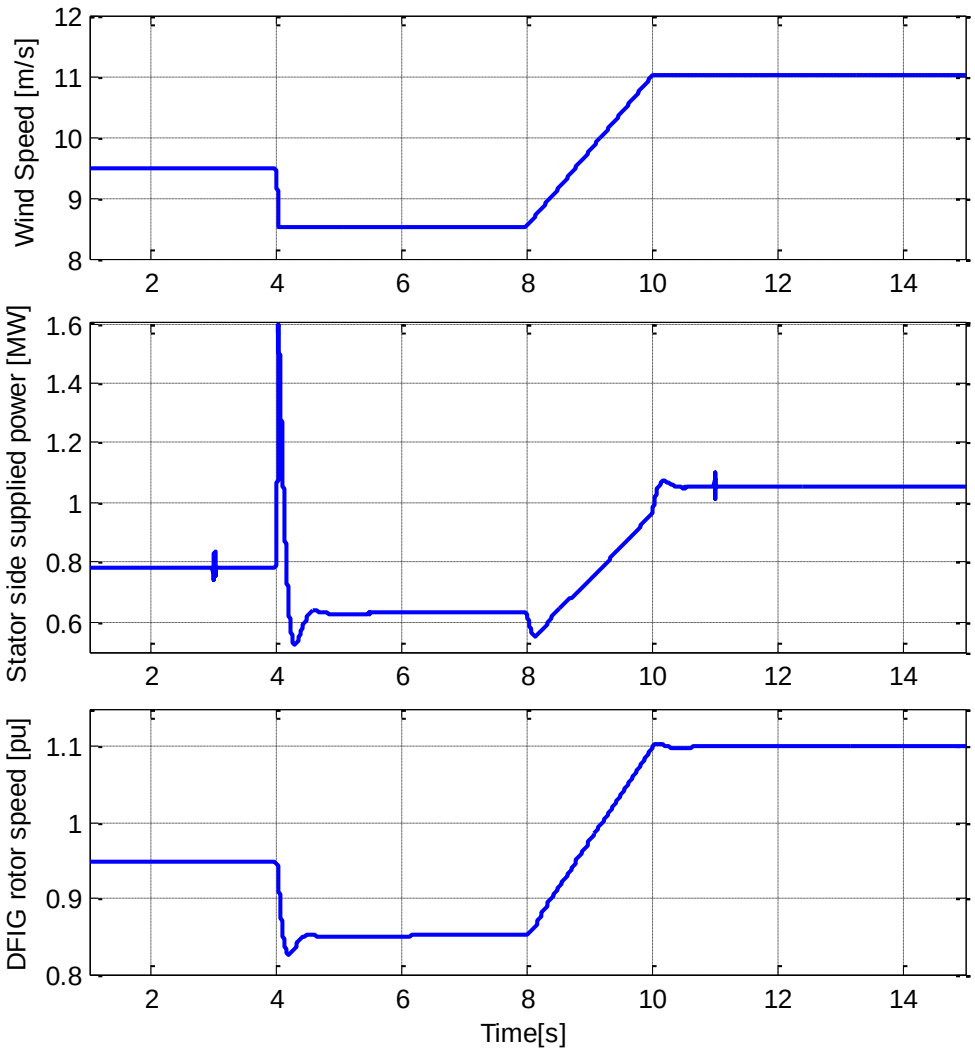

Figure 7.11 Waveforms of (a) wind speed, (b) stator supplied power and (c) Rotor speed

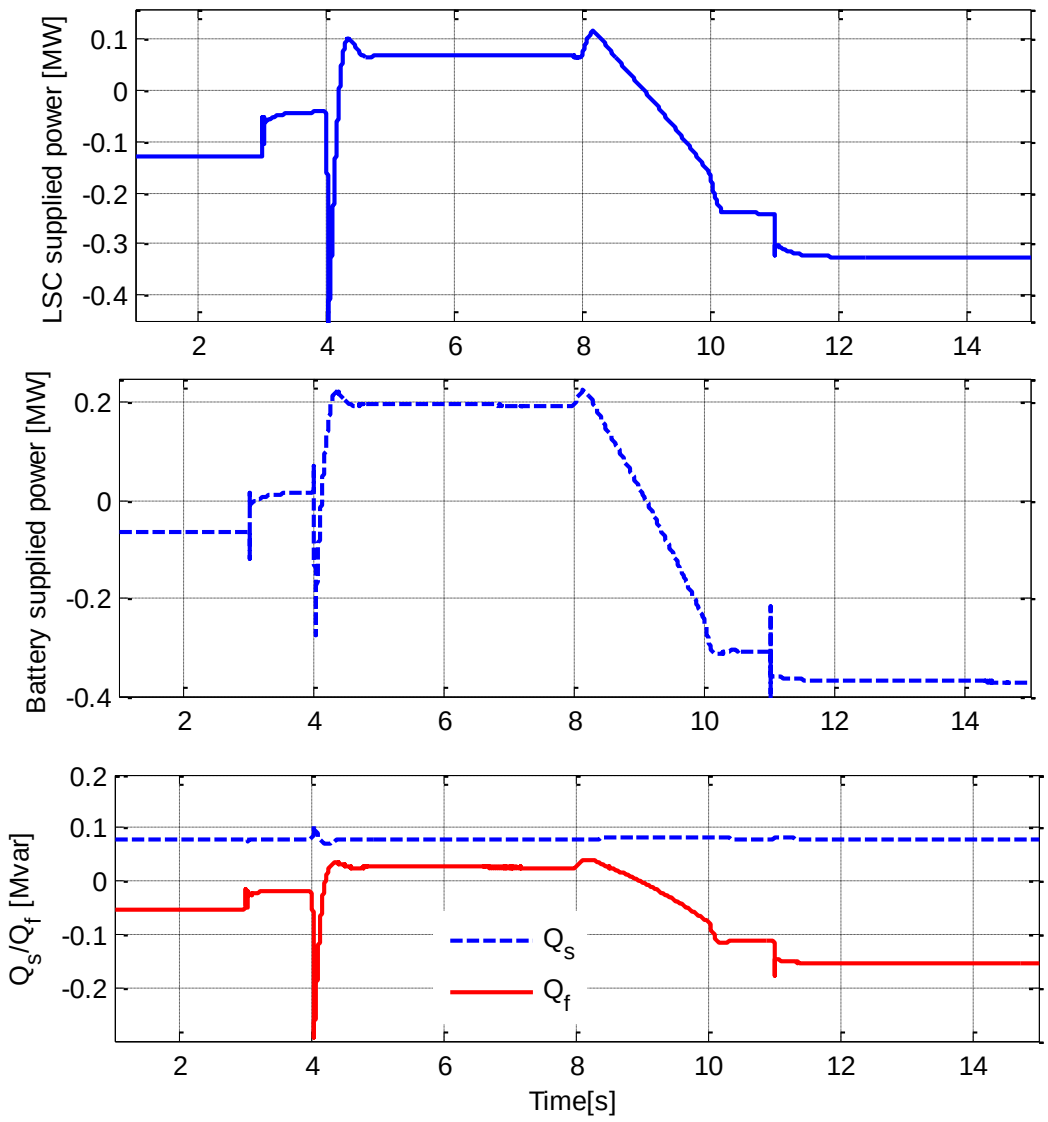

Figure 7.12 Waveforms of (a) LSC power (b) Battery supplied power and (c) Reactive power supplied by GSC and stator side

discharging of the battery, the DC-link voltage changes slightly but is regulated within 1% of the rated DC voltage. The stator side supplied reactive power is regulated to 0.08 Mvar, which is equal to the connected load. The GSC maintains the constant load voltage by suppluing (if positive) or absorbing (if negative) the reactive power from the system as shown in Figure 7.12(c).

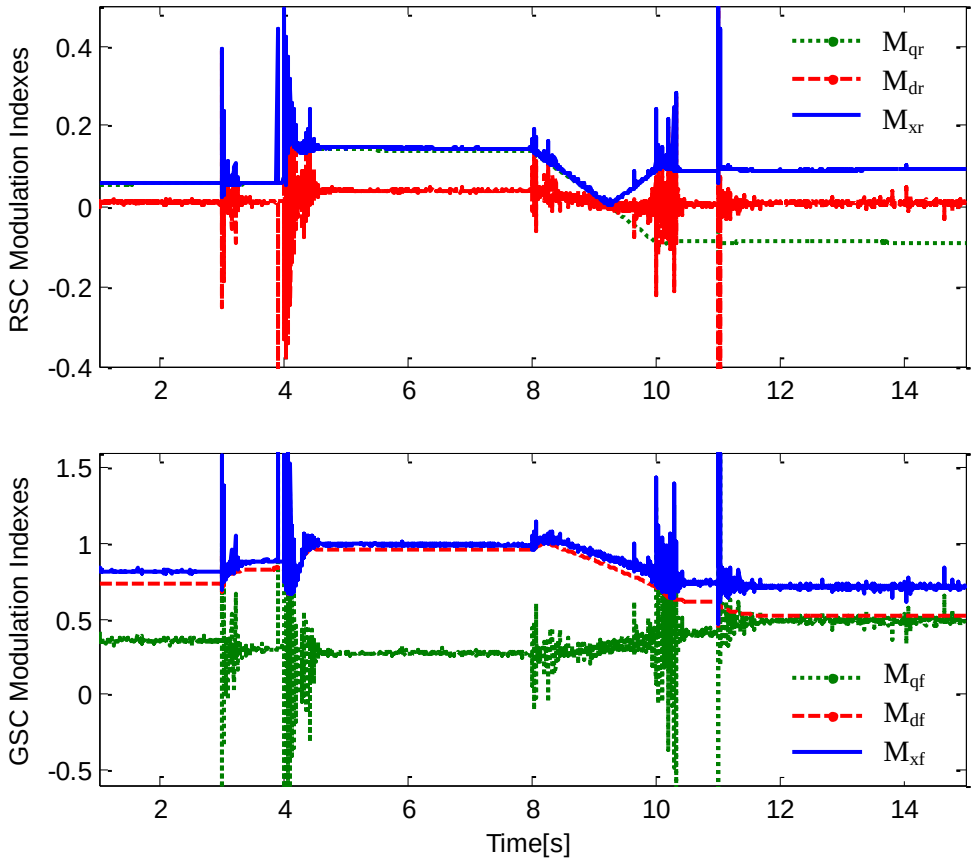

Figure 7.13 RSC and GSC modulation indexes

Case II: High wind speed operation:

When the wind speed is high, the size of storage device required will be also high. Since the storage system is expensive technology, its size will be limited. Limited size of storage device will have limited charging and discharging rates i.e limited current rating of the battery. As explained above, the pitch control mechanism is use to protect the battery system from getting overcharge. Here the wind speed is varied from 8 m/s to 15 m/s, and the rate of storing of energy (battery power) in the battery storage system is limited to 0.5 MW. When the wind speed is high, the amount of additional power to be

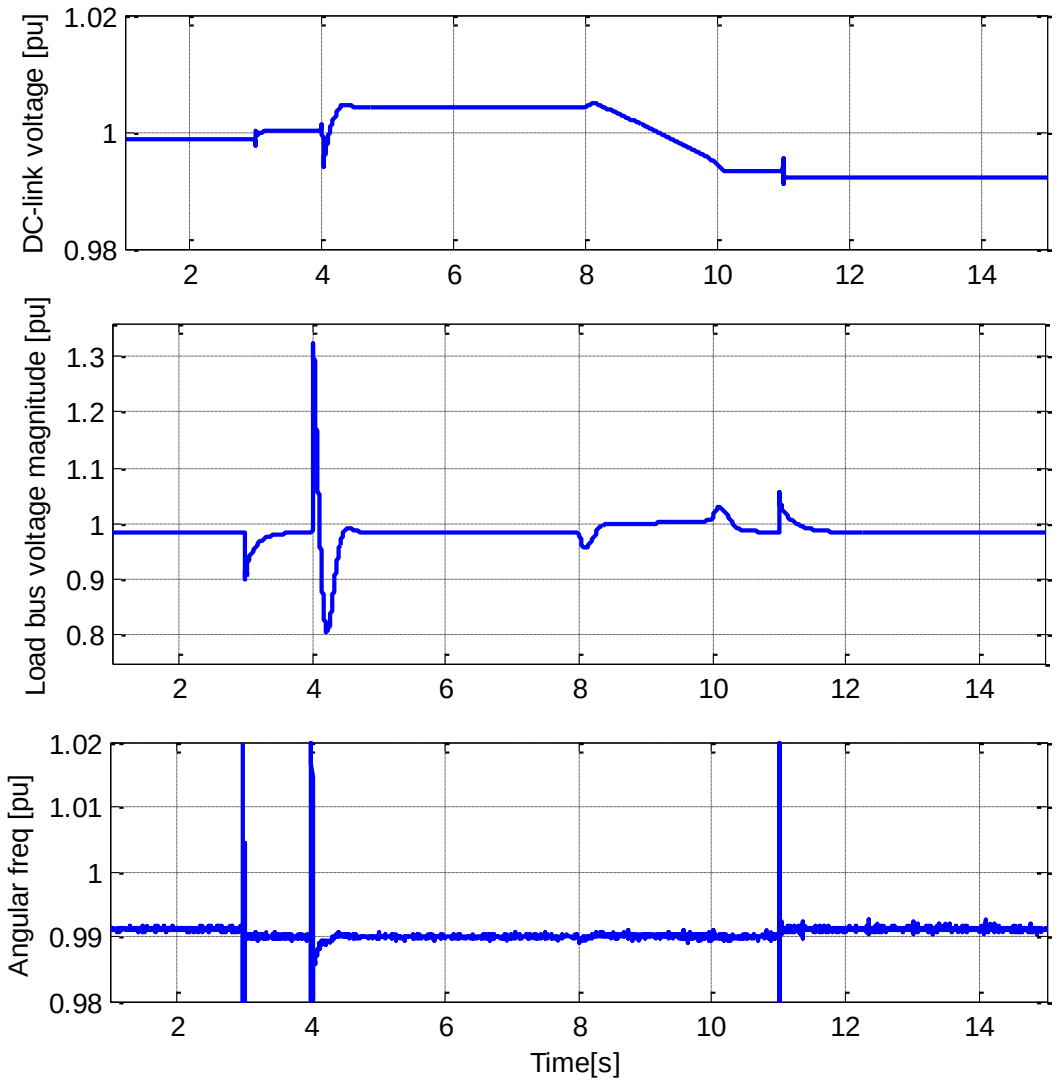

Figure 7.14 Waveforms of the (a) DC-link voltage, (b) load bus voltage magnitude and (c) angular synchronous frequency of the system

stored in the battery increases because of increase in mechanical input power to the DFIG wind turbine, the connected load being same throughout the study period. When the power to the battery reached the limiting value, the pitch control system in DFIG will be activated to reduce the amount of mechanical power extracted from wind turbine as shown in Figure 7.15.

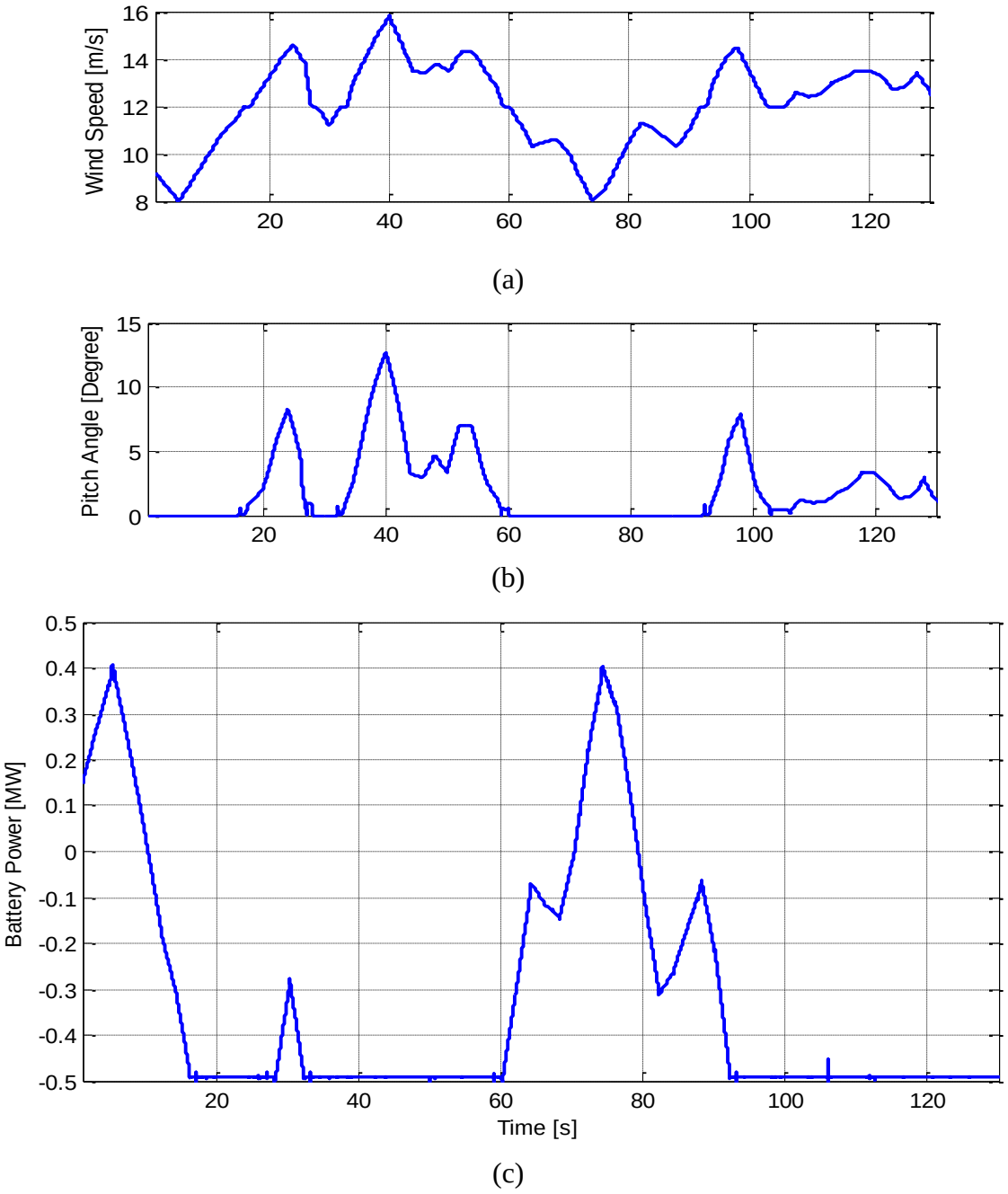

Figure 7.15 Waveforms of (a) wind speed (b) pitch angle and (c) battery power

7.8 Steady State Analysis

The steady state operating points of the DFIG Wind Turbine Unit can be obtained by making all the time derivatives equal to zero in the dynamic equations. The steady

state equations of the DFIG system used in this analysis, presented in Chapter 4, are given below:

$$V_{qs} = r_s I_{qs} + \omega_e L_s I_{ds} + \omega_e L_m I_{dr} \tag{7.121}$$

$$V_{ds} = r_s I_{ds} - \omega_e L_s I_{qs} - \omega_e L_m I_{qr} \tag{7.122}$$

$$V_{qr} = r_r I_{qr} + (\omega_e - \omega_r) L_m I_{ds} + (\omega_e - \omega_r) L_r I_{dr} \tag{7.123}$$

$$V_{dr} = r_r I_{dr} - (\omega_e - \omega_r) L_m I_{qs} - (\omega_e - \omega_r) L_r I_{qr} \tag{7.124}$$

From the droop control settings:

$$\omega_e = \omega_o - \kappa_{\omega-P} P_{load} \tag{7.125}$$

$$V_m = V_0 - \kappa_{V-Q} Q_{load} \tag{7.126}$$

Here, the overall system is isolated. Unlike the DFIG connected to grid system, the voltage at the stator (V_{qs}, V_{ds}) as well as the overall system's frequency are unknown. The droop control is implemented to regulate the stator voltage (same as the load bus voltage) magnitude V_m and system frequency ω_e. As shown in above six equations, for given rotor speed (ω_r) or wind speed (V_w), nominal frequency (ω_o), nominal voltage magnitude (V_0) and instantaneously measured active and reactive loads (P_{load}, Q_{load}), (7.121) - (7.126) is a system of six equations and ten unknowns (V_{qs}, V_{ds}, ω_e, V_m, V_{qr}, V_{dr}, I_{qs}, I_{ds}, I_{qr} and I_{dr}). As a result, four constraints have to be specified so that an operating point can be determined. Since the overall system is isolated, the stator voltage here is aligned along the q-axis so that:

$$V_{qs} = V_m \tag{7.127}$$

$$V_{ds} = 0 \tag{7.128}$$

In the wind energy conversion applications, it is reasonable to impose a constraint on the electrical torque (or rotor speed) for maximum power captured.

Mechanical Torque = Electro-magnetic Torque

$$T_m = \frac{3P}{4} L_m \left[I_{qr} I_{ds} - I_{dr} I_{qs} \right] \tag{7.129}$$

In the DFIG, the rotor side is connected to the load bus through back-to-back power converters and the battery storage system is connected in parallel with the DC-link of converter whose steady state equations are given by:

DC-link capacitor does not exchange any DC-current during steady state, i.e.:

$$\frac{3}{4}\left(M_{qr} I_{qr} + M_{dr} I_{dr}\right) + \frac{3}{4}\left(M_{qL} I_{qf} + M_{dL} I_{df}\right) - I_b = 0 \tag{7.130}$$

where M_{qr} and M_{dr} are RSC modulation indexes, I_{qr} and I_{dr} are current flowing into RSC, where M_{qL} and M_{dL} are LSC modulation indexes, I_{qf} and I_{df} are currents flowing out from LSC to load bus and I_b is the battery supplied current. Here, it should be noted that during steady state, DC-link voltage V_{dc} is constant so $M_{qr} = \frac{2V_{qr}}{V_{dc}}$ and $M_{dr} = \frac{2V_{dr}}{V_{dc}}$.

Using Kirchhoff's voltage law (KVL) from LSC to load bus as shown in Figure 7.1,

$$M_{qL} \frac{V_{dc}}{2} = r_f I_{qf} + \omega_e L_f I_{df} + V_{qs} \tag{7.131}$$

$$M_{dL} \frac{V_{dc}}{2} = r_f I_{df} - \omega_e L_f I_{qf} + V_{ds} \tag{7.132}$$

Now the constant load drawn current is given by (7.18) as:

$$I_{qLL} = \frac{2}{3} \frac{PV_{qs} + QV_{ds}}{V_m^2} \tag{7.133}$$

$$I_{dLL} = \frac{2}{3}\frac{PV_{ds} - QV_{qs}}{V_m^2} \tag{7.134}$$

Similarly, the non-linear load drawn current is given by (7.19) as:

$$I_{qnL} = \frac{2}{3}\frac{P_{non}V_{qs} + Q_{non}V_{ds}}{V_m^2} \tag{7.135}$$

$$I_{dnL} = \frac{2}{3}\frac{P_{non}V_{ds} - Q_{non}V_{qs}}{V_m^2} \tag{7.136}$$

Non-linear load representation using (7.17) is given as:

$$P_{non} = P_o\left(\frac{V_m}{V_0}\right)^3\left(\frac{\omega}{\omega_0}\right)^3 \tag{7.137}$$

$$Q_{non} = Q_o\left(\frac{V_m}{V_0}\right)^3\left(\frac{\omega}{\omega_0}\right)^3 \tag{7.138}$$

In the linear RL loads, from (7.15),

$$V_{qs} = r_L I_{qL} + \omega_e L_L I_{dL} \tag{7.139}$$

$$V_{ds} = r_L I_{dL} - \omega_e L_L I_{qL} \tag{7.140}$$

Now, using KCL during steady state at the load bus:

$$I_{qf} = I_{qs} - I_{qLL} - I_{qnL} - I_{qL} + C_m\omega_e V_{ds} \tag{7.141}$$

$$I_{df} = I_{ds} - I_{dLL} - I_{dnL} - I_{dL} - C_m\omega_e V_{qs} \tag{7.142}$$

In DFIG wind turbine unit, during steady state the power output from the DFIG wind turbine as well as battery supplied current are assumed constant, i.e. ω_r, T_m and I_b are known. Then the DFIG wind turbine unit has 22 steady state Equations (7.121)-(7.142) and 22 unknowns which are: V_{qs}, V_{ds}, ω_e, V_m, I_{qs}, I_{ds}, I_{qr}, I_{dr}, I_{qf}, I_{df}, M_{qf},

M_{df}, M_{qr}, M_{dr}, I_{qL}, I_{dL}, I_{qnL}, I_{dnL}, I_{qLL}, I_{dLL}, P_{non} and Q_{non}. Hence unique solution of the DFIG wind turbine unit can be obtained.

7.8.1 Steady State Characteristics

Figure 7.16 to Figure 7.19 shows the steady-state characteristics obtained by solving Equations (7.121)-(7.142) under the assumptions that the power output from the DFIG wind turbine as well as battery supplied current are constant and the active constant load as well as reactive constant load are varied then the system electrical frequency as well as the load bus voltage magnitude changes as shown in Figure 7.16 and 7.17. Figure 7.18 and 7.19 show the changes in active and reactive non-linear loads with variation in system voltage magnitude and frequency. Hence, whenever there is an increase in load, the frequency and voltage decreases according to droop control Equations (7.118-7.119) as a result nonlinear load decreases and vice-versa.

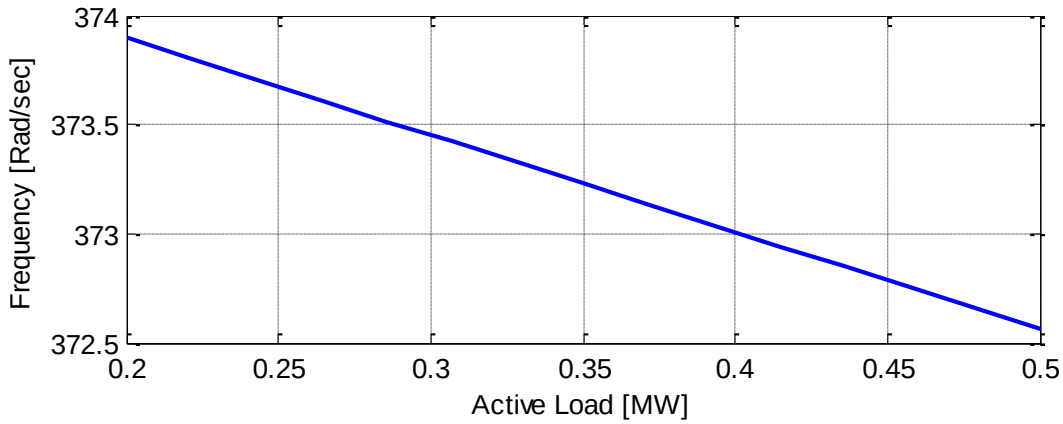

Figure 7.16 Variation of system angular frequency with change in active load

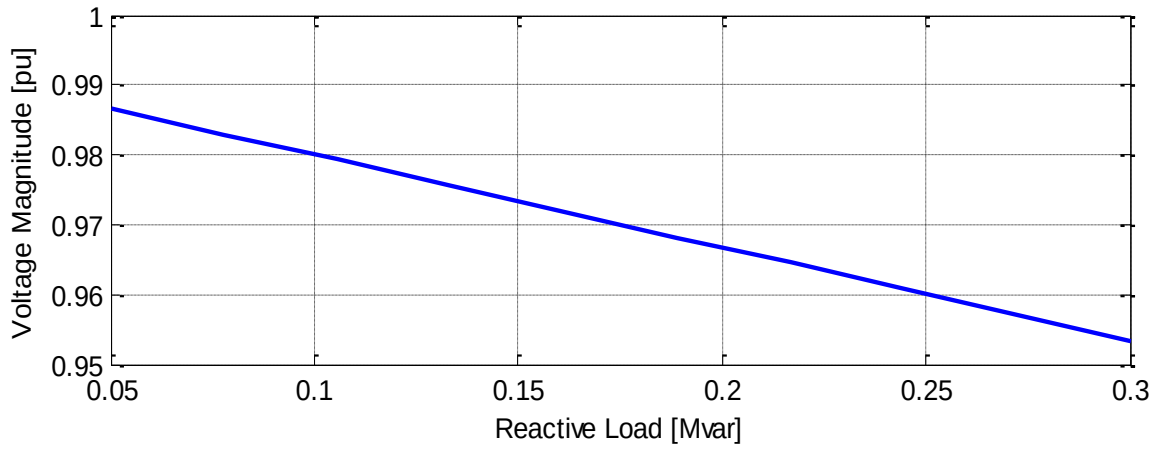

Figure 7.17 Variation of load bus voltage magnitude with change in reactive load

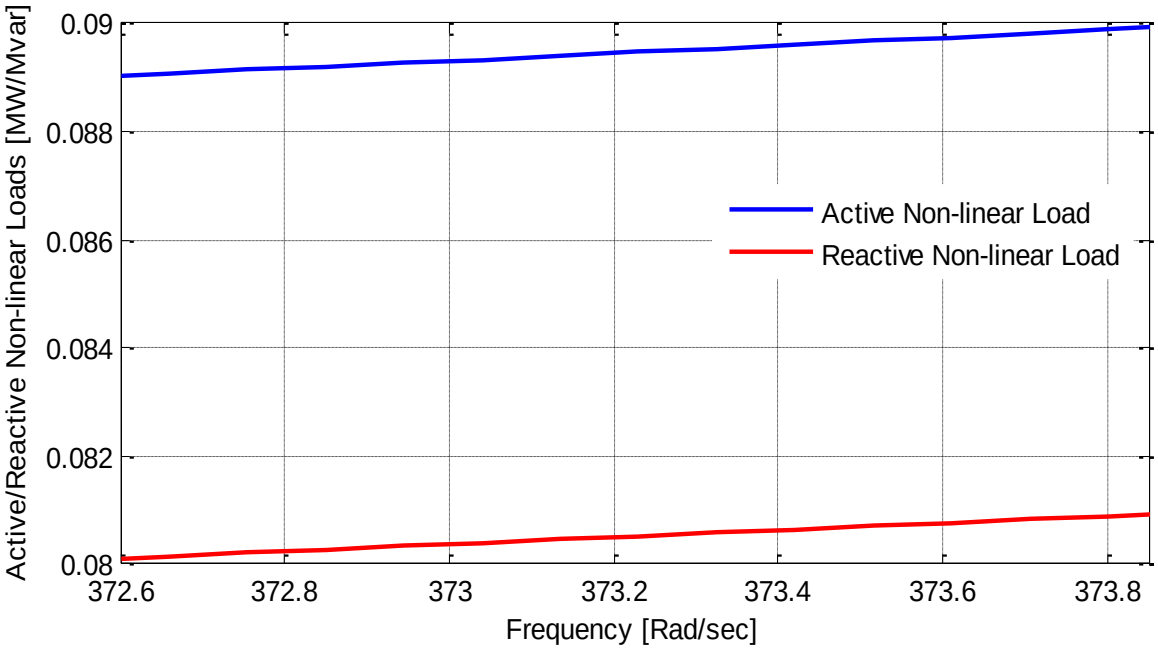

Figure 7.18 Variation of system non-linear loads with change in frequency

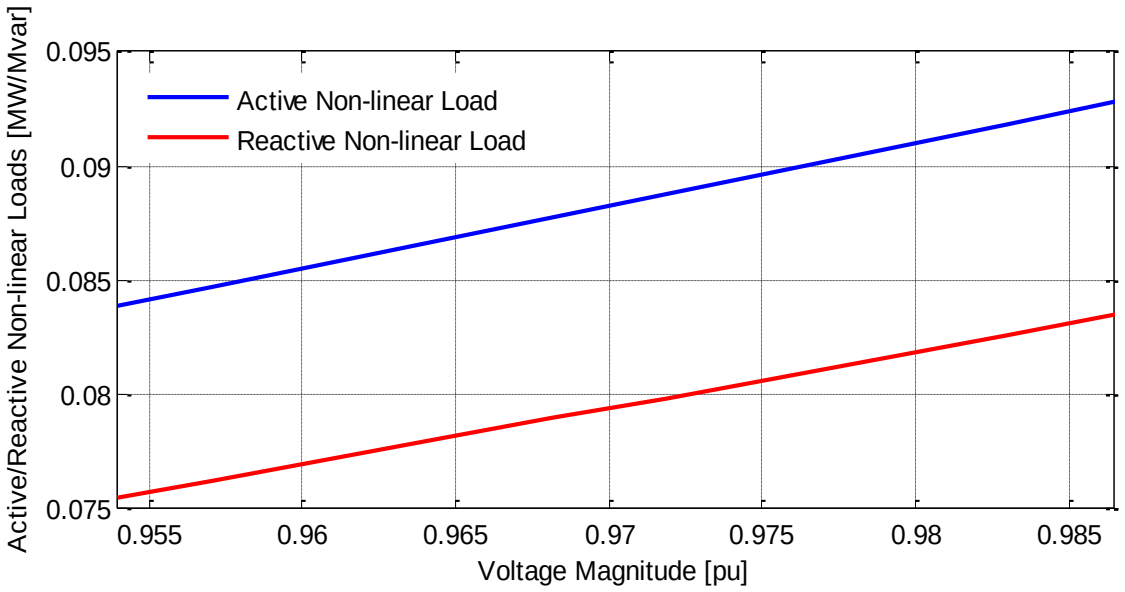

Figure 7.19 Variation of system non-linear loads with change in voltage magnitude

Hence, in this chapter, the autonomous operation mode of the DFIG is presented. The modeling of different components and controller design is shown. The effectiveness of the proposed control system is evaluated for under and over generation conditions with the connected load consisting of RL, linear, and non-linear loads. Excellent performance of the overall system is verified by analyzing the operation during both transient and steady state conditions. Chapter 8 presents the summary of the work done in this thesis and discusses the contributions made as well as possible extensions that can be done based on the results obtained in this work.

CHAPTER 8

CONCLUSIONS AND FUTURE WORK

8.1 Summary

A detailed simulation model of a DFIG-based wind turbine system with variable-speed variable-pitch control scheme is developed for the 1.5 MW wind turbine connected to the power grid. All of the primary components are modeled including the aerodynamic system of wind turbine, DFIG, rotor mechanical system, the overall control system, and the power grid. The stator side flux estimator is designed using LPF and a PLL system is embeded with the DFIG model which gives the reference angle to align the stator side voltage along the q-axis. The dynamic performance of the developed model is then assessed using the variable wind speed inputted into the model. This study provides a complete explanation of the overall DFIG-based wind turbine system dynamics, particularly in regards to the performance of the control system for the optimum wind power extraction and output power regulation operation.

The steady state model of the DFIG-based wind turbine system with variable-speed variable-pitch control scheme is presented and is used to analyze its aerodynamic, mechanical, and electrical operating characteristics. The active power flow direction in the stator and rotor sides of the machine during various rotor speeds is explained thoroughly based on the steady state power flow curves obtained. It is observed from the steady state power curve that a smaller power rated DFIG can be coupled with higher power rated wind turbine without overloading the DFIG. In the DFIG, it is seen that the

rotor voltage magnitude increases when the slip of the machine (both negative and positive) increases and is mimimum when machine runs at synchronous speed. So, rotor voltage rating limits the speed range of the DFIG. From the converter rating viewpoint, higher rated rotor speed of the machine is better as the current through converter is lower in the rated regime because the electromagnetic torque that machine has to develop at higher speed is lower for the same (rated) power output. On the other hand, higher rated rotor speed requires higher gear ratio, i.e. bigger size gearbox should be used. Hence, a suitable compromise must be reached between the gearbox size and the sizing of the power converters to minimize the cost of overall wind turbine system.

The steady state reactive power capability of the DFIG wind turbine is studied by plotting the PQ diagram and the following observations have been made:

- The reactive power capability of the machine is limited by rotor current rating, rotor voltage rating, and stator current rating.
- At low rotor speed, the rotor voltage limits the reactive power generation capability whereas at higher rotor speed, the rotor current limits the reactive power generating capability and the stator current limits the reactive power absorption capability.
- When the machine operates at higher power (more than 82 % of rated power), the reactive power that the DFIG can supply is not enough to meet the required power factor demanded by the grid code.
- The reactive power capability of the DFIG gets improved when the turbine operates in pitch control mode.

Hence, the deficiency in reactive power supplied by the DFIG compared to what is needed to meet the grid code requirements is fulfilled by installing the STATCOM at

the PCC. The maximum rating of the STATCOM needed to achieve the steady state reactive power requirement can be calculated from the PQ diagram of the overall DFIG and STATCOM system.

A simulation model of the STATCOM is developed to study its dynamic characteristics. The developed STATCOM is connected at the PCC of the DFIG wind turbine system connected to the weak distribution grid for steady state and dynamic voltage regulation purpose. Simulation results have shown that STATCOM helps to keep the steady state terminal voltage of the DFIG system to its rated voltage during the entire operation region of the DFIG. STATCOM maintains the fast voltage regulation (or voltage restoration) at the PCC during step change in reactive load causing voltage swelling or sagging. STATCOM does this by dynamically exchanging the reactive power with the power grid.

In series compensated transmission line, series capacitor effectively redues the net line reactance. So, such line absorbs less reactive power which helps to regulate the steady state voltage at the DFIG terminal and enhances the power carrying capability of the transmission line. Moreover, a GSC in the DFIG connected to power grid through series compensated line has to supply less amount of reactive power to maintain constant terminal voltage.

Finally, in this thesis, the capability of autonomous operation of a DFIG-based wind turbine system with battery energy storage system connected in parallel with the DC-link capacitor of ac/dc/ac converter has been investigated. The control system for this proposed arrangement of the DFIG is able to regulate the standalone system's frequency and voltage magnitude within the specified limits. Implemented control system also

shows the ability to operate standalone system in under as well as over-generated condition. In an over generation situation, extra power will be stored in the battery whereas in an under generation situation, battery will supply the deficient power. The modeled wind turbine extracts maximum power from the wind and pitch control is implemented to protect the battery from getting overcharged. The system has been tested for low as well as high wind speed inputs and results obtained demonstrate the excellent dynamic and steady state performance.

8.2 Contributions

The main contributions of this thesis are explained below:

- Simulation model of a DFIG-based wind turbine system with variable-speed variable-pitch control scheme for wind turbine control and generator control to decouple active and reactive power output is systematically developed for grid connected as well as standalone operation mode. Detailed models of all components of the DFIG-based WECS have been derived and their operation is explained clearly. In the standalone operation, the performance of the proposed control system is assessed for the connected load consisting of RL, linear and non-linear loads.
- The steady state analysis of the overall DFIG wind turbine system connected to grid is done after explaining clearly the steady state equations used. The steady state operation modes of the DFIG wind turbine sytem based on the rotor speed are explained clearly. It is shown that, DFIG can generate more than 100 % of power output in super-synchronous operation region if higher size wind turbine is used.

- The steady state reactive power capability of the DFIG is derived in the form of P-Q diagram without making any assumptions to simplify the calculation. The P-Q diagram of DFIG is obtained for both MPPT and pitch control operation modes. It is observed that the reactive power capability gets improved in the pitch control operation mode. The PQ diagram of the overall DFIG with STATCOM connected at the PCC is derived from which maximum size of STATCOM needed to satisfy steady state reactive power requirement can be calculated.
- The power rating of the GSC in the DFIG required for supplying reactive power to fulfill the grid code requirement is found out to be more than three times the GSC required to operate in unity power factor operation mode. The GSC size required is even more if the grid is operating in under-voltage condition. So, installation of the STATCOM having excellent dynamic reactive power capability at the PCC, where reactive power is needed, is proposed to secure stable operation of the overall wind turbine and power grid hence fulfilling the grid code requirement. The support provided by the STATCOM connected at the PCC of the DFIG wind turbine during disturbances in the grid side is studied and found that the STATCOM helps to improve dynamic performance of the DFIG-based wind turbine system significantly.
- Effectiveness of series compensated line for better steady state voltage regulation and enhancing the power carrying capability of the line is demonstrated through the dynamic and steady state simulation results.

8.3 Future Work

This thesis has unlocked many gates for the future researchers to work further on the variable-speed variable-pitch DFIG-based wind turbine system and its voltage regulation. The following points are identified as potential future work based on the results of the present thesis:

- Analysis of the dynamic behavior of a wind farm consisting of multi-DFIG wind turbines. The interest would be to study the overall dynamics of the wind farm at the PCC, the effect of unequal wind speed distribution on the mechanical and electrical power variation within the wind farm.
- Interaction of the DFIG wind turbine system with more realistic power grid models, where other type of generators like synchronous generators are also present. Similar study can be done in those power grids to evaluate the support provided by the use of a STATCOM.
- The steady state characteristics of the DFIG wind turbine system shows the better performance of the system at higher rated rotor speed. For example machine needs to develop less electromagnetic torque at higher rotor speed operating at rated power as a result the stator as well as rotor side current decreases which results in smaller current rating required for ac/dc/ac converter and improved efficiency of the WECS. Reactive power capability of the DFIG also gets better at higher rotor speed generating rated active power. At the same time, higher rotor speed requires higher gear ratio and the higher voltage magnitude is developed at the rotor side. Considering these facts, furthur study can be done for the higher speed operation of the DFIG wind turbine.

- Three phase symmetrical voltage swelling and sagging have been studied in this thesis that can be extended to observe the response of the system to other types of grid side disturbances.
- In this thesis, simulation results show that the dynamic performance of the DFIG-based wind turbine is improved with the use of a STATCOM. Future work can be done to analyze the harmonics in the system due to the introduction of STATCOM and evaluate techniques to mitigate the system harmonics.
- In the autonomous operation of the DFIG Wind Energy Conversion Unit, simulation study is done for the balanced three phase loads. Future work can be done to study the performance of the proposed control system in case of 1) unbalanced three phase loads, 2) disturbances in the load side like faults, abrupt voltage change and explore the ways to stabilize the overall system during those situations.

REFERENCES

[1] Hyong Sik Kim and Dylan Dah-Chuan Lu, “Wind Energy Conversion System from Electrical Perspective - A Survey,” *Smart Grid and Renewable Energy*, vol. 1, no. 3, pp.119-131, Nov. 2010.

[2] Francoise Mei, “Small Signal Modeling and Analysis of Doubly Fed Induction Generator in Wind Power Applications,” *Ph.D. dissertation*, Control and Power Group Dept of Electrical and Electronic Engineering Imperial College London University of London.

[3] Q. Wang and L. Chang, “An intelligent maximum power extraction algorithm for inverter-based variable speed wind turbine systems,” *IEEE Trans. Power Electronics*, vol. 19, no. 5, pp. 1242-1249, Sept. 2004.

[4] Danish Wind Industry Association. Know how: Guided tour. [Online]. Available: http://www.windpower.org.

[5] Raymond W. Flumerfelt and Su Su Wang, "Wind turbines," in AccessScience, ©McGraw-Hill Companies, 2009, [Online]. Available: http://www.accessscience.com.

[6] Wind Energy Background [Online]. Available: http://www.dolcera.com.

[7] Jianzhong Zhang, Ming Cheng, Zhe Chen and Xiaofan Fu, “Pitch Angle Control for Variable Speed Wind Turbines,” *Electric Utility Deregulation and Restructuring and Power Technologies*, pp. 2691-2696, 6-9 April 2008.

[8] Stephan Engelhardt, Istvan Erlich, Christian Feltes, J¨org Kretschmann, and Fekadu Shewarega, “Reactive Power Capability of Wind Turbines Based on Doubly Fed Induction Generator,” *IEEE Trans. on Energy Conversion*, vol. 26, no. 1, pp. 364-372, March 2011.

[9] Asynchronous Generators [Online]. Available: http://www.windturbines.net.

[10] S. Muller, M. Deicke and RikW. De Doncker, “Doubly fed induction generator systems for wind turbines,” *IEEE, Industry Applications Magazine*, vol. 8, iss. 3, pp. 26-33, May/June 2002.

[11] W. Qiao and R. G. Harley, “Power quality and dynamic performance improvement of wind farms using a STATCOM,” *in Proc. 38th IEEE Power Electronics Specialists Conference*, June 17-21, 2007, pp. 1832-1838.

[12] V. Akhmatov, “Analysis of dynamic behavior of electric power systems with large amount of wind power,” *Ph.D. dissertation*, Technical University of Denmark, Kgs. Lyngby, Denmark, Apr. 2003.

[13] R. Datta and V. T. Ranganathan, "Variable-speed wind power generation using doubly fed wound rotor induction – a comparison with alternative schemes,' *IEEE Trans. Energy Conversion*, vol. 17, no. 3, pp. 414-421, Sept. 2002.

[14] M. V. A. Nunes, J. A. Pecas Lopes, H. H. Zurn, U. H. Bezerra, and R. G. Almeida, "Influence of the variable-speed wind generators in transient stability margin of the conventional generators integrated in electrical grids," *IEEE Trans. Energy Conversion*, vol. 19, no. 4, pp. 692-701, Dec. 2004.

[15] J. Morren and S. W. H. de Haan, "Ridethrough of wind turbines with doubly-fed induction generator during voltage dip," *IEEE Trans. Energy Conversion*, vol. 20, no. 2, pp. 435-441, Jun. 2005.

[16] W. Leonard, *Control of Electrical Drives*, Springer, New York, 2001.

[17] N. Mohan, T. M. Undeland, and W. P. Robbins, *Power Electronics: Converters, Applications and Design*, Clarendon Press, Oxford, UK, 1989.

[18] R. Pena, J. C. Clare, and G. M. Asher, "Doubly fed induction generator using back-to-back PWM converters and its application to variable-speed wind-energy generation," *IEE Proc. Elect. Power Appl.*, vol. 143, no. 3, pp. 231-241, 1996.

[19] J. Carrasco, L. Franquelo, J. Bialasiewicz, E. Galvan, R. Guisado, M. Prats, J. Leon, and N. Moreno-Alfonso, "Power-electronic systems for the grid integration of renewable energy sources: A survey," *IEEE Trans. Industrial Electronics*, vol. 53, no. 4, pp. 1002–1016, Jun. 2006.

[20] A. Petersson, T. Thiringer, L. Harnefors, and T. Petru, "Modeling and experimental verification of grid interaction of a DFIG wind turbine," *IEEE Trans. Energy Convers.*, vol. 20, no. 4, pp. 878–886, Dec. 2005.

[21] S. L. Andreas Petersson and T. Thiringer, "A DFIG wind-turbine ridethrough system influence on the energy production," *in Proc. NORDIC Wind Power Conf.*, pp. 1–7, Mar. 2004.

[22] L. Xu, D. Zhi, and B. Williams, "Predictive current control of doubly fed induction generators," *IEEE Trans. Industrial. Electronics*, vol. 56, no. 10, pp. 4143–4153, Oct. 2009.

[23] J. Arbi, M.-B. Ghorbal, I. Slama-Belkhodja, and L. Charaabi, "Direct virtual torque control for doubly fed induction generator grid connection," *IEEE Trans. Industrial Electronics*, vol. 56, no. 10, pp. 4163–4173, Oct. 2009.

[24] B. Rabelo, W. Hofmann, J. da Silva, R. de Oliveira, and S. Silva, "Reactive power control design in doubly fed induction generators for wind turbines," *IEEE Trans. Industrial Electronics*, vol. 56, no. 10, pp. 4154–4162, Oct. 2009.

[25] S. Shao, E. Abdi, F. Barati, and R. McMahon, “Stator-flux-oriented vector control for brushless doubly fed induction generator,” *IEEE Trans. Industrial Electronics*, vol. 56, no. 10, pp. 4220–4228, Oct. 2009.

[26] B.H. Chowdhury and S. Chellapilla, “Double-fed induction generator control for variable speed wind power generation,” *Electric Power Systems Research*, vol. 76, iss. 9-10, pp. 786-800, June 2006.

[27] L. Xu and P. Cartwright, “Direct active and reactive power control of DFIG for wind energy generation,” *IEEE Transactions on Energy Conversion*, vol. 21, iss. 3, pp. 750-758, Sept. 2006.

[28] D.W. Zhi and L. Xu, “Direct power control of DFIG with constant switching frequency and improved transient performance,” *IEEE Transactions on Energy Conversion*, vol. 22, iss. 1, pp. 110-118, Mar. 2007.

[29] L. Xu and Y. Wang, “Dynamic Modeling and Control of DFIG Based Wind Turbines under Unbalanced Network Conditions,” *IEEE Transactions on Power Systems*, vol. 22, no. 1, Feb. 2007.

[30] T. Brekke and N. Mohan, “Control of a doubly fed induction wind generator under unbalanced grid voltage conditions,” *IEEE Transactions on Energy Conversion*, vol. 22, iss. 1, pp.129-135, Mar. 2007.

[31] Bakari Mwinyiwiwa, Yongzheng Zhang, Baike Shen, and Boon-Teck Ooi, “Rotor Position Phase-Locked Loop for Decoupled P-Q Control of DFIG for Wind Power Generation,” *IEEE Transactions on Energy Conversion*, vol. 24, no. 3, pp. 758-765, Sept. 2009.

[32] Shuhui Li, Timothy A. Haskew, Rajab Challoo, and Marty Nemmers, "Wind Power Extraction from DFIG Wind Turbines Using Stator-Voltage and Stator-Flux Oriented Frames," *International Journal of Emerging Electric Power Systems*, vol. 12, iss. 3, Article 7, 2011.

[33] Mustafa Kayıkc¸ı and Jovica V. Milanovi´c, “Reactive Power Control Strategies for DFIG-Based Plants,” *IEEE Trans. on Energy Conversion*, vol. 22, no. 2, pp. 389-396, June 2007.

[34] Torsten Lund, Poul Sorenson and Jarle Eek, “Reactive Power Capability of a Wind Turbine with Doubly Fed Induction Generator,” *Wind Energy*, vol. 10, iss. 4, pp.379-394, Apr. 2007.

[35] D. Santos-Martin, S. Arnaltes, and J.L. Rodriguez-Amenedo, “Reactive power capability of doubly fed asynchronous generators,” *Electric Power Systems Research*, vol.78, pp.1837-1840, 2008.

[36] Thomas Ackerman, *Wind Power in Power System*, Royal Institute of Technology, John Wiley & Sons, Inc., England, 2005.

[37] Wei Qiao, and Ronald G. Harley, "Grid Connection Requirements and Solutions for DFIG Wind Turbines," *in Proc. IEEE Energy 2030*, Atlanta, GA, USA, 17-18 Nov. 2008.

[38] Tim Poor, "Using FACTS Technology To Address Grid Interconnection Issues for Wind Farms," *Electric Energy Publications Inc*., American Superconductor, 2010.

[39] R. Fadaeinedjad, G. Moschopoulos, and M. Moallem, "Using STATCOM to Mitigate Voltage Fluctuations due to Aerodynamic Aspects of Wind Turbines," *in Proc. IEEE Power Electronics Specialists Conference*, pp. 3648 - 3654, 15-19 June 2008.

[40] B. Pokharel and Wenzhong Gao, "Mitigation of disturbances in DFIG-based wind farm connected to weak distribution system using STATCOM," *in Proc. IEEE North American Power Symposium*, pp. 1-7, 26-28 Sept. 2010.

[41] Willi Christiansen and David T. Johnsen, "Analysis of requirements in selected Grid Codes," [Online]. Available: http://www.frontwind.com.

[42] Chong Han, Alex Q. Huang, Mesut E. Baran, Subhashish Bhattacharya, Wayne Litzenberger, Loren Anderson, Anders L. Johnson, and Abdel-Aty Edris, "STATCOM Impact Study on the Integration of a Large Wind Farm into a Weak Loop Power System," *IEEE Trans. on Energy Conversion*, vol. 23, no. 1, Mar. 2008.

[43] G. Reed, R. Pape, and M. Takeda, "Advantages of voltage sourced converter (VSC) based design concepts for FACTS and HVDC-link applications," *in Proc. IEEE PES 2003 General Meeting*, vol. 3, pp. 1816-1821, July 13-17, 2003,.

[44] Jorge Martinez Gracia, "Voltage Control in Wind Power Plants with Doubly Fed Generators," Ph.D. Thesis, Alaborg University, Denmark, Sept. 2010.

[45] Wei Qiao, Ganesh Kumar Venayagamoorthy, and Ronald G. Harley, "Real-Time Implementation of a STATCOM on a Wind Farm Equipped With Doubly Fed Induction Generators," *IEEE Trans. on Industry Application*, vol. 45, no. 1, pp. 98-107, Jan./Feb. 2009.

[46] T. J. E. Miller, *Reactive Power Control in Electric System*, John Wiley & Sons, Inc., USA, 1982.

[47] Amir Ostadi, Amirnaser Yazdani, and Rajiv K. Varma, "Modeling and Stability Analysis of a DFIG-Based Wind-Power Generator Interfaced With a Series-Compensated Line," *IEEE Trans. on Power Delivery*, vol. 24, no. 3, pp. 1504-1514, July 2009.

[48] F.A. Bhuiyan, and A. Yazdani, "Multimode Control of a DFIG-Based Wind-Power Unit for Remote Applications," *IEEE Trans. on Power Delivery*, vol. 24, iss. 4, pp. 2079-2089, 2009.

[49] Yunwei Li, D.M. Vilathgamuwa, and Poh Chiang Loh, "Design, analysis, and real-time testing of a controller for multibus microgrid system," *IEEE Trans. on Power Electronics*, vol. 19, iss. 5, pp. 1195-1204, 2004.

[50] Haihua Liu, Hongzhong Ma, Lin Chen, Guanghe Li, Tongkuang Liu, and Feng Zhao, "Modeling and Control of DFIG Based Wind Turbine/Storage System in Islanded Operation," *in Proc. IEEE International Conference on Sustainable Power Generation and Supply*, pp. 1-6, 6-7 April 2009.

[51] John P. Barton and David G. Infield, "Energy Storage and Its Use with Intermittent Renewable Energy," *IEEE Trans. on Energy Conv.*, vol. 19, no. 2, June, 2004.

[52] Mohamed Rashed, Abd El-Hady Ghanem, Adel El-Sayes, and III. Mansy, "Control Strategy for an Isolated DFIG Based Micro-Grid with Integrated Super-Capacitors," *the Online Journal on Electronics and Electrical Engineering*, vol. 1, no. 2.

[53] Evangelos I. Vrettos, and Stavros A. Papathanassiou, "Operating Policy and Optimal Sizing of a High Penetration RES-BESS System for Small Isolated Grids," *IEEE Trans. on Energy Conversion*, vol. pp, iss. 99, pp. 1-13, April, 2011.

[54] Krause, O. Wasynczuk, and S. D. Sudhoff, *Analysis of Electric Machinery and Drive Systems*, IEEE Press, Wiley-Interscience, John Wiley & Sons, Inc., New Jersey, 2002.

[55] Yi Guo, John N. Jiang, and Choon Yik Tang, "Nonlinear Control of Wind Power Generation Systems," *in Proc. IEEE Power Systems Conference and Exposition*, pp. 1-7, 15-18 Mar. 2009.

[56] Davide Aguglia, Philippe Viarouge, Rene Wamkeue, and Jerome Cros, "Optimal Selection of Drive Components for Doubly-Fed Induction Generator Based Wind Turbines," LEEPCI Laboratory, Laval University, G1K 7P4 Quebec (QC), CERN - European Organization for Nuclear Research, Electric power converter Group, CH-1211 Geneva 23 UQAT, Abitibi-Témiscamingue Quebec University, J9X 5E4 Quebec (QC) Canada, Switzerland.

[57] Florin Iov, Anca Daniela Hansen, Poul Sørensen, and Frede Blaabjerg, "Wind Turbine Blockset in Matlab/Simulink," Aalborg University, Denmark, March 2004.

[58] Boubekeur Boukhezzar and Houria Siguerdidjane, "Nonlinear Control of Variable-Speed Wind Turbine Using a Two-Mass Model," *IEEE Trans. on Energy Conversion*, vol. 26, no. 1, pp. 364-372, March 2011.

[59] Wei Qiao, Wei Zhou, J.M. Aller, and R.G. Harley, "Wind Speed Estimation Based Sensorless Output Maximization Control for a Wind Turbine Driving a DFIG," *IEEE Trans. on Power Electronics*, vol. 23, no. 3, pp. 1156-1169, May 2008.

[60] Hansen, and G. Michalke, "Voltage grid support of DFIG wind turbines during grid faults," *in Proc. European Wind Energy Conference and Exhibition*, May 2007.

[61] E. Tremblay, A. Chandra, and P. Lagace, “Grid-side converter control of DFIG wind turbines to enhance power quality of distribution network," *in Proc. IEEE Power Engineering Society General Meeting*, Jun. 2006.

[62] Endusa Billy Muhando, Tomonobu Senjyu, Aki Uehara, Toshihisa Funabashi, and Chul-Hwan Kim, “LQG Design for Megawatt-Class WECS With DFIG Based on Functional Models' Fidelity Prerequisites,” *IEEE Trans. on Energy Conversion*, vol. 24, no. 4, pp. 893-904, Dec. 2009.

[63] Gan Dong, “Sensorless and Efficiency Optimized Induction Machine Control with Associated Converter PWM Modulation Schemes," *Ph.D. dissertation,* Tennessee Technological University, Dec. 2005.

[64] Myoung-Ho Shin, Dong-Seok Hyun, Soon-Bong Cho, and Song-Yul Choe, “An Improved Stator Flux Estimation for Speed Sensorless Stator Flux Orientation Control of Induction Motors,” *IEEE Trans. on Power Elex.*, vol. 15, no. 2, pp. 312-318, Mar. 2000.

[65] Parsons et al., “Grid Impacts of Wind Power: A Summary of Recent Studies in the United States”, *Wind Energy*, vol. 7, no., pp. 87-108, 2004.

[66] D. Feng, B.H. Chowdhury, M.L. Crow, and L. Acar, “Improving voltage stability by reactive power reserve management,” *IEEE Trans. on Power Systems*, vol. 20, no.1, pp. 338-345, February 2005.

[67] Gabriela Glanzmann, *FACTS Flexible Alternating Current Transmission Systems*, EEH - Power Systems Laboratory ETH Z¨urich, Jan. 2005.

[68] Ben-Sheng Chen, and Yuan-Yih Hsu, “An Analytical Approach to Harmonic Analysis and Controller Design of a STATCOM,” *IEEE Trans. Power Delivery*, vol. 22, pp. 423-432, Jan. 2007.

[69] M. Salles, J. R. Cardoso, A. P. Grilo, C. Rahmann, and K. Hameyer, “Control Strategies of Doubly Fed Induction Generators to Support Grid Voltage,” *in Proc. IEEE Electric Machines and Drives Conference*, pp. 1551-1556, May 2009.

[70] Daniel Karisson and David J. Hill, “Modelling and Identification of Nonlinear Dynamic Loads in Power System,” *IEEE Trans. Power System*, vol. 9, no. 1, pp. 157-166, Feb. 1994.

[71] C.-F. LU, C.-J. WU, and C.-C. Liu, “Dynamic modeling of battery energy storage system and application to power system stability,” *IEE Proc. Generation Transmission Distribution,* vol. 142, iss. 4, pp.429-435, July 1995.

[72] H. Karimi Davijani and O. Ojo, “Dynamic operation and control of a multi-DG unit standalone Microgrid,” *in Proc. Innovative Smart Grid Technologies (ISGT), IEEE PES*, pp. 1-7, Jan. 2011.

APPENDIX

Test System Data

Wind Turbine		**STATCOM**	
Blade radius	30.66 m	dc-link voltage	1600 V
Number of blades	3	dc-link capacitor	60 mF
Cut-in/cut-out wind speed	4/25 m/s	Link resistance r_s	0.03 Ω
Gear ratio	71.28	Link inductance L_s	1 mH
Generator and Grid Network		Switching frequency f_{sw}	1 kHz
Rated capacity	1.5 MW	**Electric Load**	
Optimal rotor speed	2158 rpm	Load resistance r_L	0.78 Ω
Stator resistance	2.3 mΩ	Load inductance L_L	2 mH
Rotor referred resistance	2 mΩ	Capacitor C_m	0.5 mF
Stator inductance	2.93 mH	P/P_{non}	0.5/0.5 MW
Rotor referred inductance	2.97 mH	Q/Q_{non}	0.2/0.2 Mvar
Mutual inductance	2.88 mH	**Wind Field**	
Shaft inertia	18.7 kg.m^2	Rated wind speed	12 m/s
No of poles	4	Air density	1.225 kg/m^3
Base Frequency	60 Hz	**Distribution Grid**	
Rated Voltage (line to line)	690 V	Voltage	690 V
dc-link Voltage	1400 V	Line resistance r_L	0.2 Ω
dc-link capacitor	60 mF	Line inductance L_L	10 mH
	Pitch Controller		
Max/min pitch angle $\beta_{max/min}$	30/0 deg	Max/min pitch rate $\dot{\beta}_{max/min}$	10/-10 deg/s

VITA

Bijaya Pokharel was born on March 4, 1985 in Dolakha, Nepal. He completed his Bachelor's Degree in Electrical Engineering from Institute of Engineering (IOE), Tribhuvan University, Kathmandu, Nepal in 2007. He joined Tennessee Technological University, Cookeville, Tennessee in January 2010 and received a Master of Science Degree in Electrical Engineering in December 2011.